TECHNISCHE UNIVERSITÄT MÜNCHEN

Fakultät für Elektrotechnik und Informationstechnik

Hybrid Optical Coherence Tomography/Optoacoustic endoscope for esophageal imaging

Zakiullah Ali

Vollständiger Abdruck der von der Fakultät für Elektrotechnik und Informationstechnik der Technischen Universität München zur Erlangung des akademischen Grades eines

Doktors der Ingenieurwissenschaften

genehmigten Dissertation.

Vorsitz: Prof. Dr. Bernhard Wolfrum

Prüfer der Dissertation:

1. Prof. Dr. Vasilis Ntziachristos
2. Prof. Dr. Oliver Hayden

Die Dissertation wurde am 27.12.2021 bei der Technischen Universität München eingereicht und durch die Fakultät für Elektrotechnik und Informationstechnik am 10.06.2022 angenommen.

Abstract

Early detection of esophageal cancer is critical to increase the success rate of treatment, with late detection leading to over 500,000 annual deaths worldwide. Moreover, late disease detection incurs healthcare costs ranging between $80,000-250,000 per patient, making esophageal cancer among the most expensive cancers to treat. White light endoscopy (WLE) is currently the prominent technique used in the detection of esophageal cancer but has limited ability to detect disease in early phases, when the disease is primarily located beneath the tissue surface. Therefore, current screening regimes rely on quadratic biopsies to increase the likelihood of detecting traces of dysplasia. This process of routine screening is however costly, invasive, and prone to sampling errors as dysplasia can be confined to very small areas and appear macroscopically identical to non-dysplastic mucosa.

To meet the increasing demand for endoscopic surveillance, less invasive 3D imaging of the gastrointestinal (GI) tract by optical coherence tomography (OCT) endoscopy, able to reveal layered esophageal structure, has been explored. However, OCT has yet to be widely accepted into clinical practice as the detection and grading of early disease remains challenging because OCT relies solely on backscattering of tissue where biological origins of differences in the measured scattering signals are difficult to decipher and imaging is limited to superficial features. Complimentarily, optoacoustic (OA) endoscopy provides 3D high resolution label-free functional imaging in-vivo and offers rich contrast at depths greater than OCT. Hence, OA is well suited for endoscopic applications revealing metabolic information of the esophageal lining. The combination of molecular imaging with OA and structural imaging with OCT modalities may provide routes for improved endoscopic diagnosis and detection of early signs of dysplasia. Here, replacement of 2D user-dependent observations following the WLE protocol with objective, quantitative, 3D measurements of the entire esophagus wall is expected to deliver morphological and pathophysiological cancer and pre-cancer features not available to WLE.

The work presented herein focused on developing a hybrid OCT-OA endoscope for imaging the human gastrointestinal tract. Clinical translational challenges to overcome included high hybrid imaging frame rates to avoid motion artifacts, large fields of view to expedite the screening procedure, careful design of sensors with a miniaturized form factor to be inserted through hollow bodily cavities and appropriate probe geometry to ensure mechanical stability during imaging. Several hybrid endoscopic design concepts such as forward /side viewing, proximal/distal rotation

and common mode/ split path illumination are discussed. The best concepts were forwarded to the development phase where each design elements including the rotational motor, ultrasound detector, capsule interface, optical probe, and back-end system performance was characterized. The optical system consisted of a customized double clad fiber coupler to combine the imaging modalities and beam shaping at the probe tip was achieved with a custom-made grin lens designed in Zemax. To select the best material for the capsule interface a transmission efficiency test of both acoustics and illumination were performed on a select number of materials with the best performing material selected as the capsule interface. The hollow shaft motors used during the study were standard models available online.

In regard to the endoscopic acoustic detector. Several single element benchtop ultra-broadband transducers with different materials, dimensions, and acoustic sensitivity profiles including axicon and spherical were developed and characterized in 3D against a broadband omnidirectional point source. The greatest performing transducers were lithium niobate based with the axicon transducer offering an elongated sensitivity beam. However, during OA imaging the spherical transducer delivered better image quality when compared to the axicon. Therefore, a rigorous 3D acoustic simulation study was conducted to demonstrate that the axicon transducer behaves differently to acoustic point and line sources. For this reason, the axicon would be better suited for microscopy applications where depth of focus could be extended. Hence an OA microscope was built to demonstrate the improved depth of focus performance with a broadband axicon detector. In response the next generation spherical detector was equipped with integrated slip rings to allow endoscopic distal rotation.

Aside from the technical development of the endoscope design, two image reconstruction methods employed for linear scanning configurations were explored in cylindrical coordinates for OA endoscopy applications. The algorithms were studied and optimized to assess the feasibility of real time B scan image reconstruction for OA endoscopy over several mm’s of depth.

Lastly the translational potential of hybrid OA-OCT endoscopic imaging was demonstrated in a controlled ex-vivo experiment by measuring excised esophageal samples from a pig and in-vivo human mucosal tissue. Synchronous helical pull back acquisitions at video rate was performed with the endoscope. The co-registered OCT-OA images revealed 3D structural and pathophysiological information of the esophageal lining that could be used to improve detection of esophageal cancer. Overall, the experimental findings reported herein show the hybrid OCT-

OA endoscope offers promising translational characteristics for imaging the human GI tract in the near future.

Contents

Chapter 1 Introduction 10
1.1. Present day Endoscopy 12
1.1.1 White light endoscopy 12
1.1.2 Optical endoscopy 13
1.1.3 Ultrasound endoscopy 14
1.2. Objectives addressed in this thesis 14
1.3. Outline of this dissertation 17
Chapter 2 Background 19
2.1. Optoacoustic Imaging (OA) 19
2.1.1 OA signal generation 19
2.1.2 OA Spatial Resolution 22
2.1.3 OA penetration depth 23
2.1.4 Existing OA endoscopes for esophageal imaging 25
2.2. Optical Coherence Tomography (OCT) 26
2.2.1 OCT signal generation 26
2.2.2 OCT spatial resolution 28
2.2.3 OCT penetration depth 29
2.2.4 Existing OCT endoscopes for esophageal imaging 30
2.3. Preceding implementations of OCT-OA endoscopes 31
2.4. Summary and discussion 32
Chapter 3 Optoacoustic endoscopy sensor development 33
3.1. Optoacoustic transducer characterization 34
3.1.1 Optoacoustic transducer characterization rig 35
3.2. Optoacoustic transducer architecture for endoscopy 36
3.2.1 Desired sensor specifications 37
3.3. Piezoelectric Transducer Crystals 38
3.3.1 First generation benchtop Transducers 39
3.3.2 Second generation benchtop Transducers 43
3.3.3 Third generation Benchtop transducers 47
3.4. Raster scanning optoacoustic mesoscopy 52
3.5. 3D optoacoustic transducer simulations 54
3.6. Raster scanning optoacoustic microscopy 59
3.7. Summary and discussion 71
Chapter 4 Hybrid OCT-OA endoscope design concepts 73
4.1. Forward vs side viewing probes 73
4.2. Proximal vs distal scanning 74

4.3. Balloon vs capsule endoscope interface 74
4.4. Common path vs split path imaging 76
4.5. Summary 77
Chapter 5 Optical architecture for OCT-OA endoscopy 78
5.1. Double clad fiber coupling 78
5.2. OA Optical back-end console setup 80
5.3. OCT Optical back-end console setup 80
5.4. Multimodal back-end console optical setup 82
5.5. Multimodal distal capsule optical setup 83
5.5.1 Optics on tip arrangement 83
5.5.2 Capsule cover and sealing window material 84
5.5.3 Optics on tip optomechanic simulation and conceptualization 84
5.5.4 Optoacoustic endoscopy maximum permissible exposures 88
5.5.5 Optical probe manufacturing 90
5.6. Summary and discussion 91
Chapter 6 Hybrid OCT-OA endoscopy prototypes 93
6.1. Endoscopic transducers with slip rings 94
6.2. 16mm Semi capsule prototype 95
6.2.1 Semicapsule experimental methods 96
6.2.2 Semicapsule experimental results 98
6.2.3 Discussion of semicapsule capability 105
6.3. 12.5mm Partial capsule prototype 108
6.3.1 Partial capsule experimental methods 109
6.3.2 Partial experimental results 113
6.3.3 Discussion of partial capsule capability 118
6.4. Summary and discussion 120
Chapter 7 OA endoscopy image reconstruction 122
7.1. Optoacoustic image reconstruction in cartesian coordinates 123
7.1.1 Delay and sum algorithm 123
7.1.2 Phase shift migration 125
7.1.3 Cartesian Bscan image reconstruction with simulated data 128
7.1.4 Cartesian Bscan image reconstruction with experimental data 130
7.2. Optoacoustic image reconstruction in cylindrical coordinates 132
7.2.1 Cylindrical delay and sum 132
7.2.2 Cylindrical phase shift migration 134
7.2.3 Cylindrical Bscan image reconstruction with simulated data 137
7.2.4 Cylindrical Bscan image reconstruction with experimental data 139
7.2.5 Feasability of Cylindrical Bscan image reconstruction at 50Hz 141

7.3. Summary and disucussion....143
Chapter 8 Conclusion and outlook....143
8.1. Conclusion....143
8.2. Outlook....146
Acknowledgements....150
Publications....151
References....152

List of abbreviations

WLE	White-light endoscopy
OCT	Optical coherence tomography
OA	Optoacoustics
EAC	Esophageal adenocarcinoma
CLE	Confocal laser endomicroscopy
FE	Fluorescence endoscopy
UWB	Ultra wide band
RSOM	Raster scanning optoacoustic mesoscopy
GI	Gastrointestinal
DCF	Double clad fiber
DCFC	Double clad fiber coupler
SAFT	Synthetic aperatrue focusing technique
PSM	Phase shift migration
DAS	Delay and sum
CF	Coherence factor
CDAS	Cylindrical delay and sum
CPSM	Cylindrical phase shift migration
MIP	Maximum intensity projection
MPE	Maximum permissible energy

Chapter 1 Introduction

Early detection of cancer is critical to increasing the success rate of cancer treatment. In particular, esophageal cancer has a very low recovery rate the later the detection. Symptomatic presentations occur late in the course of the disease, attributing to ~ 509,000 annual deaths worldwide [1]. Aside from the high fatality rate, treatment of late diseases incurs costs in the range between $80,000-250,000 per patient lifetime making esophageal cancer among the most expensive diseases to treat in oncology [2]. In the western world 50% of esophageal cancers are known as adenocarcinoma (EAC). This condition has an identifiable precancerous stage (Barrett's esophagus) that can be monitored by endoscopic surveillance [3]. Figure 1 reveals progression of cancer growth from normal lining to invasive carcinoma, an intermediate transition called dysplasia prior to the growth of carcinoma offers a stage at which the disease can be treated using endoscopic interventions such as radio frequency ablation. Unfortunately, due to aging and more overweight population the incidence rates of Barret's esophagus and esophageal cancer are increasing.

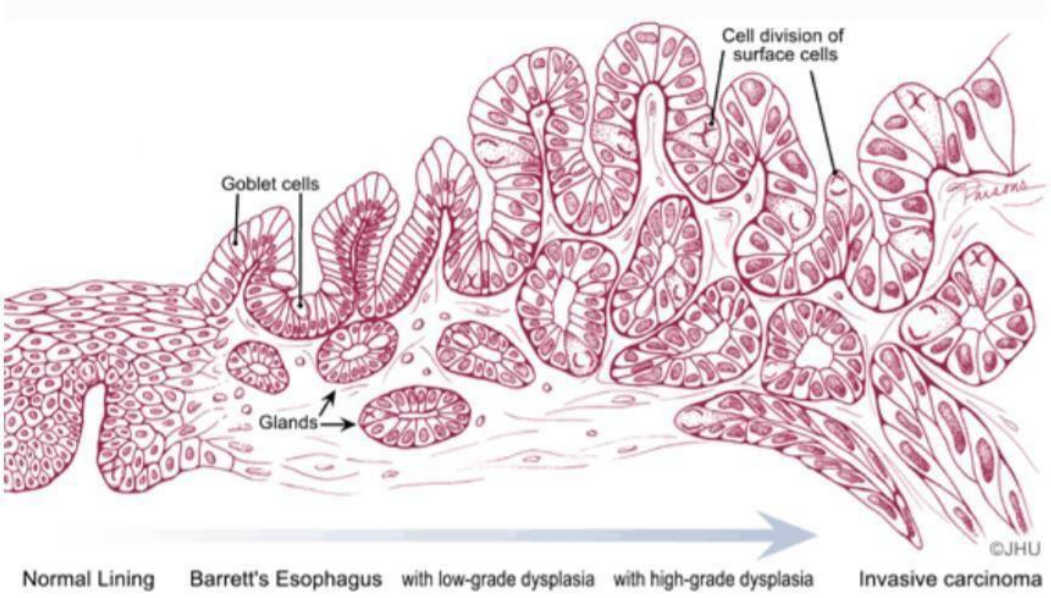

Figure 1: Progression of cancer growth from normal lining to invasive carcinoma [4]

Today white light endoscopy (WLE) is a prominent technique used in the detection of esophageal cancer; however, the imaging modality provides poor contrast of biological tissue. Therefore, current screening regimes rely on identifying Barrett's segments and performing quadraticbiopsies within a region to increase the likelihood of detecting for traces of dysplasia. The extracted samples are then carefully prepared, and contrast agents introduced before performing

pathological analysis. This process of routine screening is under dispute because it is costly, invasive and prone to sampling errors as dysplasia can be confined to very small areas and appear macroscopically identical to non-dysplastic mucosa. Sampling for quadratic biopsies may result in false negatives in whom dysplasia is present but undetected during the procedure. Furthermore, patients who have Barrett's esophagus and are at low risk of progression to EAC, undergo unnecessary biopsies leading to extensive waiting lists [2].

To overcome such problems and meet the increasing demand for endoscopic surveillance, research has led to the rapid emerging area of early disease detection within the field of biophotonics. Two prominent imaging modalities include optical coherence tomography (OCT) and optoacoustic imaging (OA).

Optical coherence tomography (OCT) is a high-resolution and noncontact imaging technique that measures back-scattered radiation generated from an infrared light source directed at the tissue under examination. OCT is capable of having 3D tomograms of the internal microstructures of various biological samples, based on scattering and reflecting. The OCT signal is obtained from the interference between the beam back-reflected from the reference arm and the light backscattered from the internal layers of the sample, which depends on intrinsic refractive index gradients. However, OCT imaging is unable to present the optical absorption property of the sample and limited to a penetration imaging depth of ~1mm [4].

OA relies on irradiating the tissue surface with low energy pulses of laser light with optical wavelengths from the ultraviolet to near–infrared spectrum. Local absorption of electromagnetic energy is accompanied by rapid heating, which subsequently leads to thermal expansion and the generation of wideband ultrasonic emission. An image of the absorption distribution can be recovered by detecting the ultrasonic waves as they propagate to the surface [5]. Additionally, OA has the ability to penetrate deeper than OCT imaging [131].

To overcome current problems associated with esophageal imaging a hybrid endoscope performing simultaneous OCT–OA endoscopy could improve patient outcomes. Although previous attempts of hybrid OCT-OA endoscopes have focused on miniaturization for small animal organs which exhibit poor contact with the human esophagus and reduced SNR. Additionally, all designs suffer from low frame rates leading to motion artifacts and thereby limit clinical translation. Hence, the goal of this work is the technical development of a hybrid optical and optoacoustic endoscope for esophageal tracking of the human GI track, combining the

structural information obtained from OCT with the pathophysiological data acquired from OA. The instrument would have the potential to perform in vivo early staging of precancerous conditions to improve the probability of detecting for dysplasia by replacing two dimensional qualitative and user dependent observations with objective, quantitative, three-dimensional measurements of the entire esophagus wall, delivering morphological and pathophysiological cancer and pre-cancer features not available to white light endoscopy.

1.1. Present day Endoscopy

1.1.1 White light endoscopy

There are three main types of commercial white light endoscopes for examining the esophagus including fiber bundle, optics on tip and capsule endoscopes. Compared to the first two, capsule endoscopy is a less invasive examination method that does not require sedation during the examination process and reduces the patient's discomfort [135]. Furthermore, the capsule (Fig 2) has the advantage of being able to swallow, so this practice could be administered by a nurse, simplifying the surveillance examination. However, capsule endoscopy faces several limitations; for example, it cannot obtain biopsies or perform therapy and once swallowed it cannot be controlled remotely, and images may be limited by position and transit as it moves through the gastrointestinal tract [6].

Figure 2: The PillCam Capsule Endoscope [7]

The main limitation of all these white light endoscopes is that they employ purely white light intensity-based imaging, thereby providing poor contrast images of the esophageal tissue surface. Current screening regimes rely on endoscopes identifying Barrett's segments and performing quadratic biopsies every 2 cm's within the region to increase the likelihood of detecting for traces of high-grade dysplasia. The extracted samples are then carefully prepared and contrast agents

introduced before performing image analysis [8]. Unfortunately, this strategy has a high false negative rate as the endoscopist is simply guessing where to extract a biopsy of interest for further examination in spite of the fact that dysplasia can be confined to very small regions and appear macroscopically identical to non-dysplastic mucosa under the presence of white light.

1.1.2 Optical endoscopy

The use of optical techniques for early detection of esophageal cancer in-vivo is a rapidly emerging area within the field of biophotonics and is currently being explored as an alternative to WLE. Early studies of optical coherence tomography [19-24] , fluorescence endoscopy [14-18], confocal laser endomicroscopy [9-13] have demonstrated promising results of early stage dysplasia detection.

Confocal laser endomicroscopy (CLE) is a promising imaging tool that allows microscopic subsurface imaging of the gastrointestinal tract in-vivo. The imaging modality permits direct histologic imaging in vivo where changes in vessels, connective tissue and in the cellular architecture can be evaluated during routine endoscopy examinations [9,11-13]. CLE human clinical trial studies were able to distinguish cancerous from normal epithelium via in-vivo histology with high accuracy. The diseased tissue was diagnosed immediately during routine endoscopy facilitating early treatment of esophageal cancer [11,12]. Although the acquisition of confocal images without movement artifacts in a known problem limiting the number of good images during surveillance and the intrinsic limitation of photon scattering in tissue limits penetration depths up to <250µm [12]. Therefore, only the mucosal layer can be visualized by CLE. Finally, CLE interrogates superficial lumen volumes with small field of views (<0.1mm^3) preventing application for surveillance endoscopy [9, 13].

Fluorescence endoscopy (FE) holds potential to improve diagnosis and guide therapy during endoscopic examination. FE enables real-time visualization of complex biochemical processes involved in both normal and disease states in-vivo with labels that can be applied during the endoscopic examination [14-18]. In particular, a fluorescent label has been shown to bind specifically to high grade dysplasia and adenocarcinoma and thereby emit light when excited at a specified wavelength to distinguish pathology in-vivo [18]. A recent in-vivo human pilot study based on a custom-built fluorescence endoscope paired to a high-definition white light endoscope demonstrated 33% improved dysplasia and early EAC lesion detection in Barrett's esophagus patients with fluorescence endoscopy compared to WLE [15]. However, translation from bench to

bedside remains challenging because of production of the imaging agent, safety and toxicity requirements and relatively high initial costs [16]. A further restriction is the higher level of clinical regulatory requirements to satisfy when compared against label-free imaging methods.

OCT endoscopy has exhibited promising images of the human esophagus wall revealing layered mucosal features [19]. A recent comparative study demonstrated dysplasia detection of 33.7% with OCT endoscopy compared to 5.7% with random biopsies using the standard WLE procedure [20]. Despite these merits, OCT endoscopy has yet to be widely accepted into clinical practice as the grading and detection of dysplasia remains challenging since the biological origins of differences in the scattered signals of healthy and neoplastic tissue are difficult to interpret [21,22]. Moreover, OCT imaging is limited to superficial structures, impairing clinical applications[23,24]. OCT endoscopy is discussed further in section 2.2.4

1.1.3 Ultrasound endoscopy

Endoscopic ultrasound (EUS) is an invasive procedure to assess esophageal cancer staging, by producing cross-sectional images of the gastrointestinal tract over large field of views [25-28]. The modality allows determination of tumor invasion depth and local lymph node metastasis. An EUS image is formed following the pulse-echo principle where reflections of the interrogation sound wave occur between the structures of the esophageal lining. The strength of the reflection results in single amplitude and the time it takes to return to the probe provides the information to generate an image. Although there is little difference between the anatomical features andtherefore the strength of reflections within the lining are weak. Hence, EUS exhibits poor imagingcontrast thereby limiting application for the detecting of early phase neoplasia in-vivo or visualization of tumor metastasis [30,31]. Furthermore, clinical trials have suggested that pre- treatment EUS for high grade dysplasia or intramucosal esophageal adenocarcinoma is unnecessary and might in fact be misleading as a result of low detection accuracy [32-34]. Therefore, EUS today requires methods to enhance image contrast to improve accuracy to realizethe full potential of the imaging modality [32-34].

1.2. Objectives addressed in this thesis

Optoacoustic imaging is a hybrid approach, which uses light pulses absorbed by interrogating biological tissue to induce the emission of sound waves, which are detected by an ultrasound

receiver [5]. Optoacoustics offers greater imaging depths when compared to purely optical imaging methods which rely on ballistic photons and higher contrast when compared against ultrasound endoscopy. Due to these features, the modality could be a powerful tool for the evaluation and staging of malignant tissue within the human body. Presently optoacoustic mesoscopy operating at ultra-wideband (UWB) ultrasound frequencies offers unique imaging characteristics by detecting optical absorption through several millimeters of depth with resolutions in the range of tens of micrometers [35,36]. This performance has been implemented as raster scanning optoacoustic mesoscopy (RSOM) to yield detailed visualization of different skin features, including dermal vasculature [37,38] or melanoma related angiogenesis [39], and the label-free quantification of inflammation associated with psoriasis, eczema or vasculitis [36].

Mesoscopic performance could also be useful in human gastrointestinal (GI) endoscopic applications to yield similar sub-surface visualization of optical contrast associated with vascularization and angiogenesis, possibly leading to better staging of cancer with optoacoustic endoscopy. Although over the last two decades the developments in optoacoustic endoscopy suffer from low imaging frame rates due to low pulse repetition rates and slow scanning units [40-49]. Consequently, motion artifacts during in-vivo scanning results in inaccurate spatial mapping and misinterpretation of data. Additionally, most present endoscope designs are based on small-animal studies with the intention to further miniaturize the probe to use via the working channel of white light endoscopes. These are unsuitable for human esophageal imaging due to an insufficient SNR and lateral resolution stemming from longer working distances [40-47].

The work reported within this thesis works towards the development of a video rate optoacoustic capsule endoscope suitable for human GI tract imaging. To improve the diagnostic potential of the endoscope, OCT is integrated into the design to provide 3D image fusion of molecular features from the absorption of OA light and anatomic structures from the scattering of OCT light. Hybrid imaging or image fusion has proven extremely useful for treatment and diagnosis in the fields of cardiology, oncology, and neurology, enabling localization of tumors and lesions, planning for radiotherapy, surgery and is fostering a new clinical environment where scientists across several specialties are collaborating for more accurate interpretation and improved patient outcome [50,51].

The main objectives of this this thesis include:

1. Development of an ultra-broadband optoacoustic endoscopic detector

The image performance in optoacoustic endoscopy depends markedly on the design of the transducer employed. Ideally high-resolution performance is required over several mms of depth. Initially a series of benchtop endoscopic detectors were manufactured and characterized following the development of a 4D optoacoustic transducer characterization rig. In particular, two detection geometries, spherical and axicon with central apertures for collinear illumination were explored for endoscopy with the axicon demonstrating an elongated sensitivity profile useful for endoscopy. The best performing transducers were integrated into a RSOM setup to assess OA image performance. Surprisingly, the spherical outperformed the axicon detector during imaging experimentation. As a result, a rigorous 3D kwave simulation was conducted to study the total impulse response of spherical and axicon detectors as a function of point and line sources. Based on experimental and simulation observations the axicon exhibited characteristics more useful for microscopy than endoscopy and therefore an optoacoustic axicon microscope was built to exploit the elongated sensitivity profile of the detector. The spherical detector design was elected to be further advanced into an endoscopic form factor.

2. Development of a video rate hybrid OCT-OA capsule endoscope

Several endoscopy design element concepts including forward/side viewing, proximal/distal scanning, balloon/capsule interface and common mode/split path illumination are illustrated with advantages and disadvantages discussed. The superior design elements are adopted into the first 16 mm optoacoustic endoscope prototype. Sensor characterization is performed to benchmark the endoscopic optoacoustic detector against the benchtop detector and imaging performed with several phantoms to evaluate video rate acquisition up to 50Hz Bscan rate and volumetric imaging. Following additional experiments, a secondary more user-friendly hybrid OCT- OA prototype with a 12.5mm diameter encompassing a smaller detector was developed. The secondary prototype was also characterized at 30Hz video rate with phantoms and followed by imaging of an ex-vivo pig esophageal sample and human mucosa tissue.

The reconstruction methods previously applied for RSOM in cartesian coordinates are extended to cylindrical coordinates for optoacoustic endoscopy. A Kwave simulation is performed to generate the optoacoustic endoscopy data in rotational mode over 360^0 and two algorithms in particular including delay and sum and phase shift migration are implemented to reconstruct B scans in cylindrical coordinates. A feasibility study of real time B scan reconstruction at 50Hz frame rate is performed to determine the best algorithm to apply in practice.

1.3. Outline of this dissertation

This work is outlined per chapter is as follows:

Chapter 2 presents the theoretical background of optical coherence tomography and optoacoustic imaging. The fundamentals of each modality are introduced describing the signal generation mechanism, image formation, resolution, and penetration depth characteristics. An in depth literature review of previous single modality OCT and OA endoscopy is provided. The chapter concludes with a discussion on the few implementations of OCT-OA hybrid endoscopes thus far.

Chapter 3 focuses on the development of optoacoustic endoscopic transducers. Two detection geometries, spherical and axicon are investigated with central aperture for collinear illumination. Several sensors with different materials and dimensions were manufactured. A robust characterization rig was designed to test all detectors in a controlled manner in 4D against a broadband omnidirectional point source. The best performing transducers were lithium niobate based with the axicon exhibiting an elongated sensitivity beam useful for endoscopy. However, in practice during OA imaging of a suture the axicon suffered from low lateral resolution when compared to the spherical detector. A meticulous 3D kwave study was performed to understand the behavior of the axicon transducer, the sensor was found to behave differently to acoustic line and point sources whereas the spherical transducer depicts a similar response. Observations indicated the axicon would be better catered towards microscopic applications and therefore an axicon optoacoustic microscope was built to validate the hypothesis. Alternatively, the spherical detector was selected to be further enhanced for endoscopic applications as the sensors lateral resolution remained independent of the acoustic sources shape under investigation.

Chapter 4 explores a number of endoscope design concepts, based on scanning technique,

illumination configuration, tissue to capsule interface and OCT-OA signal acquisition. The advantages and disadvantages of each concept are discussed, and the best concepts selected to be incorporated into the hybrid capsule design.

Chapter 5 presents the optical architecture of the hybrid endoscope, the back-end console optical architecture combining OCT and OA illumination into a single double clad fiber is detailed. In addition, an in-depth analysis on ZEMAX is performed to design the distal end capsule optics setup including an optical probe attached to the double clad fiber. The probe performs OCT-OA beam conditioning prior to interrogating esophageal tissue and is housed inside the endoscope which in turn is used to drive the B scan frame rate and the maximum permissible energy limits in-vivo. This lays the foundation to advance the design by augmenting scanning and sensing elements around the optical probe to produce the hybrid endoscope.

Chapter 6 describes the hybrid endoscopes developed including the 16mm semi capsule prototype and the 12.5mm partial capsule prototype. The 16mm semi capsule endoscope, an optoacoustic only endoscope was characterized, and imaging performance determined by imaging phantoms arranged in an Archimedean spiral with a pitch of 3mm in B scan and C scan mode at 50Hz frame. The limitations of the semi capsule prototype were addressed in the second-generation capsule called the 12.5mm partial capsule prototype which enabled hybrid OCT-OA imaging. Characterization was repeated and phantom, ex-vivo pig esophagus as well as in-vivo human mucosal tissue were imaged at 30 Hz B scan frame rate.

Chapter 7 adapts previous reconstruct methods including delay and sum and phase shift migration from cartesian coordinates to cylindrical coordinates for optoacoustic endoscopy. Both algorithms' capabilities are explored in simulations and experiments. Cylindrical Bscan image reconstruction at 50Hz is investigated to determine whether the algorithms could be applied with our endoscope for real time surveillance.

Finally, in chapter 8, the main findings of this thesis are summarized and the future advancements of the hybrid endoscope for in-vivo application are provided.

Chapter 2 Background

This chapter introduces the fundamentals of Optoacoustic imaging and Optical coherence tomography. The signal generation process is described and limitations on resolution and penetration depth are provided. In addition, previous implements of Optoacoustic, OCT and hybrid OCT-OA endoscopes for gastrointestinal applications are provided.

Subchapter 2.1 describes the OA signal generation process. Theoretical limits of lateral and axial resolution are explained and OA penetration depth is discussed. Previous implementations of OA endoscopes for imaging the esophagus are given.

Subchapter 2.2 explains the OCT signal generation process. Spatial resolution constraints are revealed and OCT's limited penetrated depth is highlighted. Previous implementations of OCT endoscopes for esophageal imaging are detailed.

Subchapter 2.3 lists previous implementations of hybrid OCT-OA endoscopes designed to date with design limitations listed preventing clinical adoption for human GI imaging.

2.1. Optoacoustic Imaging (OA)

2.1.1 OA signal generation

The optoacoustic effect is the generation of ultrasound signals via the absorption of modulated electromagnetic illumination typically in the nanosecond range. A standard dark field configuration is depicted in Figure 2.1. Localized heating within an absorber via modulated excitation gives rise to thermal expansion. This procedure is followed by relaxation where the thermal energy is converted to a broadband low amplitude acoustic signal usually measured by an ultrasound transducer. An image of the absorption distribution can be recovered by detecting the acoustic waves as they propagate to the surface using an array of ultrasonic transducers or mechanically scanning with a single element transducer. Although the effect dates to 1880, where Alexander Graham bell observed sound generation by the absorption of modulated sunlight [52], the first instances of OA imaging in the biomedical sector were considered in the mid 1990 due to light source advancements [53-56]. Ever since, research in the field has led to significant developments of dedicated light source technology, broadband ultrasonics, and image reconstruction. In response, the modality has shown to offer label free in-vivo functional and

molecular imaging with increased penetration when compared to purely optical techniques. OA imaging is considered now one of the largest research areas within the field of biophotonics.

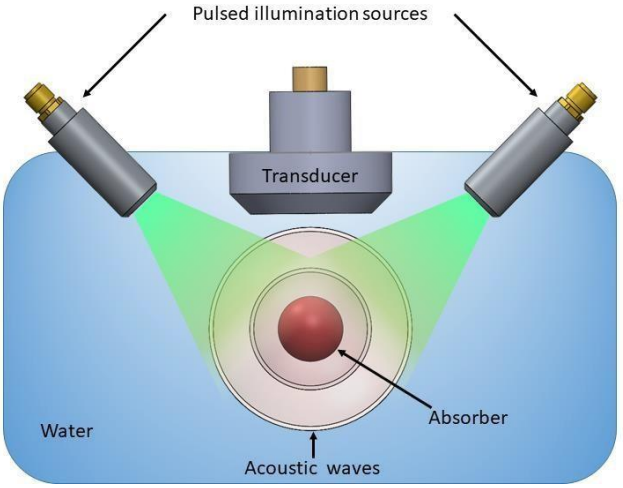

Figure 2.1. Dark field optoacoustic configuration. Pulsed illumination sources interrogate a spherical absorber within a water tank to generate broadband spherical waves detected by an ultrasound transducer. To generate a volumetric image, the light source and detector is scanned around the absorber. There are two essential parameters for the generation of an optoacoustic wave called thermal and stress relaxation times [57]. The thermal relaxation time (t_{th}) is given by:

$$t_{th} = \frac{d_c^2}{a_{th}} \tag{2.1}$$

Where d_c is the desired spatial resolution, α_{th} is the thermal diffusivity (approximately $1.4 \times 10^{-3} cm^2 s^{-1}$ in soft tissue). The stress relaxation time is given by:

$$t_s = \frac{d_c}{v_s} \tag{2.2}$$

Where v_s is the velocity of sound in the medium (average propagation speed in soft tissue is reported as 1540m/s). Hence, for a desired resolution of $d_c = 20\mu m$ in soft tissue the thermal and stress relaxation times should be less than $t_{th} = 2.85ms$ and $t_s = 13ns$. For optoacoustic generation the laser pulse duration should satisfy both criteria. In practice, lasers below 10 nanosecond duration are promoted.

During pulsed excitation, the increase in volume expansion can be mathematically expressed as:

$$\frac{dV}{V} = -kp + \beta T \tag{2.3}$$

Where k is the isothermal compressibility (Pa^{-1}), p is the change in pressure (Pa), β is the thermal coefficient of volume expansion(K^{-1}) and T expresses the change in temperature (K) given by:

$$T = \frac{n_{th}A_e}{\rho C_v} \tag{2.4}$$

Here, n_{th} is expressed as the percentage of light absorbed. A_e is the specific optical energy deposition (J/m^3) , ρ is the mass density (kg/m^3) and C_v is the specific heat capacity at constant volume [J/(kgK)]. Assuming the time parameters criterion are satisfied the increase in volume expansion is negligible ($\frac{dV}{V} = 0$) and therefore the initial pressure rise p_0 from equation 2.3 can be expressed as:

$$p_0 = \frac{\beta T}{k} \tag{2.5}$$

Substituting equation 2.4 into 2.5 and defining the Gruneisen parameter Γ we obtain:

$$p_0 = \frac{\beta}{k\rho C_v} n_{th}A_e = \Gamma n_{th}A_e \tag{2.6}$$

Assuming linear optical absorption, A_e is proportional to optical fluence F (J/cm^2) . Therefore, equation 2.6 can be expressed as:

$$p_0 = \Gamma n_{th}\mu_a F \tag{2.7}$$

Where μ_a is the optical absorption coefficient (cm^{-1}). The initial pressure p_0 being proportional to the optical absorption and fluence gives rise to a acoustic wave propagation at the speed of sound in the medium governed by the wave equation [57]:

$$(\nabla^2 - \frac{1}{v_s^2}(\frac{d^2}{dt^2}))\, p(r,t) = -\frac{\beta}{C_p}\frac{dH}{dt} \tag{2.8}$$

Where C_p is the specific heat capacity at constant pressure [J/(kgK)], H is the thermal energy

deposited per unit volume per unit time. Solving equation 2.8 with the Green function under delta-pulse excitation with zero ultrasound attenuation, the optoacoustic wave can be expressed as:

$$p_{\delta T}(r,t) = \frac{1}{4\pi v_s^2}\frac{d}{dt}\left[\int dr' \frac{p_0(r')}{|r-r'|}\delta\left(t - \frac{|r-r'|}{v_s}\right)\right] \tag{2.9}$$

Where $p_0(r')$ is the initial pressure at location r'. For pulsed illumination with finite duration, the optoacoustic wave generated is determined by convolution:

$$p(r,t) = \int_{-\infty}^{\infty} dt' p_{\delta T}(r, t-t') S(t') \tag{2.10}$$

where S(t) is the temporal profile of the pulse.

2.1.2 OA Spatial Resolution

Optoacoustic spatial resolution is a function of the broadband ultrasound frequencies generated given excitation with a nanosecond pulsed laser to meet time confinements. Depending on the size of an optical absorber, generated frequencies can range from several hundreds of kilohertz to hundreds of megahertz with smaller absorbers owing to higher frequencies. Although, as propagation of sound experiences frequency-dependent acoustic attenuation by soft tissues, optoacoustic spatial resolution scales with depth. Other resolution limiting factors include detector bandwidth, aperture geometry and element size.

If the impulse response of an optoacoustic detector has a gaussian profile, the axial resolution can be estimated by [126]:

$$R_a \approx 0.88\frac{v_s}{B} \tag{2.11}$$

where B is the -6 dB frequency bandwidth of the sensor.

On the other hand, under diffuse illumination the lateral resolution for a focused detector is acoustically limited and can be approximated by [126]:

$$R_{l_a} \approx 0.71\lambda_0 \frac{f}{\frac{D}{2}} \tag{2.12}$$

where λ_0 is the acoustic wavelength, f is the focal length and D is the sensor diameter

For superficial applications, an optically focused interrogation beam offers improved lateral resolution defined by the focus beam diameter, though penetration depth is sacrificed as a focused beam significantly suffers from optical scattering. In this instance, lateral spatial resolution is purely limited by optical diffraction which is a function of wavelength and lens numerical aperture (NA):

$$R_{l_o} \approx 0.5\frac{\lambda}{NA} \tag{2.13}$$

where λ is the laser wavelength, NA is the numerical aperture of focusing lens. Axial resolution remains acoustically limited by equation 2.11.

2.1.3 OA penetration depth

For purely optical imaging, the depth is typically limited to superficial applications due to optical absorption and substantial light scattering in tissue. As depicted in Figure 2.2 the optical absorption is a function of wavelength, hence appropriate selection of wavelength allows for increased penetration depth. Acoustic attenuation on the other hand is orders of magnitude lower in tissue. This characteristic allows excited optical absorbers at greater depths to be resolved acoustically. Hence Optoacoustics realizes images with increased penetration depth and high spatial resolution in comparison to pure optical imaging methods. The hybrid modality's penetration depth is limited by the combination of optical and acoustic attenuation.

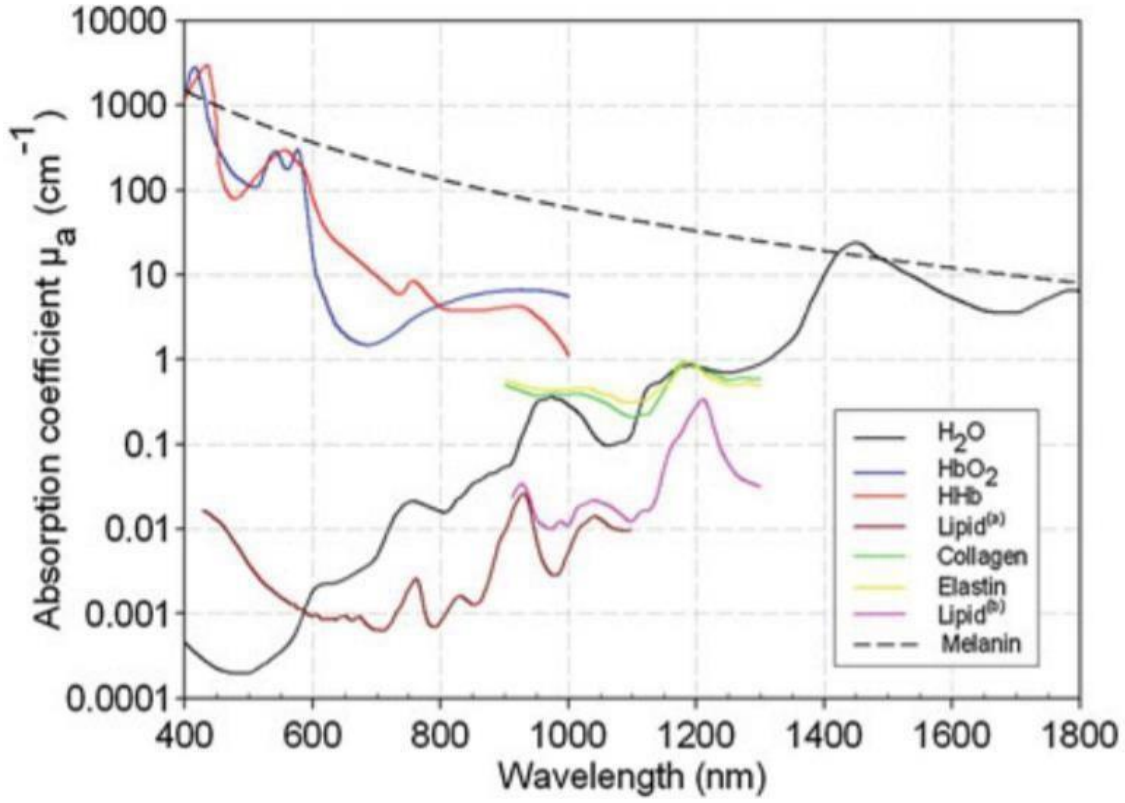

Figure 2.2. Absorption coefficient spectra of endogenous tissue chromophores. Red line: oxyhemoglobin, blue line: deoxyhemoglobin, black line: water (80% by volume), brown line: lipid (a) (20% by volume in tissue), lipid (b), pink line, black dashed: melanin, Collagen (green line) and elastin (yellow line) spectra [57].

The optoacoustic optical attenuation can be expressed by the effective attenuation coefficient derived from diffusion theory:

$$\mu_{eff} = (3\mu_a(\mu_a + \mu_s^{'}))^{1/2} \tag{2.14}$$

where μ_a is the absorption coefficient and μ'_s is the reduced scattering coefficient. Within homogenous scattering media beyond a depth of 1mm, electromagnetic waves become diffuse and irradiance decays exponentially as a function of depth. The $1/\mu_{eff}$ depth at which the irradiance has reduced by 1/e is termed the penetration depth. For instance, at a laser wavelength of 700 nm interrogating tissue comprised with concentrations of HbO_2 and HHb, water and lipids provides an estimated value of $\mu_{eff} \sim 1.3 cm^{-1}$. The $1/\mu_{eff}$ penetration depth in this instance is therefore approximately 0.8 cm [5]. This finding suggests beyond the first millimeter; light is attenuated by a factor of 4 for each additional centimeter depth.

The optoacoustic acoustic attenuation in soft tissue can be approximated by [58]:

$$\alpha = 10^{0.075\ cm^{-1}MHz^{-1}} \tag{2.15}$$

Assuming a central transducer frequency of 10MHz over a depth of 1 cm we obtain an optical attenuation coefficient of μ_{eff}~1.3 and acoustic attenuation of α =5.6. The total attenuation of sound and light is therefore at least one order of magnitude per centimeter limiting penetration depths in the several centimeter range. Regardless carefully designed optoacoustic imaging systems with sensitive detectors, optimized light delivery and image reconstruction have demonstrated penetration depths up to several centimeters [53-58]. For optoacoustic endoscopy, to realize the hemoglobin vascular network within the lumen we employ a 532nm light source with 1 ns pulse duration to acquire high resolution contrast rich images with penetration depth limited to a few millimeters.

2.1.4 Existing OA endoscopes for esophageal imaging

Existing OA esophageal endoscopes have been realized in small-animal studies with the intention to miniaturize the probe and use the probe via the working channel of white light endoscopes. A distal scanning probe was reported with a frame rate of 4Hz [45]. Albeit distal endoscope micromotors commonly impose a reduction in the field of view due to driving cables crossing over the imaging plane and micro-motors used cannot sustain the transducer load in side-looking mode, constraining to rotate a 45-degree mirror to reflect both sound and light lowering sensitivity and SNR. A catheter scanning probe showed full field of view capability yet at a slow frame rate of 5Hz [46]. More recently, a proximal scanning probe demonstrated full field of view with at frame rate of 50Hz [47]. However, the design suffers from poor lateral resolution, low signal to noise ratio and exceeds the exposure of pulse energy on tissue($\sim 30\mu J$). Being proximally scan, it suffers from scanning uniformity imposed by the need of a torque coil and optical fiber stress due to bending of the torque coil causing variations in the index of refraction resulting in variations on the optoacoustic illumination intensity at the tissue end. Moreover, fiber-optic coupling rotary joints are needed which reduce coupling efficiency and increases system complexity. These designs are suitable only for small GI imaging and not useful for imaging the larger human esophageal lumen with sufficient SNR and lateral resolution due to longer working distances. To image the full circumference of the human lumen optoacoustic capsules probe have been explored.

A prototype capsule shaped acoustic resolution optoacoustic probe was used to characterize the intestinal structures of Crohn's disease of rabbits in-vivo. However, the imaging speed was limited due to the pulse repetition rate of 10 Hz and optoacoustic signals were averaged 30 times to improve signal to noise ratio [48]. Hailong He et al recently proposed a novel 360^0 rotatory optoacoustic endoscopes to image the human lumen. Though the probe was limited by laser repetition rate and rotational scanning unit to a frame rate of 2.5 Hz [49] suffering from motion artifacts during in-vivo scanning resulting in inaccurate spatial mapping and misinterpretation of data. Accordingly, there is presently no optoacoustic endoscope suitable for human GI imaging.

2.2. Optical Coherence Tomography (OCT)

2.2.1 OCT signal generation

The first experiments of optical coherence tomography (OCT) date back to 1989 in the laboratory of James G. Fujimoto, PhD with data reported in Science journal in 1991 [59]. Shortly afterwards the first clinical prototype for ophthalmic applications was installed in 1993 at the new England eye center, Tufts university school of medicine in Boston, Massachusetts USA [60]. Since then, OCT has significantly grown owing to ophthalmic applications, esophageal cancer detection, intravascular imaging and skin cancer diagnosis [19-24,61-63].

Similar to optoacoustics, OCT guides a laser beam to the tissue under examination, albeit light is reflected off the tissue structure rather than absorbed. The back reflected waves are processed to measure the depth at which reflection occurred. Measurements are performed on electromagnetic waves rather than acoustic waves; where the reflected waves cannot be directly measured. For this reason, interferometric detection is employed, where a percentage of the laser beam is optically directed to the sample under test and the remaining percentage is guided to a reference arm. The light from both paths combine at the interferometric output where waves can interfere constructively or destructively. The interference pattern is measured with a high-speed photodetector converting the light intensity into an electrical signal. To describe the signal generation process graphically, OCT interferometric setups are depicted in Fig 2.3. The first implementation was the time domain configuration as depicted in Fig 2.3a, here an adjustable reference arm was modulated for each depth scan. The back reflected signals from both arms combine and only interfere when both optical paths match. The resultant interference fringe patterns are measured by a photodetector. To determine the magnitude of reflected light from sample the Hilbert amplitude of the interference signal is taken. An OCT A-scan line providing

the depth profile of sample reflectivity is measured at a single point by scanning the reference arm in depth with intensity signals recorded on the photodiode. B-scan cross sectional images are generated by laterally scanning the sample beam.

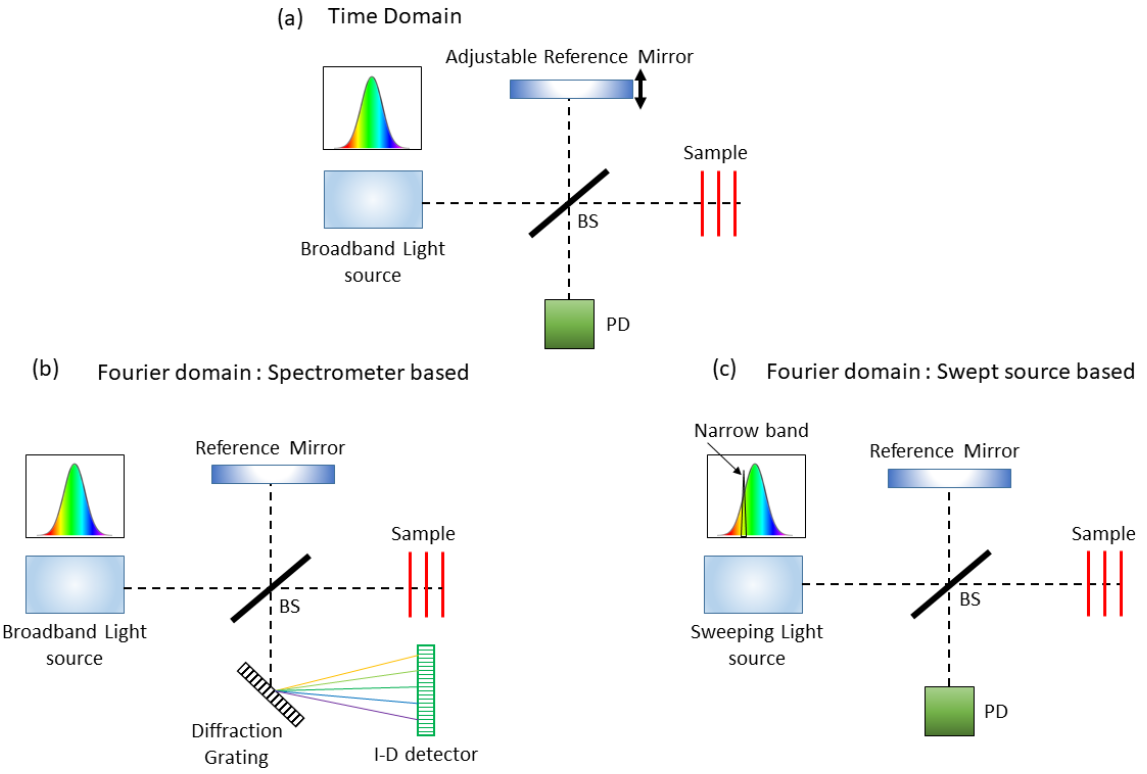

Figure 2.3. OCT configurations including (a) Time domain with adjustable Reference arm (b) Fourier domain: spectrometer based for wavelength separation (c) Fourier domain: Swept source based which sweeps a narrowband line over the broadband source in time. All three implementations measure an interference pattern with a photoelectric detector. BS: beam splitter, PD: photodiode, I-D: 1D line scan detector

To increase imaging speed, Fourier domain OCT configurations were developed to generate A-scan lines without the need for mechanically scanning of the reference mirror (Fig 2.3b and Fig 2.3c). The spectrometer-based setup replaces the photodiode with a diffractive element to spatially separate different wavelength contributions into a line image which is measured by a line scan camera. Each read out of the camera produces a spectral interferogram with a superposition of fringe patterns that contains information to reconstruct a OCT-A scan line. Alternatively, the swept source setup replaces the broadband light source with an optical source which rapidly sweeps a narrow band over a broadband of wavelengths. Over one sweep, each wavelength emitted from the light source and resultant interferogram is detected sequentially by a high-speedphotodiode. For each sample point the interferograms contains information over depth simultaneously similar to the spectrometer configuration. To generate OCT A-scan lines that

represent structural features, a fast Fourier transformation is performed on measured interferograms and corresponding complex values squared to determine intensity values.

When comparing the Fourier methods, the spectrometer domain (SD) methods imaging speed is limited by the line scan rate of the camera whereas for the sweep source (SS) method the sweep rate and analog to digital conversion limits acquisition [64-66]. SD-OCT is useful for applications requiring high axial resolution from broadband light sources with shorter operating wavelengths. Alternatively, SS-OCT's ability to shift wavelength swiftly offers higher imaging speed and deeper sample imaging when compared to SD-OCT. Due to the rapid technological advancements towards SS-OCT, fast OCT imaging at wavelengths of 1300 and 1060nm have paved the way for volumetric and real time imaging. In our case we employ a 1060nm SS-OCT laser to take advantage of high imaging speed by tuning wavelength through internal laser optical components over the photoelectron response of line scan cameras used in SD-OCT. In addition, in OCT endoscopy where the fiber is continuously moving, image artifacts arise as a result of changes in polarization. These changes can be compensated by low cost swept source-dual balanced detectors provided by OCT laser manufacturers .

2.2.2 OCT spatial resolution

In OCT, the lateral resolution is defined by the optical interrogation spot size, hence similar to optoacoustic imaging with a focused beam, the OCT lateral resolution can also be calculated using equation 2.13. The axial resolution is determined by the coherence properties of the light source and detector sampling rate. In air the axial resolution of an OCT system is given by the round-trip coherence length of the source δ_a:

$$\delta_a = \frac{2\ln(2)}{\pi}\frac{\lambda_0^2}{\Delta\lambda_{FWHM}} \tag{2.16}$$

Where λ_0 is the central wavelength and $\Delta\lambda_{FWHM}$ is the spectral bandwidth . From equation 2.16 it is evident that central wavelength is proportional to axial resolution. Figure 2.4 depicts OCT axial resolutions at a spectral bandwidth and central wavelength. Axial resolution degrades at higher wavelengths and smaller spectral bandwidths. Figure 2.4 also shows a dotted red curve line overlaid on the plot representing the absorption of water over central wavelength. In our casewe employ a 1060nm OCT light source to minimize optical absorption of the water used for

acoustic coupling of waves generated via the optoacoustic effect.

The OCT A-line depth is defined by the maximum fringe frequency which can be measured because the maximum frequency of the interferogram determines the maximum decodable depth. Hence the A-line depth can be given by the number of samples N per A-line on the full recorded spectral width $\Delta\lambda$:

$$z = \frac{1}{4}\frac{\lambda_0^2}{\Delta\lambda} N \tag{2.17}$$

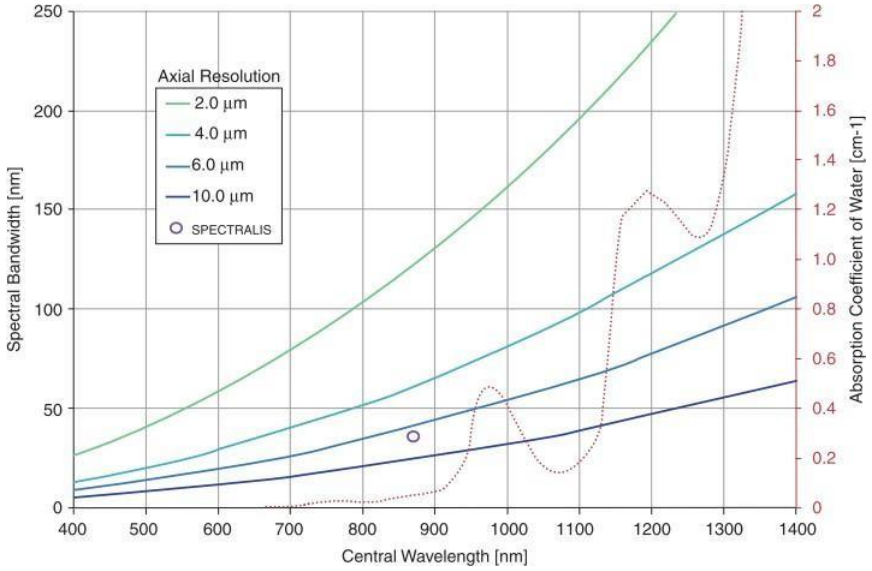

Figure 2.4 Spectral Bandwidth as a function of central wavelength plotted for axial resolutions in the range of 2-10µm. The relationship between bandwidth and central wavelength suggests that bandwidth needs to be increased for longer central wavelengths to maintain the same resolution. The absorption curve of water shows not all wavelengths are equally suitable to maximize imaging depth potential. Retrieved from [67]

2.2.3 OCT penetration depth

OCT penetration depth is determined by the systems optical depth of focus, optical absorption and scattering within the sample under test. Assuming a gaussian focusing beam, the depth of focus can be approximated by:

$$d = \frac{n\lambda_0}{2\pi NA^2} \tag{2.18}$$

where NA is the numerical aperture of the focusing lens and n is the refractive index of the medium. Beyond the optical focal depth, the back reflected signal strength is significantly weak. By virtue Back-reflected signals undergoing multiple back scatter within tissue decay exponentially in depth degrading signal to noise ratio. Beyond one mean free path which corresponds to 1-2mm in biological tissue where the back–scatter signal is significantly weak and multiple scattering become dominant limiting the overall penetration depth of OCT.

2.2.4 Existing OCT endoscopes for esophageal imaging

OCT endoscopy has shown great potential to increase diagnostic accuracy of dysplasia detection due to its high resolution, volumetric and subsurface imaging capabilities. In-vivo studies in the 2000s demonstrated that endoscopic OCT could be used to detect metaplasia in Barretts esophagus patients as well as describe structural features in OCT images and develop criteria to differentiate healthy tissue and high-grade dysplasia from low grade dysplasia. These studies provided the feasibility for clinical application accelerating OCT technology development. To date, advances in swept source laser technology, data acquisition and increased scanning probe speeds have enabled several megahertz of high-speed OCT endoscopy.

A balloon-based imaging providing real time volumetric scans developed by NinePoint Medical, was employed in several multicenter and longitudinal clinical studies [20]. From recovered OCT scans a diagnostic algorithm to detect dysplasia with an accuracy 87% was established [20]. Hatta et al [68] performed several clinical studies with the system to develop esophageal squamous cell carcinoma staging criteria from OCT cross-sectional imaging with an accuracy of 90.1%. A tethered capsule providing high resolution circumferential OCT scans was introduced to enable Barrett's esophagus screening. The device has been used in clinical studies exceeding 100 patients with early results demonstrating feasibility, high patient acceptability, and strong potential for clinical impact [19].

Following the plethora of endoscopic OCT developments for gastrointestinal applications over the past decade [19,20,23,24,68]. The modality is currently undergoing a period of investigation to evaluate the approach ensued by developing a standardized workflow within the clinical environment [133]. Despite all the advantages endoscopic OCT offers, the modality on its own does not completely capture all available diagnostic features in the GI tract [132,133,134]. Furthermore, relying on backscattering OCT signals alone renders precise quasi-histologic assessment a difficult task [134]. By introducing optotoacoustics to increase imaging depth and

thereby combining pathophysiological and structural information together could potentially improve metaplasia sensitivity within the esophagus. This approach could increase translational likelihood with algorithms performed on the overlaid multimodal cross-sectional images to highlight regions of interest.

2.3. Preceding implementations of OCT-OA endoscopes

A hybrid endoscope combining the structural OCT and functional OA capabilities could improve the accuracy of early staging of esophageal cancer and accelerate clinical adoption. However, imaging the human esophageal tract with an OCT-OA endoscope requires (a) synchronous high speed imaging frame rates with sufficient SNR to avoid motion artifacts, (b) co-registered large field of views to expedite the screening procedure, (c) careful design of a broadband endoscopic transducer for optoacoustics and an optical interrogation/collection probe for OCT, (d) suitable materials, mechanics, coupling medium and wavelengths for optical (OCT) and acoustic (OA) index matching, and (e) proper probe form factor to ease swallowing and maintaining optimal contact between the endoscope and esophageal circumference.

Previous implementations of OCT-OA multimodal endoscopes include a 1.25mm all optical dual OCT- OA probe for intravascular imaging [69]. However, the probe suffered from a 4 Hz Bscan rate as a result of the proximal scanning mechanism and pulse repetition rate of the optoacoustic laser (2.8 kHz). Furthermore, the optoacoustic light interrogating samples had a fluence ranging from 40 – 100 mJ/cm^2 which exceeds the maximum permissible exposure (MPE) of 20 mJ/cm^2 on the skin. Additionally, optoacoustic signals had to averaged 25-50 times to compensate for thepoor SNR.

Dai et al [70] demonstrated a 1 mm-diameter multimodal endoscope combining OCT, optoacoustic and ultrasound designed for intravascular coronary imaging. The capabilities of the trimodal endoscope was showcased using a mouse ear, human hand and human arteries with atherosclerotic plaques, although a fluence value of 10 mJ/cm^2 was only provided for the mouse experiment. The system speed was limited by a low repetition rate optoacoustic laser (20 Hz) and a slow approach of time-domain OCT. As a result, the probe was prone to significant motion artifacts. In addition, the SNR of acoustic measurements was reduced due to an optical redirection of ultrasound/photoacoustic signals to an unfocused detector.

A 5 mm hybrid OCT-OA-US prototype endoscope was characterized and used to image human ovarian tissues [71]. Each modality was sequentially acquired, extending the overall scanning duration. Other limitations include a slow OA imaging speed attributed to a 15 Hz pulsed laser, data acquisition performed by using two DAQ cards on two PC's, sub-mm OA-US lateral resolution, and employing 1 mJ/pulse which significantly exceeds the MPE limit of skin as listed above.

The approaches above [69-71] focus on miniaturization of multimodal OCT-OA endoscopes for imaging small animal internal organs or intravascular applications in humans. These solutions exhibit poor contact matching with human esophageal lumen dimensions and would therefore need to be inserted inside the working channel of a WLE for imaging. However, the added propagation distance to reach the lumen surface with a miniature sensor leads to a loss of SNR, thereby violating the maximum permissible energy level. Furthermore, all designs suffer from low multimodal frame rates limiting clinical translation as a result of extended imaging sessions. Hence, presently there are no hybrid OCT-OA probes designed for human esophageal imaging.

2.4. Summary and discussion

In the first half of this chapter, the principles of optoacoustic imaging and previously reported optoacoustic endoscopes for esophageal imaging were discussed. This included the details of the fundamental criterion to be satisfied for the optoacoustic signal generation. Spatial resolution expressions derived highlighted the importance of developing optoacoustic detectors with appropriate geometry and bandwidth. An analytical analysis of penetration depth was performed to highlight the challenges of increasing imaging depth. Furthermore, the translational limitations of existing esophageal optoacoustic endoscopes were discussed.

In the second half of this chapter, akin to the first half discussed the theoretical background of optical coherence tomography and present-day OCT endoscopes employed for esophageal imaging. The interferometric OCT detection of back reflected light signal following tissue interrogation were explained in both time and Fourier domains. Expressions for the lateral and axial OCT resolutions were defined to highlight the importance of selecting the optimal excitation wavelength for a desired application. Limited OCT penetration depth attributed to optical scattering deep in biological tissue. Finally, an in-depth review was performed on present day OCT endoscopy employed for imaging the gastrointestinal tract.

Lastly previous implementations of OCT-OA endoscopes were surveyed. The limitations of

each design were listed to highlight that none of them would be suitable for imaging the human esophageal tract.

Chapter 3 Optoacoustic endoscopy sensor development

The architecture of the transducer used in optoacoustic endoscopy has a significant impact on image quality. To visualize the human esophagus, high resolution is required over an extended depth of focus. Broadband single element benchtop detectors namely spherical and axicon were developed and characterized with central aperture for collinear illumination. The imaging depth potential of each detector was assessed by imaging tilted phantoms and biological samples.

Subchapter 3.1 Introduces an optoacoustic sensor characterization rig to determine the optoacoustic total impulse response of each detector under test. Several benchtop axicon and spherical transducers with different materials and dimensions were built and characterized to measure depth of focus, lateral/axial resolution, transducer bandwidth, focal length, and spatial sensitivity profiles. The best performing transducers were lithium niobate based with the axicon sensor exhibiting a pencil beam elongated sensitivity beam useful for endoscopy although following further investigation described in 3.2 and 3.3 the axicon produced blurry images when imaging phantoms mimicking blood vessels and therefore the spherical transducer design was opted for further development into a more capsule friendly casing.

Subchapter 3.2 Presents a raster scanning optoacoustic mesoscopy setup employing the spherical and axicon detectors to image a tilted suture phantom. The spherical transducer generated an OA image resolving the tilted suture at focus and blurred out of focus and whereas the axicon sensor surprisingly generated a blurred OA image over the entire tilt.

Subchapter 3.3 performs a meticulous 3D acoustic simulation of the spherical and axicon transducers in Kwave to determine the reasoning behind the axicon’s degraded lateral resolution when performing OA imaging as opposed to OA characterization. Simulation result suggest the axicon detectors spatial response is functions of the acoustic source shape i.e., line or point source, whereas the spherical spatial response is independent of acoustic source shape. This observation indicated the axicon would be better accommodated towards microscopic applications and the spherical design to be further optimized into an endoscopic form factor.

Subchapter 3.4 unveils an elongated focus optoacoustic microscope with matched Bessel beam illumination and the ultrabroadband axicon transducer. In a controlled experiment axicon-mode optoacoustic microscopy employing Bessel beam illumination extended depth of focus 17x compared to configurations using Gaussian illumination with spherically focused transducers. The advantages of Bessel beam-axicon detection optoacoustic microscopy was showcased by imaging a tilted mouse ear with a 5-µm-diameter Bessel beam, reaching imaging depths greater than 4.2 mm.

3.1. Optoacoustic transducer characterization

Currently, single element ultrasound transducers are characterized by measuring the electrical impulse response to an omnidirectional acoustic source placed at the focal point [72-75]. This is done by either recording pulse echo signals from a planar reflector, albeit with a limited acoustic source bandwidth [76], or by using a calibrated needle hydrophone to generate an acoustic source of higher bandwidth while the detector is operating in receiver mode [73,77]. However, hydrophone bandwidths are typically limited to 25 MHz and the needle thickness limits the smallest measurable lateral resolution of the sensor. A standardized approach to characterize optoacoustic detectors with parameters such as bandwidth, focal distance, depth of focus, diverging angle, and lateral and axial resolutions is still missing. Such a characterization method would benefit both the scientific and industrial communities by enabling corrections for otherwise unknown detector aberrations, leading to optimal optoacoustic image quality.

Light absorbing materials have been exploited to characterize optoacoustic detectors by generating broadband point sources of acoustic waves using nanosecond pulsed lasers. These materials include sutures [74], microspheres [78], or mixtures of carbon black and PDMS [75]. However, a suture absorbing light pulses does not generate an omnidirectional point source, hindering the measurement of optoacoustic sensitivity maps. Characterization with microspheres is difficult due to a tedious sample preparation and alignment procedure. Furthermore, the sphere itself may exhibit deformations and therefore generate distorted acoustic sources. Producing a thin layer of PDMS mixed with carbon black is challenging, Buma, T., et al. reported a layer thickness of 25 µm, which limits the generation of higher frequency signals. A broadband optoacoustic concave transmitter with a 100 nm-layer of chromium has been proposed as a source to generate focused ultrasound waves for transducer characterization; however, manufacturing the transmitter requires precise sputtering control over a plano-concave spherical glass to ensure uniform film thickness [79].

We propose a simple and fast method to characterize transducers with bandwidths exceeding 100 MHz by interrogating a 100nm gold film using a nanosecond-pulsed, focused laser beam, thereby generating an ultra-broadband omnidirectional optoacoustic point source with a flat spectral response [72]. The systems lateral resolution would then be limited by the spot size of the focused beam. The optoacoustic signal strength generated is dependent on the laser energy density and absorption coefficient of the thin film; the signals are inherently broadband and therefore suitable to investigate the optoacoustic bandwidth limits of the transducer being tested. This approach allows us to obtain four-dimensional data (3 spatial in XYZ and 1 temporal axes) by scanning around the point source in the three spatial directions and acquiring the temporal response at each position. The total impulse response sensitivity maps from single element transducers are therefore obtained from different planes and bandwidth, focal distance, depth of focus, diverging angle, lateral and axial resolutions are calculated.

3.1.1 Optoacoustic transducer characterization rig

Figure 3.1 displays the proposed optoacoustic transducer characterization rig. A 532nm light source with a 1 ns pulse width and operates at 2 kHz repetition rate (Wedge HB532, Bright Solutions, Italy). A polarizing beam splitter and a beam dump were used to regulate the energy per pulse. For triggering, a 90:10 beam splitter was used to divert 10% of the light into a photodetector. The remaining 90% of light was spatially filtered to improve beam efficiency and focused with a 4X objective lens to a spot size of around 12 µm (4X Olympus RMS4X). To align the 100 nm gold film-plate to the focal plane of the objective and generate an omnidirectional optoacoustic point source, a manual XYZ translation stage (PT3/M, Thorlabs) is used. The pulse energy used to probe the gold film was about 50 nJ.

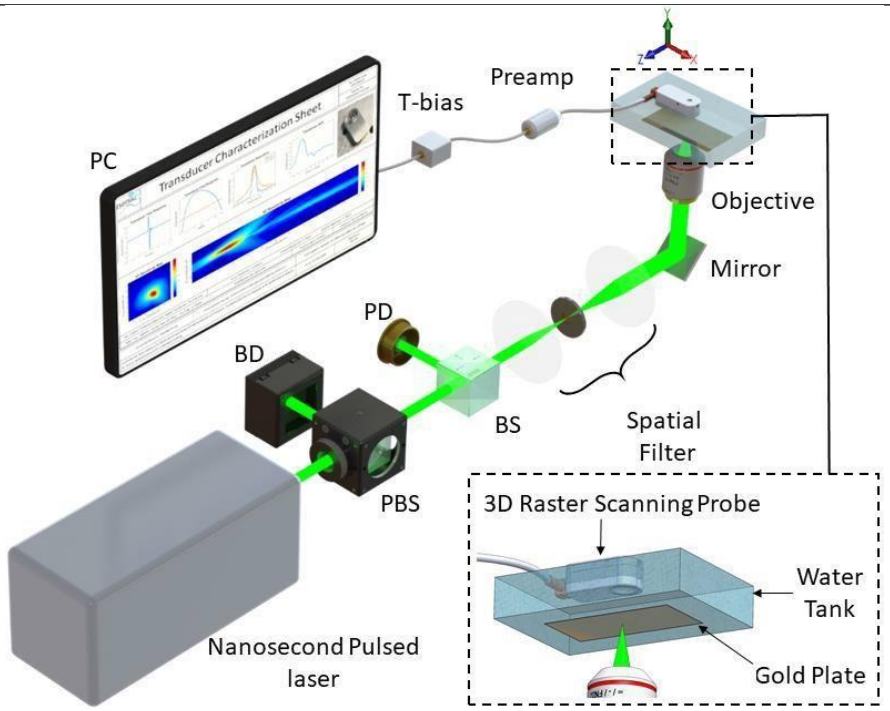

Figure 3.1: Ultra-broadband single element ultrasound transducer characterization rig used to measure the total impulse response. PBS: polarizing beam splitter, BS: beam splitter, BD: beam dump, PD: photodiode.

Each transducer was attached to an XYZ motorized stage (MTS50-Z8 in 3-Axis XYZ Configuration, Thorlabs) for fine linear scanning over the optoacoustic point source using deionized water as the acoustic coupling medium. The active element of each detector was mounted facing the acoustic source and synchronized with the motorized stages. To produce the sensor's characterization maps, the raster scanner was programmed to sweep along the XY and XZ planes, using 200 signal averages per step to reduce the effect of laser pulse-to-pulse varianceand background signal. Prior to data acquisition, the temporal optoacoustic signals were externallypre-amplified with a 30 dB amplifier (Sonaxis SA, France) and attached to a T-bias (ZFBT- 4R2GW+, Mini-Circuits). An ATS9373 DAQ card (AlazarTech, Canada) was selected to collect the optoacoustic data, which was synchronized to the board's external trigger port via thephotodetector signal. LabVIEW was used to monitor signal processing, and MATLAB was used to analyze the data. The transducers discussed in this chapter were all characterized with this characterization system.

3.2. Optoacoustic transducer architecture for endoscopy

Optoacoustic mesoscopy employs ultra-wideband (UWB) ultrasound frequencies to detect optical absorption across several millimeters of depth with resolutions in the range of tens of micrometers [35,36]. This capability has been introduced as raster scanning optoacoustic mesoscopy (RSOM),

which allows for accurate visualization of various skin features such as dermal vasculature [80,81] or melanoma-related angiogenesis [82], as well as label-free quantification of inflammation in psoriasis, eczema, and vasculitis [36]. To generate highly accurate images of tissue, RSOM utilizes tomographic concepts by appointing detectors with broad acceptance angles and integrating signals acquired over different projections by mathematical inversion.

In gastrointestinal (GI) endoscopic applications, mesoscopic performance may also be helpful to achieve similar surface visualization, associated with vascularization and angiogenesis, potentially leading to improved cancer staging. For example, the average human esophagus wall is 5.26 mm thick for males and 4.34 mm thick for females [83], and it is highly vascularized, with vessels varying in size from tens to hundreds of micrometers inside the mucosa [84]. Because of the variability in vascular size and depth, the optoacoustic frequency content generated is inherently broadband, hence ultrasound detectors with central frequencies up to 50 MHz and bandwidths ranging from a few to 100 MHz are needed to provide appropriate esophageal layer resolution [85] matching the characteristics of RSOM transducers. Although, Optoacoustic endoscopy, differs from RSOM in two major respects. First, imaging hollow organs usually necessitates rotating rather than raster scanning detector designs, which require transducer designs with different requirements than those used in RSOM. Second, unlike tomographic imaging, which can achieve high imaging efficiency synthetically, rotational endoscopy does not collect strongly overlapping projections due to the outward looking detector's geometry. As a consequence, image quality is highly determined by the detector's requirements. Additionally, endoscopes are often restricted by the need for miniaturized form factors in order to achieve sizes suitable for entry into cavities and hollow structures.

3.2.1 Desired sensor specifications

The desired optoacoustic endoscopic detector specifications were therefore driven by the transducer (model no HFM23) employed in the RSOM system, where resolutions, central frequency and -6dB bandwidth were reported at 20µm, 50MHz and 100MHz respectively. For optoacoustic skin imaging the transducer overlooks the sample with reduced propagation distance to maximize SNR. Hence, for optoacoustic endoscopy a side viewing sensor to face the esophageal wall is desired. To drive detector miniaturization and align the optical excitation beam with the transducers sensitivity beam a central aperture is required. In addition, for ease of swallowability the diameter of the transducer should be comparable to the size of commercially available white light capsules which are reported to be less than a maximum diameter of 13mm [121,122].

Similar to the HFM23 transducer, existing optoacoustic endoscopes have employed focused transducers (previously explored in 2.1.4) to achieve lateral resolutions in the range of tens of microns in the mesoscopic regime but their depth of focus is limited to hundreds of microns by the nature of their spherical geometry and bandwidth characteristics. Resolving depth information with spherical transducers therefore requires computationally intensive reconstruction algorithms, such as back projection [86] and model-based [87] methods, which can limit the ability to achieve high quality real-time volumetric imaging. In contrast, axicon transducers include conical lenses, which focus ultrasound waves along the axial direction. This configuration yields a pencil beam sensitivity profile with high lateral resolution over an extended depth of focus.

For optoacoustic applications, we hypothesized that axicon detectors' elongated sensitivity profiles may allow reconstruction-free image processing over greater depths than spherical detectors. Although elongated sensitivity profiles for optical [88] and ultrasound imaging [89, 90] have been investigated, there was only one study on single-element axicon transducers for optoacoustics in 2009 [91], which used lower central frequencies and bandwidths than those suitable for optoacoustic imaging. Therefore, we developed and compare the performance of single element axicon and spherical geometries both with central aperture as required for coaxial OA illumination. The desired transducer specifications for optoacoustic endoscopy are summarized in Table 3.

Desired Specification	**Value**
Lateral/Axial Resolution	20µm
-6dB Bandwidth/Central Frequency	100MHz/50MHz
Directivity	Sphereical & Axicon
Architecture	Side viewing with central aperture
Size	Diameter <13mm

Table 3: Optoacoustic endoscopic transducers desired specifications.

3.3. Piezoelectric Transducer Crystals

Certain crystal materials by virtue of the piezoelectric effect when deformed by application of an external stress generate a corresponding electrical signal. During transducer development two piezoelectric transducer crystals were considered due to their excellent acoustic to electrical conversion efficiency, including Lead Zirconate Titanate(PZT) and Lithium Niobate (LiNO3). PZT based ultrasonic actuators are well known for their excellent piezoelectric properties and can be shaped in almost any shape or size. However, considering the toxicity of lead, there is a general

awareness for the development of environmental lead-free materials. On the contrary, LiNO3 exhibits a high Curie temperature and excellent piezoelectric coupling coefficient making it attractive for lead-free ultrasound measurement. Transducer directivity was achieved by directly shaping the PZT active element while a glass shaped lens was mounted onto a planar LiNO3 detector. The main benefit of directly shaping the active element to achieve acoustic focusing opposed to shaping a glass lens is the ability to avoid potential secondary acoustic reflections occurring within the glass lens and thereby deteriorating image quality along the axial axis. The first series of prototypes manufactured were to be characterized and experimented in benchtop configurations.

3.3.1 First generation benchtop Transducers

The first-generation single element transducers built were PZT-based, the cross-sectional view of the spherical equivalent design is depicted in Fig 3.2a. Both side looking transducers featured a central aperture of 1mm for coaxial illumination and acoustic signals were coupled via a micro dot connector. The CMF156 axicon transducer (Fig 3.2b) had a aperture diameter of 9.5mm with cone angle of 130º and the CMF155 spherical transducer (Fig 3.2c) had a aperture diameter of 8mm with a radius of curvature of 8mm. Note the presence of cracks on the active elements manifested during the manufacturing process. From the temporal and spectral response of the spherical detector (Fig 3.2e) we determine a focal length of 8.4mm and -6dB bandwidth of 24MHz and central frequency of 28MHz. From the temporal and spectral response of the axicon detector (Figure 3.2f) we determine the maximum sensitivity position to be at 8.85mm and -6dB bandwidth of 35MHz and central frequency of 22.5MHz. The spherical transducer appeared to be twice as sensitive as the axicon detector

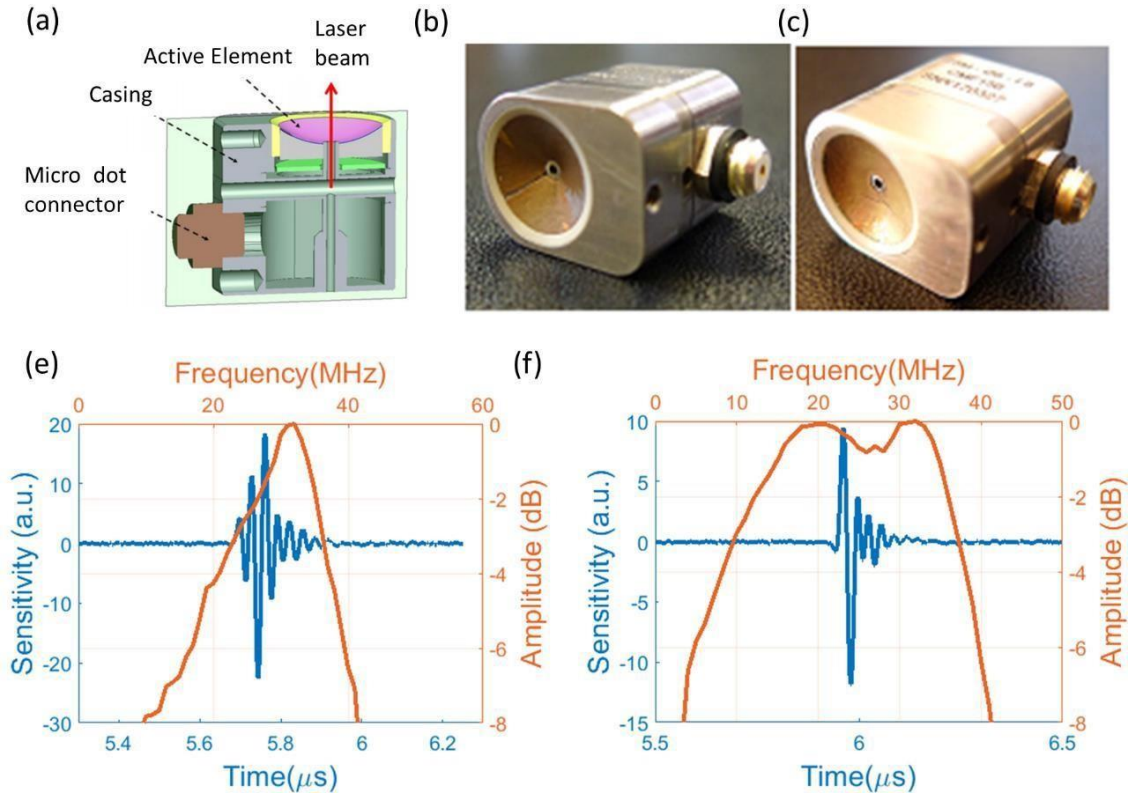

Figure 3.2: (a) Cross sectional representation of the first generation of benchtop PZT based transducers where the central aperture for laser beam illumination is 1mm in diameter (b & c) photos of the axicon (CMF156) and spherical transducers (CMF155) built respectively. (e) Temporal and frequency response of the spherical transducer (f) Temporal and frequency response of the axicon transducer.

The spatial sensitivity maps in the XY plane for each sensor are depicted in Figure 3.3(a-b). From these maps we determine the corresponding lateral and axial resolutions for each transducer Fig 3.3(c-d). The cracks present of the surface elements result in distortions of the sensitivity profiles as reflected in the sensitivity profile maps. In particular, the spherical transducers XY spatial profile (Fig 3.3a) shows strong secondary lobes surrounding the focus. The axicon transducers XY spatial profile (Figure 3.3b) also depicts a secondary lobe albeit significantly weaker compared to the spherical. The lateral resolutions and axial resolutions measured for the sphericaldetector were 57 µm and 67µm respectively. The lateral resolutions and axial resolution measuredfor the axicon detector 65µm and 56µm respectively.

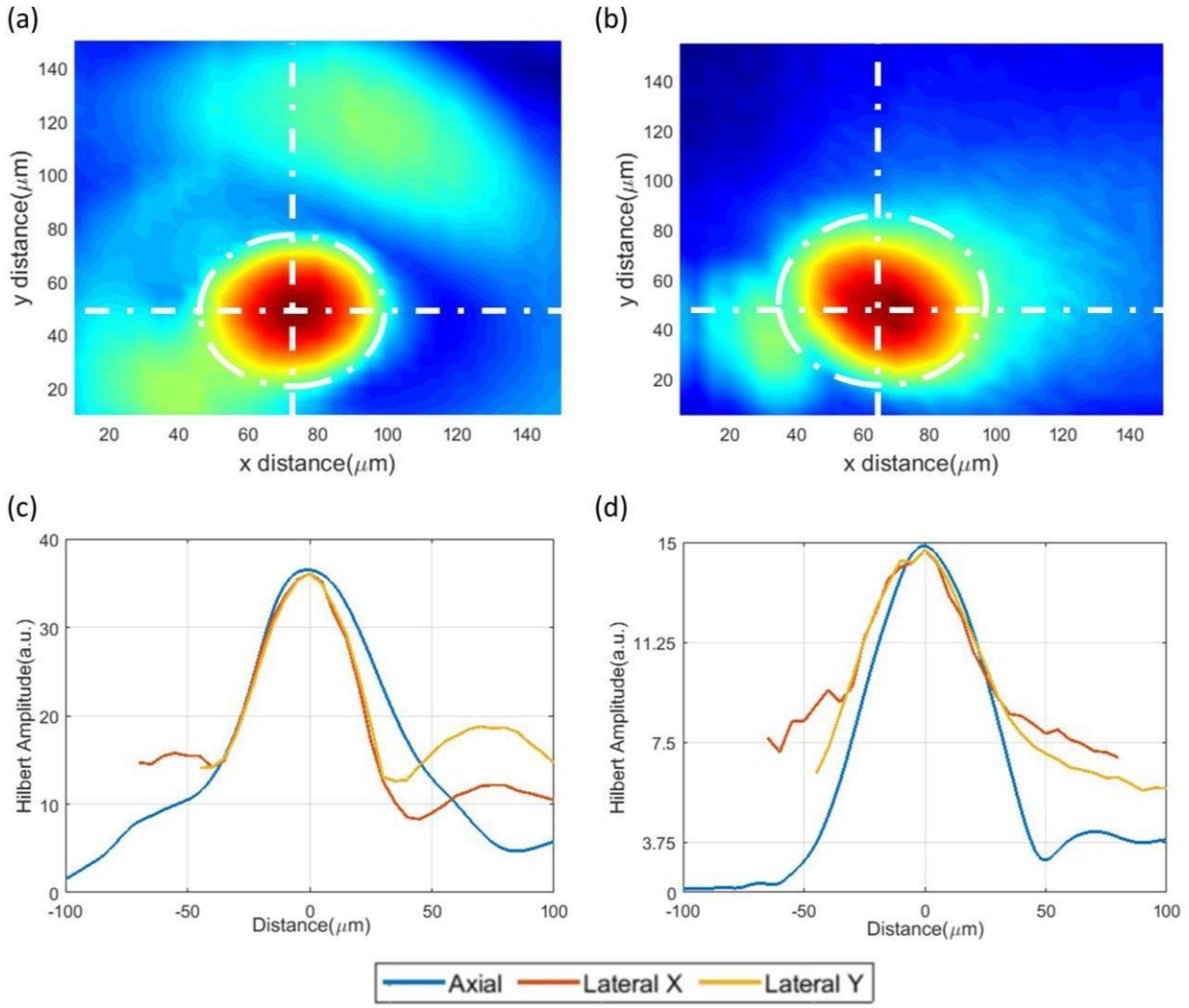

Figure 3.3 (a-b) Optoacoustic transducer sensitivity maps at XY focal planes of (a) CMF155 spherical transducer (b) CMF156 axicon transducer (c-d) Axial and lateral Hilbert resolutions of each transducer respectively.

The spatial sensitivity map in the XZ plane for each sensor are depicted in Figure 3.4(a-b). The spherical transducers XZ spatial response Fig 3.4(a) shows a strongly distorted spatial map with two foci and the axicon transducers XZ map shows an elongated sensitivity profile less distorted in comparison. From figure 3.4(c) we estimate a depth of focus 1.7mm for the axicon transducer. For the spherical transducer a depth of focus of 3.1mm is measured as a result significant sensitivity aberrations manifested as a result of the surface cracks present on the active elements.

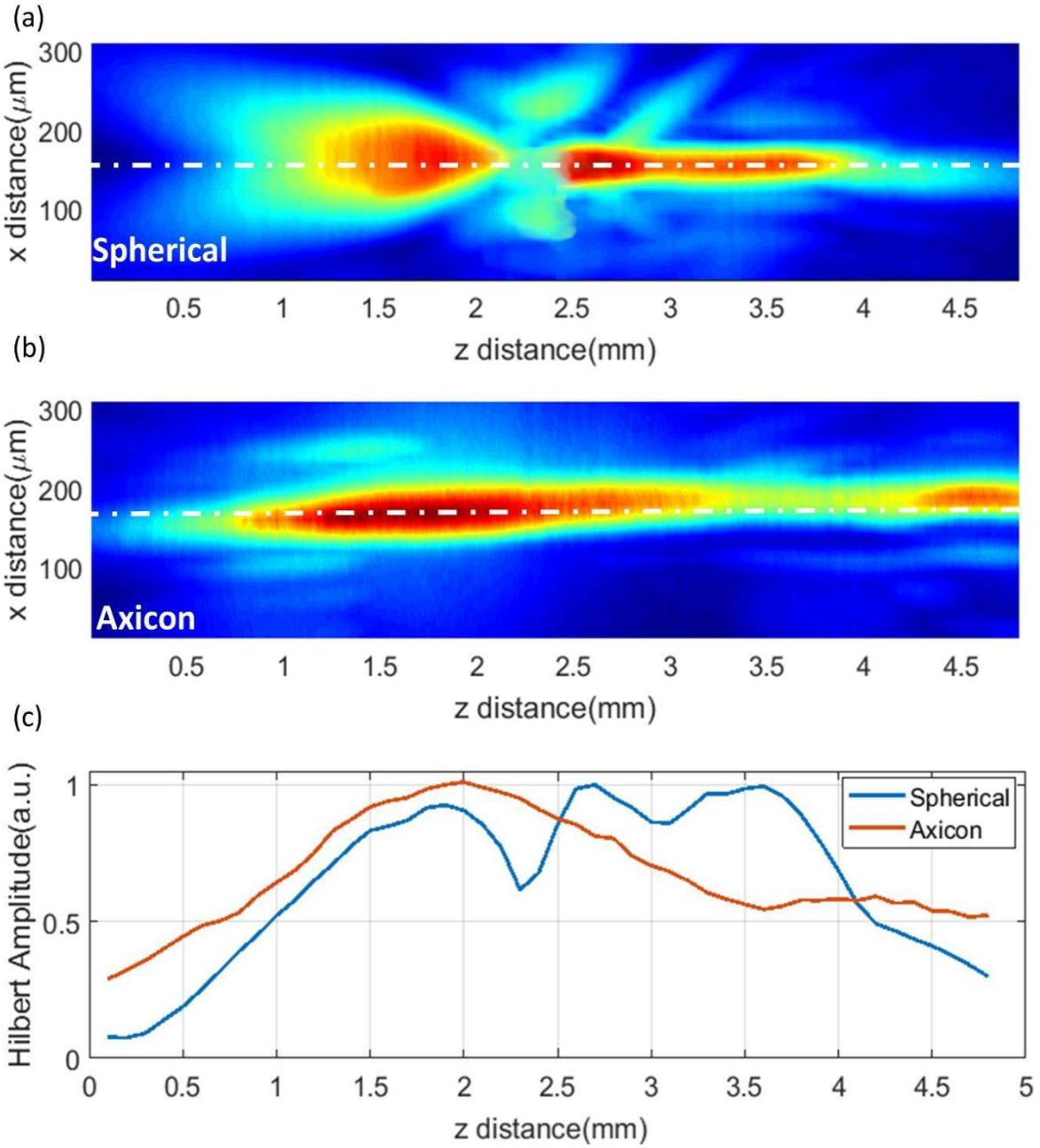

Figure 3.4 (a-b) Normalized Optoacoustic transducer sensitivity maps at XZ planes of (a) CMF155 spherical transducer (b) CMF156 axicon transducer (c) Normalized line scans following the dotted white line trajectory in Fig 3.4 (a-b) along the z distance

Analyzing the characteristics of the first generation of the PZT benchtop transducers we find they are not suitable for optoacoustic endoscopy. The frequency characteristics which around 22.5-28MHz central frequency and -6dB bandwidth of 24-35MHz are below the required central frequency of 50MHz and -6dB 100MHz bandwidth. The resolutions need to be improved from 50-70μm to 20 μm to provide high resolution imaging. The manufacturing process needs to be improved to prevent surface cracks from manifesting on the active elements which degrade the spatial sensitivity response of the transducers. Finally, the detectors require miniturzation to

approach the <13mm diameter requirement for ease of swallowability. For all these reasons a second generation of PZT benchtop spherical and axicon detectors were built with the aim of delivering performance closer to the desired specifications listed in Table 3.

3.3.2 Second generation benchtop Transducers

The cross-sectional view of the second-generation side looking benchtop PZT detector is depicted in Fig 3.5a. The overall size of the sensor was reduced by replacing the micro dot connector with a micro coax cable. A pre-amplifier was integrated inside the sensor to improve signal to noise ratio (SNR). To permit coaxial illumination, the transducer casing had to modified to integrate internal optics including a 90° mirror and the central aperture increased from 1mm to 2mm to ensure the beam is not obstructed as it propagates inside the casing. Fig 3.5b shows a photograph of the second generation CMF163 spherical transducer and CMF171 axicon transducer. The active element designs including, focal length, cone angle; diameter remained the same as the first generation of PZT sensors. Unfortunately cracks are still present on the active elements of the new transducers. From the temporal and spectral response of the CMF163 spherical detector (Fig 3.5c) we determine a focal length of 8.5mm with central frequency 39 MHz and -6dB bandwidth of 55MHz respectively. From the temporal and spectral response of the CMF171 axicon detector (Fig 3.5d) we determine the maximum sensitivity position to be at 10mm and central frequency of 32MHz and -6dB bandwidth of 52MHz. The spherical transducer appeared once more to be approximately twice as sensitive as the axicon detector.

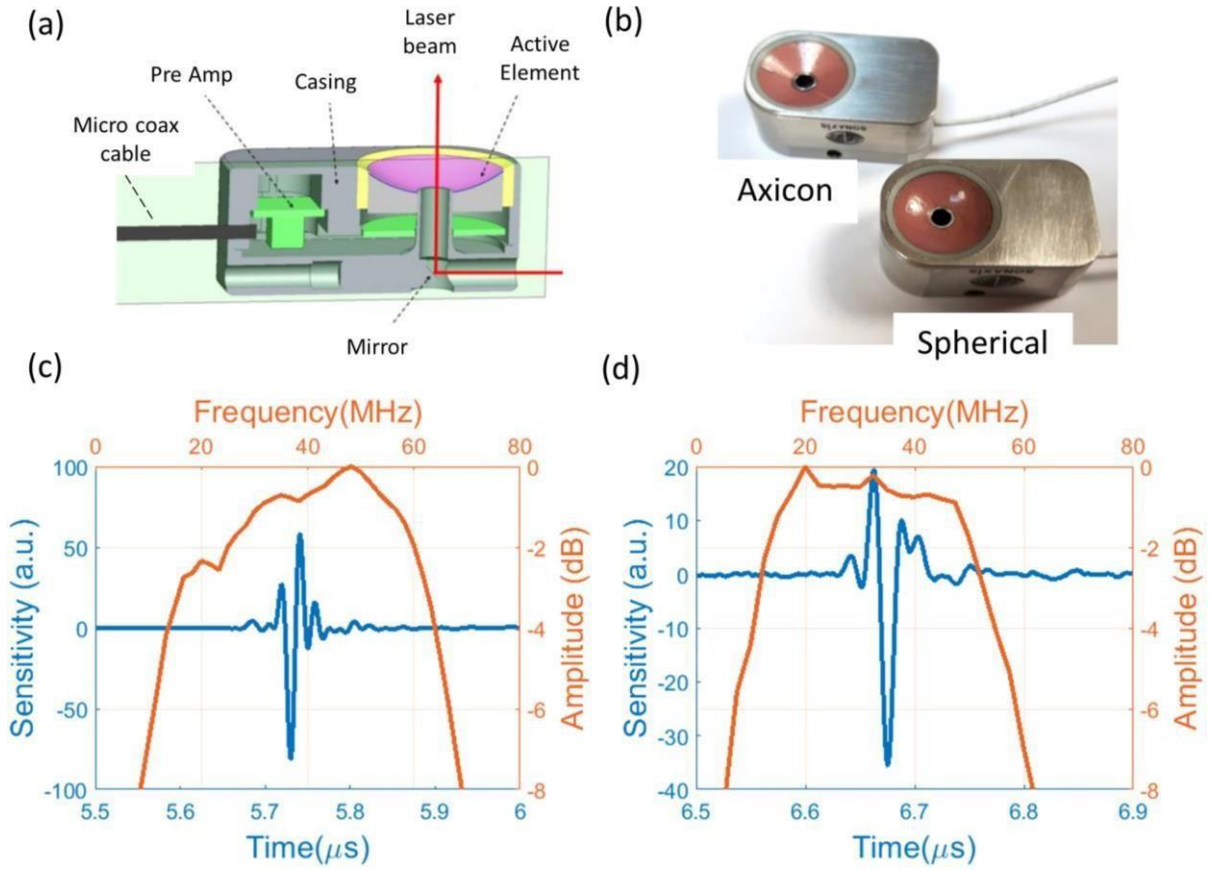

Figure 3.5: (a) Cross sectional representation of the second generation of benchtop PZT based transducers where the central aperture for laser beam illumination is 2mm in diameter (b) photo of the axicon (CMF171) and spherical transducers (CMF163) built respectively. (e) Temporal and frequency response of the spherical transducer (f) Temporal and frequency response of the axicon transducer.

The spatial sensitivity maps in the XY plane for each transducer are depicted in Fig 3.6(a-b). From these maps we determine the corresponding lateral and axial resolutions for each transducer as shown in Fig 3.6(c-d). Several secondary lobes surrounding the main foci in both transducers XY planes are observed as a result of the cracks present on the active elements. These lobes degrade resolution and reduce SNR. When attempting to determine the lateral resolutions in X and Y for the spherical transducer illustrated in Fig 3.6c we measured x=38µm and y=124µm. The corresponding axial resolution for the spherical detector was 34 µm. Similarly, from Fig 3.6d for the axicon transducer we measured lateral x= 43 µm, lateral y =74 µm and axial = 37 µm. The asymmetry in lateral resolution and the strong background signal observed in the lateral line scans are attributed to the surface aberrations.

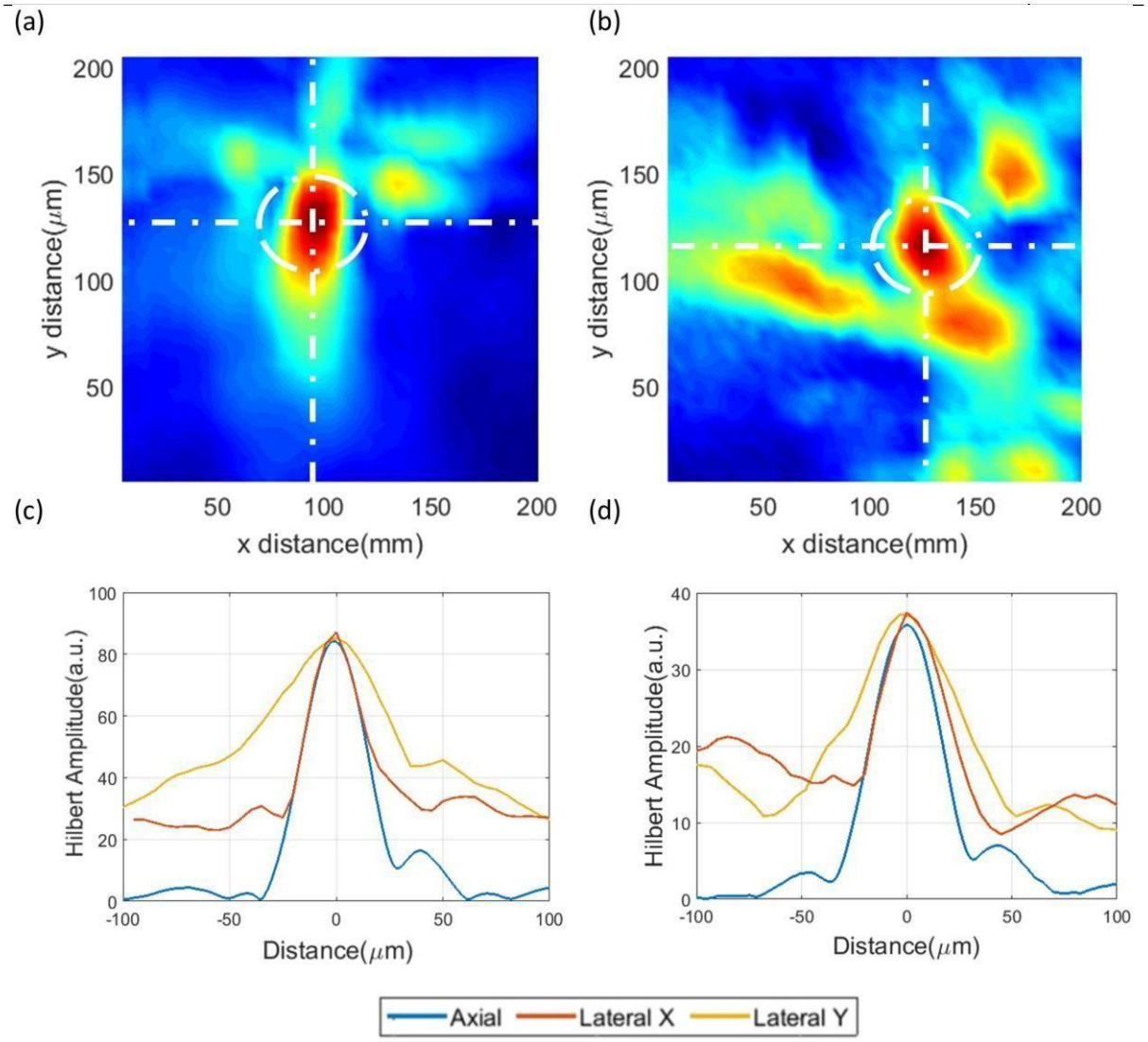

Figure 3.6 (a-b) Optoacoustic transducer sensitivity maps at XY focal planes of (a) CMF163 spherical transducer (b) CMF171 axicon transducer (c-d) Axial and lateral Hilbert resolutions of each transducer respectively.

The spatial sensitivity map in the XZ plane for each transducer is depicted in Figure 3.6(a-b). The CMF163 spherical transducers XZ spatial response Fig 3.6(a) shows a smeared oval shaped profile measured over 200µmx1000µm. The CMF171 axicon transducer displays a significantly distorted elongated sensitivity profile with multiple foci and was measured over 300µm x 6000µm. From the normalized line scans along z (Fig3.6c) we determine a depth of focus of 870 µm for the spherical transducer and 1.56mm for the axicon transducer.

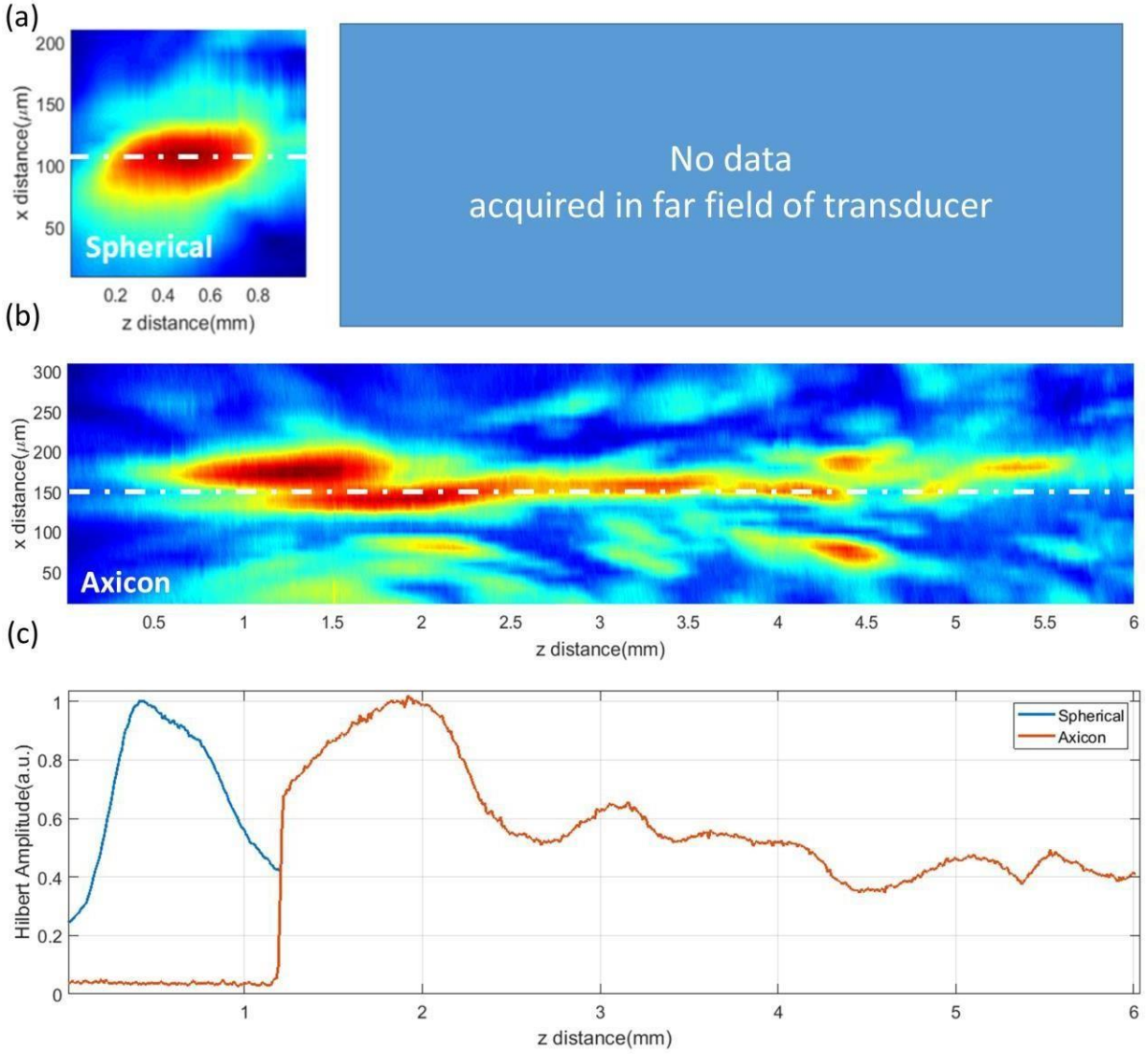

Figure 3.7 (a-b) Normalized Optoacoustic transducer sensitivity maps at XZ planes of second generation PZT benchtop transducers (a) CMF163 spherical transducer (b) CMF171 axicon transducer (c) Normalized line scans following the dotted white line trajectory in Fig 3.7(a-b) along the z distance

Analyzing the performance of the second-generation benchtop PZT transducers we found an improved performance in frequency response with central frequency and bandwidths reaching ~35MHz and 50MHz respectively. However, these specifications are still below the required 50MH central and 100MHz -6dB bandwidth. We observed a degraded lateral resolution when compared against the first-generation transducers as a result of significant distortion observed in the XY spatial planes. The origin of these distortions measured in the sensitivity profile are a result of the cracks generated during the shaping of the active element into a spherical or axicon shape. Clearly from the characterization of the CMF163 and CMF171 transducers, we conclude they are not suitable for optoacoustic endoscopy and requirement further enhancement prior to

proceeding to imaging. We realized the main problems lies with shaping of the active element to achieve spherical or axicon acoustic directivity. To avoid this procedure, we sought to shape a glass lens to achieve directivity and then mount the lens onto the active element to form the transducer. This technique has been previously employed in the manufacturing of broadband spherically focused transducers for RSOM delivering bandwidths up to 100MHz and resolution in the 20µm range. In addition, during course of testing the CMF163 and CMF171 transducers we found internal preamp circuit to be very unstable significantly reducing the lifetime of the sensors and therefore for the time being removed the preamp circuit for the next generation of sensors until a more stable solution was developed. Finally, the very thin micro coax cable was very prone to electromagnetic noise and required significant shielding. Although, when thick aluminum shielding was applied, the fragile connection between the casing and thin wire broke on several occasions prolonging the characterization procedure. Hence, the next generation of transducers were to focus on miniaturized connectors in place of thin cables.

3.3.3 Third generation Benchtop transducers

The third generations of transducers developed were $LiNO_3$ based with a glass lens shaped to a spherical and axicon profile. The active element designs including, focal length, diameter; central aperture remained the same as the second generation transducers. The only change made was a reduction of cone angle from 130° to 114.4° to facilitate simpler manufacturing of the glass lens for the axicon transducer by utilizing standard glass polishing instruments. The attributes of these benchtop transducers were measured against the glass lens $LiNO_3$ based transducer deployed for raster scanning mesoscopy (HFM23). The schematics of each transducer and their response at focus are depicted in Figure 3.8 (a-c) and corresponding temporal/ frequency curves of each transducer are presented in Fig 3.8 (d-f). The three fabricated sensors exhibit an ultra-broad bandwidth detection performance with central frequency and −6 dB bandwidth (BW) of 72.5 MHz (BW 105 MHz), 60 MHz (BW 97 MHz) and 55 MHz (BW 94 MHz) for the HFM23, HFM36 and HFM37, respectively. However, among the sensors at focus, the spherical transducer with no central aperture (HFM23) has the highest signal amplitude, demonstrating 4 times higher relative acoustic sensitivity (peak-to-peak signal amplitude) than the spherical transducer with central aperture (HFM36). Because of the relative sensor size, propagation losses to focus, and medium absorption at central frequency, this is similar to the 4.06 higher sensitivity anticipated. Furthermore, when the influence of transducer shape was compared with central apertures, the

spherical (HFM36) detector showed 2.85 times greater sensitivity at focus than the axicon detector (HFM37). The measured focal distances and divergence angles for these transducers were 3.05 mm (52º), 7.98 mm (51º) and 8.60 mm (50º) for the HFM23, HFM36 and HFM37, respectively. Due to the excellent performance of these transducers, we performed a more in depth analysis when measuring resolution and depth of focus.

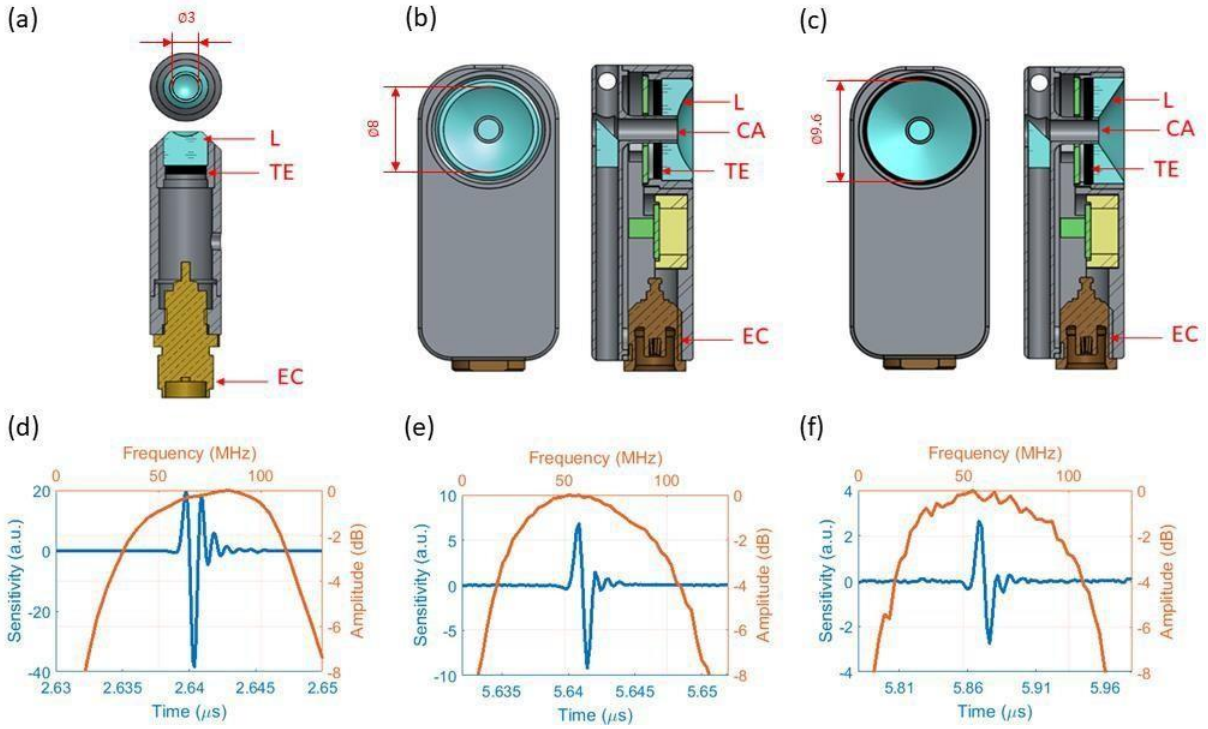

Figure 3.8 (a-c) illustrates the LiNO3 based detectors (a) A spherical transducer with acoustic lens of 3 mm-curvature radius previously utilized for RSOM (HFM23, Sonaxis SA, France). (b) and (c) depict central aperture transducers, spherically (HFM36, Sonaxis SA, France) and conically (HFM37, Sonaxis SA, France) focused, respectively. The spherical transducer had a curvature of 8mm, and the conical transducer had a 114.4^0 apex angle with diameter of 9.6 mm; both with a 2mm-central hole. TE: Transducer element, EC: Electrical Connector, L: Acoustic Lens, CA: Central Aperture Window. Figures (d-f) are the Optoacoustic transducer temporal and frequency responses of (c) HFM23, (d) HFM36 and (e) HFM37 sensors

Fig. 3.9 shows the sensitivity maps obtained at the focal plane of each transducer. The sensitivity symmetry of the HFM23 detector is circular, with a weaker secondary spot overlapping the primary one (marked in Fig 3.9a). The corresponding sensitivity maps for the HFM36 and HFM37 detectors are shown in Figs 3.9(b-c), with minor symmetry distortions. Acoustic lens deformations during processing may be to blame for these astigmatic aberrations. Figures 3.9d-f display the lateral and axial spatial resolutions for each transducer. Full-bandwidth resolutions of approximately 28 μm and 18 μm for the lateral and axial, respectively, are obtained by all three

detectors. Their similar sensitivity bandwidth is responsible for their similar resolutions. By virtue of the ultra-broad band sensitivity featured in these detectors, we looked into the effect of acoustic bandwidth on each detector's precise lateral resolution, as shown in Fig 3.9g. Starting at 15 MHz, an exponential relationship between resolution and frequency band was discovered. Despite the fact that frequencies above 85 MHz have a lower contribution to lateral resolution performance for the characteristic signal sensitivities of these transducers, the resolution limit was only achieved at maximum bandwidth. As shown in Fig 3.9h, this was also true for the axial resolution.

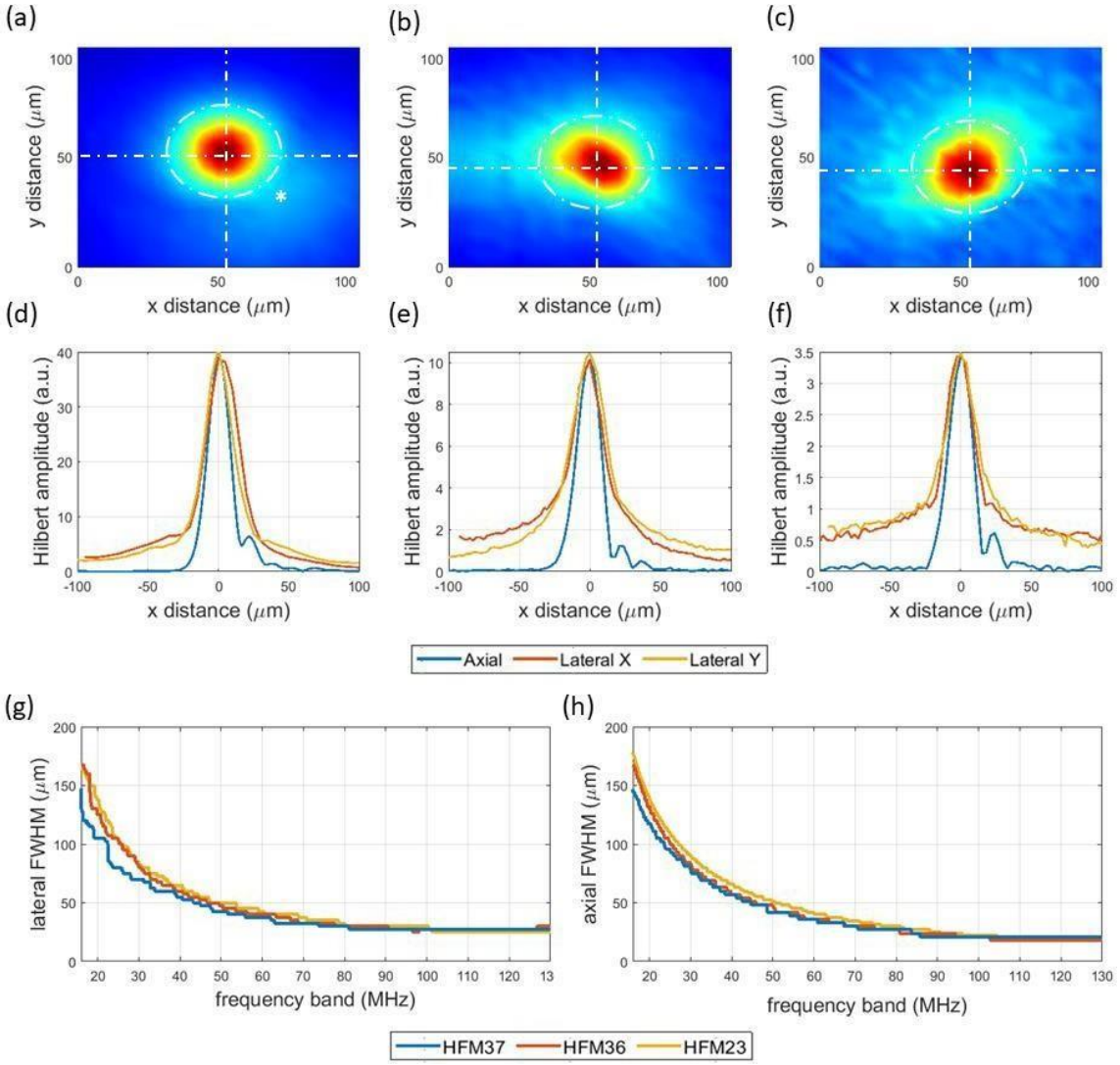

Figure 3.9 (a-c) Normalized Optoacoustic transducer sensitivity maps at XY focal planes of (a) HFM23 spherical transducer (no hole) (b) HFM36 spherical transducer with central aperture (c) HFM37 axicon transducer with central aperture. (d-e) Axial and lateral Hilbert resolutions of each transducer respectively. (g-h) Lateral and axial resolutions as a function of transducer frequency band for all three detectors respectively.

The sensitivity maps for each transducer are shown in Fig. 3.10 in the (lateral) X and (axial) Z directions. The XZ sensitivity maps for the spherical detectors (HFM23 Fig 3.10a, HFM36 Fig 3.10b) support the focusing behavior predicted from these geometries, with low frequency lobes visible in the near field due to the shorter propagation distance. In comparison, as shown in Fig 3.10c, the XZ sensitivity map for the axicon detector (HFM37) is defined by a thin pencil beam over an extended depth. In Fig 3.10d, the depth of focus for all three transducers is compared, yielding 220 µm and 250 µm for the spherical cases (HFM23 and HFM36, respectively) and 1050 µm for the axicon case (HFM37), which is 4.2 times that of the spherical equivalent with central aperture (HFM36). The axicon transducer maintains 40 µm lateral resolution over a 950 µm depth of focus and remains below 60 µm over a 1050 µm depth of focus, as shown in Fig 3.10e. While the axicon detector has a greater depth of focus than its spherical counterparts, it has a lower sensitivity when compared to the equivalent spherical detector with central aperture at focus (HFM36). Owing to the similar divergence angle measured for the spherical transducers, the HMF23 measured a depth of focus approximately 30 µm smaller than the HFM36 detector.

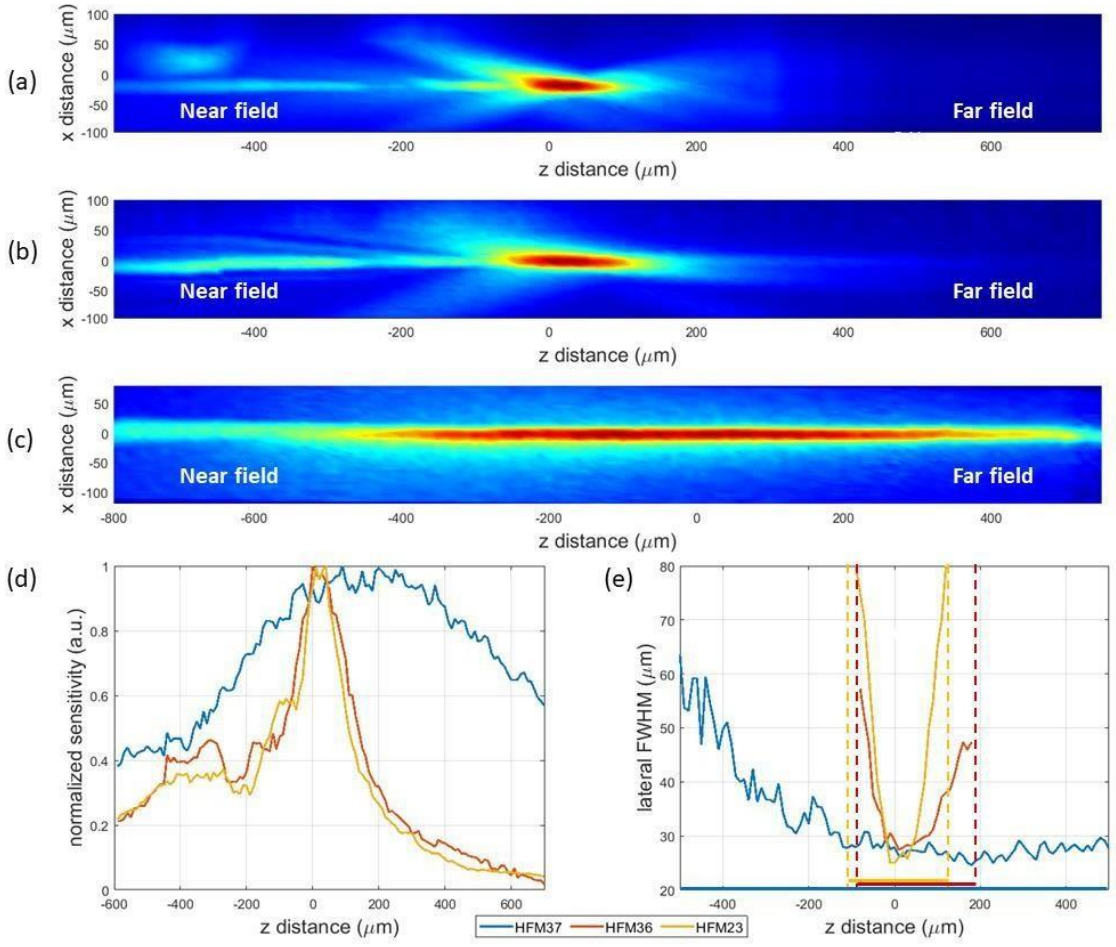

Figure 3.10: (a-c) Normalized Optoacoustic transducer sensitivity maps at XZ focal planes of (a) HFM23 spherical transducer (no hole) (b) HFM36 spherical transducer with central aperture (c) HFM37 axicon

transducer with aperture. (d) Normalized depth of focus line scans of transducers. Note: Z=0 corresponds to the focal point of the HFM23 and HFM36 sensors (e) Lateral resolution as a function of the transducer depth of focus.

Using our dedicated characterization system (Fig 3.1), we were able to demonstrate axicon ultrasound detection with broad 94 MHz-bandwidth (at a −6 dB cut off) and extended pencil beam optoacoustic spatial sensitivity with a depth of focus of 1050 µm and maintained 40 µm-lateral resolution over 950 µm. To our knowledge, we are the first group reporting the sensitivity performance of a high frequency broadband axicon ultrasound transducer. Our results show that a broadband ultrasound sensor with a axicon sensitivity field can be used to overcome the loss of resolution in optoacoustic imaging that spherical detectors experience at greater depths. However, the balance between sensitivity and depth of focus is a limiting factor. Although the depth of focus (compared with spherical detectors) has increased by 4.2 times with our axicon transducer, the overall sensitivity has been reduced by 2.85. Increased preamplification may compensate for some sensitivity loss. Furthermore, during the manufacturing procedure, it is possible that sphericity was introduced into the axicon lens, because the effective 4 mm theoretical depth of focus for our transducer design was not achieved.

We compared our built spherical transducer (HFM36) to an existing RSOM spherical detector (HFM23) with no central hole to determine the effective change in the sensitivity field induced by the presence or absence of a hole in a transducer (Figs. 3.9a, b and 3.8a, b). Our sensitivity maps show that a central hole in a spherical detector of up to one third of the sensor diameter has only a minor impact on the shape of the transducer's sensitivity map (Fig. 3.9,3.10), while decreasing overall ultrasound sensitivity proportional to the hole's area. The sensitivity fields of both spherical transducers were found to be identical. As a result, we expect reconstruction algorithms for spherical transducers without apertures, such as virtual point detectors or delay multiply and sum beamforming algorithms, could also be applied for the spherical transducer with central aperture in this study.

The characterization experiments of the third-generation detectors confirm they meet the required specifications listed in Table 3 for optoacoustic endoscopy. The only caveat is that they require further miniaturization to be housed inside a rotationally scanning probe and fulfill the <13mm diameter requirement. To determine whether the spherical or axicon transducer should be further developed into a friendlier endoscopic casing, a raster scanning unit was built to assess the optoacoustic spatial resolution and imaging depth of each transducer.

3.4. Raster scanning optoacoustic mesoscopy

To examine the imaging depth potential of the third-generation transducers a raster scanning optoacoustic mesoscopy system was constructed to image an inclined 100µm polyamide 6 suture with a tilt angle of 15.5º installed on a 3D printed mount. The setup as depicted in figure 3.11a consisted of a 1 ns-pulse width, 532nm light source operating at 200 Hz repetition rate (Wedge HB532, Bright Solutions, Italy). The energy per pulse was regulated by means of a polarizing beam splitter and a beam dump. A 90:10 beam splitter was employed to divert 10% of the light towards a photodetector for triggering. The remaining 90% of light was fiber coupled to a multi-mode fiber with a low divergence GRIN lens mounted at the distal probe tip. The transducer under test was mounted to an XYZ motorized stage (MTS50-Z8 in 3-Axis XYZ Configuration, Thorlabs) to perform raster scanning over the tilted optoacoustic line source with deionized water employed as acoustic coupling medium. This imaging configuration is illustrated with thespherical transducer in Figure 3.11b. Each detector was installed with the active element facing the acoustic source and aligned with the motorized stages. Co-axial optoacoustic pulse illumination was provided by inserting the GRIN probe in the transducer's central aperture channel.

A continuous raster XY scan was performed by triggering light source with the motorized stages over a field of view of 3mm x 10mm with a pixel size of 10µm. The temporal optoacoustic signals were pre-amplified externally with an 30dB amplifier (Sonaxis SA, France) and connected to a T-bias (ZFBT-4R2GW+,Mini-Circuits) prior to data acquisition. Both optoacoustic and photodetector signals were acquired by an integrated ATS9373 DAQ card (AlazarTech, Canada) controlled by LabVIEW and data processed in MATLAB.

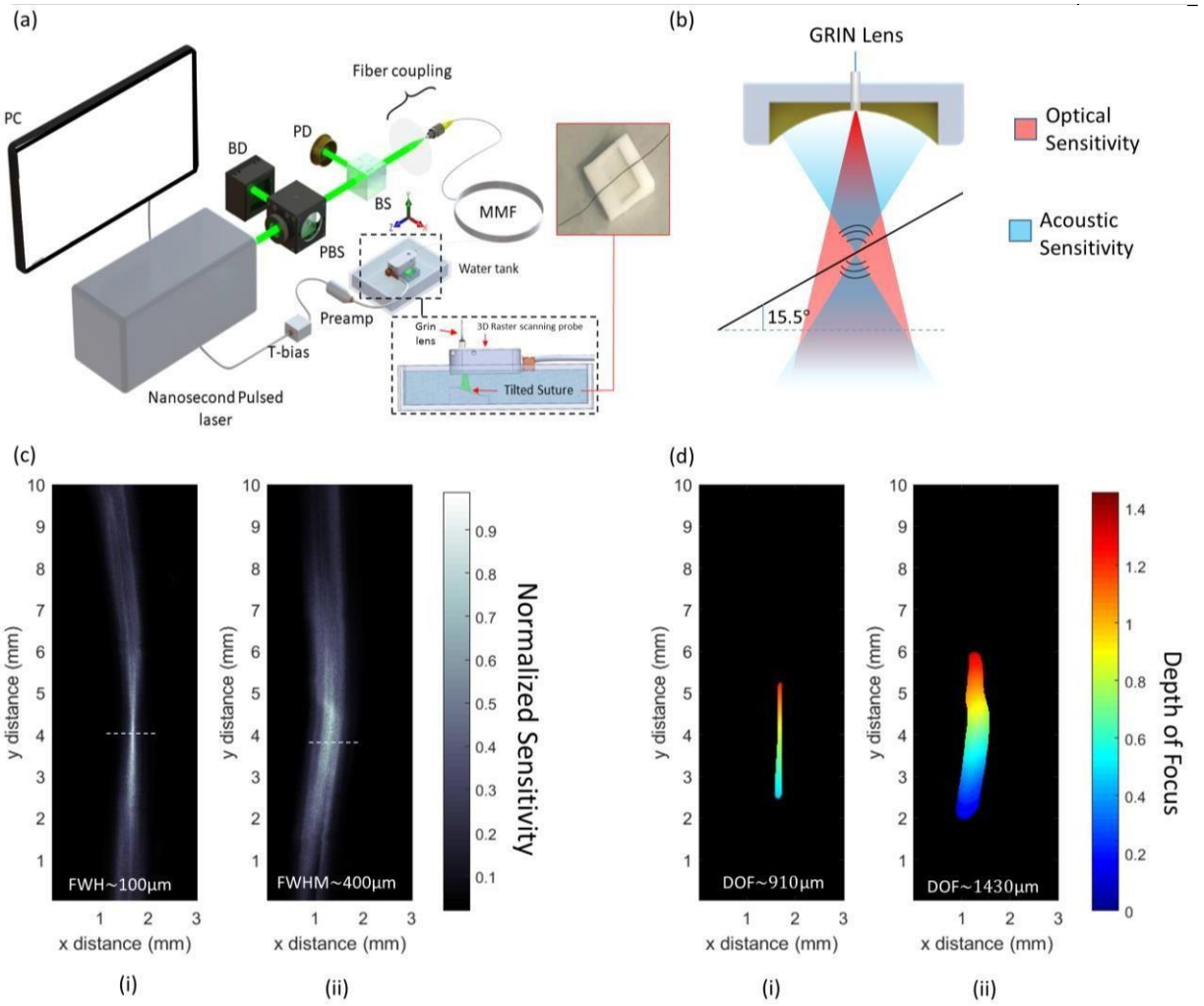

Figure 3.11 Raster Scanning Optoacoustic mesoscopy of a 100µm titled suture with the third-generation optoacoustic endoscopy transducers (a) Depicts the raster scanning optoacoustic mesoscopic imaging unit to scan a tilted 100µm suture, PBS: Polarizing beam splitter, PD: photodiode, BD: beam dump, MMF: multimode fiber. (b) Illustrates mesoscope imaging configuration with the spherical detector to image the titled suture. (c) Normalized maximum intensity projections of the optoacoustic response with the (i) spherical HFM36 detector and (ii) axicon HFM37 detector. (d) Optoacoustic depth maps thresholded upto each sensors depth of focus and bounded by the lateral resolution with the (i) spherical HFM36 and (ii) axicon HFM37 detector.

The normalized maximum intensity projections acquired with the spherical and axicon detectors are shown in Fig 3.11c. The spherical transducer correctly resolved the 100 µm suture at focus and reduced in lateral resolution moving away from focus as shown in Fig 3.11c(i). The axicon transducer Fig 3.11c(ii) measured a full width half maximum value of 400 µm at the maximum sensitivity and remained the much the same over the entire field of view. To determine imaging depth of focus of each configuration the normalized maps in Fig 3.11c were threshold to >0.5 and endcoded in depth to unveil the depth of focus maps as illustrated in Fig 3.11d. The spherical transducer (Fig 3.11d(i)) measured a depth of focus of 910µm whereas the axicon transducer (Fig

3.11d(ii)) measured a depth of focus of 1430 µm. Surprisingly, whereas the spherical detector correctly resolved the suture at focus, the axicon detector produced a blurred image. Although the depth of focus did indeed increase with the axicon detector by approximately ~500µm, we found lateral resolution is 14x lower measuring at 400µm compared to the 28µm determined during transducer characterization. To explain the discrepancy in axicon transducer resolution, an in-depth analysis with multiple 3D acoustic simulations were conducted mimicking the characterization and imaging conditions.

3.5. 3D optoacoustic transducer simulations

The axicon transducer exhibited lower lateral resolution during imaging than characterization. To demystify this behavior, we employed the MATLAB toolbox: Kwave [92] to simulate the characterization and imaging conditions in 3D with a broadband spherical and axicon transducer of similar dimensions to HFM36 and HFM37. Figure 3.12 illustrates the 3D Kwave simulation configurations to obtain the XY and XZ sensitivity field response to a point and line source for the spherical and axicon transducers. Due to limited GPU memory, we simulated 3D half scale detectors with central frequencies of approximately 32MHz. We did not take into account the glass shaped lens and performed simulations with the active elements directly shaped to spherical or axicon to achieve directivity. Note: Although the HFM36 and HFM37 transducers do have a 2 mm central aperture, a stainless-steel channel with wall thickness of 0.5mm surrounds the aperture; hence the effective overall aperture considering the transducer active region to be simulated is 3mm. For this reason, the half scale transducers in Fig 3.12(b-e) show a 1.5mm central aperture. Our kgrid propagation medium parameters included medium sound speed =1500m/s, medium density =1000kg/m^3. Acoustic medium attenuation in water was taken into account with the following parameters a_0=2.17e^{-3}, y=2, BonA=4.96. Simulation sample rate was set to 400MHz and the maximum supported frequency was upto 75MHz. Further information about maximum supported frequency and acoustic attenuation parameters can be found in [92]. Two acoustic sources were simulated in 3D space including a 10µm point source and a 10µm line source with a strength of 1 Pa. To generate the XY and XZ sensitivity maps the simulated acoustic sources were raster scanned in the transverse and sagittal planes respectively. These conditions were employed all for simulations and are listed in Table (a) in Fig 3.12.

Fig 3.12(b-c) depicts the simulation configurations mimicking the characterization experiment in section 3.3. Fig 3.12(b) illustrates a diagram of the half scale HFM36 transducer positioned at

focus to image in a 10 µm broadband point source emitting frequencies upto 75MHz. Similarly, Fig 3.12(c) shows the half scale axicon transducer also positioned to image the same point source. To mimic the raster scanning imaging of a titled suture, we generated a 10 µm line source; although the tilt was removed as we would generate the sensitivity response in the XZ plane. Fig 3.12(d) shows the half scale HFM6 spherical transducer positioned at focus to image a 10 µm suture and Fig 3.12 (e) similarly shows the half scale HFM37 axicon transducer positioned to image the same 10 µm suture.

(a)

Simulation Parameters			
Grid Size	420	Speed of sound	1500m/s
Full Grid Size	4.2mm	Sample Rate	400MHz
X , Y , Z grid size	10µm,10 µm, 25µm	Max Frequency	75MHz
Acoustic source	10µm point source and 10µm line source		
Source strength	1 pascal		
Attenuation parameters	$\alpha_0 = 0.00217$, $y = 2$, BonA = 4.96		
Transducer scale	½ scale in 3D		

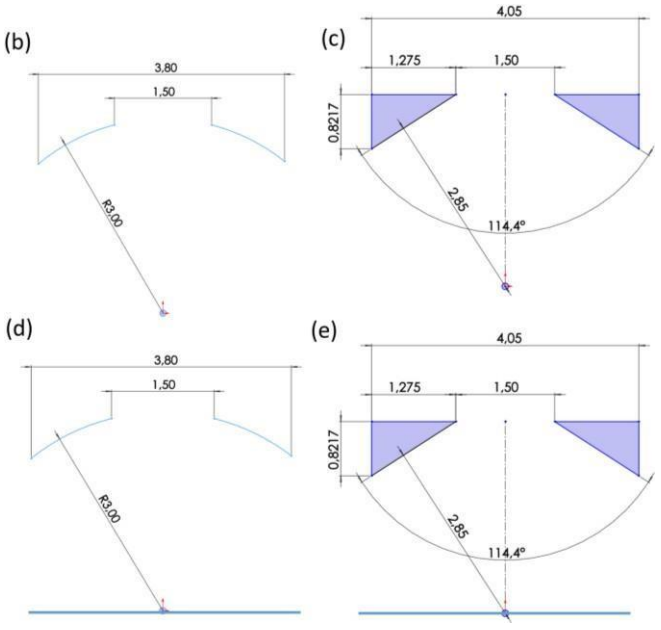

Figure 3.12: 3D K-wave simulation configurations (a) The simulation parameters utilized during the 3D acoustic simulations (b-c) Simulation configuration mimicking characterization experimentation in section 3.3 with (b) ½ scale HFM36 spherical transducer and (c) ½ scale HFM37 axicon transducer imaging a point source. (d-e) Simulation configuration mimicking suture experimentation in section 3.4 with (d) ½ scale HFM36 spherical transducer and (e) ½ scale HFM37 axicon transducer imaging a point source.

The normalized generated XY and XZ sensitivity maps for a 10µm point and line source for the half scale spherical and axicon transducers are illustrated in Fig 3.13. Where Fig 3.13a is a pictorial representation of the acoustic source shape generated from the target point source and the impulse response of this source for each transducer are depicted in the XY sensitivity plane (Fig3.13b-c) and the XZ sensitivity plane (Fig 3.13d-e).

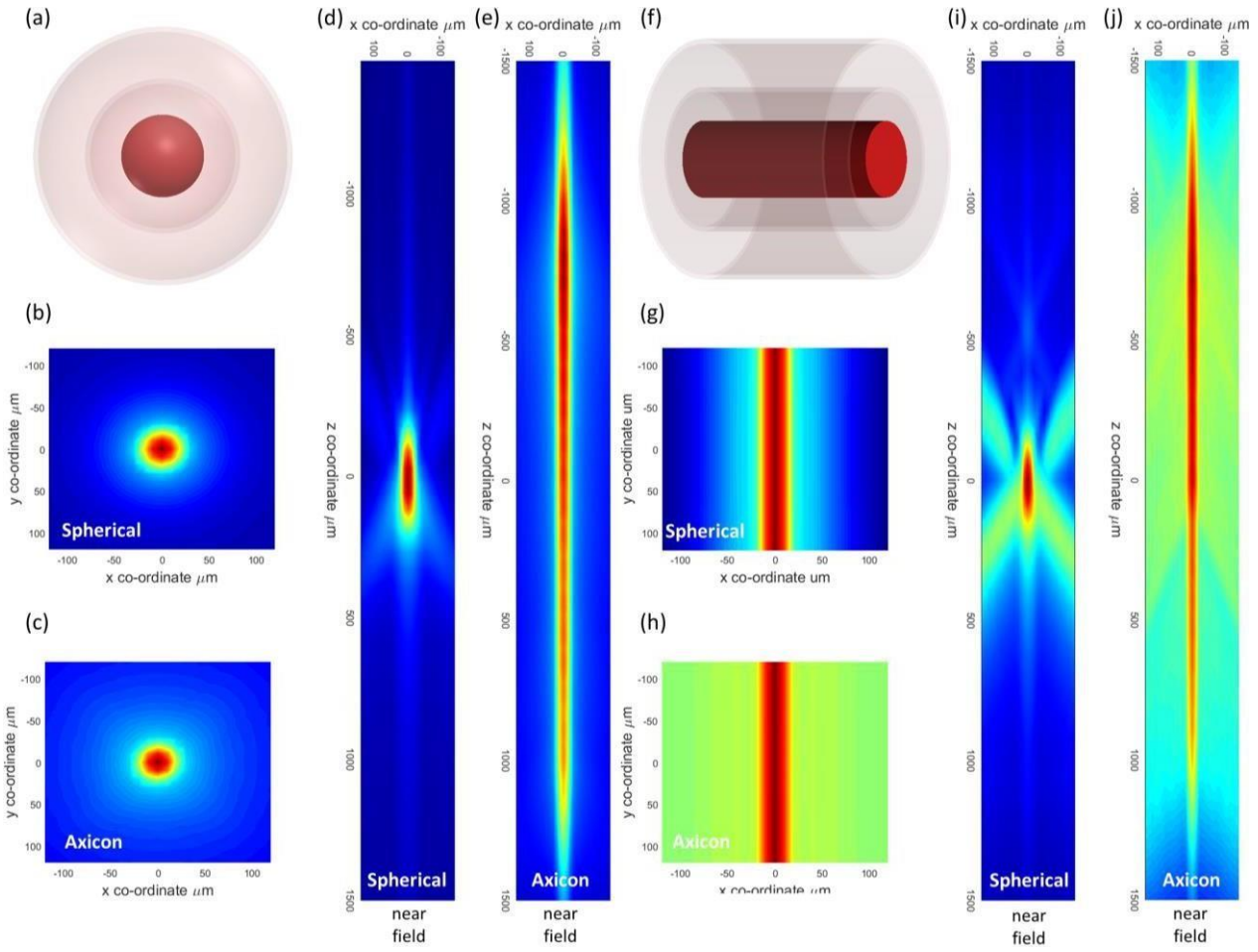

Figure 3.13: 3D Simulations of Spherical and Axicon transducers on kWave with respect to a point and line source. Figure (a) illustrates a diagram of the acoustic point source generated in kwave. Figures (b,c) are the XY and (d,e) are the XZ sensitivity map measured by scanning around a 10 µm point source for the HFM36 and HFM37 half scale sensors respectively. Figure (f) illustrates a diagram of the acoustic line source generated in kwave. Figures (g-h) are the XY and (i, j) are the XZ sensitivity map measured by scanning around a 10µm line source for the HFM36 and HFM37 half scale sensors respectively.

As shown in Fig 3.13c the spherical detector depicts a ball shape sensitivity volume with a restricted a depth of focus of 260µm. The axicon transducer (Fig 3.13d) features a thin pencil beam with an extended depth of focus of 2.65mm. The sensitivity asymmetry observed within thepencil beam is a result of the central transducer aperture. Comparing the shape of the sensitivity maps in Figs 3.13b-e to the experimental measurements acquired with the characterization unit insection 3.3 figures 3.9 and 3.10, they are in good agreement albeit a reduced lateral resolution of ~45µm as a result of the simulated central frequency of 32MHz.

The experimental characterization of the HFM37 transducer in Fig 3.10c measured a depth of focus of 950µm whereas the half scale simulated HFM37 transducer in Fig 3.13d exhibited a depth of focus 2.65mm. The reason for this discrepancy is as a result of sphericity introduced when manufacturing the lens and ultra-broadband nature of the experimental point source exceeded frequencies over 100MHz where acoustic attenuation is higher through the propagationmedium, in contrast the simulation was restricted upto 75MHz.

Fig 3.13f is a pictorial representation of a line source generated when optoacoustically exciting a 10µm line source. Figures 3.13 (g) & (h) demonstrate the XY sensitivity maps of half scale HFM36 spherical and half scale HFM37 axicon transducers response to the 10µm line source respectively. In this instance the spherical still measures a FWHM of 45 µm, however the axiconFWHM cannot be measured as the acoustic signal does not drop below 50% of maximum signal.Figures 3.13 (i) & (j) depict the XZ sensitivity maps of half scale spherical and axicon transducersrespectively in response to the 10µm line source. From the XZ spherical sensitivity map, the spherical sensitivity volume is still observed with low frequency signals detected out of focus, though the low amplitude signal strength measured out of focus does not degrade the detectors lateral resolution. The axicons XZ map sensitivity shows a pencil beam with deteriorated lateral resolution as the sensor measures high amplitude low frequency signals when the source is off- axis with respect to the sensor. This result relates to the reduced lateral resolution in the tilted suture experiment with the HFM37 transducer in Fig 3.11. The sensitivity asymmetry along the line profile is once again attributed to the central aperture of the axicon transducer.

To further analyze these observations, we perform normalized line scans on the focal planes of each detector with respect to the point and line source as shown in Figure 3.14. From Figure 3.14 (a) we observe the detectors response decreases rapidly as we move away from the point source. 100µm away from the point source, the spherical detectors signal strength drops to 7% whereas the axicon drops to 18%. Figure 3.14 (b) illustrates that 100 µm away from the line source the spherical signal drops to 18%. The discontinuity observed at positions ±40µm in the spherical scan profile is due to the presence of the central aperture. The axicon detectors drops to approximately 53% of the signal 30 µm away from the source and effectively levels off at this value.

Here, we have shown for the first time, a concise evaluation and comparison, both experimentally and in simulation, the influence of broadband axicon and spherical geometries with central apertures when imaging linear point and line OA sources. The simulations are in excellent agreement with the experiment results of these detection geometries. Surprisingly, whereas the

spherical detector correctly resolved a line source at focus, the axicon detector produced a blurred image. By virtue of the different acoustic waves produced by the point and line sources, i.e. spherical and cylindrical, respectively, the spherical detector could sustain lateral resolution at focus for both cases; however lateral resolution strongly deteriorates when using axicon detection to image line sources. This is due to strong low frequency ultrasound sensitivities outside the axicon focal region, therefore detecting acoustic signal off-axis perpendicular to the direction of the scan. Hence the axicon transducers spatial resolution is a function of both illumination and the type of generated optoacoustic wave geometry name spherical or cylindrical. Consequently, this characteristic is not very useful for imaging the vasculature inside the esophageal lining for optoacoustic endoscopy and thereby producing blurred images.

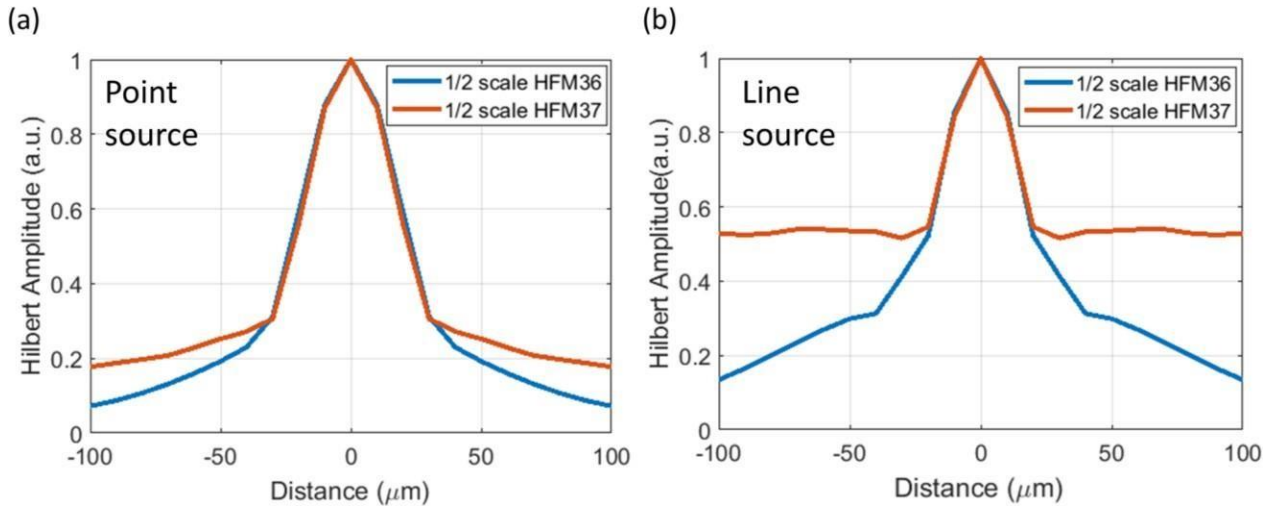

Figure 3.14: Normalized lines scans across the XY sensitivity maps of half scale HFM36 spherical and HFM37 axicon transducers of the 10µm point source (a) and 10µm line source (b)

Alternatively, optoacoustic axicon transducers could be deployed in optoacoustic microscopy where the off-axis acoustic signals are restricted by the narrow illumination size such as a Bessel beam to generate optoacoustic point sources. This configuration would allow us to exploit the pencil beam sensitivity profile of an axicon detectors response to a point source as shown in Figs 3.10c and 3.13e enabling fast volumetric optoacoustic microscopy imaging. Our results advocate the use of spherical detection for optoacoustic endoscopy and further explore the benefits of utilizing axicon detection in optoacoustic microscopy.

3.6. Raster scanning optoacoustic microscopy

From the experiments and simulations in sections 3.3-3.5 we found the axicon transducer is not suitable for optoacoustic endoscopy but could be employed for optoacoustic microscopy to overcome the tradeoff between high lateral resolution and restricted depth of focus in microscopes applying Gaussian beam illumination, which is diffraction limited and thus has a confined focal range (Rayleigh range). Spherically focused transducers are often employed for detection in OA microscopy because their spatial acoustic sensitivity profile complements the optical sensitivity profile of Gaussian illumination, which maximizes the overall optoacoustic sensitivity [93]. Although the combination of Gaussian beam illumination and spherically focused transducers provides excellent sensitivity, this configuration only provides high resolution imaging at the Gaussian beam focal plane [94-96]. To generate 3D images, the sample must be scanned in the axial direction over the same focal plane due to the narrow focus. As a result, existing OA microscopy configurations are inadequate for volumetric imaging applications that are time sensitive or require sample motion, such as full-body zebra fish imaging, measuring thick optically transparent samples, or cell imaging and counting.

Unlike Gaussian beams, which have point foci, so-called ideal Bessel beams have line-shaped foci because they are not diffraction restricted. In practice, Bessel beams are approximated by passing collimated Gaussian illumination through a conical (axicon) lens, which creates a line shape optical sensitivity profile that allows imaging over greater depths without sacrificing lateral resolution [97,98]. As a result, in many optical imaging modalities, such as light sheet microscopy, optical coherence tomography, and second harmonic generation [99-104], Bessel beam illumination has been investigated as a means of increasing imaging depth.

In optoacoustic microscopy, attempts to increase imaging depth using Bessel beam illumination have also been documented. For example, red blood cells were imaged with 7 µm lateral resolution over a depth of 1 mm using an OA microscope with Bessel beam illumination [105]. In two imaging studies of mouse ears, using Bessel beams instead of Gaussian beams resulted in a 7-fold increase in imaging depth. These systems' lateral resolutions/depths-of-focus were stated to be 1.6 µm/483µm [106] and 300 nm/229 µm [107], respectively. However, these microscopes used unfocused or spherical transducers with acoustic profiles that were mismatched to the line foci of the optical Bessel beam, reducing optoacoustic sensitivity in the axial direction. This issue was solved by imaging zebra fish with a lateral resolution of 2.4 µm and a depth-of-focus of 635 µm using optical axicon interferometric ultrasound detection combined with Bessel beam illumination

[108]. Granted optical interferometric detection necessitates a thermally stabilized continuous wave light source and a high-speed balanced photodetector with a large bandwidth, increasing the system's cost. Furthermore, since the beam paths are vulnerable to temperature variations and micro-vibrations, optical ultrasound identification requires precise beam path orientation and environmental monitoring. Furthermore, trigger synchronization between the photodetector and optoacoustic laser is needed, which adds to the difficulty of data acquisition. Finally, the photodetector's interferometric signals require calibration and restoration to reconstruct the initial optoacoustic signal.

The axicon transducer's thin cylindrical axial sensitivity field could complement the optical profile of a Bessel beam, allowing for a simple low-cost approach to sense acoustic waves with increased sensitivity along the axial path, optimizing usable imaging depths in OA microscopy and facilitating rapid volumetric imaging. We set out to see if the depth-of-focus in OA microscopy could indeed be maximized by matching the ultrasound detector sensitivity to Bessel beam illumination with an ultra-broadband axicon transducer, while also assessing the results of mismatches in illumination and detection geometry. As a result, we created a custom OA microscope that allows for the flexible interchanging of illumination and detector units while maintaining the same imaging field-of-view.

The inverted optoacoustic microscope with interchangeable illumination optics and broadband transducer is illustrated in Figure 3.15a. A light source with a wavelength of 532 nm and a pulse width of 1 ns power the microscope (Wedge HB532, Bright Solutions, Italy). A polarizing beam splitter and a beam dump were used to control the interrogation energy per pulse. For trigger, a 90:10 beam splitter was used to divert 10% of the light into a photodetector. Prior to optoacoustic excitation, the remaining 90% of light was spatially filtered to clean and expand the beam. A 0.25 NA 10X plan achromat provided Gaussian illumination with a spot size of approximately 5 µm. (RMS10X, Olympus, Japan). Alternatively, by replacing the objective lens with an axicon lens (AX255 UVFS, Thorlabs, USA), axicon illumination with an FWHM of approximately 5 µm was obtained.

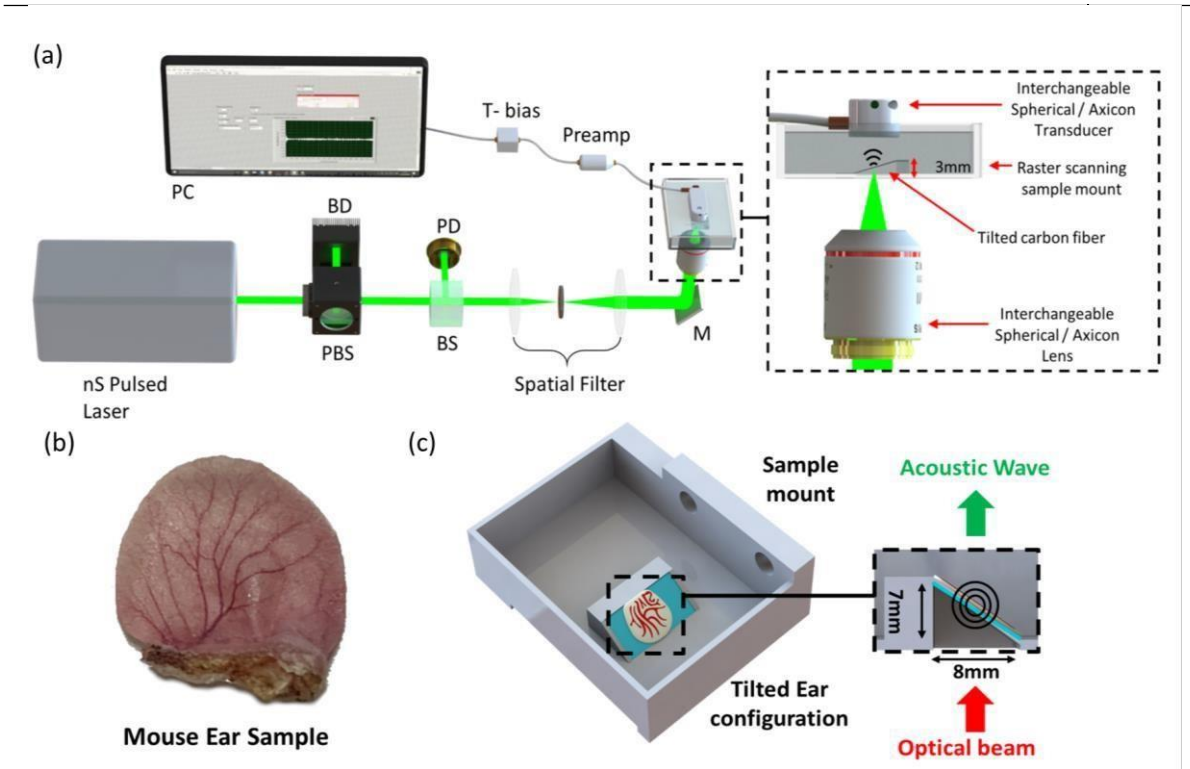

Figure. 3.15: Optoacoustic transducers and optoacoustic microscopy experimental setups for imaging a carbon fiber and ex-vivo mouse ear. Cross sectional and enface views of (a) HFM36 spherical and (b) HFM37 axicon transducers with central apertures. TE: Transducer element, EC: Electrical Connector, L: Acoustic Lens, CA: Central Aperture Window. (c) Depicts the optoacoustic microscope setup and tilted carbon fiber imaging configuration. PBS: Polarizing beam splitter, BS: beam splitter, BD: Beam dump, PD: Photodiode, M: Mirror. (d) An excised mouse ear sample sealed with a hot blade. (e) Illustration of the ex-vivo experimental setup wherein the mouse ear is placed on a tilted transparent optical window within a 3D printed tank.

Each acoustic transducer was installed to face the illumination source and aligned to the optical beam using a manual XYZ conversion stage for OA microscopy imaging (Fig. 3.15a). All four possible excitation and detection combinations (Gaussian-spherical, Gaussian-axicon, Bessel-spherical, and Bessel-axicon) were assessed by imaging a 7 µm diameter carbon fiber immersed in deionized water and fixed with a tilt angle of 23.2º over a height of 3mm inside a 3D printed water tank with a planar optical window for transmission mode OA microscopy. The carbon fiber was precisely adjusted along the illumination-detection axis using a motorized XYZ scanner with a linear stage for the X scanning direction (M-511, Physik Instrumente, Germany) and two lightweight precision linear stages for the Y and Z scanning directions (MTS50-Z8, Thorlabs, USA). A raster scan was conducted with each illumination and detector combination after the optical beam, transducer, and carbon fiber were matched (Fig. 3.17a (i-iv); scan speed: 2 mm/s, scan resolution: 500 nm x 800 nm, field-of-view: 6 mm x 0.128 mm). For the Gaussian and Bessel beams, pulse illumination energies of 10 nJ and 2 µJ were used, respectively. Prior to data

acquisition, the temporal optoacoustic signals were pre-amplified externally with a 30 dB amplifier (Sonaxis SA, France) and wired to a T-bias (ZFBT-4R2GW+, Mini-Circuits, USA). A DAQ card (ATS9373, AlazarTech, Canada) synchronized to the external trigger port via the photodetector signal was used to acquire optoacoustic signals. LabVIEW (National Instruments, USA) was used to manage data collection, and MATLAB was used to process the data and produce 2D maximum intensity projections (MathWorks, USA). Amira-Avizo was used to create 3D volumetric projections (Thermo Fisher Scientific, USA).

Using a beam profiler (SP620U, Ophir, USA) with a secondary 10X plan achromat lens (RMS10X, Olympus, Japan) and an 80 mm-optical spacer, the Gaussian and Bessel illumination profiles were measured along the optical axis moving away from the illumination lens surface. The Gaussian and Bessel beam profiles at maximal irradiance around the optical axis are shown in Fig. 3.16(a & b). To determine the illumination spatial confinement for each setup, the FWHM and relative peak irradiances were determined along the optical axis. The Gaussian beam confinement measured at 50 μm optical plane intervals over a $\pm$300 μm axial distance around the focal point as seen in Fig. (3.16c). The Bessel beam confinement estimated at 1 mm optical plane intervals over an axial span of 12 mm traveling away from the axicon lens surface is depicted in Fig. (3.16d). The approximate origin for the Bessel beam experiment was set to approximately 6 mm from the surface of the axicon lens.

Importantly, owing to their non-diffracting nature, Bessel beam optical profiles always exhibit secondary concentric rings circling an inner lobe, as seen in Fig 3.16b, which produces unnecessary secondary optoacoustic signals interfering with the signal produced from the central lobe, lowering lateral image resolution. The image projection acquired for the Bessel-axicon and spherical configurations was subjected to MATLAB's built-in blind-deconvolution algorithm (deconvblind) to remove image artifacts and background signal emanating from the secondary lobes of the Bessel beam. The Bessel beam profile (see Fig. 3.16b) was used as reference for initial estimate of the point spread function to improve deconvolution. This technique has previously been shown to suppress side lobe artifacts in optoacoustic microscopy [106,107].

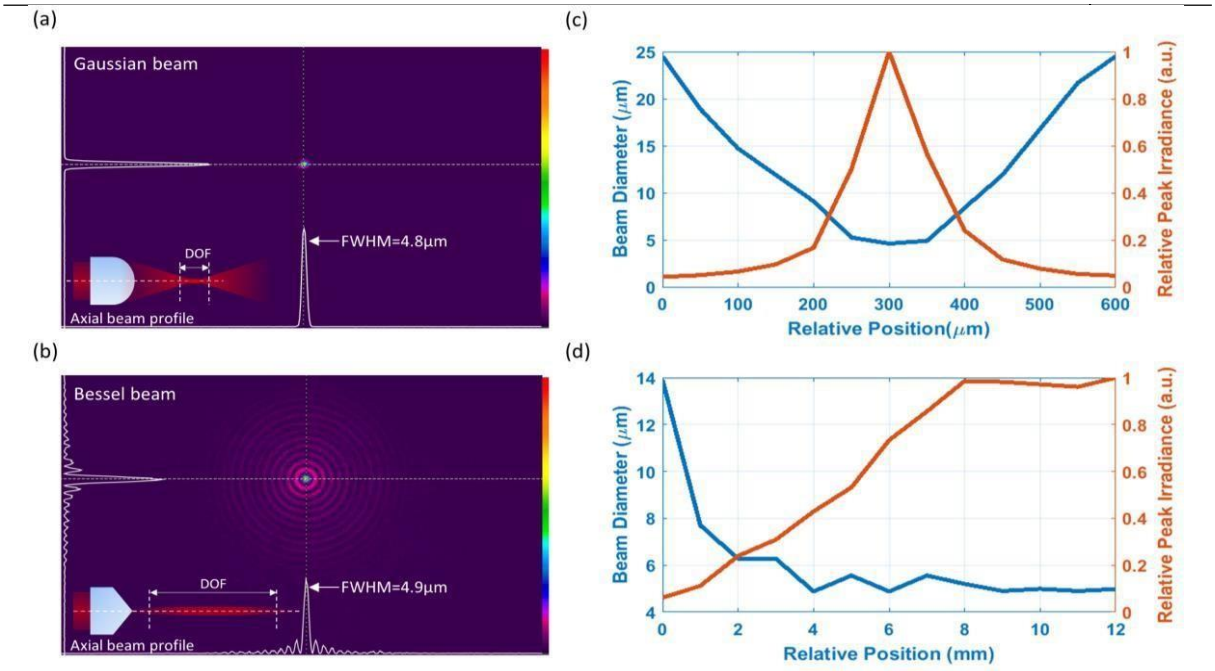

Figure. 3.16: Illumination beam profiles for optoacoustic microscopy. (a) Gaussian and (b) Bessel beam profiles measured at the lateral plane passing through the point of maximum irradiance. Relative peak irradiances and diameters of (c) a Gaussian beam measured at 50 μm optical planes through the optical focus. (d) A Bessel beam central lobe at 1 mm optical planes along the optical axis moving away from the axicon lens. Note: The arbitrary origin for the Bessel beam case is set to be 6 mm away from the surface of the axicon lens.

We used optical beam profile measurements to quantify the transverse strength distributions of the beams at various points along their propagation path. The FWHM illumination beam diametersof approximately 5 μm for both the Gaussian beam and the central lobe of the Bessel beam are seen in Fig. 3.16(a) and (b). The Gaussian beam exhibits light confinement inside the 5 μm-spot,as predicted, while the Bessel beam exhibits a transversal pattern of lower amplitude concentric circles around the 5 μm central lobe. Bessel beams have these concentric rings as a natural property, with each ring (including the central lobe) having the same amount of energy. As a result, the concentric rings emit unnecessary secondary optoacoustic signals that interact with the signal produced by the central lobe, reducing imaging lateral resolution. In optoacoustic microscopy, the Gruneisen relaxation effect [105] and blind deconvolution [106-107] have been used to suppress Bessel beam side lobes related artifacts. The blind deconvolution algorithm is also used here since it is a computationally efficient and cost-effective approach (see Fig 3.19). For both light patterns, the beam profile and relative peak irradiance were determined along the optical axis. The FWHM and relative peak irradiance of the Gaussian beam at 50 μm optical plane spacing intervals obtained around the optical axis over a ±300 μm axial range from the focal point as seen in Fig. 3.16(c). The maximum irradiance calculated at focus is used to normalize the peak

irradiance. We verified a minimum beam diameter of approximately 5 μm at focus for the Gaussian illumination and measured a depth-of-focus of 108 μm. The FWHM and relative peak irradiance of the Bessel beam central lobe at 1 mm optical plane spacing intervals obtained over an axial range of 12 mm traveling away from the axicon lens is seen in Fig. 3.16(d). During the Bessel beam evaluation, the approximate origin was set to approximately 6 mm from the axicon lens's surface. The diameter of the Bessel beam decreases with distance, averaging 5 μm over an 8 mm span. The central lobe of the Bessel beam's relative irradiance increases with distance, approaching a peak at a relative location of 8 mm where the Bessel beam is fully formed.

With our inverted OA microscope, we explored the effect of matching illumination and detection profiles on imaging performance using four distinct configurations of Gaussian and Bessel illumination and spherical and axicon transducer detectors (Fig. 3.17a). Intensity normalized MIP images of a tilted 7 μm-carbon fiber for all four illumination-detection setups are seen in Fig. 3.17b. Paired with Gaussian illumination (Fig 3.17b(i-ii)), both spherical and axicon detection resolved the carbon fiber with an FWHM of 7 μm at the illumination focal point, thus detecting the fiber over a total axial distance (depth-of-focus) of approximately z = 225 μm. The carbon fiber was resolved at the point of peak optoacoustic strength with an FWHM of 7 μm using Bessel illumination and spherical detection (Fig 3.17b(iii)), while the tilted fiber was detected over the whole field-of-view of 6 mm x 0.128 mm. However, between y = 0 mm and y = 1 mm, and y = 4 mm and y = 6 mm, the normalized optoacoustic intensity for the Bessel-spherical combination decreased dramatically, and the fiber was scarcely distinguishable. At y = 0.65 mm and y = 4.4 mm, the normalized amplitude for the Bessel-spherical pair was roughly 13% of the normalized maximum value, while the equivalent imaging distance in that range was z = 1.98 mm. The spherical nature of the detector concentrates sensitivity at the focal point, resulting in a dramatic decrease in intensity away from the center of the image. Finally, the implementation of Bessel beam illumination and the axicon transducer (Fig. 3.17b(iv)) shows the tilted carbon fiber with increased signal-to-noise ratio over the entire depth of 3 mm (SNR). The optoacoustic intensity drops to 30% of the normalized maximum intensity at y = 0 mm and to 23% of the normalized maximum intensity at y = 6 mm when Bessel illumination and axicon detection are combined where the FWHM was 7 μm over almost the whole field-of-view.

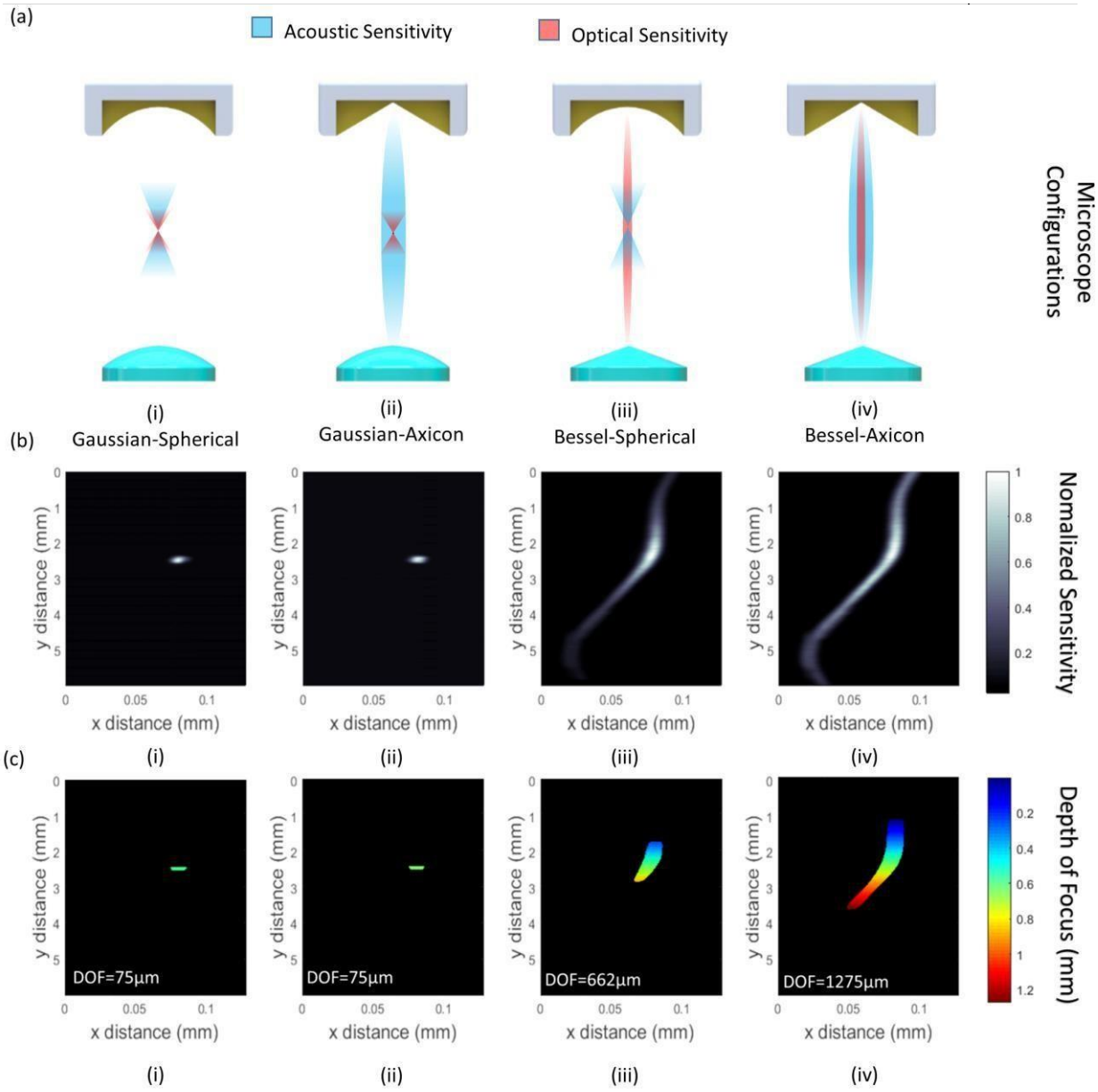

Fig. 3.17: Optoacoustic microscopy of a tilted 7 µm-carbon fiber using different acoustic and illumination configurations. (a) Illustrations of the four optoacoustic microscopy configurations: (i) Gaussian beam – spherical transducer, (ii) Gaussian beam – axicon transducer, (iii) Bessel beam –spherical transducer, (iv) Bessel beam – axicon transducer. (b) Depictions of the normalized maximum intensity optoacoustic images. (c) Corresponding false-color depth maps displayed within the depth-of-focus and lateral resolution for each imaging configuration.

We generated false-color depth maps from the MIP images in Fig(3.17b) to visualize the depth-of-focus and lateral resolutions for the four imaging setups (Fig 3.17c). The depth-of-focus was calculated by extracting the axial range where the normalized MIP is greater than 50%, and the lateral resolution was calculated as the FWHM through the carbon fiber for each imaging depth within the depth-of-focus. The Gaussian illumination resulted in a depth-of-focus of 75 µm,

regardless of whether the transducer was spherical (Fig. 3.17c(i)) or axicon (Fig. 3.17c(ii)). The depth-of-focus is increased by 9-fold to 662 μm when Bessel illumination is used in conjunction with the spherical transducer (Fig. 3.17c(iii)). As predicted, the depth-of-focus is maximized to 1275 μm when Bessel illumination is combined with axicon detection (Fig. 3.17c(iv)). As compared to Bessel illumination with spherical detection, the paired Bessel illumination and axicon detection results in a doubling of the depth-of-focus and a 17-fold improvement in the depth-of-focus as compared to Gaussian illumination coupled with any of the transducers.

We imaged a freshly excised mouse ear (Fig 3.15d) positioned on a tilted cover slit mounted within a customized 3D printed water tank at a height of 7 mm and an inclination angle of 41.2^{o} to test the image quality of our proposed OA microscope setup in biological samples with irregular surfaces. The tilted mouse ear was imaged using all four optical illumination and acoustic detection configurations (scan speed: 2 mm/s, scan resolution: 1 μm x 10 μm, field-of-view: 8 mmx 5 mm). For Gaussian and Bessel beam illuminations, the pulsed energies were set to about 80 nJand 8 μJ, respectively. The 3D and 2D top- and side-view maximal intensity projections obtainedby imaging the titled mouse ear with a combination of Gaussian illumination and spherical detection are shown in Fig. (3.18a-c). The vasculature can be seen at over depth of about 700 μm.The Gaussian illumination with the axicon detector case Fig. (3.18d-f) yields comparable results,with vessels visible over a depth of 700 μm. Bessel illumination and spherical detection, on the other hand, enable visualization of vasculature to a depth of 2.8 mm (Fig. 3.18). (g-i). Finally, Bessel illumination combined with axicon identification exposes the entire vasculature of the mouse ear over a depth of 4.2 mm (Fig. 3.18). (j-l). The ability to see tiny vessels in the upper region of the scan, which would otherwise be hidden with any of the other setups, is allowed by the preservation of high resolution over the entire depth of the ear.

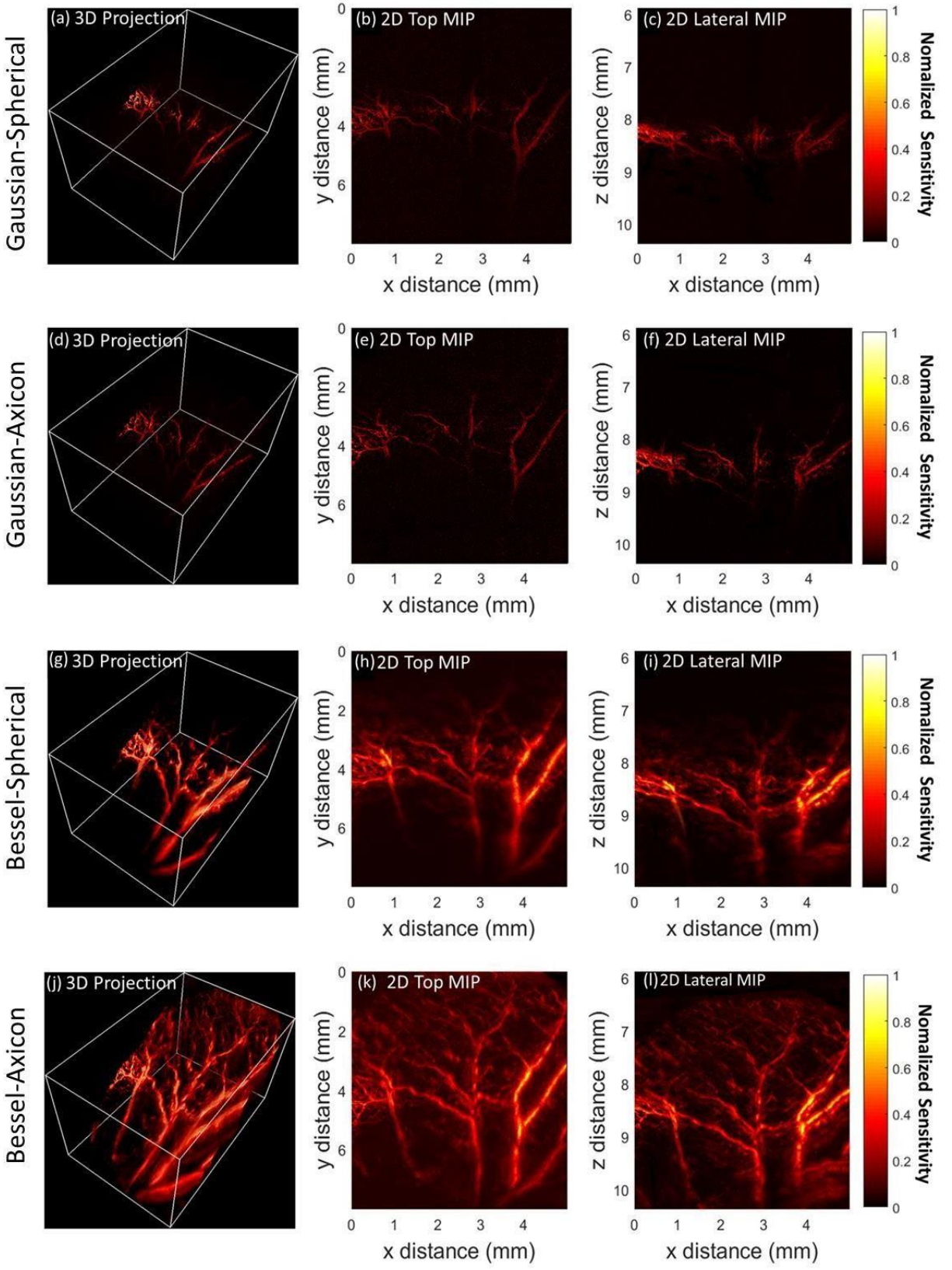

Figure. 3.18: Optoacoustic microscopy of a tilted mouse ear imaged with all four combinations of Gaussian or Bessel illumination and spherical or axicon transducers for detection. The sample was scanned using the same experimental configurations depicted in Fig. 3.17a(i-iv). 3D projections, 2D (top), and lateral (MIPs) of the mouse ear scanned with the following illumination/transducer combinations: (a-c) Gaussian-Spherical, (d-f) Gaussian-Axicon, (g-i) Bessel-Spherical, and (j-l) Bessel-Axicon.

To improve resolution and minimize background noise, the blind deconvolution algorithm in MATLAB was used to reduce image artifacts caused by the secondary side lobes of the Bessel illumination beam (Fig. 3.19). Figure 3.19a displays the raw MIP of the mouse ear collected using a combination of Bessel illumination and axicon detection. Deconvolving the initial image (Fig. 3.19a) with the Bessel beam profile in Fig 3.16b yielded the deconvolved projection seen in Fig. 3.19b. The position of the line profile calculation for the raw and deconvolved data, shown in Fig. 3.19c, is shown by the dotted white lines in both Figs. 3.19a and 3.19b. After deconvolution, the line profiles display a 10% decrease in background signal, resulting in a 2.1 dB rise in SNR and an improvement in vessel width definition from 132 µm to 75 µm.

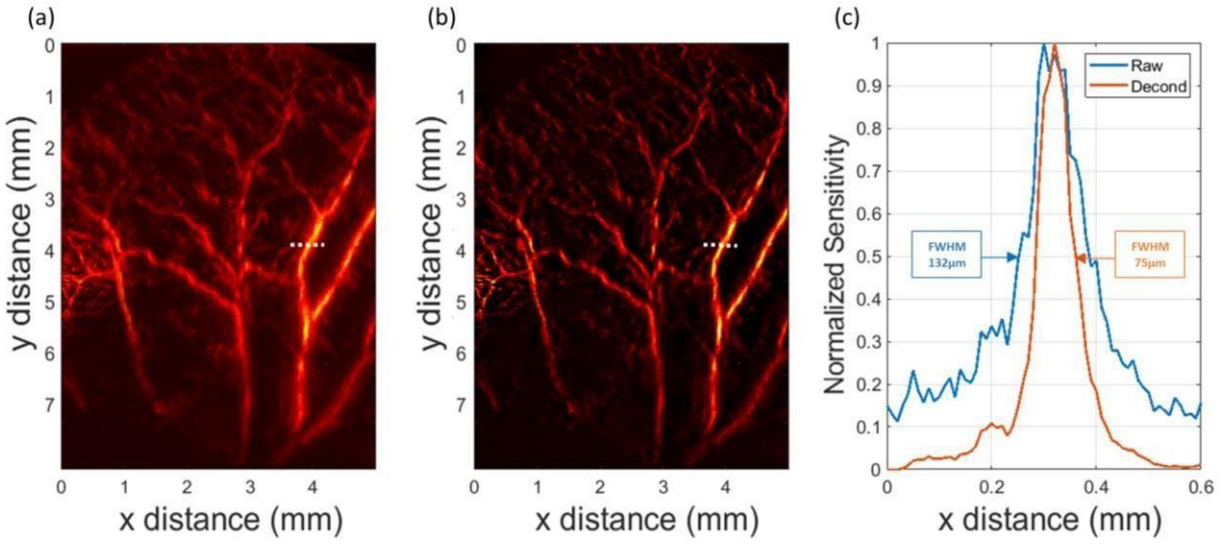

Figure. 3.19: Deconvolution of an optoacoustic microscopy MIP image of the vasculature of a mouse ear from the combination of Bessel illumination and axicon detection. (a) The raw and (b) deconvolved MIP images. (c) A comparison of FWHM measurements between the raw and deconvolved images, showing an improvement in image resolution and reduction in background noise.

Since Gaussian illumination restricts imaging depth within the Gaussian beam's Rayleigh spectrum, which can reach up to a few tens of microns to maintain high lateral resolution at the focal plane, current OA microscopy setups are sub-optimal for volumetric imaging or time-sensitive applications. We have introduced a new OA microscope configuration that enables detection over ultra-long depths of focus while maintaining high lateral resolution over many millimeters. We prove that combining Bessel illumination with optoacoustic axicon detection allows for one-order-of-magnitude increase in imaging depth-of-focus when compared to Gaussian illumination-based optoacoustic microscopy, and doubles the imaging depth-of-focus when compared to an unmatched combination of Bessel illumination and focused detection with a spherical transducer.

An optoacoustic microscope's depth-of-focus can be improved by integrating Bessel illumination with matched axicon detection without losing lateral resolution. Previous attempts to use Bessel illumination to improve depths-of-focus in optoacoustic microscopy [105-108] have been hindered using unfocused or spherical transducers for detections, which restrict SNR and sensitivity along the axial direction. On the other hand, Optoacoustic signal detection by optical interferometry with Bessel beam illumination is subject to strict beam path synchronization and atmosphere regulation since the difference between optical paths is vulnerable to vibrations and ambient temperature. Additionally, light sources and high-speed photodetectors are also needed, increasing device complexity and expense [109]. Here, we have shown a simple low-cost approach for increasing imaging depth of focus by combining the optical sensitivity profile Bessel beams with the thin cylindrical-acoustic response of our axicon transducers which offers a 17-fold higher depth of focus compared to Gaussian illumination combination with either spherical or axicon detection (Fig. 3.17c). The Bessel beam-axicon transducer setup allowed images of the entire vasculature network over a depth of 4.2 mm while imaging an excised tilted mouse ear (Fig 3.18j-l). Combining Bessel beam with a spherical transducer in contrast, restricted the field-of-view to 66% of the ear vasculature (Fig. 3.18g-i), while Gaussian illumination with either detector limited the overall imaging depth to 700 µm and the field-of-view to 17% of the ear vasculature (Fig. 3.18a-f).

Although Bessel beam illumination allows for greater focal depth without compromising the inner lobe spot size, secondary lobes circling the inner lobe produce unnecessary optoacoustic signals, reducing the optoacoustic image's overall lateral resolution. By deconvolving the OA image with the point spread feature of the Bessel illumination, the lateral resolution in a Bessel beam-axicon transducer aligned OA microscope setup can be increased. We discovered that the Bessel beam's side lobes (Fig. 3.16b) emit secondary optoacoustic signals that interact with the signal produced by the inner lobe, reducing lateral resolution and contrast. Recent attempts to suppress Bessel beam side lobe artifacts include the nonlinear Gruneisen relaxation effect, blind deconvolution, or interferometric detection [105-108]. Though, the nonlinear Gruneisen method raises application cost and interferometric detection increases experimental difficulty. In response, we took a similar approach to Jiang, B., et al. [106] and used blind deconvolution to perform post-processing suppression of side lobes, which is computationally efficient and cost-effective. We deconvolved the obtained optoacoustic images using the Bessel beam's optical beam spatial profile (Fig. 3.16b) to boost resolution of a blood vessel (Fig. 3.19) by a factor of 1.7 and reduce background signal by 2.1 dB.

There are several benefits of using axicon acoustic detection for microscopy. For example, also when used in conjunction with Gaussian illumination, axicon detection allows an elongated acoustic sensitivity field in which the illumination can be positioned using a spatial light modulator (SLM) at various points along the axial direction. As a result, high-resolution volumetric imaging is feasible without adjusting the sample or imaging device mechanically. Combining Bessel illumination with axicon ultrasound detection provides three major benefits. To begin with, the setup is resistant to axial misalignment of the light profile, detector, and sample. The relative axial alignment can be coarse due to the extended overlapping span of the matched illumination and detection sensitivity resulting in small influence on image lateral resolution. Second, the improved depth-of-focus allows for high-resolution imaging of irregular objects, where Gaussian illumination and spherically focused detectors can only partially image superficial features. Therefore, OA imaging of full-body zebra fish [96,109], OA endomicroscopy [110,111], and OA flow cytometry [112,113] are all examples of volumetric imaging using Bessel illumination matched with axicon transducers in life sciences. Finally, since axial adjustment is not necessary, quick dynamic processes occurring in uneven surfaces or volumes can be imaged using OA microscopy [114,115].

The depth of imaging in optoacoustic microscopy can be expanded more by increasing the size of the axicon detector or eliminating the central transducer aperture, while the lateral resolution can be enhanced by reducing the size of the Bessel illumination central lobe by using an axicon lens with a greater physical angle. However, reducing the central lobe diameter of a Bessel beam limits the optical depth-of-focus of the beam [97,98]. Future research will concentrate on using the axicon detector's central aperture by developing an axicon probe that can be housed inside the transducer and thus allow reflection mode Bessel beam- axicon mode OA microscopy for in-vivo experiments. In addition, further studies will be performed to create a thin optical pencil beam with no secondary side lobes, eliminating the need for post-processing deconvolution. Furthermore, a built-in transducer pre-amplifier will be introduced to increase the axicon transducer's sensitivity and thereby improve image SNR.

Ultimately, we obtain unparalleled imaging depths of focus for optoacoustic microscopy while maintaining high lateral resolution by carefully matching Bessel illumination to a broadband axicon optoacoustic transducer. While lateral resolution remains a function of illumination spot size, we show that when using Gaussian beams, the depth-of-focus is limited by the illumination, but is otherwise limited by the ultrasound detection sensitivity field when using Bessel beams. As a result, our proposed design greatly decreases the trade-off between imaging depth and resolution, allowing us to achieve lateral resolutions of 7 µm with imaging depths greater than 4.2mm. The high lateral resolution and extended depth-of-focus provide fascinating possibilities for potential biological and clinical applications, such as deep microscopic molecular imaging of complete samples and tissues with uneven surfaces.

3.7. Summary and discussion

In this chapter, several benchtop PZT and $LiNO_3$ optoacoustic endoscopy transducers were built with spherical and axicon directivity. The performance all transducers were assessed by designing an optoacoustic transducer characterization rig to determine each sensors lateral/axial resolution, depth of focus, relative sensitivity, focal point, and divergence angles by scanning around a broadband omnidirectional point source. Planar $LiNO_3$ active element transducers with glass lenses shaped to achieve directivity delivered superior performance compared to the PZT based transducers where the active elements were directly shaped to achieve directivity. The axicon transducer exhibiting a thin elongated sensitivity beam useful for endoscopy to retain high lateral resolution over an extended imaging depth when compared against the spherical detector of similar size.

To evaluate the increase in imaging depth with high lateral resolution a raster scanning optoacoustic mesoscope was developed to image a tilted 100µm suture with a tilted angle of 15.5° with each $LiNO_3$ transducer. The spherical transducer was able to correctly resolve the 100µm suture at focus with lateral resolution reducing as the acoustic source moves away from the focus. The axicon transducer surprisingly generated a blurred image of the suture with a full width half maximum value of 400µm.

To explain the discrepancy in lateral resolution of the axicon transducer between the characterization and imaging results. A meticulous 3D kwave study was performed to simulate

the spherical and axicon transducers built and mimic the characterization and imaging experiments. A point source and line source were generated and scanned in 3D with both transducers to mimic the broadband omnidirectional source in the characterization rig and the 100µm suture in the imaging experiment. The simulated spherical transducer was able to correctly resolve the point and line at focus whereas the axicon was able to correctly resolve the point and unable to resolve the line source. This is due to strong low frequency ultrasound sensitivities outside the axicon focal region, therefore detecting acoustic signal off-axis perpendicular to the direction of the scan. Therefore, the axicons lateral resolution is a function of both the illumination employed and the type of generated optoacoustic wave geometry namely spherical (point) or cylindrical (line). Consequently the axicon is not suitable for imaging the vasculature in the esophagus. As an alternative, axicon transducers could be employed with a narrow Bessel beam in optoacoustic microscopy to exploit the axicon beams pencil beam sensitivity profile achieved when scanning the point source.

Hence, an optoacoustic microscope was built to evaluate the imaging capabilities of the axicon transducer. By matching Bessel beam illumination with the axicon transducers thin pencil beam we demonstrated a 17x increase in imaging depth of focus when compared to the standard gaussian illumination and spherical detection configuration. The proposed Bessel-axicon configuration reduced the compromise between high lateral resolutions and imaging depth of focus. Accordingly, the matched sensitivity line profile of the Bessel-axicon paves the way towards a number of new applications in the field of optoacoustic microscopy.

Overall, we found the axicon transducer developed is not well suited for endoscopic applications because the sensors spatial resolution is a function of the acoustic source under investigation. When imaging sutures mimicking bloods vessels, the axicon transducer produced blurry images whereas the spherical transducer was able to correctly resolve them at focus. Hence, the spherical transducer was selected to be further enhanced into a friendlier enclosure for optoacoustic endoscopy and alternatively the axicon elongated foci was exploited in optoacoustic microscopy

Chapter 4 Hybrid OCT-OA endoscope design concepts

In this chapter design concepts for the hybrid OA-OCT capsule endoscope are proposed. Advantages and disadvantages of each design element including forward vs side viewing probes, proximal vs distal scanning, balloon vs capsule interface and common mode vs split mode imaging are articulated. The design concepts favoring video rate hybrid acquisition with a small endoscopic form factor are elected to the integrated into the final design.

4.1. Forward vs side viewing probes

Forward viewing probes are either raster or spiral scanned depending on the actuator (Fig 4.1b); this technique provides high magnification with a small field of view. In side view configuration, the probe is deployed in radial scanning mode (Fig 4.1a), where the sensor rotates over 360º to capture a 2D B-scan image in cylindrical coordinates. Helical scans are achieved with a pullback/push forward mechanism to capture a 3D volumetric C-scan. For imaging the esophageal lumen, where relatively large image coverage is required, the side viewing configuration is favored for our design.

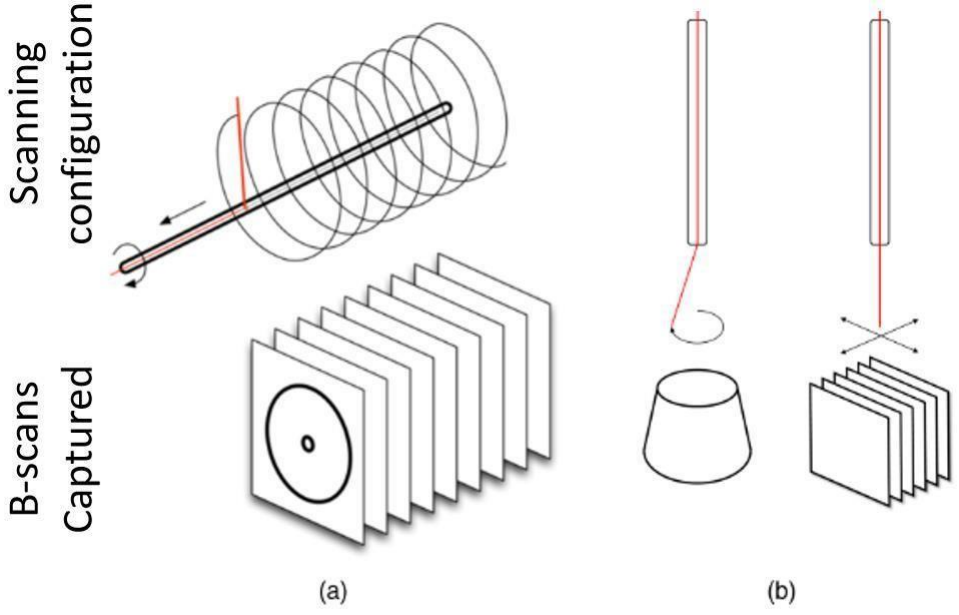

Fig. 4.1. Endoscopic operating principle for scanning: (a) side-viewing configuration rotates the light with longitudinal pullback to generate a series of radial images for three-dimensional reconstructions. (b) forward-viewing configuration scans the light in two-dimensions to achieve volumetric imaging. Retrieved from [116]

4.2. Proximal vs distal scanning

Proximal and distal scanning probe configurations are depicted in Figure 4.2. Proximal rotation is transmitted via a long torque cable to the distal imaging optics which limits speed and scanning uniformity. During operation, fiber stress induced distortion due to bending of the torque coil results in index variations within a rotating fiber resulting in image artifacts. A further disadvantage is the need for a fiber-optic rotary joint coupling OCT and OA wavelengths simultaneously, which reduces overall coupling efficiency and increases system complexity. Placing distal motors at the end tip of the probe imposes a reduction in the field of view due to driving cables crossing over the imaging plane. For these reasons, the distal-base scanning concept is favored to provide stable high speed rotational scanning with 360^0 field of view. Although a hollow shaft motor is required to guide the grin probe through the shaft from the proximal to the distal end. In addition, the hollow shaft motor will need to support the load of the transducer during rotation.

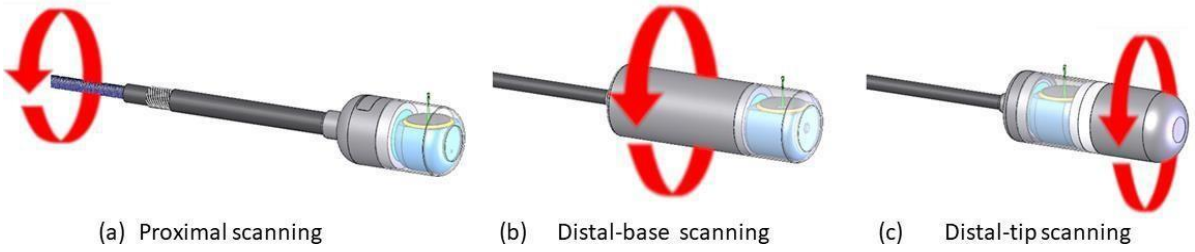

Figure. 4.2. Side viewing endoscopic probe proximal and distal scanning concepts: (a) proximal scanning concept without motor inside capsule. (b) Distal base scanning endoscope with motor situated at the proximal end of the probe. (c) Distal tip scanning enoscope with motor fixed at the tip of the probe.

4.3. Balloon vs capsule endoscope interface

The interface between endoscope and biological tissue is crucial, for optoacoustics where good contact is essential to maximize acoustic coupling transmission. Figure 4.3 illustrates two possible probe to tissue interface concepts. A water inflatable balloon sleeve allows the probe to make precise contact with the irregular esophageal lumen shape whereas a rigid capsule coveris designed to slightly stretch the esophageal wall.

The flexibility of the balloon provides the endoscopist more control to ensure contact with respect to the esophagus wall. Nevertheless, the balloon may also collide with rotating parts

within the capsule, particularly when the balloon is forced to be contracted by the esophagus. A mechanism will be required to prevent this such as applying a constant pressure to ensure minimal distension, but this could become too rigid for the tissue. This raises concerns as inflating the balloon within the esophagus can cause discomfort in patients. In addition to pressure monitoring an additional mechanism will be required to control the water level within the balloon. These components increase device complexity and steer towards increased probe size.

Rigid OCT capsules on the contrary as described in 2.2.4 have been deployed in several in-vivo clinical trials delivering distortion free high-resolution cross-sectional images of the esophagus. The Rigid capsule concept offers a more user-friendly assembly procedure and has been proven to provide high-quality optical images. During early stage testing a rigid capsule also provides a more straightforward interchangeable interface without technical assistance, thereby hastening overall development through iterative experimentation. Hence, a rigid capsule cover is favored over the balloon, though should experimentation reveal the profound need for a balloon sleeve the design could be adapted accordingly.

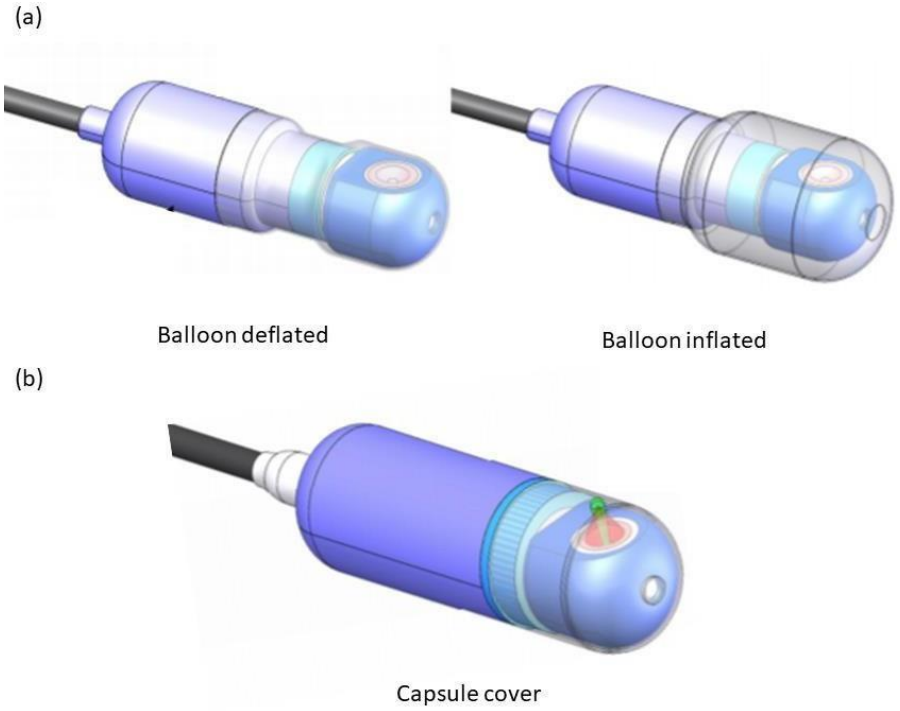

Figure 4.3: probe to tissue interface designs. (a) an inflatable balloon interface design concept (b) a rigid capsule cover concept.

4.4. Common path vs split path imaging

For the hybrid endoscopic imaging modality, we had two options to realize simultaneous dual-mode imaging. As shown in Figure 4.4, the first option would be a common-path design, where OCT and OA share identical optical components. The other option would be a split-path design, which means OCT and OA will use different optical components, with an additional motor specifically designed for OCT inside the probe. The benefit of the split-design is the freedom to realize very high-speed OCT imaging with dense sampling of the esophagus, while OA can run at an A-scan rate of several KHz or tens of KHz. However, the added motor also encompasses that the split-design cannot realize full 360-degree side imaging, as the motor wire will inevitably block a part of the light to the esophagus. Therefore, the common-path design, which is simpler in structure, is taken as the design scheme for the endoscopic probe

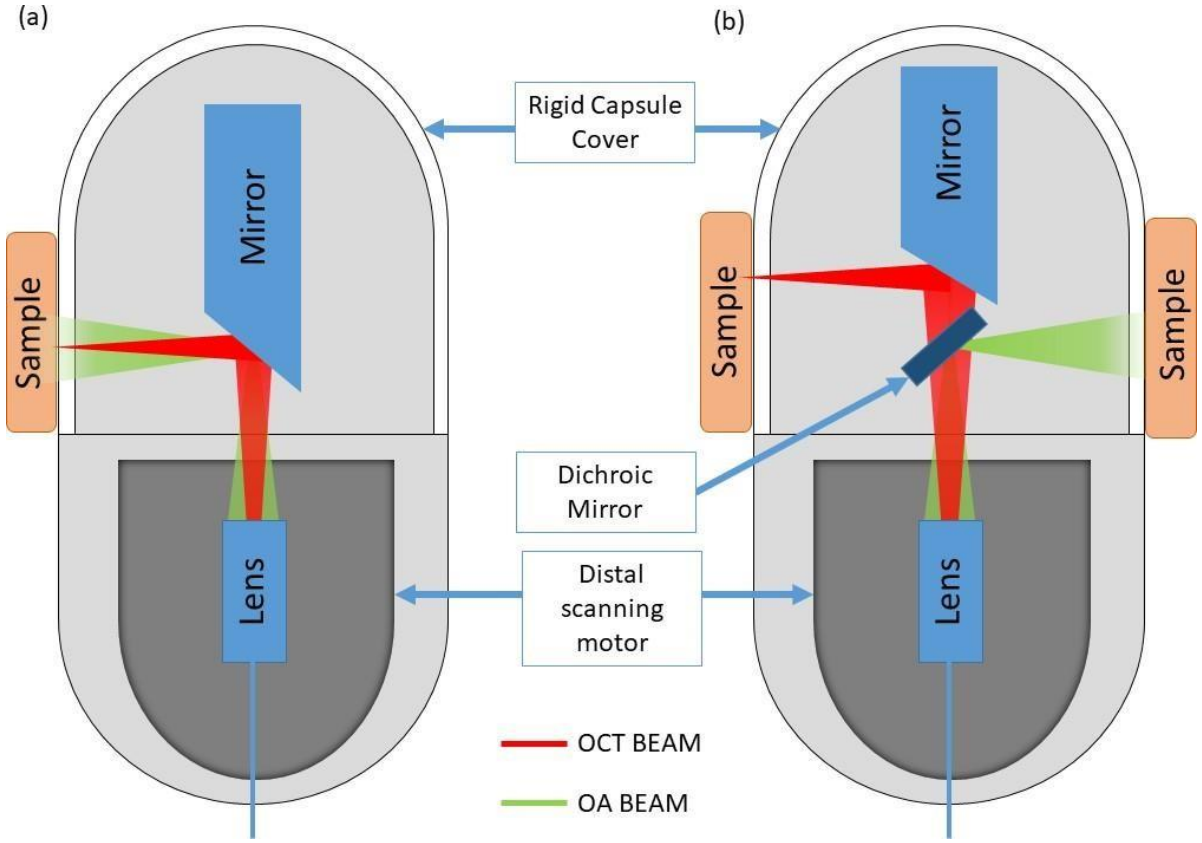

Fig. 4.4: (a) Common path hybrid OCT-OA optical setup imaging the same target simultaneously (b) Split path hybrid OCT-OA imaging optical setup, a dichroic mirror splits the excitation beams into separate paths.

4.5. Summary

Several endoscopy design concepts were introduced in this chapter with pros and cons discussed. The best concepts were elected to lay the foundation of the hybrid endoscopes composition consisting of a side viewing capsule based common path endoscope with rotation performed at the distal base of the probe.

Chapter 5 Optical architecture for OCT-OA endoscopy

OCT requires focusing of the light on the esophagus whereas OA requires diffused illumination to allow photons to penetrate deeper into tissue and thereby increase the OA imaging penetration depth. At the same time, the maximum optical energy employed restricting SNR is a function of the interrogation spot size, imaging frame rate and repetition rate of the laser source. In this chapter a custom made double clad fiber coupler (DCFC) combining OCT-OA into a single fiber is introduced. The backend optical architectures incorporating the DCFC for OA and OCT are discussed in single mode operation followed by hybrid mode. The optics on tip are designed in ZEMAX and the maximum permissible energy's based on the OA interrogation spot size are determined following the ANSI laser safety standards.

5.1. Double clad fiber coupling

To combine OCT and OA beams a custom double clad fiber coupler (DC1060LJFA) was developed by Castor Optics. This approach offers a 4 μm fiber core with single-mode operation for NIR (near-infrared) wavelengths used in OCT while the 105 μm inner fiber clad can be used to transmit the visible pulsed wavelengths for optoacoustics. The specifications of this fiber are depicted in Figure 5.1. OCT Light in the single mode core of the double-clad fiber (Port A) is guided through the coupler with virtually no loss (≤0.5 dB). Optoacoustic pulses are injected into the multimode fiber of the DCF (Port J) with ≥75% transfer. The DCF at Port S guides both wavelengths to the hybrid endoscope. Port R could be used for Optoacoustic pulse to pulse energy correction although this was not performed during the course of this work.

Single Mode Wavelength Range[a]	960 - 1260 nm
Single Mode Core Insertion Loss[b]	≤0.5 dB
Multimode Inner Cladding Transfer (Port J to S)[c]	≥75%
Multimode Inner Cladding Transfer (Port J to R)	≥1%
Max CW Power Level	500 mW
Port Configuration	2x2
Fiber Lead Length and Tolerance[d]	1 m +0.075 m/-0.0 m
Connectors[d]	See Drawing
Package Size	Ø0.12" x 2.76" (Ø3.2 mm x 70 mm)
Jacket	Ø900 µm Hytrel® Loose Tube
Pigtail Tensile Load	10 N
Operating Temperature Range	-40 to 85 °C
Storage Temperature Range	-40 to 85 °C

Fiber Specifications		
Fiber Type	Double-Clad Fiber	Multimode Fiber
Core Diameter (Nominal)	4 µm	105 µm
Core NA	0.19	0.22
Cut-Off Wavelength	≤960 nm	-
Inner Cladding Diameter	102 µm	-
Inner Cladding NA	0.24	-
Outer Cladding Diameter	125 µm	125 µm

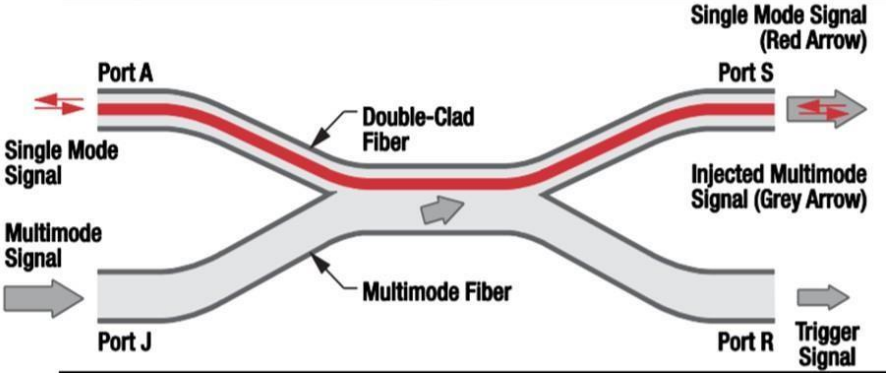

Figure 5.1: Specifications of custom made double clad fiber coupler (DC1060LJFA)

The transmission efficiency from Port J to S is valid between 400nm to 1600nm except for the water absorption region centered at 1383nm. Over 1600nm the performance slowly drops. This characteristic is advantageous for multispectral optoacoustic imaging, where several light sources of different wavelengths could be coupled into the the same fiber. Another favourable optoacoustic feature is the 105 µm multimodal core diameter, this suggest that during fiber coupling the spot size at focus can be on the order of several tens of microns. A larger spot size reduces the likelihood of burning the fiber, especially at high pulse repetition rates.

Single mode wavelength operating range within the fiber core is 960-1260nm. OCT light sources within this wavelength region are readily available at 1060nm, this is because there is a local minimum with respect to the absorption of water as depicted in figure 2.4. Furthermore, water will be present in the optical beam path employed as the main acoustic coupling medium for optoacoustics. To reduce optical attenuation of water within the beam path for OCT, a 1060nm light source is promoted for our endoscope.

5.2. OA Optical back-end console setup

The optoacoustic optical back-end console setup is illustrated in figure 5.2 consists of a ns-pulse width, 532nm Q-Switched DPSS laser with an operating repetition rate in the range of 1-100kHz (ONDA, Bright Solutions, Italy). The energy per pulse was regulated by means of a polarizing beam splitter and a beam dump. A 90:10 beam splitter was employed to divert 10% of the light towards a photodetector for triggering. The remaining 90% of light was coupled into port S of the double clad fiber coupler to guide the optical beam to the endoscope. Fiber coupling is performed by focusing the 2.2mm collimated laser beam output from the laser with a 60mm Thorlabs achromatic doublet lens (AC254-060-A-ML) to a spot size of 18.5µm, a factor of 5.6 smaller than the inner DCFC fiber cladding. The optoacoustic signals measured during rotational scanning were pre-amplified externally with an 30dB amplifier (Sonaxis SA, France) and connected to a T- bias (ZFBT-4R2GW+, Mini-Circuits) prior to data acquisition. Both optoacoustic and photodetector signals were acquired by a dual channel integrated ATS9373 DAQ card (AlazarTech, Canada) controlled by LabView and data analyzed in MATLAB.

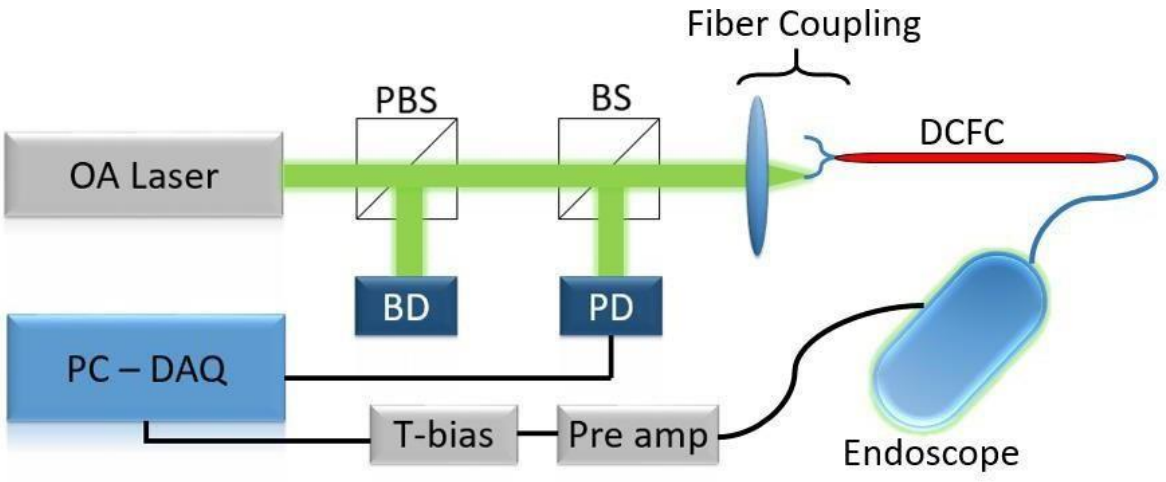

Figure 5.2: Optoacoustic optical back-end setup. PBS: polarizing beam splitter, BS: beam splitter, BD: beam dump, PD: photodiode, DFCF: double clad fiber coupler

5.3. OCT Optical back-end console setup

A swept source laser from insight photonic solutions inc with a central wavelength of 1060nm at a tunable A-line rate in the range from 85 kHz to 650 kHz was selected for OCT imaging. The insight laser is based on the vernier tuning effect to sweep the wavelength and uses akinetic technology to obtain precise electronic control of the spectral laser output over time. The OCT

setup is depicted in figure 5.3 where the sample arm consists of a 90:10 fiber spliced to Port A of the DCFC with almost no loss. The reference arm consists of a free space collimator and DCFC for dispersion and length matching. Back scattered light from the sample arm and reference arm are combined via 50:50 couplers prior to interferometric detection using a high-performance balanced photodetector by Insight solutions.

The detector consists of two balanced photodiodes and an ultra-low-noise, high-speed transimpedance amplifier. Matching the two photodiodes results in an excellent common mode rejection ratio (CMRR), leading to better noise reduction. The detector outputs include a balanced RF-output from the transimpedance amplifier, and the Monitor+ and Monitor- ports allow the response of each photodiode to be observed individually to verify performance of each leg independently. The RF output is connected to a single channel of an integrated ATS9373 DAQ card (AlazarTech, Canada) acquired by LabView and post processed in MATLAB to generate OCT A-lines.

During wavelength sweeping, for each sweep, the laser generates a short electrical pulse termed the sweep trigger which is connected to the external trigger port of the ATS9373 card. The swept source laser also sends out sample clock signals where each pulse represents a change of the swept wavelength. To ensure sample acquisition from the photodetector is performed at the correct time point, synchronized with the change of wavelength, the sample clock signal from the OCT laser is provided to the DAQs external clock input. However, for the Insight laser, during a wavelength sweep, not every sample clock corresponds to a valid wavelength. Therefore, the laser sends a data validity flag to the computer. Thus, during a sweep, only sampled data corresponding to valid wavelengths are kept for OCT data processing.

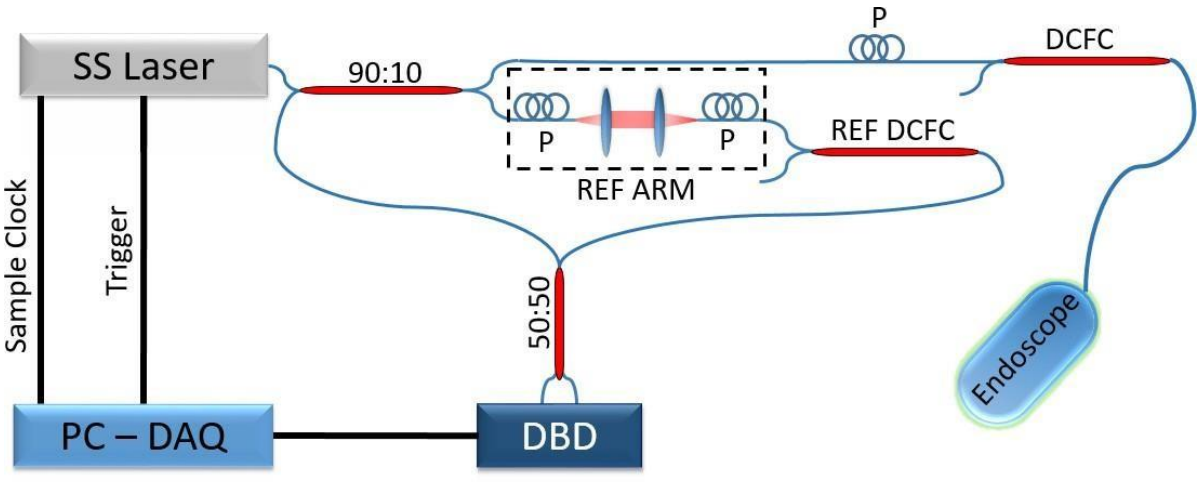

Figure 5.3: OCT optical back-end setup. PBS: polarizing beam splitter, BS: beam splitter, BD: beam dump, PD: photodiode, DFCF: double clad fiber coupler, DBD: Dual balanced detector

5.4. Multimodal back-end console optical setup

The multimodal configuration is presented in figure 5.4 comprises of the same optical elements utilized in standalone operation. In regard to data acquisition, the main difference here is that hybrid triggering is based on the master-slave laser configuration. As the repetition rate of the OCT SS laser is higher than the of the OA laser, in this approach, the OCT laser triggers the OA laser by means of an electronic pulse divider (Model: PRL-220A, Pulse research lab, USA). Two signals are derived from the OCT laser, namely the clock and the A-line sweep signal. The OCT clock is configured as the sampling clock rate input for the DAQ card, whereas the frequency of the sweep line signal is divided by a multiple number with an external divider to drive the OA laser and trigger the DAQ card for hybrid acquisition. DAQ channel A is dedicated to read the photodiode signal from the OCT sensor whereas channel B reads the OA transducer signal. The advantage of this configuration is that standalone or hybrid operation is permitted without adjustment of the optical setup. Therefore, future incremental improvements of each modalities optical setup will not interfere with the others. The OA trigger photodiode used during single mode operation is this instance is left unconnected.

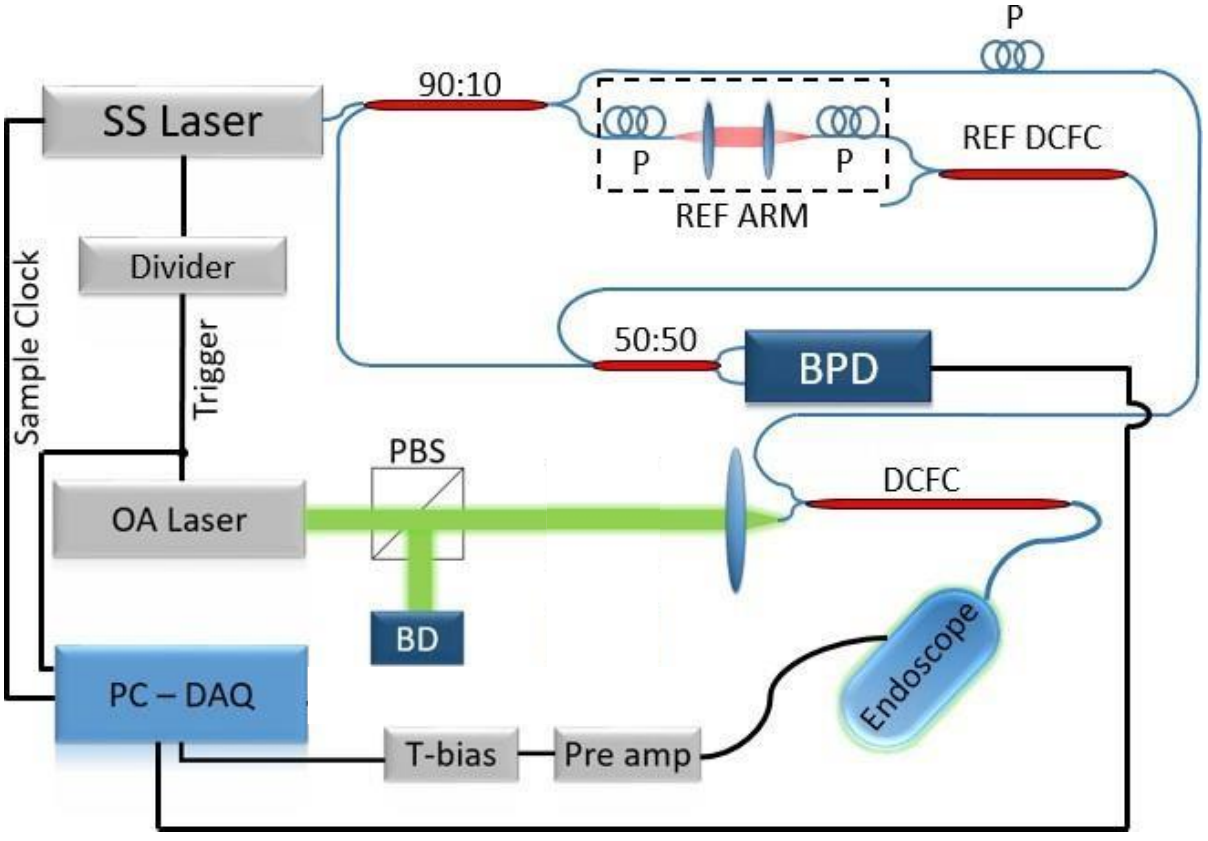

Figure 5.4: Multimodal back-end setup. PBS: polarizing beam splitter, BS: beam splitter, BD: beam dump, DFCF: double clad fiber coupler, BPD: Balanced photodiode.

5.5. Multimodal distal capsule optical setup

To achieve high resolution superficial OCT imaging a focused beam interrogating tissue is required whereas diffuse illumination with OA is necessary to permit deeper tissue imaging. A single lens solution conditioning each beam delivered via the double clad fiber was favored to simplify the manufacturing and testing of the hybrid endoscope. The lens would be optimized to focus the 1060nm OCT wavelength on the tissue sample and in consequence the lens chromatic aberration at the optoacoustic wavelength of 532nm would result in diffuse illumination on the sample. In addition to the lens, the multimodal front end optical setup consisted of a mirror to re-directing light towards the esophagus wall, a sealing window to prevent the acoustic coupling medium from leaking inside the transducer and the optical capsule cover.

5.5.1 Optics on tip arrangement

The optics on tip configuration is presented in figure 5.5. The input OCT-OA optical beams from the double clad fiber are conditioned to focus the OCT light just below the esophageal tissue surface and in return the optoacoustic beams wavelength would experience chromatic aberration shifting the optical focus between the capsule cover and sealing window. As a result, diffuse optoacoustic illumination would interrogate the esophageal tissue. A 45° mirror redirects the illumination coming from the lens towards the esophageal wall and travels through a planar sealing window installed to prevent the acoustic coupling medium from leaking inside. Both illumination beams travel through the acoustic coupling medium and capsule cover before interrogating the esophageal tissue surface.

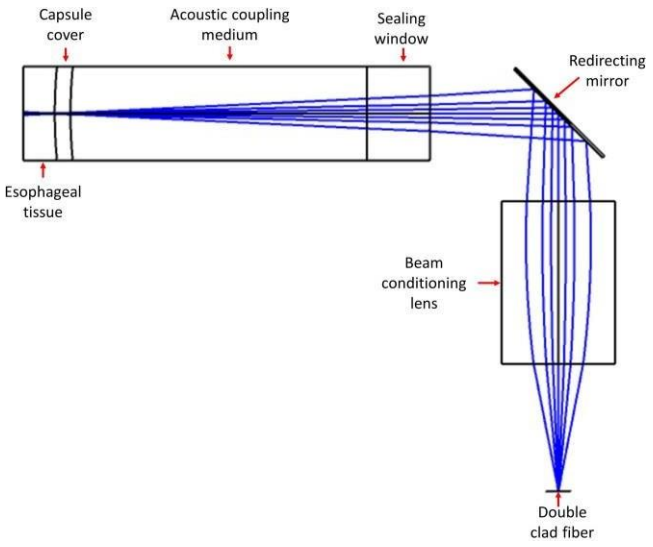

Figure 5.5: Optics on tip endoscope configuration

To minimize optical attenuation of OCT light through the acoustic coupling medium heavy water which has lower absorption than water at 1060nm is selected to be employed. Aiming to design the beam conditioning lens, all the optical properties of the elements within the beam path between lens and esophageal tissue had to be first determined.

5.5.2 Capsule cover and sealing window material

Several different transparent and biocompatible materials were explored to determine the best material to utilize for the capsule cover and sealing window. Important characteristics included maximum OA and OCT light transmission as well as minimal acoustic attenuation. Table 5.1 highlights the various materials acoustic and optical properties tested at the wavelengths and acoustic frequencies of interest. PMMA SG7 Altuglas offered the highest optical transmission efficiency and lowest ultrasound attenuation at 50 and 100MHz frequencies. Therefore, PMMA SG7 was elected to manufacture the capsule cover and sealing window.

Material	Commercial name	Manufacturer	Distributor	Ref	Density	Hardness	Acoustic impedance (Mrayl)	Absolute reflection coefficient with water	US Attenuation @ 50MHz (np/m)	US Attenuation @ 100MHz (np/m)	Transmission 400nm (T0,25mm)	Transmission 600nm (T0,25mm)	Transmission 1060nm (T0,25mm)	Transmission 1340nm (T0,25mm) (dB)
PEBAX	PEBAX	Arkema	VELOX	Pebax 2533 SA01 MED	1	27 shore D	1,58	0,03	not measured	not measured	70,35%	75,89%	59,75%	null
PEBAX	PEBAX	Arkema	VELOX	Perbax 7233 SA01 MED	1,01	69 shore D	2,15	0,18	4680	11300	82,40%	87,82%	81.11%	78
PA	Rilsan Clear	Arkema	VELOX	Rilsan Clear G170 MED	1,05	84 shore D	2,43	0,24	4520	9400	98,12%	98,59%	93,19%	98
PETG	Sky green	SK Chemicals	VELOX	SkyGreen S2008	1,27	110 R (>>80 shD)	2,91	0,32	2440	3720	97,04%	98,08%	95,36%	95
PC	Calibre	Megarad	VELOX	PC CALIBRE 2061-10	1,2	>>80 shore D	2,7	0,29	3380	5490	96,23%	97,47%	93,80%	97
TPU	Isoplast	Lubrizol	VELOX	TPU ISOPLAST 2530	1,2	121 R (>>80shD)	2,89	0,32	4110	7430	98,51%	98,82%	93,20%	98
PMMA	PMMA SG7	Altuglas	Altuglas International	ALTUGLAS SG7	1,17	M64 Rockwell	2,87	0,32	2270	3350	98,70%	99,40%	95.35%	101
Rexolite									not measured	not measured	87,00%	88,70%	not measured	not measured
Glass (ref)	Glass	Verre Industrie	Verre Industrie	Glass BOR/011	2,2	480 Knoop	11,79	0,78	2880	not measured	95,85%	96,88%	96,92%	99

Table 5.1 Optical and ultrasound transmission efficiencies measured with several optical materials. Fields highlighted in red show low performance whereas fields highlighted in green show the best material satisfying the optical and acoustic requirements.

5.5.3 Optics on tip optomechanical simulation and conceptualization

Owing to the complexity of the optical system in figure 5.5 fashioning the OCT and OA beams simultaneous with a single lens is challenging. We decided to design the optical system on Optic Studio developed by Zemax. Optic Studio provides a set of 3D optical space analysis, optimization, and simulation tools to design optical probes. Furthermore, the software offers seamless integration to CAD software's and is readily utilized by several lens manufactures; hence design files could simply be set to manufacture the probe. To design the beam conditioning lens, the setup in figure 5.5 was generated with arbitrary thicknesses and diameters in Optic studio. The

OCT beam coming from the single mode core of the double clad fiber was modelled following gaussian beam optics and the OA beam arriving from the multi-mode inner core of the double clad fiber was modelled using ray optics. The materials refractive indices and absorption coefficients were taken into account to correctly simulate the optical beam propagation. The main requirement of the lens was to focus the OCT beam just below the tissue surface. Two main parameters including the distance between the redirecting mirror to esophageal tissue and spot size of the interrogation OCT beam at focus had to be defined in Optics studio's merit function editor before optimization of the optical system could commence. Here, we set an OCT target spot size of 20µm spot size to match the lateral resolution of the optoacoustic transducer as defined in table 3 and we define the distance between directing mirror to esophagus to be 8mm. This fixed distance parameter defines the capsule diameter to be 16mm. Although this diameter is larger than the desired <13mm diameter listed in table 3, sourcing of components with a slightly larger capsule was more straightforward thereby accelerating developing. Hence, the first endoscopic prototype built would concentrate towards troubleshooting technical problems experienced with a slightly larger capsule to hasten the development of the probe with future developments focused towards miniaturization.

Following optical system optimization on Optic studio with capsule diameter and OCT spot size defined two unique solutions are presented in figure 5.6. The first solution employs a grin lens to focus the incoming OCT-OA beams as illustrated in figure 5.6a and the second solution performs focusing with a micro lens. The green beams represent the 532nm pulse OA illumination

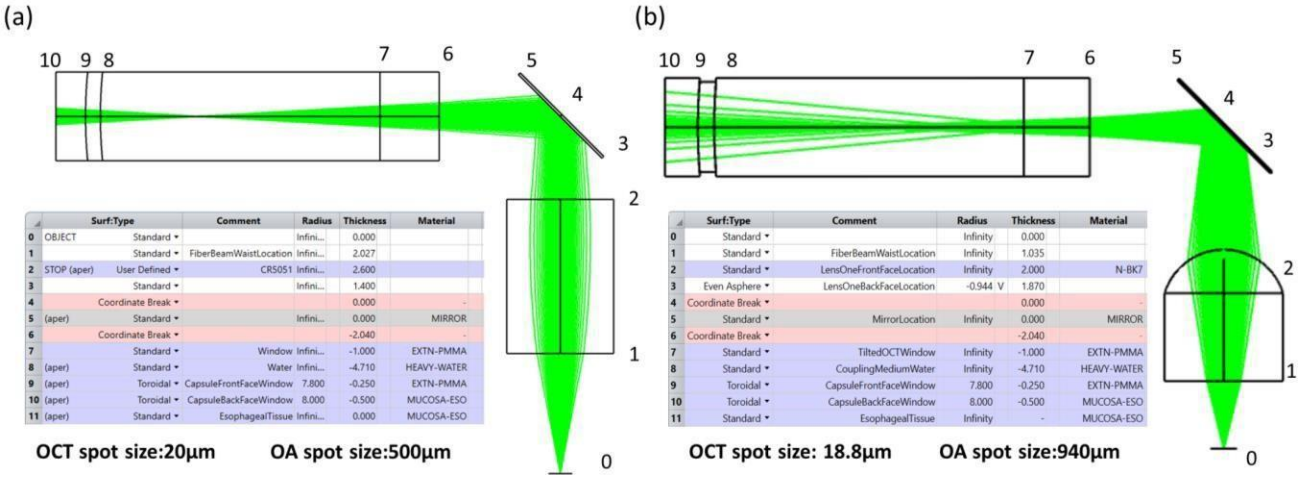

Figure 5.6 Optics on tip simulation solution with a (a) grin lens and (b) micro lens. The tables list the thicknesses, materials, and radius of curvatures of the elements within each setup. The simulated green beam is the optical beam evolution of the multimodal OA 532nm light exiting the inner cladding of the DCF starting at position plane 0.

The simulated OCT spot size was measured 500µm inside esophageal tissue and OA spot size is measured at the boundary between PMMA capsule cover and esophageal tissue (at surface 9). These simulations laid the foundation to generate opto-mechanical schematics for the sealing window, mirror and capsule cover within the beam path. The optical elements were designed with semi-diameters to satisfy both solutions in figure 5.6 and thereby allow for interchanging the micro/grin lens optical design probes.

Figure 5.7 illustrates a drawing of the sealing window which is required to prevent water leaking into the central transducer aperture used to guide OA and OCT light. The optical sealing window was manufactured with PMMA altuglas SG7's, due to its excellent optical transmission efficiency as presented in table 6. To suppress specular reflections affecting OCT, the window at the air-glass interface was to be coated with an anti-reflective coating at 1060nm and 532nm. The window would therefore be optically transparent for the OCT-OA illumination wavelengths.

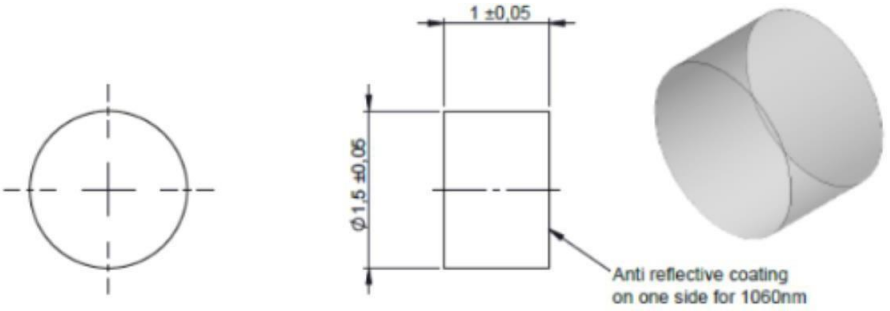

Figure 5.7: Drawing of the optical sealing window to be installed inside the transducer central aperture

Decoupling the rotation from the fiber-optic delivery system is achieved with a 45° integrated mirror inside the endoscopic transducer. The mirror deflects the OCT and OA through the central aperture of the transducer, effectively performing the rotation coupling at the distal end of the probe, inside the capsule. Figure 5.8 shows the designed 45° mirror which is silver coated with reflectivity ≥ 95% for optimal reflection at the OCT and OA wavelengths.

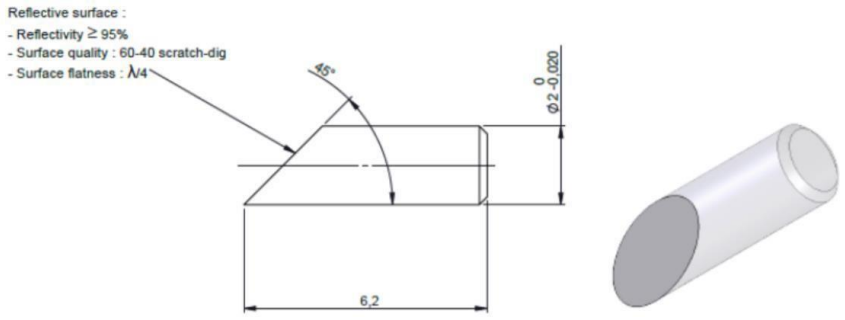

Figure 5.8: silver coated 45° mirror designed to be integrated inside the endoscopic transducer

Providing a protective barrier between esophageal tissue and the transducer during imaging, figure 5.9 presents the PMMA capsule cover with thickness 250µm following the simulations in figure **5.6.** A Fiducial marker with a thickness of 70µm was embedded on the internal capsule surface to compensate for rotational motor instability during imaging.

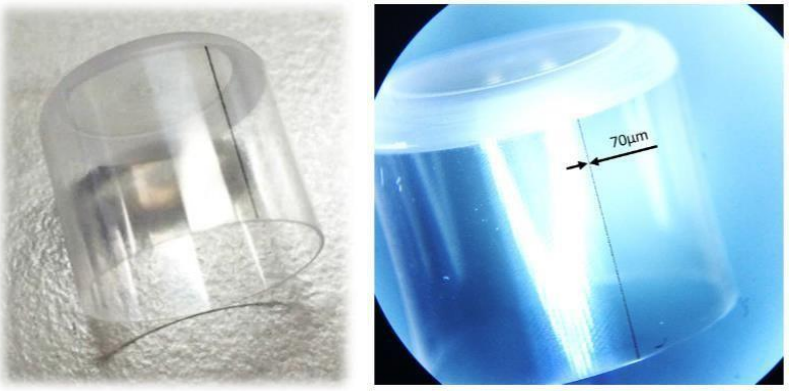

Figure 5.9: PMMA capsule cover with 70µm fiducial line marker to compensate for rotational motor instability

To visualize the optical system integrated with all components inside a spherical transducer, figure 5.10 represents a conceptual render of the optical system employing the grin lens solution.

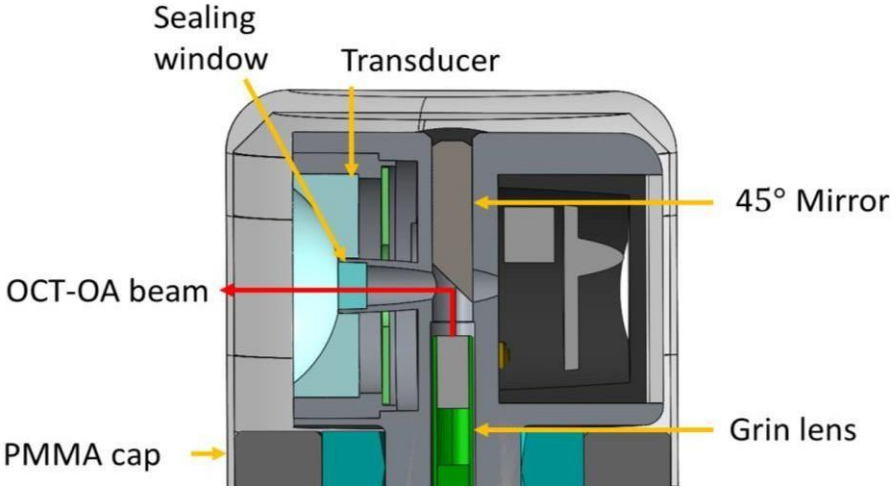

Figure 5.10: Conceptual render of front-end optical system integrated inside a spherical transducer to perform OCT-OA imaging

With the interrogation beam spot sizes defined in figure 5.6 we can now define the maximum permission energy when imaging the human esophagus as a function pulse repetition rate and Bscan frame rate.

5.5.4 Optoacoustic endoscopy maximum permissible exposures

In GI tract endoscopy OCT relies on the detection of scattered radiation between the layers of esophageal lining whereas optoacoustics signals are generated via the absorption of optical energy of the microvasculature. Thermal damage of the esophageal lining occurs should the microvasculature absorb a considerable amount optical energy. To define this limit, we referred to the maximum permissible exposures which are a set of maximum laser energy values to which the eye or skin may be exposed without effects or injury occurring in normal circumstances. The levels have been established in standard ANSI Z136.1 for wavelengths and exposure durations in the eye or skin. Due to a lack of scientific data on laser safety level on esophageal tissue, we base our safety requirements on laser radiation of human skin, although we understand that the MPE of esophageal tissue might be lower than that of the skin.

For repetitively pulsed lasers the MPE is always the smallest MPE value determined by the application of the ANSI Rules 1 and 2 [ANSI Std. Z136.1-2000 (8.2.3.2)] applied over the area of the limiting aperture of 3.5 mm for skin imaging .

$$MPE = \min[MPE_{rule1}, MPE_{rule2}] \tag{5.1}$$

Each of the MPE rules are defined as follows:

MPE Rule 1 (Single Pulse): No single pulse in a train of pulses shall exceed the MPE for a single pulse of the same pulse duration. For laser pulse duration of 1ns to 100 ns the single pulse radiant exposure over the wavelength of 400-700nm is 20 mJ/cm^2. Our laser has pulse duration of 1 ns with an operating wavelength of 532nm.

$$MPE_{rule1} = 20\frac{mJ}{cm^2} \tag{5.2}$$

MPE Rule 2 (Average Power): The average MPE per pulse distributed over a number of laser pulses (N) over the exposure time(t) is given by:

$$MPE_{rule2} = \frac{MPE_T}{N} \tag{5.3}$$

Where N is the number of pulses during the exposure period given by the product of the pulse repetition rate(PRR) and exposure time (t) and the MPE_T radiant exposure for an exposure time between 100 ns to 10 s over the wavelength range of 400-700nm from the ANSI safety table is given by:

$$MPE_T = 1.1 * 10^4 t^{0.25} J/m^2 = 1.1 * t^{0.25} J/cm^2 \tag{5.4}$$

Therefore, the average MPE per pulse distribution as a function of PRR and exposure time t is given as follows:

$$MPE_{rule2} = \frac{1.1 * t^{0.25}}{Int(PRR * t)} J/cm^2 \tag{5.5}$$

Note: the number of pulses in an exposure is always considered as an integer for laser hazard evaluations. The exposure time interrogating the same sample location is a function of the laser spot size at the capsule window interface, in our case we apply the limited aperture for skin imaging with a diameter of 3.5 mm.

Applying the MPE rules on the optical systems depicted in figure 5.6 at arbitrary rotational speeds 30Hz and 50Hz at pulse repetition rates 50 kHz and 100 kHz we obtain table 5.2. Applying the limited aperture for skin with a diameter of 3.5 mm the MPE limits for both optical systems will be the same because there interrogation spot sizes are less than 3.5mm. The most restricted MPE is 1.04mJ/cm^2 at the highest repetition rate (100kHz) , lowest speed (30Hz). Alternatively, the least restricted MPE is 3.05 mJ/cm^2 at the lowest repetition rate (50 kHz), highest speed (50 Hz) . For esophageal imaging a high frame rate is desirably to rapidly scan the full gastrointestinal tract and high repetition is necessary to provide high resolution imaging. However, at the same time with a fixed interrogation spot size the MPE becomes more restricted. Ultimately the SNR of the

endoscope determines the maximum operating frame rate and repetition rate to obtain optoacoustic images with acceptable contrast and sufficient penetration depth without exploiting the MPE.

Imaging configuration	Frame rate 30Hz Rep Rate 50kHz	Frame Rate 50Hz Rep Rate 50kHz	Frame rate 30Hz Rep rate 100kHz	Frame rate 50Hz Rep rate 100kHz
MPE Rule 1 $\left(\frac{mJ}{cm^2}\right)$	20	20	20	20
MPE Rule 2 $\left(\frac{mJ}{cm^2}\right)$	2.08	3.05	1.04	1.53
Final MPE $\left(\frac{mJ}{cm^2}\right)$	2.08	3.05	1.04	1.53

Table 5.2. Optoacoustic endoscopy MPE limits for grin and microlens optics on tip systems at frame rates 30, 50 Hz and pulse repetition rates of 50, 100 kHz at wavelength 532nm and pulse width 1ns.

5.5.5 Optical probe manufacturing

Opto-mechanical probe assembly drawings presented in figure 5.11 were sent to several optical manufactures to query for production costs. Grintech was selected to manufacture the grin lens design without any changes required to the original design introduced in figure 5.6. The micro lens solution was unfortunately too difficult to realize following feedback from several manufacturers. Therefore, the microlens design was abandoned and all efforts focused on the adoption of the grin lens solution for the endoscope.

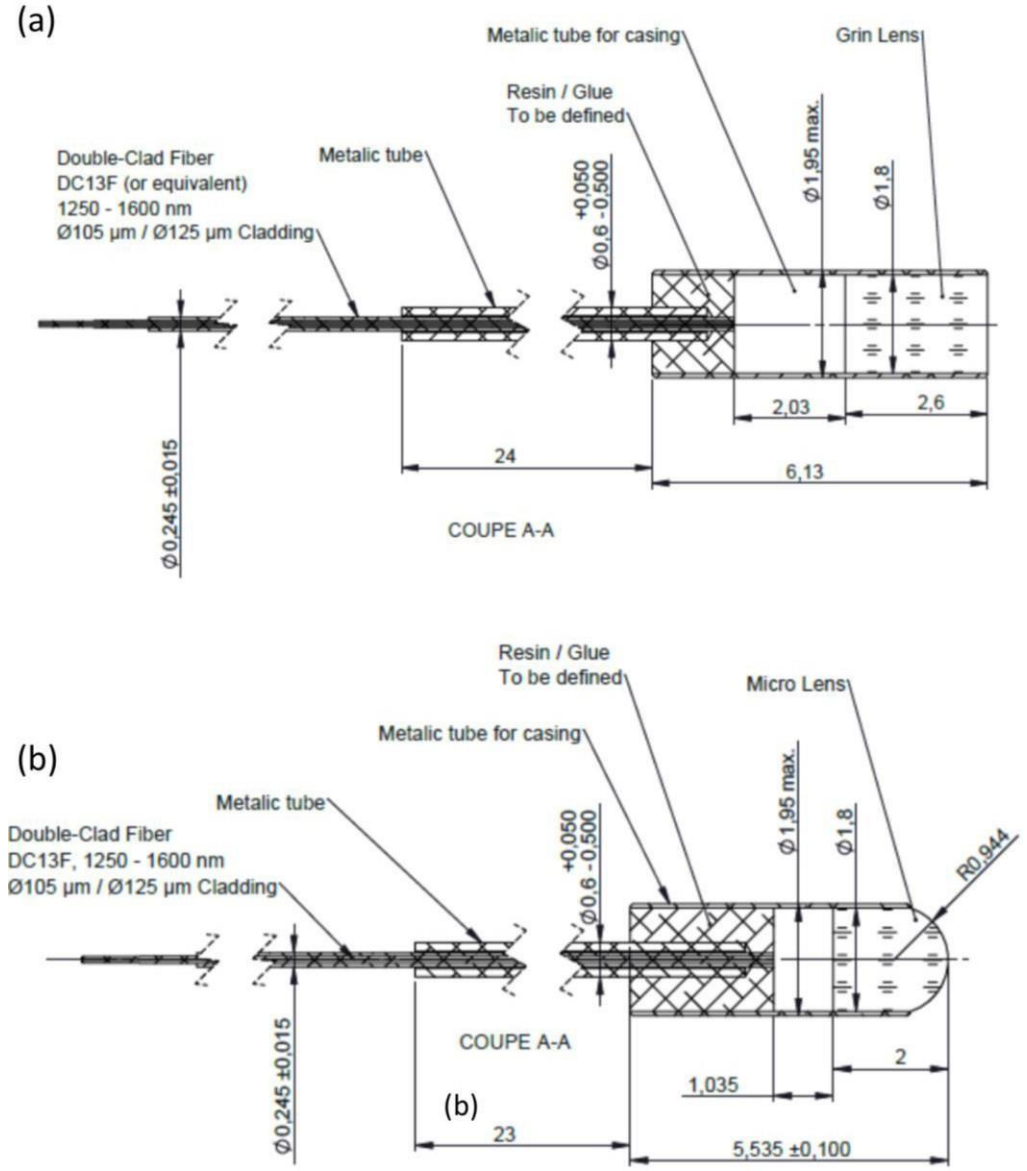

Figure 5.11: Optomechanics of the optics on tip lens solution for OCT and OA endoscopy (a) The grin lens probe schematic (b) The micro lens probe schematic.

5.6. Summary and discussion

The hybrid optical system for hybrid OCT-OA endoscopy was presented in this chapter. A custom made double clad fiber coupler was designed to simplify the hybrid system by guiding OCT and OA light through a single fiber. This robust system allows for single modality or multimodality imaging without adjusting the optics and incremental improvements in one modality will not interfere the back end optical setup of the other modality. For example, the 532nm optoacoustic back end optical setup could be extended to include multiple lasers to perform multispectral optoacoustic endoscopy without interfering the OCT back-end setup.

Both modalities were synchronized by following the master-slave configuration where the OCT

laser was the master and the OA laser the slave.

To design the front-end optical setup, several materials transmission properties at the optical and acoustic wavelengths of interest were analyzed, PMMA SG7 offered the lowest optical and acoustic attenuation and was therefore selected when manufacturing optical elements used in the front-end configuration. Two concepts of the front-end optical setup were simulated on Optic studio, one including a grin lens and the other a micro lens. Each system was designed by optimizing the lens shape and size to focus the OCT beam just below the esophagus wall surface. Subsequently the OA beam was focused inside the endoscope because of chromatic aberration experienced by the lens. Hence the OA beam spot interrogating tissue is diffused to permit photons to travel deeper into tissue and increase the optoacoustic imaging depth. Although when attempting to reach out to manufactures to produce the designs, we discovered the micro lens solutions was too difficult to realize and therefore all efforts were focused on the grin lens solution.

From the Optic studio simulations, we determine the MPE values for each system for optoacoustic endoscopy derived from ANSI Std. Z136.1-2000 (8.2.3.2)]. The impact of interrogation spot size, scanning speed and repetition rate on the MPE limit was discussed. The methodology presented here provides a workflow to accelerate development towards the final device. Opto-mechanical system behavior was simulated to meet project requirements and define the MPE limit. The same process could be extended to microscopic, linear scanning or tomographic applications. The MPE limit could then be used as justification to purchase the correct laser operating at a specific repetition rate or alternatively a scanner running at a predetermined speed. Notably as the MPE limit reduces optical interrogation pulse energy and the optoacoustic systems overall sensitivity must proportionally increase to retain contrast and penetration depth over several mm’s.

Chapter 6 Hybrid OCT-OA endoscopy prototypes

Imaging the human esophageal tract with an OCT-OA endoscope requires (a) synchronous high speed imaging frame rates with sufficient SNR to avoid motion artifacts, (b) co-registered large field of views to expedite the screening procedure, (c) careful design of a broadband endoscopic transducer for OA and an optical interrogation/collection probe for OCT, (d) suitable materials, mechanics, coupling medium and wavelengths for optical (OCT) and acoustic (OA) index matching, and (e) proper probe form factor to ease swallowing and maintaining optimal contact between the endoscope and esophageal circumference. In this chapter two prototypes named the 16mm semicapsule and 12.5mm partial capsule are presented. Both prototypes achieved 360º video rate imaging speeds upto 50Hz (semicapsule) and 30Hz (partial capsule) by integrating low friction miniature slip rings into the transducer casing, allowing the positioning of a hollow shaft motor at the proximal end of the endoscope tip and preventing obstruction from driving cables over the field of view.

The 16mm semicapsule built operated only in optoacoustic imaging mode because of an internal OCT back reflection reducing SNR which occurred within the grin lens designed. We characterized the optoacoustic semi capsule's lateral resolution at 50Hz Bscan rate by imaging a phantom consisting of twelve 100 µm sutures arranged in an Archimedean spiral with a pitch of 3 mm, and demonstrated a volumetric pullback spiral scan of 1790mm^3 at 0.24Hz. To simulate scattering of light in esophageal tissue, the acoustic coupling medium of water was replaced with various concentrations of an intralipid solution to determine an estimated penetration depth of ~0.84mm in the human esophagus and validated our findings ex-vivo pig esophagus. Our results demonstrate proof-of-principle translational potential of optoacoustic endoscopy for delivering 3D functional information at video rate of the human esophagus.

Subsequently a partial capsule was built with a reduced diameter of 12.5mm to ease swallowing and the grin lens modified to suppress the internal OCT back reflection. With these changes made, we presented for the first time a 12.5 mm, 360^0, 30 Hz-frame rate, synchronous hybrid OCT – OA capsule endoscope designed for imaging the human esophageal tract. We demonstrate the ability to acquire high resolution 3D synchronous OCT-OA helical scans at video rate in phantoms and ex-vivo pig esophageal tissue and human mucosal tissue.

6.1. Endoscopic transducers with slip rings

In view of the quality of lithium niobate technology as discussed in chapter 3, we decided to use the glass lens technology with spherical directivity for the endoscopic transducers. The initial endoscopic probe (HFM38) designed for a 16 mm semicapsule prototype is illustrated in figure 6.1. The transducer houses a 45º mirror to redirect the excitation beam towards the esophageal wall and a PMMA window to prevent water leaking inside the sensor. A spherical glass lens with a focal length of 6 mm is mounted on the $LiNO_3$ substrate. A preamplifier could also be integrated inside the casing to improve SNR, although at present acoustic measurements made were externally as the preamp circuit required further miniaturization to be integrated inside. To enable high speed rotation two precision copper slip ring joints installed on the transducers shaft couple, the electrical broadband signal measured by the transducer.

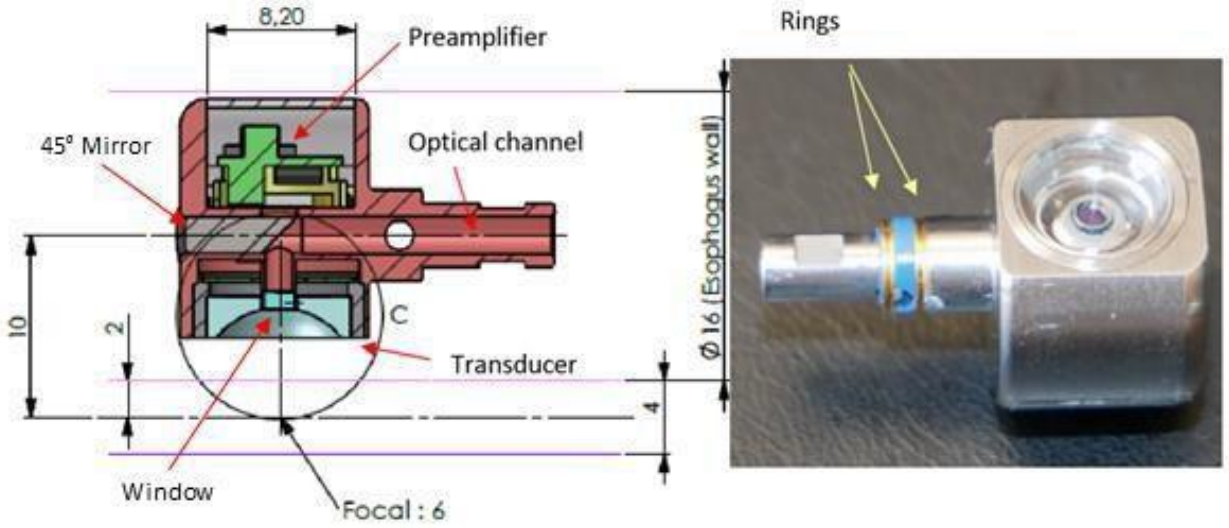

Figure 6.1: (a) Schematic and photo of the 16mm semicapsule endoscopic transducer (HFM38)

The slip ring coupling configuration is depicted in figure 6.2. When the rings are spinning, the pins maintain electrical connection. To minimize friction induced electrical noise during rotation, the rings are covered with a 5µm- thick gold layer. Two pins are in contact with each ring, making four V contact points per pole, thereby reducing the risk of losing the electrical contact during rotation. To further support electrical contact between the rings and pins, a brass casing around the joint ensures the pins are unable to stretch outwards. The brass enclosure is also grounded to the coaxial cable transmitting optoacosutics signals to reduce electromagnetic interference.

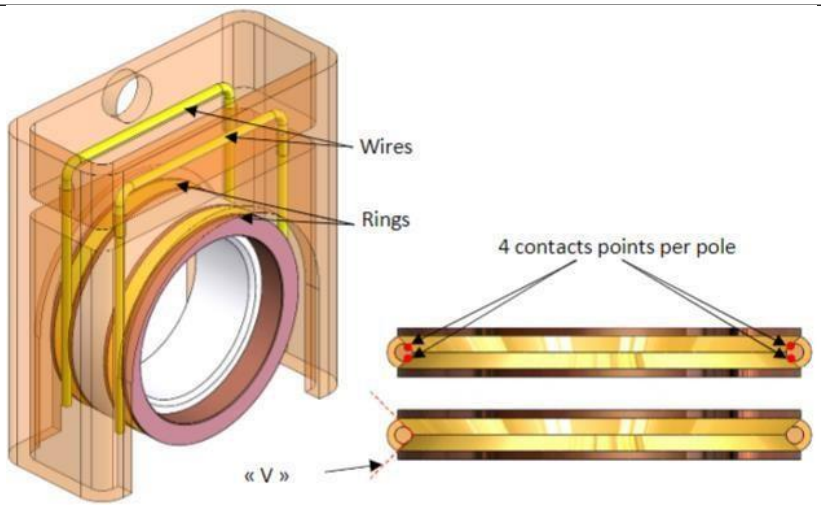

Figure 6.2: Transducer slip ring coupling configuration

6.2. 16mm Semi capsule prototype

Following the manufacturing of the grin lens design in 5.11a, we tested OCT and OA beam characteristics in air as shown figure 6.3. To verify the accurate realization of the lens with correct optical focusing ability, the back focal length was measured by moving the Grin lens mounted on a translation stage to the point where maximal back reflected light from the mirror is achieved. The back focal length was measured as 8.07 mm in air. This is again in agreement with the designed value of 8.10 mm in air in Zemax. Alternatively, the spot sizes at the OCT beam focus were measured with a 5µm resolution CCD. The OCT beam was found to be 19.6µm and the OA beam being 500µm as expected following the simulation from figure 5.6. During these experiment a strong OCT back-reflection was found from the GRIN lens itself. A comparison of OCT A-scans using a normal free space lens and the design GRIN lens is shown in Figure 6.3a. The back-reflection from the GRIN lens was found to be high for imaging, as it saturates the dynamic range of the data acquisition device. The cause of this strong back-reflection was found to originate between the flat surfaces inside the GRIN lens. To suppress this phenomenon and improve OCT SNR another grin lens had to be designed without planar interfaces between optical elements inside the lens. For this reason, we decided to use the current lens with the semicapsule in optoacoustic mode only and extend future designs to include OCT with a modified grin lens.

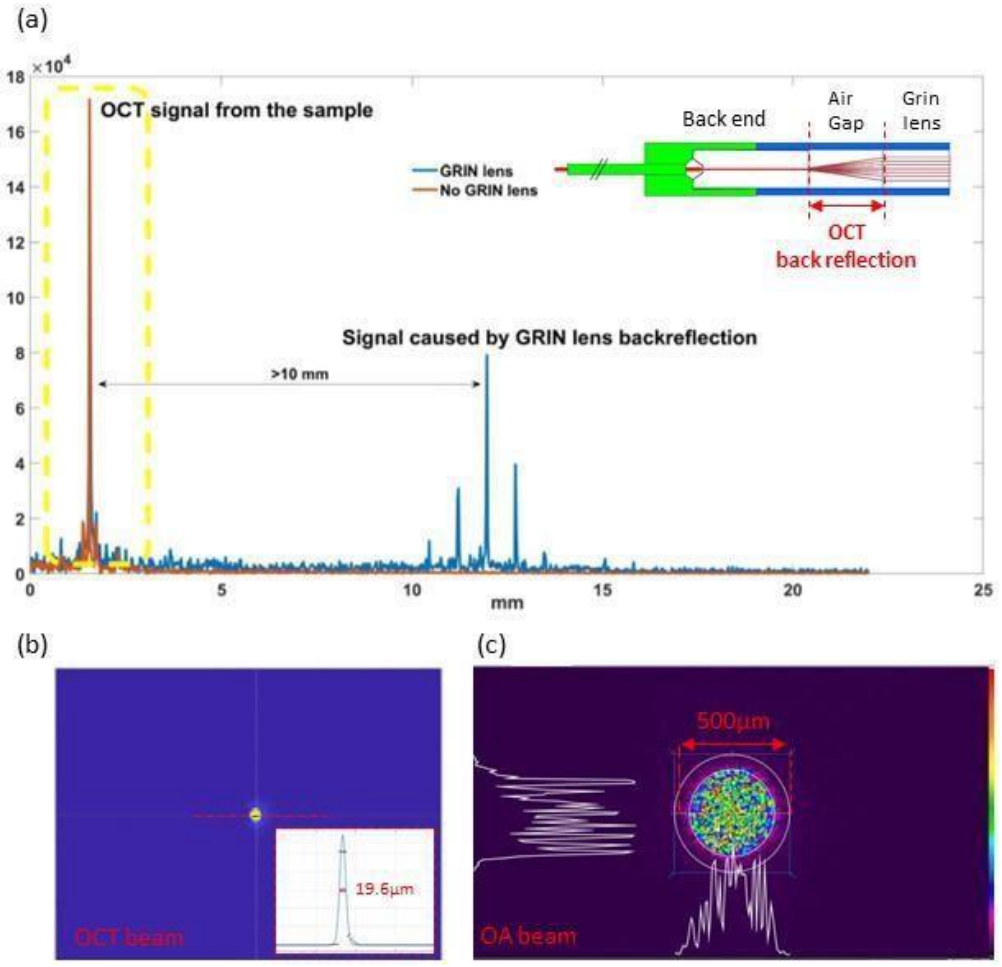

Figure 6.3: OCT-OA optical beam characterization of the custom made grin lens (a) OCT signal measured from the grin lens and a free space lens from a mirror at focus. The backreflected signal depicted reduces OCT SNR. (b) and (c) are the OCT and OA beam profiles measured at the OCT focal length with a CCD camera to measure beam size.

6.2.1 Semicapsule experimental methods

Figure 6.4 shows the semicapsule prototype benchtop experimental configuration, which consists of a 1 ns-pulse width 532nm Q-Switched DPSS laser with a working repetition rate of 1-100kHz (ONDA, Bright Solutions, Italy). A polarizing beam splitter and a beam dump were used to adjust the energy per pulse. For triggering, a 90:10 beam splitter was used to redirect 10% of the light into a photodetector. The remaining 90% of light was coupled into a fiber and directed to the optoacoustic semi capsule endoscope.

The proposed 16mm semi capsule consists of an ultrafine hollow shaft miniature motor to enable optoacoustic coaxial illumination with a custom-designed GRIN lens attached to the distal tip of an optical fiber (GRINTECH, Germany). This optical probe is carefully inserted inside a customized side-looking spherical focused transducers with a central aperture for illumination

(SONAXIS, France). The transducer features a 45^{o} optical mirror and a sealing window mounted at the central aperture of the detector to allow co-axial illumination. Implementing customized low friction miniature gold slip rings (STATICE, France) to permit electrical coupling of high frequency ultrasound signals, thus preventing obstruction from driving cables across the field of view, allows for full 360^{o} unobstructed field of view. The capsule is encapsulated in heavy water and covered by a cylindrical PMMA capsule cover with a thin fiducial marker for synchronization and interpolation of high frame rate B scans (see figure 5.9).

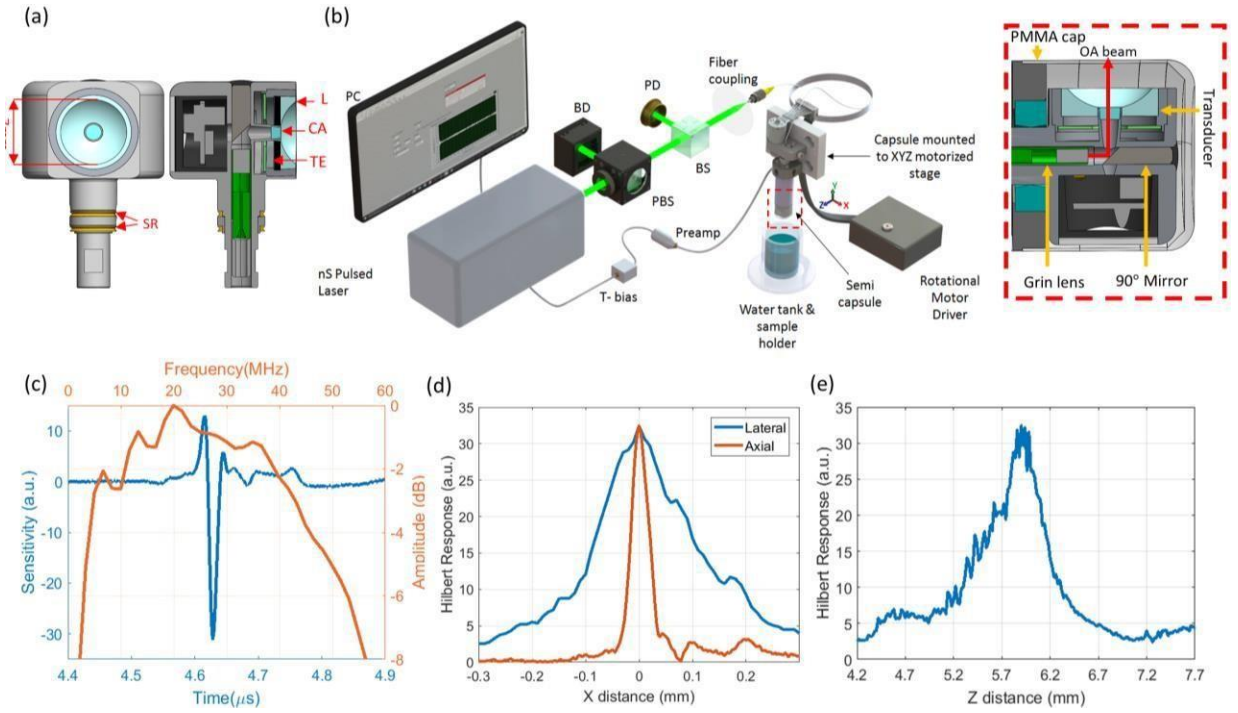

Figure 6.4: semicapsule endoscopic transducer characterization (a) Cross-sectional and en-face view of the endoscopic transducer with a central aperture. TE: Transducer element, EC: Electrical Connector, L: Acoustic Lens, CA: Central Aperture Window, SR: Slip rings. (b) Benchtop optoacoustic endoscopy experimental setup. PBS: polarizing beam splitter, BS: beam splitter, BD: beam dump, PD: photodiode. (c) Optoacoustic transducer temporal and frequency response. (d) Axial and lateral Hilbert transducer resolutions (e) Hilbert depth of focus response.

An ESCON module 24/2, 4-Q servo driver was used to drive the rotational motor using ESCON studio on a PC. Prior to data acquisition at a sampling rate of 500 MHz, the optoacoustic signals measured during rotational scanning were pre-amplified externally with a 30dB amplifier (Sonaxis SA, France) and attached to a T-bias (ZFBT-4R2GW+, Mini-Circuits). To allow for controlled repositioning and 3D Helical pull-back scans, the semi capsule prototype was mounted to an XYZ linear motorized stage (MTS50-Z8 in 3-axis XYZ Configuration Thorlabs). A ATS9373 DAQ card (AlazarTech, Canada) was used to collect the optoacoustic data, which was

synchronized to the board's external trigger port via the photodetector signal. LabVIEW was used to manage signal processing, and MATLAB was used to analyze the results.

The temporal/frequency response at focus, axial/lateral resolutions, and depth of focus independent of rotation were calculated by linear raster scanning the semi capsule against a 20 µm suture in the XZ plane by moving the transducer away from the acoustic source produced by the suture (x steps = 5 µm, z steps = 10 µm).

A phantom consisting of twelve 100 µm sutures arranged in an Archimedean spiral with a pitch of 3 mm as depicted in Figure 6.5 (a) was imaged to show 50 Hz Bscan frame rate with 100 kHz pulse repetition rate (31.4 µm focal plane lateral sampling interval). To assess the effect of laser pulse repetition rate and Bscan frame rate on lateral resolution at the focal plane, the phantom was designed to ensure one of the sutures would reside in the focal plane of the transducer.

Over the course of 4.16 seconds, a 3D helical pull back optoacoustic scan of a stainless-steel mesh arranged in an Archimedean spiral with a pitch of 3 mm (Figure 6.6a) was conducted at 50 Hz Bscan rate and 100 kHz repeat rate with a pullback speed of 2.4 mm/s, accumulating a volume of 1700 x 2000 x 208 (ρ, φ, z) voxels (or 5mm x 360º x 10mm or 1790mm^3). To mimic the scattering of light interrogating biological tissue, this experiment was repeated by replenishing the acoustic binding medium with regulated titration concentrations of intralipid (IL) solution. A 20% IL solution was diluted to six separate test IL concentrations: 0.015, 0.031, 0.062, 0.125, 0.25, and 0.5 percent. Under the same conditions an ex-vivo pig esophageal sample mounted inside a 50 ml- Falcon tube was imaged to demonstrate translational potential. A heated blade was utilized during extraction of the esophageal to preserve the esophageal vascular network. The pulse laser energy used during all imaging experimentation was kept constant at ~ 12 µJ corresponding to a fluence value of $6.1\frac{mJ}{cm^2}$ which exceeds the MPE limit by a factor of 4 assuming the limiting aperture criterion of 3.5mm.

6.2.2 Semicapsule experimental results

Figures 6.4a and 6.4b demonstrate the configuration and setup of the proposed endoscopic transducer. As seen in Figure 6.4c, the transducer demonstrated broadband detection response with a central frequency of 28 MHz and a -6dB bandwidth of 50 MHz during characterization. Afocal length of 6 mm was determined by the temporal response. The axial and lateral resolutions

were measured to be 35 μm and 200 μm, respectively, as seen in Figure 6.4d. The Hilbert plot in Figure 6.4e was used to quantify a 700 μm depth of focus.

To assess the lateral resolution performance of the endoscope as a function of laser pulse repetition rate and scanning speed, we first imaged a phantom consisting of twelve 100 μm sutures arranged in an Archimedean spiral with a 3 mm pitch (Figure 6.5a). The Bscan acquired at 50 Hz frame rate and pulse repetition rate of 100 kHz is shown in Figure 6.5(b). The B scan illustrates the transducers near field, focus, and far field response, with sensor sensitivity peak intensity at the focal plane, which is positioned 2mm away from the capsule surface.

We acquired continuous scans at the maximum frame rate (50 Hz) with different laser pulse repetition rates (20 kHz to 100 kHz), accompanied by scans at the maximum repetition rate (100 kHz) with different frame rates (10 Hz to 50 Hz) to determine the effect of the arc sampling interval and scanning speed on the lateral resolution at focus. We obtained a series of 10 continuous revolutions for each case and measured the lateral resolution for each rotation scan. For each condition, the median and interquartile ranges (IQR) of the measurements were used as indicators of resolution and variability.

The arc sampling intervals and number of A lines collected per revolution at a constant B scan frame rate of 50 Hz for pulse repetition frequencies ranging from 20 kHz to 100 kHz as shown in Table (c) in Figure 6.5. The median lateral resolution ranges between 229 and 234 μm with repetition frequencies ranging from 40 to 100 kHz. However, at 20 kHz, the median lateral resolution decreases to 289 μm. The reduced lateral arc sampling interval of 157 μm at the focal plane is responsible for the decreased median lateral resolution of 289 μm at 20 kHz laser pulse rate. This case provided values ranging from 209 μm to 485 μm, as predicted due to a violation of a Nyquist sampling requirement requiring sampling of twice the resolvable lateral resolution. This will equate to a 100 μm arc sampling interval for our endoscopic transducer. Furthermore, as the repetition rate increases from 20 to 100 kHz, the variability between revolutions decreases due to improved angular sample resolution per B frame; as a result, the IQR decreases from 187 μm to 16 μm.

The arc sampling intervals and number of A lines collected per revolution at a constant laser pulse repetition rate of 100 kHz for B frame scanning frequencies ranging from 10 Hz to 50 Hz is shown in Table (d) in Figure 6.5. The corresponding lateral resolution distribution measurements are plotted in Figure 6.5 (f). In this case, the median lateral resolution improved from 234 μm (50 Hz)

to 207 µm (10 Hz), nearly matching the transducer's lateral resolution of 200 µm as shown in Figure 6.4. While decreasing frame rates often results in an improvement in arc sampling interval, no substantial improvement in the IQR, which fluctuated between 12-16 µm, was observed in this case over the 10-50 Hz test B frame rates.

(a)

(b)

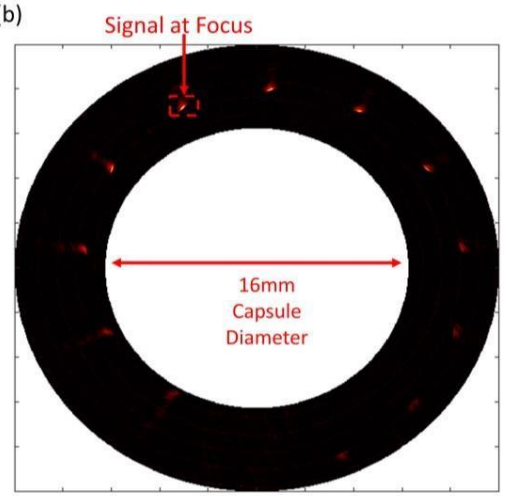

(c)

PRR (kHz)	Rad/s at 50 Hz	mrad at PRR	Arc interval (μm)	A lines per revolution
100	314.15	3.141	31.41	2000
80	314.15	3.926	39.26	1600
60	314.15	5.235	52.35	1200
40	314.15	7.853	78.53	800
20	314.15	15.71	157.1	400

(d)

Frame rate	Rad/s	mrad at PRR 100kHz	Arc interval (μm)	A lines per revolution
50	314.15	3.141	31.41	2000
40	251.3	2.513	25.13	2500
30	188.5	1.885	18.85	3333
20	125.6	1.256	12.56	5002
10	62.83	0.628	6.28	10005

(e)

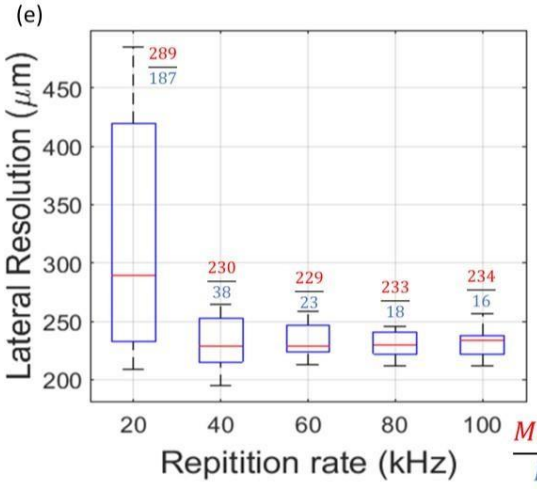

(f)

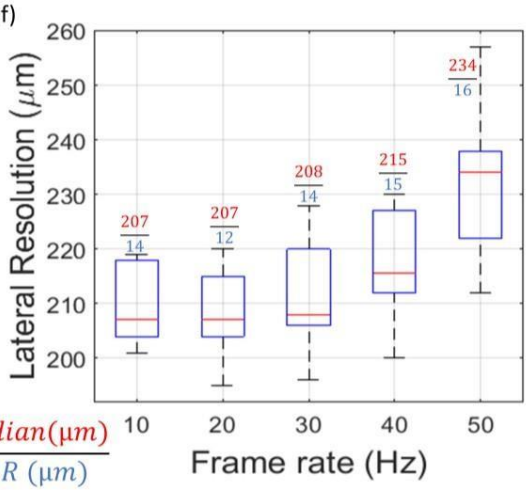

Figure 6.5: 50 Hz Bscan frame rate (a) Twelve sutures with 100µm thickness arranged in an Archimedean spiral phantom with a pitch of 3mm. (b) 360º B scan image of phantom acquired at 50Hz frame rate and 100kHz pulse repetition rate. (c) Table listing the number of A lines per revolution and arc sampling interval at the

transducer focal plane as a function of pulse repetition rate at a fixed frame rate of 50Hz. (d) Table listing the number of A lines per revolution and arc sampling interval at the transducer focal plane as a function of frame rate at a fixed pulse repetition rate of 100kHz (e) Lateral resolution measured at transducer focus at 50Hz frame rate as a function of laser pulse repetition rate under the same experimental configurations listed in table (c) . (f) Lateral resolution measured at transducer focus at 100kHz laser pulse repetition rate as a function of B scan frame rate under the same experimental configurations listed in table (d).

Overall, by decreasing the B scan frame rate and using a higher laser pulse repetition rate, arc sampling spacings are shortened, but the number of A scans per revolution increases, affecting file size and memory usage. Nonetheless, using a 30 Hz scan rate and a 100 kHz repetition rate, we obtained arc sampling intervals of less than 18.8 µm, suggesting no noticeable change in the median value of the lateral resolution corresponding to one tenth of the transducer lateral resolution.

We then continued to explore the endoscope's volumetric imaging capabilities. We conducted a Cscan of a stainless steel mesh arranged in an Archimedean spiral set at a pitch of 3 mm (Figure 6.6a) that acted as a phantom sample, with a minimum diameter of 16 mm and a maximum diameter of 22 mm, which falls within the range of a human esophagus diameter [117]. The 3D projection of the helical scan at 50 Hz and 100 kHz repetition rate pulled back over 10 mm at 2.4 mm/s is presented in Figure 6.6(b). With an arc sampling resolution of 31.4 µm at focus (r = 6 mm), an axial sampling resolution of 3 µm (Fs = 500 MHz), and a helical pitch of 48 µm, the complete scan took 4.16 seconds. The 2D maximum top and axial intensity projections produced from the helical scan are shown in Figure 6.6(c) and (d), respectively, with the fiducial marker and focal plane highlighted. The overall intensity projections demonstrate that, as predicted for afocus transducer, the intensity values are greatest at focus; however, the mesh continues to be distinguishable over the whole field of view and across the total depth of 3 mm.

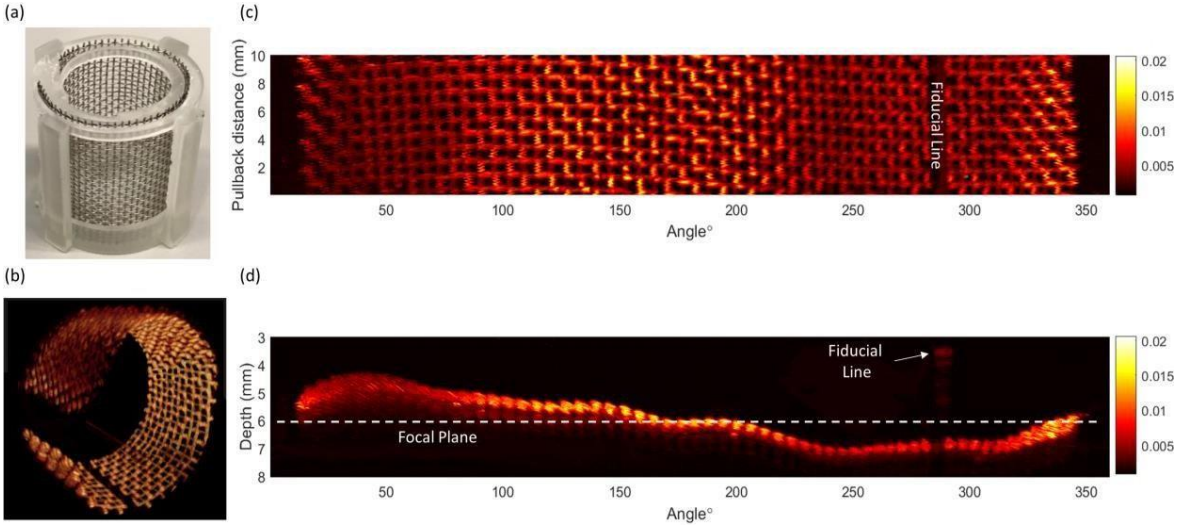

Figure 6.6: Helical volumetric Cscan over 10 mm longitudinal pullback distance at 50 Hz Bscan rate and 100 kHz repetition rate (a) Aluminum phantom mesh mounted in an Archimedean spiral with a pitch of 3 mm. (b) 3D polar projection of Helical optoacoustic scan generated on Amira (c) 2D maximum intensity projection of Helical scan depicted in Cartesian coordinates. (d) 2D Axial maximum intensity projection of Helical scan depicted in Cartesian coordinates.

We embedded the mesh in an intralipid (IL) solution at various concentrations to test the endoscope's imaging penetration depth under light scattering conditions similar to those found in the human esophagus. To prevent signal saturation and to limit the study to intensities within the dynamic spectrum of the mesh in the scattering media, the maximal intensity projections from top and side views of the volumetric scans were obtained with the signal from the fiducial marker masked out.

The highest signal intensity was 15.9 mV at 0.015 % IL (Figures 6.7a and 6.7b), and the entire mesh was visible over the entire 3 mm depth of the mesh. The overall signal intensity was decreased to 14 mV at 0.031 % IL (Figures 6.7c and 6.7d), but the entire mesh remained visible over the entire depth. The overall signal intensity fell to 11.9 mV at 0.062 % IL (Figures 6.7e and 6.7f), with the mesh still perceptible over the whole 3 mm depth but the grid pattern in the far field losing definition. The highest signal intensity was 8.1 mV at 0.125% IL (Figures 6.7g and 6.7h), and the mesh in the far field was no longer visible, reducing the imaging depth to 2.53 mm. The combined signal intensity and depth were further decreased to 7.5 mV at 0.250 % IL (Figure 6.7i and 6.7j), and the mesh was only visible in the near field, reducing the imaging depth to 1.88 mm. Finally, at 0.50 % IL (Figures 6.7k and 6.7l), the overall signal intensity fell to 4.05 mV, the mesh grid pattern disappeared, and the imaging depth was decreased to 1.22 mm.

The amount of light available for OA generation from tissue is affected by light scattering and diffusion. We measured the reduced scattering coefficient, μ_s', at 532 nm for the IL solutions in our experiments based on previously recorded values for IL concentration [118] to approximate the predicted imaging depth in the human esophagus. The μ_s'values for each IL concentration are shown in Table (m) in Figure 6.7. (0.015 % to 0.5 %).

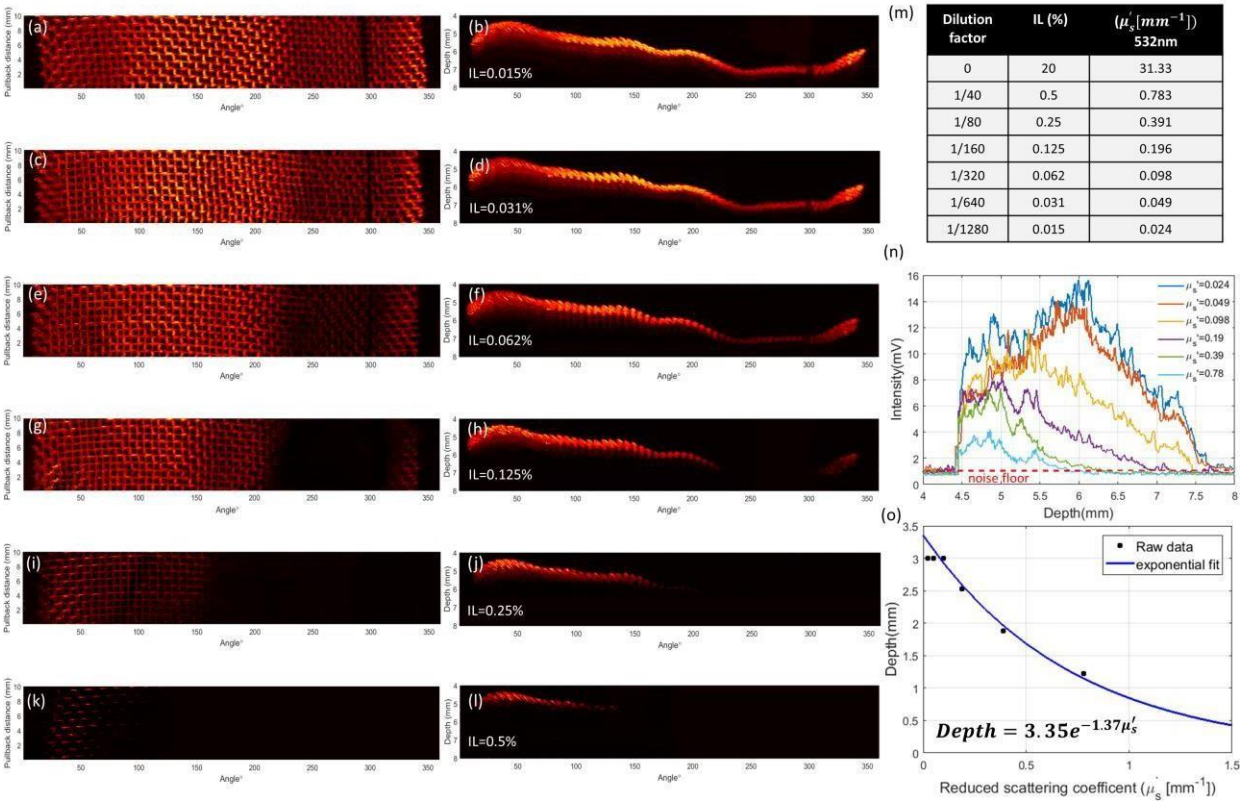

Dilution factor	IL (%)	($\mu_s'[mm^{-1}]$) 532nm
0	20	31.33
1/40	0.5	0.783
1/80	0.25	0.391
1/160	0.125	0.196
1/320	0.062	0.098
1/640	0.031	0.049
1/1280	0.015	0.024

Figure 6.7: 360º Helical volumetric scanning over 10 mm longitudinal pullback distance with intralipid solution. Figures (a,b) depict the 2D top and side maximum intensity projections with 0.015% intralipid solution. The corresponding figure pairs (c,d), (e,f) , (g,h) , (i,j) , (k,l) represent the 2D projections with 0.031% , 0.062%, 0.125%, 0.25%, 0.5% intralipid concentration. (m) Table listing the corresponding reduced scattering coefficient μ_s' at each IL concentration at 532nm (n) illustrates the maximum intensity profile as a function of depth for all scattering coefficients (o) Highlights the relationship between depth and reduced scattering coefficient.

The maximal strength values for the volumetric mesh images as a function of depth are shown in Figure 6.7(n). We used these results to calculate the point at which the amplitude fell below the noise level and used it as an indicator of the imaging depth that could be achieved using our OA endoscopic setup for each scattering state. For the low scattering cases of $\mu_s' = 0.024$ and $\mu_s' = 0.049$, we found that the strength depth profiles agree with the response of our focused detector (see Figure 6.4e). In these instances, the highest amplitude is seen at 6 mm, which corresponds to the transducer's focal point. The peak amplitude shifts towards the transducers near field response for μ_s' at and above 0.098, as anticipated due to decreased light penetration and increased scattering. This shift implies that the transducer's focal distance should be adjusted close to the sample's surface, matching the transducer's highest sensitivity to the attainable light penetration required for OA signal generation, thereby improving the SNR and thus penetration depth under high scattering media conditions.

The relationship between μ_s' and penetration depth is seen in Figure 6.7(o). An exponential equation of the form 3.35exp(-1.37μ_s') is used to curve fit to the experimental data. μ_s'=1.01 $\pm$ $0.14 mm^{-1}$ at 526 nm has previously been recorded in a healthy human esophagus [119]. At a 100 kHz pulse repetition rate and 50 Hz Bscan frame rate, we expect an imaging penetration depth in the human esophagus of ~0.84 mm exceeding the MPE by a factor of 4, assuming an insignificant change in μ_s' from 526 nm to 532 nm and following our derived expression for the penetration depth and μ_s'.

Next an ex-vivo female pig esophagus (Figure 6.8a) installed inside a 50 mL falcon tube was imaged to confirm our phantom model and illustrate translation potential of our endoscope. The 3D volume of the obtained pullback scan at 50 Hz B scan rate and 100 kHz over a 12 mm pullback distance at 2.4 mm/s is shown in Figure 6.8(b). With an arc sampling resolution of 31.4 µm at focus, an axial sampling resolution of 3 µm, and a helical pitch of 48 µm, the whole scan was captured in 5 seconds. Figure 6.8 (c) and (d) show B scans from the helical pull back scan obtained from two arbitrary positions, illustrating the capability to gather data over a 360° field of view. The 2D enface and axial maximum intensity projections obtained from the helical scan are shown in Figures 6.8(e) and (f), respectively, with the fiducial marker and capsule surface emphasized. Even though the vascular network had collapsed, and the blood had drained in the ex-vivo setting, remnants of blood in vessels were still visible throughout a 360° field of view and up to a penetration depth of 1.2 mm.

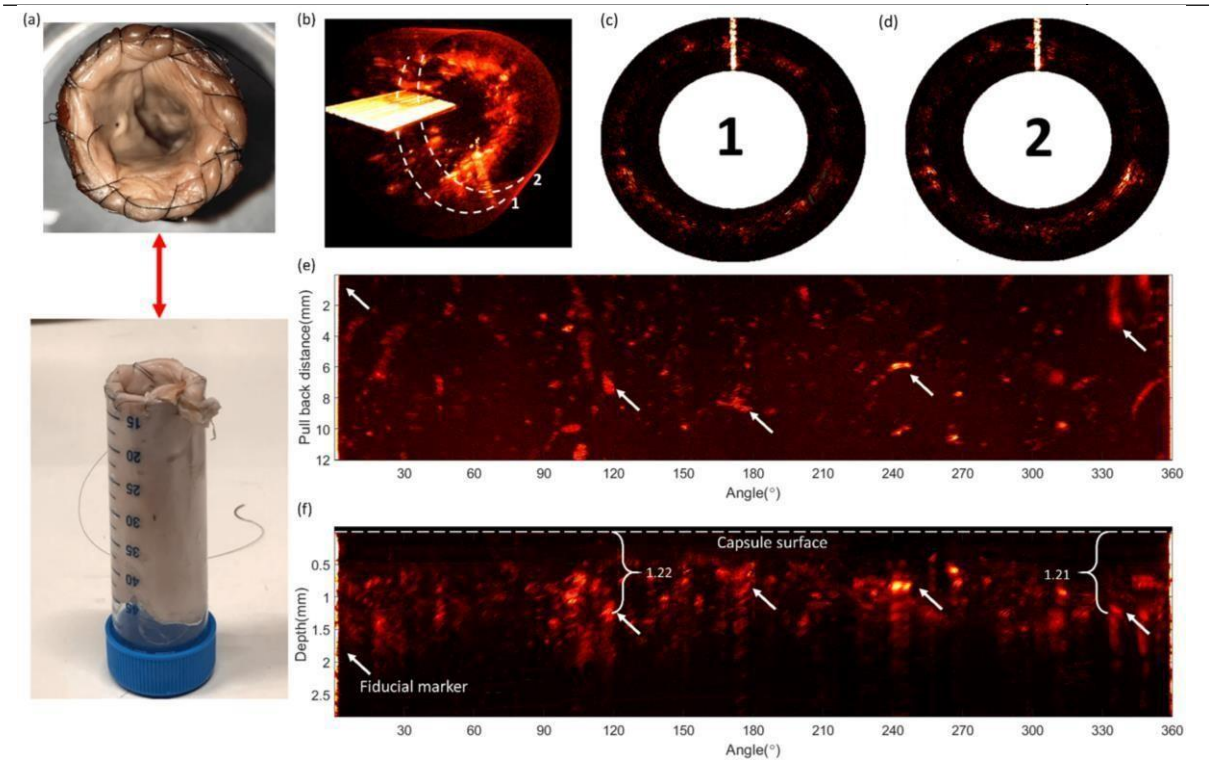

Figure 6.8: 360º helical volumetric scanning of an *ex-vivo* female pig esophagus over a 12 mm longitudinal pullback distance. (a) *Ex-vivo* pig esophagus sample mounted on a 50 mL-Falcon tube for support (b) 3D volumetric render of helical scan (c,d) B scans taken at unique positions within the helical scan. Maximum intensity projection for (e) enface and (f) side views.

6.2.3 Discussion of semicapsule capability

Optoacoustic endoscopes have inadequate fields of view, poor B scan frame rates, improper probe construction, and insufficient SNR for human esophageal imaging, despite their great potential for GI tract diagnostics. By combining a side-looking broadband-based transducer electrically coupled with slip rings and a central aperture for coaxial illumination, we have produced the first 50 Hz, complete 360° field of view optoacoustic capsule endoscope. We revealed imaging of 1700 x 2000 x 208 (ρ, φ, z) voxels at a volume rate of 0.24 Hz. At 100 kHz laser repetition frequencies, we demonstrated imaging depths of 3 mm in low scattering media and an average imaging depth of ~0.84 mm for esophagus-mimicking phantoms and penetration depth of 1.2 mm in ex-vivo pig esophagus.

An optoacoustic capsule endoscope in radial imaging configuration of the GI track was previously introduced by our group [49]. This method permitted for the first time continuous 360-degree imaging, but the B frame rate was limited to 2.5 Hz, preventing quick volumetric scanning. By inserting the rotation coupling directly onto the transducer housing inside the capsule with

customized miniature slip rings, we were able to achieve a 20-fold higher B scan frame rate. To our knowledge, this is the first-time video-rate optoacoustic capsule endoscopy has been allowed at 50Hz, which could lead to real-time GI optoacoustic endoscopy surveillance and minimize motion artifacts. The effects of pulse repetition rate (20-100 kHz) and B scan frame rate (10-50 Hz) on lateral resolution were investigated. The increasing pulses available on each rotation period causes a reduction in angular sampling resolution as the laser pulse repetition rate is increased or B scan frame is decreased (number of A lines per revolution). We discovered that sampling at 1/10th of the transducer lateral resolution at focus produced the best lateral resolution. Transducer characterization revealed a lateral resolution of 200 µm, necessitating arc sampling of 20 µm at focus. The arc sampling interval was 33 µm ($\varphi = 0.18°$) at 100 kHz pulse repetition rate and 50 Hz B frame rate, resulting in a deterioration of the overall lateral resolution to 234 µm with an interquartile deviation size of 16 µm. Reducing the B scan frame rate to 30 Hz at the same repetition rate results in an arc sampling period of 18 µm ($\varphi = 0.1°$), increasing the lateral resolution to 208 µm, closer to the transducer's optimum attainable value. Reducing B scan frame further decreased arc interval to 6.2 µm (φ =0.035°) at 10 Hz; however, this does not result in a resolution increase.

We demonstrate the ability to achieve rapid volumetric imaging at 0.24 Hz over a total volume of $5\ mm \times 360° \times 10\ mm$ (ρ, φ, z) or 1790 mm^3, with a high sample resolution of $3\ \mu m \times 0.18° \times 48\ \mu m$ (ρ, φ, z). This high-resolution volumetric imaging speed enables the ability to scan the entire human esophagus in under 2 minutes, up to a length of 250 mm [120]. The abilityto collect vast volumes quickly allows for study of many high-risk areas within the human GI tract, including large Barrett's esophagus segments. The OA imaging penetration depth in non- scattering media was greater than 3 mm. However, we demonstrate that the penetration depth depends exponentially on the dispersion of the medium. In low dispersion cases ($\mu' \leq 0.049$), the maximal transducing sensitivity is maintained at focus; however, light diffusion dominates the transducing sensitivity profile in higher dispersion media and shifts the maximum sensitivity intothe near field of the transducer. Following the exponential relation of an increasing μ', we approximate a depth of 0.84 mm (assuming μ' ~1.01 @ 532 nm) in the human esophagus with ourendoscope. A helical pullback scan of an ex-vivo pig esophagus at the same volumetric rate of
0.24 Hz was used to validate our phantom model. Despite the fact that the sample's vascular network had collapsed, our endoscope was able to detect traces of vessels up to a depth of 1.2 mm. The imaging penetration anticipated with our phantom revealed deeper features in the pig esophagus (Figure 6.8). The discrepancy can be explained by lower acoustic frequency

components in the thick vessel in the ex-vivo sample, which experience lower propagation losses. The mesh in the phantom, for example, has a diameter of 0.25 mm, but the blood vessels in the pig esophagus measured in Figure 6.8(f) had a diameter of 0.7 mm.

This depth is similar to previous OA endsocopy studies which demonstrate image depths ~1 mm at less than five Hz of small animal esophagus or colon tissue [45, 46, 48]. These low frame rates combined with the low laser pulse repetition rates do not exceed the MPE rule 1 (20mJ/cm^2) (see section 5.5.4). Under these circumstances an imaging depth of 2 mm in pig esophagus ex-vivo was shown by He et al [49]. Increasing pulse repetition rates sets a tighter MPE limit, where the 20 mJ/cm^2 limit is no longer applicable as such the maximum for MPE is 1.53mJ/cm^2 in our caseat 100kHz repetition and 50Hz Bscan rate (see section 5.5.4.). Previously, a catheter-based optoacoustic endoscope system [47] used a 300 kHz pulse repetition rate with 30 µJ-pulse energies and a 1mm grin lens to create a collimated beam. Despite the fact that the beam spot size on the rat rectum was not disclosed, the authors stated an energy density of 15 mJ/cm^2. Following the limited aperture criterion of 3.5mm of the ANSI standard, the MPE limit is exceeded by 174- fold. These results show that optoacoustic endoscopy's translational capacity is fueled by its ability to survey the human esophagus quickly without exceeding the MPE while providing high resolution over many mm’s of depth.

The ex-vivo potential of the optoacoustic capsule design described here is a major step forward toward video-rate in-vivo optoacoustic endoscopy of the human GI tract. However, future efforts are expected to resolve capsule size, sensitivity, resolution, and motor stability compensation to translate the concept for in-vivo imaging. Although our current capsule configuration has a diameter of 16 mm, which is close to standard WLE, further miniaturization is needed to make it easier to swallow and to meet the size of commercially available white light capsules, which are usually less than 32 mm long and 13 mm wide [121,122]. For example, by decreasing the transducer size and integrating a miniature motor into the capsule, the total length and diameter can be minimized. A transducer preamplification stage may be inserted into the capsule to further improve sensitivity and image depth [49]. Shifting the focus of the transducer to the surface of the capsule would also increase the SNR when imaging in high scattering media such as the human esophagus. In addition, a transducer with a high central frequency and short focal length, as currently used in Raster scanning Optoacoustic Mesoscopy (RSOM) , could be developed [36,123] to increase the resolution of the opto-acoustic signal. In order to offset motor dysfunction during imaging, post-processing methods will be investigated.

In conclusion, a 16 mm optoacoustic capsule endoscope prototype with a side viewing central aperture endoscopic transducer with integrated optics and slips rings allowed full field of view optoacoustic imaging at 50 Hz frame rate with angular sample resolution of 0.18º at 100kHz pulse repetition rate. The practical ability was tested in 2D and 3D phantoms, where lateral resolution precision and imaging depth were illustrated. Overall, these findings show that our innovative video-rate optoacoustic capsule endoscope architecture can reduce motion artifacts during imaging, potentially paving the way for future molecular imaging of the human GI tract.

6.3. 12.5mm Partial capsule prototype

Building on the semicapsule prototype a second-generation prototype with a diameter of 12.5mm named the partial capsule was built. Improvements made included shifting the focus of the transducer at the capsule surface for improved sensitivity, Higher transducer central frequency and therefore improved lateral and axial resolutions. The size of the transducer was also miniaturized to ensure the diameter of the capsule would match the size of commercially availablewhite light capsules [121,122]. Although miniaturization of the transducer led to mechanical faultlimiting rotation speed upto 30Hz, increasing speed beyond this limit would cause water employedas the coupling medium getting sucked inside the probe, reaching the slip rings, and thereby reducing OA SNR. Finally, a new grin lens as depicted in figure 6.9 was designed to ensure this prototype could operate in hybrid OCT-OA mode. Figure 6.9a shows the semicapsule design where the two planar surface between the grin lens and back-end results in a residual back reflection signal reducing SNR. Alternatively Figure 6.9b presents the partial capsule grin lens design where an 8º polished glass spacer is inserted between the back end and grin lens optical elements to remove the planar surfaces and thereby suppress the back reflected signal which occurs in Figure 6.9a. Measuring the beam spot sizes at the capsule surface following the same methodology in 6.3 we obtain 20µm for the OCT beam and 500 µm for the OA beam.

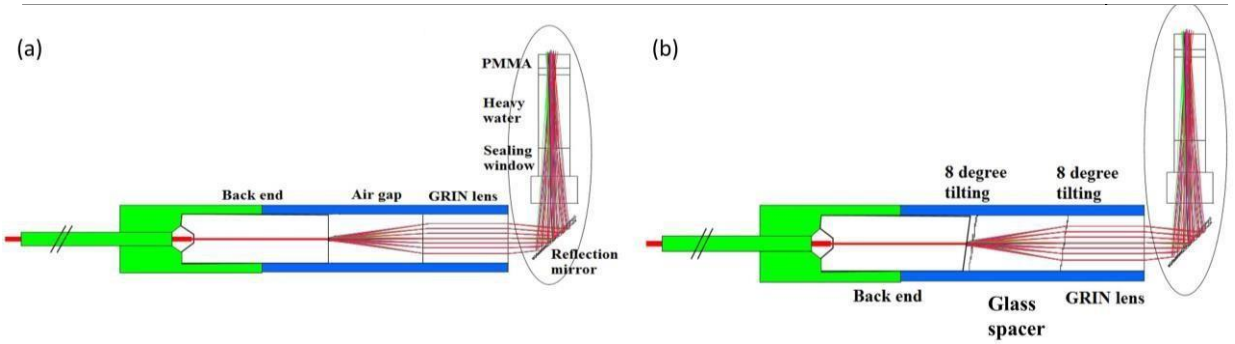

Figure 6.9: Grin lens designs for Hybrid OCT-OA endoscopy (a) semicapsule grin lens design (b) partial capsule grin lens design.

6.3.1 Partial capsule experimental methods

The partial capsule prototype and benchtop experimental setup are presented in Figure 6.10. Here a 1060nm SS OCT laser (Insight solutions, USA) operates as master at 85kHz A-scan rate and a nanosecond pulsed 532nm Q-switched OA laser (Bright solutions, Italy) operates at 42.5kHz A-scan rate in slave mode by getting triggered synchronously via a trigger divider. The 1060nm light emitted from the OCT laser is connected to a 90/10 coupler which delivers 90% of the light to the input OCT port of a custom made double clad fiber coupler and 10% of the light to a free space reference arm for dispersion and length compensation. Three manual fiber polarization controllers are placed within the optical setup to maximize OCT SNR. Alternatively, the pulsed beams emitted from the OA laser are regulated by means of the polarizing beam splitter and beam dumpbefore fiber coupled into input OA port of the custom made double clad fiber coupler. The input ports of the double clad fiber coupler combine both beams into a single double clad fiber at the output with the core carrying the OCT beam and the inner cladding carrying the OA beam. The custom-made grin lens is mounted on the tip of this fiber and installed inside the partial capsule probe.

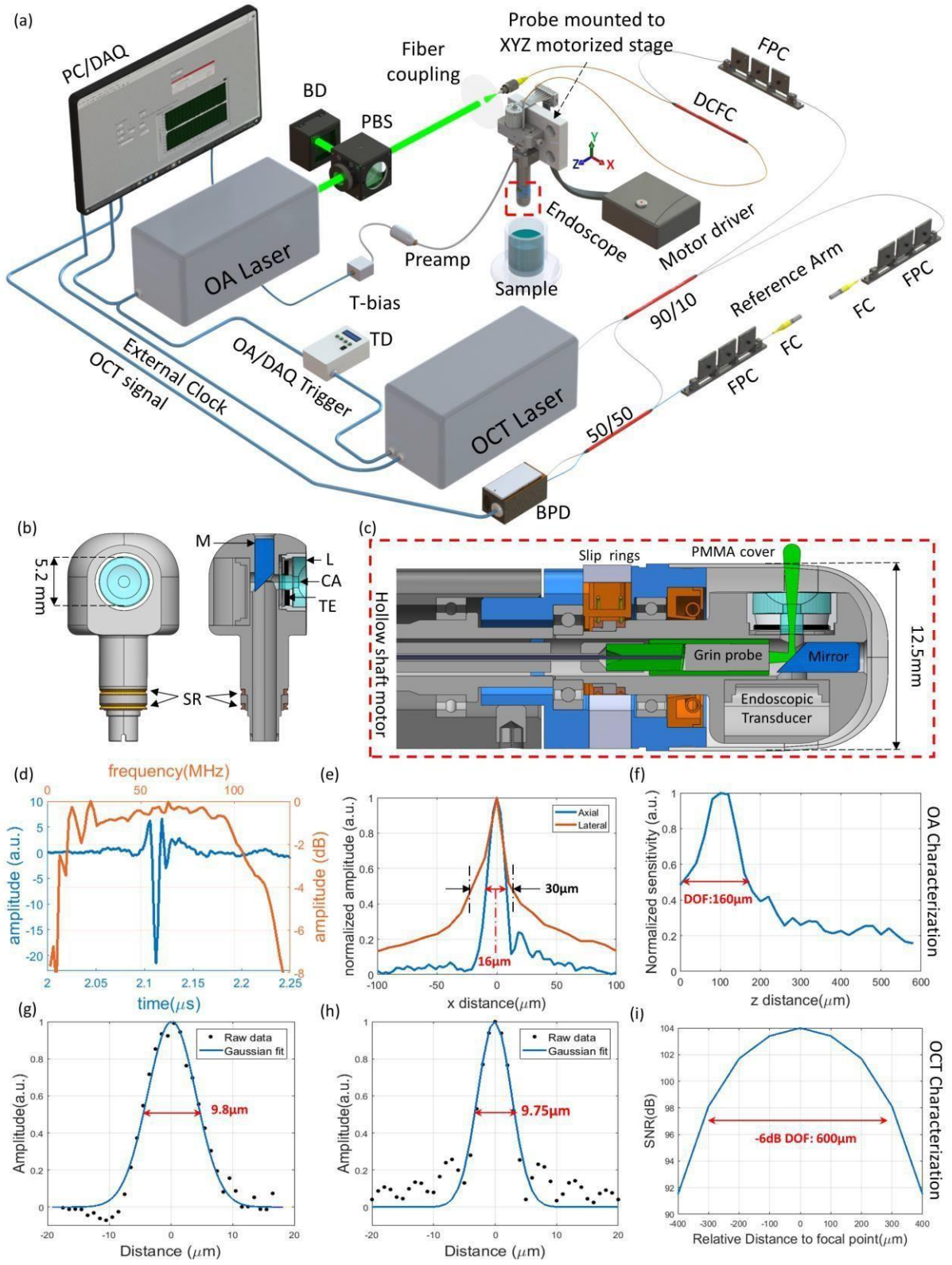

Figure 6.10: Hybrid Endoscope setup and OCT/OA modality characterization (a) Benchtop hybrid endoscopy experimental setup. PBS: polarizing beam splitter, BS: beam splitter, BD: beam dump, FPC: fiber polarizer controller, FC: fiber collimator, DCFC: double clad fiber coupler, TD: Trigger divider, BPD: Balanced photodetector. (b) Cross sectional and enface view of the endoscopic transducer with central aperture. TE: Transducer element, M: mirror, EC: Electrical Connector, L: Acoustic Lens, CA: Central Aperture Window, SR: Slip rings. (c) Cross sectional view of the hybrid endoscope. (d-f) Optoacoustic characterization including (d) Temporal signal and Bandwidth., (e) axial and lateral resolutions and (f) depth of focus. (g-i) OCT characterization including (g) lateral and (h) axial resolutions and (i) depth of focus.

The 12.5mm diameter capsule performs rotational scanning by employing a hollow shaft motor (Maxon Group, Switzerland) to house the custom-made grin lens inside a rotating side looking 1.2mm central aperture spherically focused $LiNO_3$ transducer (SONAXIS, France) as shown Fig 6.10b with integrated optics and slip rings to couple high frequency ultrasound and facilitate coaxial OCT-OA illumination by reflection from a 90^o optical reflector as illustrated in Fig 6.10c. Here the OCT beam is focused just beyond the capsule surface and the interrogation OA beam is diffuse to ensure acoustic resolution optoacoustic endoscopy. The capsule was encapsulated in heavy water with a thin cylindrical PMMA capsule lid featuring a fine fiducial marker used for synchronization and interpolation of high frame rate B scans. Full 360^o unobstructed field of view is achieved during hybrid rotational scanning, where back scattered OCT light is collected via the same interrogation grin lens and interfered with the reference arm via 50:50 couplers prior to interferometric detection using a high performance balanced photodetector (Insight solutions, USA). At the same time optoacoustics waves are measured by the transducer and pre-amplified externally with a 30dB amplifier and connected to a T-bias (ZFBT-4R2GW+, Mini-Circuits) prior to data acquisition. To perform helical scans, the capsule prototype was mounted to a XYZ linear motorized stage configuration (MTS50-Z8, in 3-axis XYZ Configuration Thorlabs) to allow for controlled linear repositioning.

To achieve rotational scanning the same hollow shaft motor and controller (Maxon Group, Switzerland) employed for the semicapsule was utilized for the partial capsule. Side illumination is facilitated also in the same manner as the semicapsule by integrating a 90^o optical reflector and a sealing window installed at the central aperture of the partial capsule detector. Slip rings are used to enable full 360^o unobstructed field of view (STATICE, France). During rotational scanning, back scattered OCT light is collected from the same interrogation grin lens and interfered with reference arm via a 50:50 couplers prior to interferometric detection using a high performance balanced photodetector (Insight solutions, USA). Meanwhile optoacoustic waves measured during rotational scanning were pre-amplified externally with an 30dB amplifier (Sonaxis SA, France) and connected to a T-bias (ZFBT-4R2GW+, Mini-Circuits) prior to data acquisition.

Data acquisition was performed synchronously on a dual channel ATS9373 DAQ card (AlazarTech, Canada) with channel A connected to the balanced photodetector used to recover the OCT A-scan and channel B connected to the T-bias of the ultrasound detector to measure the

OA Ascan. DAQ triggering and external clock signals are driven by the OCT laser to ensure the swept source signals are in sync. Signal processing was controlled in LabVIEW and data analyzed in MATLAB.

The endoscopic transducer was characterized by linear raster scanning the capsule against a 7 μm carbon fiber in the XZ plane by shifting the transducer away from the acoustic source generated via the fiber (x steps = 5 μm, z steps = 10 μm) to determine the temporal/frequency response at focus, the axial/lateral resolutions and depth of focus.

The measured OCT axial resolution using a reflective mirror was 9.75 μm in air as illustrated in Figure 6.10h, or 7.2 μm in tissue (assuming a refractive index of 1.35 in tissue). Upon the return path from the tissue, the light interfered with the reference beam through a 50/50 fiber optic coupler (TW1064R5F2A). The resultant interference signal was detected using a balanced photodetector (BPD-1, Insight solutions, USA). The size of the optical focus created by the grin lens for OCT was measured by mounting the grin lens on a 2D translation stage (M511, Physik Instrumente GmbH & Co. KG) and implementing a raster scanning to image a USAF 1951 resolution target (3'' x 3'' positive, Edmund Optics) with a step size of 1 μm. An edge-spread function (ESF) was obtained from the corresponding data at the sharp edge of the lines on the resolution target. The negative derivative of the ESF was calculated and fitted using a Gaussian model to get the line spread function (LSF) shown in Figure 6.10g. The full width at half-maximum (FWHM) of the LSF showed a lateral resolution of 9.8 μm in air for OCT. With an output power of 6 mW from the grin lens, the OCT signal-to-noise ratio (SNR) was measured using a neutral density filter and a reflective mirror. As shown in Figure 6.10i, an SNR of 104 dB was achieved at the focus. The SNR at different depth of focus of the grin lens was measured by shifting the position reflective mirror. At a distance of 400 μm away from the focus, the SNR drops to approximately 92 dB.

The capsules OCT and OA average lateral resolution and relative intensity as a function of depth over 10 frames at 30Hz were characterized by a phantom consisting of 16 sutures of 100μm thickness arranged in an Archimedean spiral with a pitch of 3mm. 8 sutures were black to absorb the 532nm light and generate optoacoustic signals along with 8 sutures being white to reflect the 1060nm light and generate OCT signals. The sutures were arranged in alternating color configuration following the Archimedean spiral as illustrated in Fig 6.11a.

A pullback helical scan at 2.4mm/s was performed to demonstrate the ability to acquire synchronous OCT-OA volumetric data at 30Hz frame rate by imaging a stainless-steel mesh arranged in an Archimedean spiral with a pitch of 3mm at 85kHz OCT/42.5kHz OA A-scan rate. In this configuration over a pullback distance of 11.5mm corresponding to a period of 4.8 seconds a OA volume comprising of 1600 x 1420 x 143 (ρ, φ, z) voxels and OCT volume comprising of 1600 x 2840 x 143 (ρ, φ, z) voxels are simultaneous acquired. To assess in-vivo imaging potential, under the same conditions albeit a pullback distance of 15mm, an ex-vivo pig esophagusembedded with 100µm suture to mimic blood vessels and in-vivo human mucosa tissue was imaged over a pullback distance of 30mm at record time acquisition time of 12.5 seconds. The OA pulse energy used during all experiments was maintained at ~12µJ.

6.3.2 Partial experimental results

The hybrid experiment setup, optoacoustic endoscopic and capsule design are given in Fig 6.10a-c and described in 6.3.1. Optoacoustic detector characterization revealed a broadband detection performance with a central frequency of 63.5 MHz and a -6dB bandwidth of 127 MHz as depicted in Fig 6.10d. The temporal response exhibited a transducer focal length of 3 mm. The axial and lateral optoacoustic resolutions were measured as 16 µm and 30µm, respectively, as shown in Fig 6.10e. A 160 µm optoacoustic depth of focus was measured from the Hilbert plot in Fig 6.10f. Alternatively the OCT beam characterization revealed an axial and lateral resolution of ~9.8µm and a -6dB depth of focus of 600µm.

To illustrate the importance of hybrid imaging and characterize the endoscopes lateral resolution as a function of depth at 30 Hz synchronous frame rate, we imaged a phantom consisting of sixteen 100 µm sutures arranged in an Archimedean spiral with a pitch of 3mm. As shown in Fig 6.11a the sutures were organized in alternating color configuration with 8 black and 8 white sutures. Fig 6.11b depicts the optoacoustic B scan acquired at 30Hz with a pulse repetition rate of 42.5kHz where only 8 sutures are visible corresponding to the black sutures which absorb the 532nm to generate optoacoustic signals. Furthermore, the optoacoustic B scan highlights the transducers far field response as intensity and lateral resolution degrades with respect to increasing axial distance from the capsule surface. Similarly, Fig 6.11c illustrates the OCT Bscan acquired at 30Hz with a repetition rate of 85kHz where the remaining 8 white sutures signals are measured because they scatter the interrogation 1060nm beam to generate OCT signals. The OCT Bscan also indicates a reduction of intensity moving away from the capsule surface. Fig 6.11d depicts a hybrid synchronous OCT-OA Bscan at 30Hz where all 16 sutures are visible only in this instance. Thus

combining complementary OA molecular absorption and scattering of radiation to measure structural features with OCT can reveal additional features not visible to either single modality.

To assess the reduction in intensity and lateral resolution of our OCT-OA endoscope as a function of imaging depth, the average intensity and lateral full width half maximum values of the sutures were measured for each modality over 10 frames. A plot of normalized OA-OCT intensity and lateral FWHM as a function of imaging depth are given in Fig 6.11e and 6.11f respectively. From Fig 6.11e the normalized optoacoustic intensity exponentially reduces moving away from capsule surface to reach a steady state value of 0.2 at a depth of 1.6mm. Similarly, the normalized OCT intensity exponentially reduces moving away from capsule surface and reaches a steady state value of ~0.04 at a depth of 1.6mm. The lateral FWHM of both OCT and OA reduces as a function of increasing imaging depth as illustrated in Fig 6.11f. The OCT Lateral FWHM degrades from 122µm to 197µm and OA lateral FWHM degrades from 125µm to 360µm. Note: for OCT the expected penetration depth is no more than 1 mm for in-vivo esophagus and deterioration of lateral FWHM over this range is only 5µm. Instead, for OA because resolution is defined by the acoustics and a higher penetration depth exceeding 1mm is expected, tomographic reconstruction in cylindrical coordinates could improve spatial resolution over extended depths.

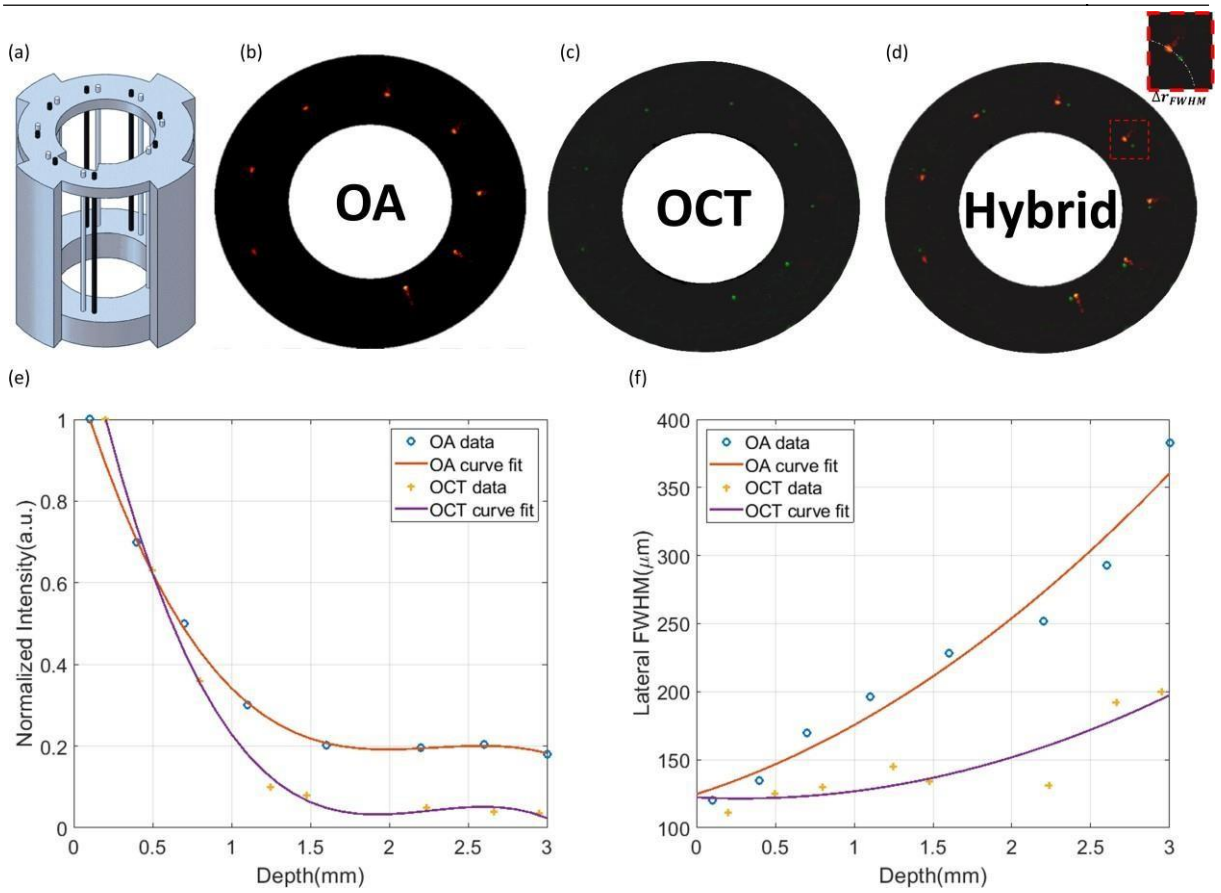

Figure 6.11: Hybrid synchronous 30 Hz OCT- OA Bscans of a hybrid suture phantom (a) 16 sutures with alternating colors of black and white of 100µm thickness are arranged in an Archimedean spiral phantom with a pitch of 3mm. 360^0 B scan images of the phantom acquired at 30 Hz (b) Optoacoustics (b) OCT and (d) Hybrid mode. (d) Normalized intensity of both modalities as a function of depth (f) lateral FWHM measured across all sutures for both modalities as a function of depth..

Next we imaged a stainless-steel mesh arranged in an Archimedean spiral with a pitch of 4mm (Fig 6.12a) to demonstrate synchronous OCT-OA volumetric endoscopic imaging at 30Hz frame rate. The minimum diameter of the mesh was 12.5mm and the maximum diameter was 16.5mm falling within the range of human esophagus diameter. Figures (6.12b, c,d) illustrate 3D projections of the OA , OCT and hybrid helical scans at 30Hz frame rate and 85kHz OCT/ 42.5kHz OA repetition rate pulled back over 11.5mm at 2.4mm/s. Both OCT and OA volumes were acquired in 4.8 seconds with an OA arc sampling interval of 27µm at capsule surface and OA axial sampling resolution of 3.75 µm (Fs = 400 MHz). The OCT arc sampling interval at the capsule surface was 13.5µm and the OCT axial sampling interval was 2.5µm. The helical pitch for both scans determined by the pullback motor was $80\mu m$. Figure 6.12(e & f) show the 2D enface maximum intensity projections of the OCT and OA scans respectively and Figure 6.12 (g & h) represent the corresponding 2D maximum axial intensity OCT and OA projections. The fiducial marker signal is present in the OA scans because the marker itself is composed of carbonfiber thereby absorbing the OA illumination and generating an OA signal whereas the capsule

PMMA cover is measured in the OCT scan due to a sharp change in refractive index between PMMA material and the acoustic coupling medium. The 2D projections indicate the intensity values of both modalities are highest near the capsule surface where both the OCT beam and OA transducer's focal planes lie. Furthermore, OCT and OA mesh signals are visible up to an axial depth of 3mm with both modalities.

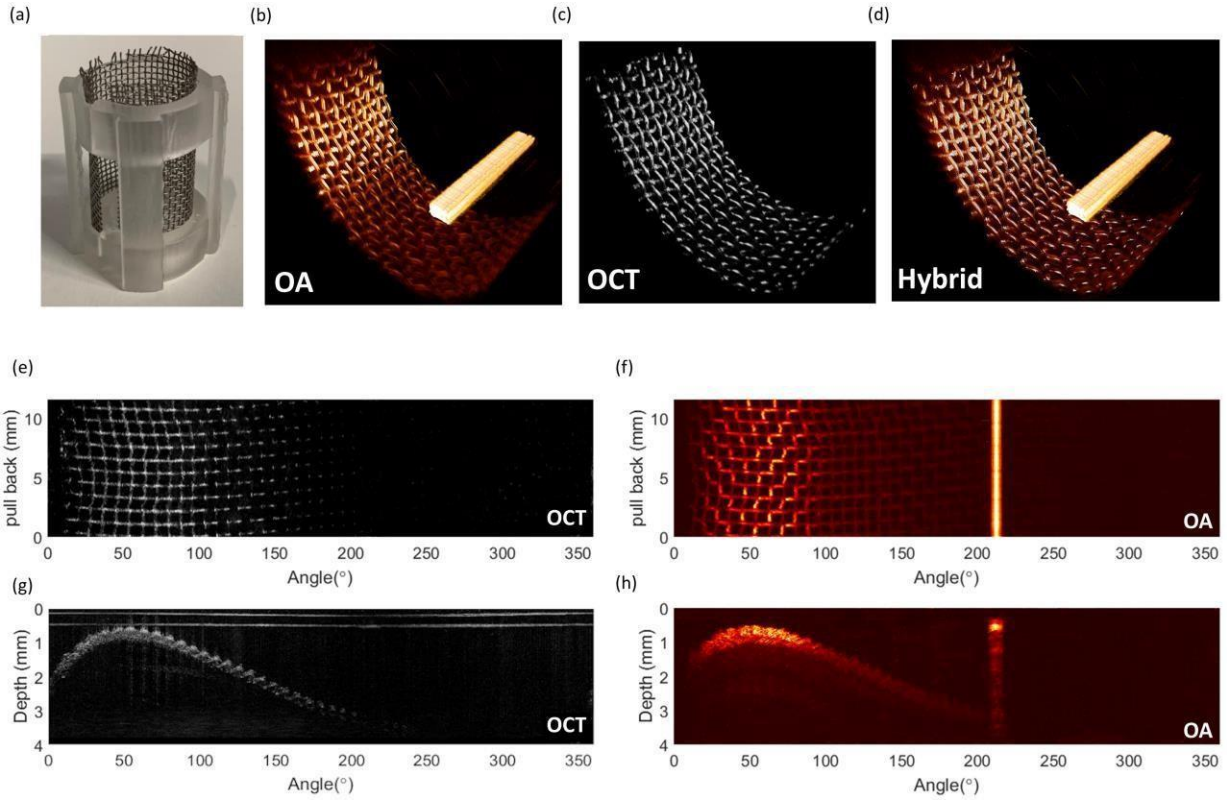

Figure 6.12: Hybrid synchronous helical volumetric scan over 11.5 mm longitudinal pull back distance at 30 Hz OCT/OA Bscan rate of a stainless-steel mesh phantom (a) Stainless steel phantom arranged in an Archimedean spiral with a pitch of 3mm in a 3D printed mount. (b) 3D projection of Optoacoustic data acquired. (c) 3D projection of OCT data acquired (d) 3D projection of Hybrid data acquired. (e-f) 2D Optoacoustic maximum intensity projections of the top and side respectively. (g-h) 2D OCT maximum intensity projections of the top and side respectively. (i-j) 2D Hybrid maximum intensity projections of the top and side respectively.

Subsequently we assessed the translational potential of our endoscope by imaging an ex-vivo pig esophagus (Fig 6.13a-b) mounted inside a 50 mL falcon tube. During extraction of the sample unfortunately the vascular network quickly collapses, and blood is drained. Therefore, to mimic the hemoglobin vascular network present within the submucosa of the esophageal lining 100µm black sutures were embedded into the esophageal wall. A pullback helical scan over 15mm with the same scanning configuration as the steel mesh experiment was performed with the esophageal sample to acquire hybrid volumetric OCT-OA data. Figure 6.13c illustrates the hybrid OCT-OA volumetric data acquired in cylindrical coordinates and Figures 6.13 (d,e & f) show polar hybrid Bscans extracted from the volume in Figure 6.13c. OCT signals provide the structure of the esophageal wall revealing the epithelium and submucosa whereas OA signals measure the vessel

mimicking sutures which add complementary information. From the polar plots the OA signals visualized are deeper in comparison to the OCT signals, this feature could enable determining tumor invasion depth. Figures 6.13g-i represent the enface maximum intensity projections of the OCT, OA and hybrid scans respectively. The OCT enface projection reveals structural information of the esophageal lumen whereas the OA enface captures the positions of the blood mimicking vessels and the hybrid enface demonstrates how the images from each modality adds complementary information when overlaid over each other.

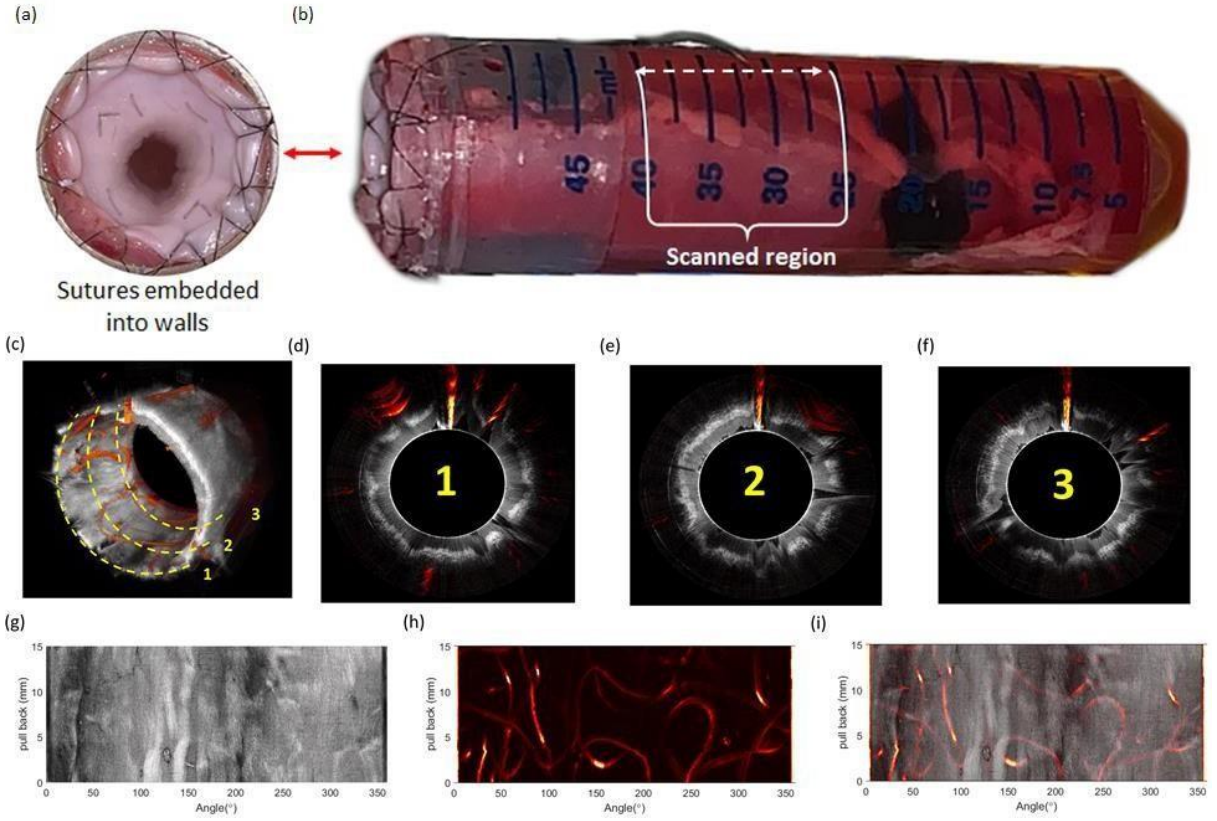

Figure 6.13: Hybrid synchronous helical volumetric scan over 15 mm longitudinal pull back distance at 30 Hz Bscan rate of an ex-vivo pig esophageal sample with black 100µm sutures embedded into the walls (a) & (b) photos of an ex-vivo pig esophagus model configured for imaging. (c) 3D volumetric render of hybrid OCT-OA data where grey scale map represents OCT data and hot colormap represents OA data (d- f) Hybrid polar B scans at selected positions extracted from the 3D volumetric data. (g-h) 2D maximum enface intensity projections of the OCT (g) , OA (h) and hybrid (i) .

To showcase in-vivo imaging prospective of our endoscope human mucosa tissue from the inferior lip was imaged over a pullback distance of 30mm over an imaging period of 12.5 seconds with the same scanning configurations of the steel mesh and pig esophagus experiments (Fig 6.12 & 6.13). The imaged region of interest is given in Fig 6.14a and the corresponding hybrid volume imaged presented in Fig 6.14b in cylindrical coordinates. Hybrid Bscan polar OCT-OA plots extracted from Fig 6.14b are illustrated in Fig 6.14c. The polar plots indicate that the OA signals originate from the submucosa layer of tissue where blood vessels are located and the OCT signals

reveals structural information of the epithelium and submucosa layers. Fig 6.14d-f depict the enface maximum intensity projection (MIP) images of the OCT, OA and hybrid datasets. The OCT MIP illustrates the structural features of the tissue whereas the OA MIP reveals the vasculature network present in the submucosal layer. The additional information gained by overlaying the data from both modalities as illustrated in Fig 6.14 may improve accuracy of early detection of esophageal cancer.

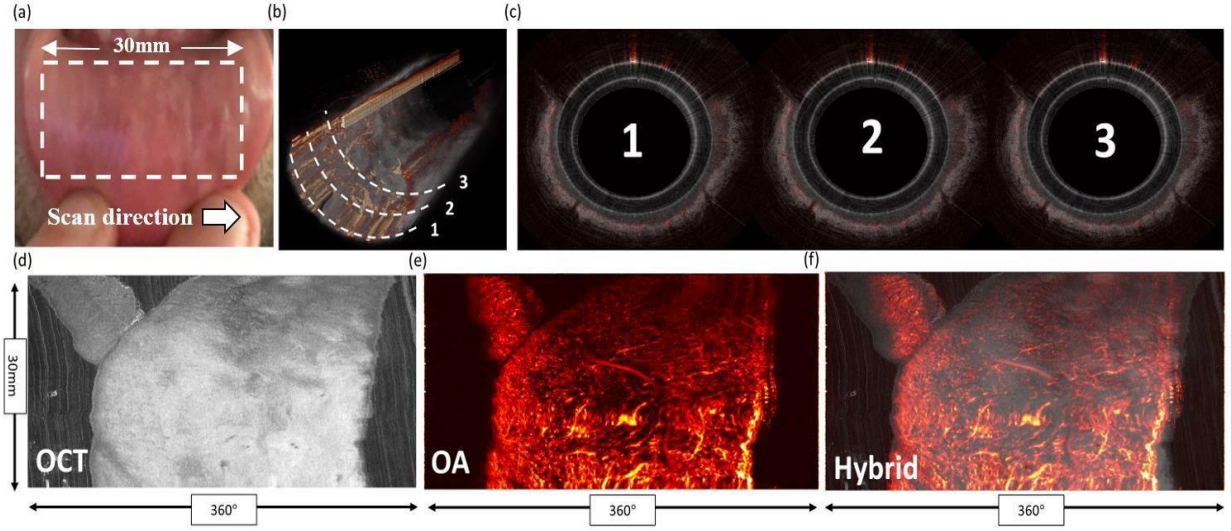

Figure 6.14: Hybrid synchronous OCT/OA helical volumetric scan over 30 mm longitudinal pull back distance at 30 Hz Bscan rate of in-vivo human mucosal tissue (a) Imaged region of interest human mucosal tissue. (b) 3D volumetric render of hybrid OCT-OA data (c) OCT/OA B scans acquired at arbitrary locations during the pullback scan. (d-f) Maximum intensity projection images of OCT, OA and hybrid respectively.

6.3.3 Discussion of partial capsule capability

Previous implementation of OCT-OA endoscopes has small fields of view, poor hybrid B scan frame rates, improper probe construction, and insufficient SNR for human esophageal imaging (section 2.3), despite their great potential for GI tract diagnostics. In this work a 12.5mm, 30Hz B scan rate 360° hybrid OCT-OA capsule endoscope was presented, setting the foundation for further imaging of the human esophageal tract. Video rate hybrid OCT-OA synchronous A scan rate was performed with a dual channel DAQ card, and a custom made double clad fiber coupler was able to efficiently couple and deliver OCT-OA light at 85kHz OCT/42.5kHz OA A-scan rate into a single double clad fiber with OCT escorted in the core and OA in the inner cladding.

The importance of combining OCT-OA imaging modalities was highlighted by imaging a hybrid suture phantom consisting of black and white sutures arranged in a Archimedean spiral, where all

sutures present were revealed only in the hybrid Bscans. Thus, the additional information gained when combining modalities could be useful when assessing dysplastic tissue or tumor morphology. In addition, imaging the hybrid phantom illustrated the intensity of both modalities is maximized just outside the capsule surface and falls exponentially with increasing depth. This is because both the OCT beam and OA transducer beam are focused just outside the capsule surface. Thus, moving away from the capsule surface not only does intensity (Fig 6.11e) reduce but so does lateral FWHM as depicted in Fig 6.11f. The reduction of lateral FWHM of OCT is not so important because penetration depth is limited to 1 mm and over this depth range the deterioration of lateral FWHM is minimal, although for OA the penetration depth could exceed 1mm thus image reconstruction in cylindrical coordinates which requires higher sampling density to improve overlap between adjacent A-scans will be required to improve the tomographic reconstruction and thereby lateral FWHM over extended depth.

A side from synchronously acquiring OCT-OA data, imaging at 30 Hz minimizes motion artifacts to allow real time surveillance of the human GI track and enable high resolution volumetric imaging as illustrated in the hybrid volumes (Fig 6.12) of the mesh acquired in 4.8 seconds over a pullback distance of 11.5mm where volumes acquired were $4\,mm \times 360° \times 11.5\,mm\,(\rho, \varphi, z)$ for each modality. The sampling resolution for OA was $3.75\,\mu m \times 0.24° \times 80\,\mu m\,(\rho, \varphi, z)$ and the sampling resolution for OCT was $2.5\,\mu m \times 0.12° \times 80\,\mu m\,(\rho, \varphi, z)$. Capturing large volumes of data presents the ability to survey large areas of the human GI which may be prone to progression such as Barrett's segments. The imaging potential of the hybrid endoscope was assessed by imaging ex-vivo pig esophagus embedded with black sutures mimicking blood vessels and in-vivo human mucosal tissue. The structural information tissue wall was captured by OCT capturing the epithelium and submucosa layers whereas the functional information of blood vasculature network was measured by optoacoustics. The hybrid overlay maximum intensity projections (Fig 6.13i & Fig 6.14f) demonstrate the additional information gained when imaging tissue thereby potentially improving diagnostic potential of esophageal cancer for better patient outcome.

The hybrid OCT-OA capsule presented here is a major step forward toward video-rate in-vivo endoscopy of the human GI tract. Future attempts will focus on improving sensitivity, imaging speed, and integrating a smaller hollow shaft motor inside the capsule in-vivo imaging. To improve sensitivity and imaging depth a transducer preamplification stage will be installed inside the transducer [49]. To improve imaging speed from 30Hz to 50Hz to match the semicapsule speed

, the mechanical sealing will be improved to prevent water leaking into the slip rings joints at rotational speeds exceeding 30Hz. A custom made miniature hollow shaft motor will also be developed and installed in the proximal end of the capsule to ensure the final design meets the size of commercially available white capsules which are usually less than 32mm long [121, 122]. Motor instability during imaging will be minimized via post-processing methods under investigation.

In summary, a 12.5 mm hybrid OCT-OA capsule endoscope prototype with a side viewing central aperture endoscopic transducer with integrated optics and slips rings allowed full field of view optoacoustic imaging at 30 Hz frame rate at 85kHz OCT/42.5kHz OA a-scan rate. The potential of our capsule was realized by capturing high resolution scans at unpresented rates in phantoms, ex-vivo pig esophagus and in-vivo human mucosal tissue by performing pull back helical scans to simultaneously acquire OCT-OA volumes. The studies presented herein showcase the translational potential of hybrid OCT-OA capsule endoscopy for delivering high resolution video rate 3D structural and functional information respectively of the human esophagus

6.4. Summary and discussion

Two capsule prototypes were presented in this chapter, a 16mm optoacoustic semicapsule and a 12.5mm hybrid OCT-OA partial capsule. The semicapsule demonstrated for the first time the ability to acquire optoacoustic data with a capsule endoscope at 50Hz. The prototypes lateral resolution was determined as a function of pulse repetition rate and B scan frame rate by an Archimedean spiral arranged with a pitch of 3 mm. Volumetric acquisition at 0.24Hz capturing 1790mm^3 voxels was demonstrated by imaging a stainless-steel mesh and penetration depth estimated at ~0.84mm in-vivo human esophagus by conducting a series of controlled experiments with intralipid concentrations employed as the coupling medium.

Building on the knowledge gained from the semicapsule prototype, a second generation prototype name the partial capsule prototype with a diameter of 12.5mm was built. The partial capsule demonstrated for the first time the ability to acquire hybrid OCT-OA endoscopy data synchronously at 30Hz frame rate. In addition, the partial capsule offered superior optoacoustic resolution and sensitivity compared to the semicapsule. Hybrid phantoms were constructed to illustrate the potential of hybrid imaging at 30 Hz. Imaging an ex-vivo pig esophagus and in-vivo human mucosal tissue, OCT was able to resolve esophageal wall layers and OA was able to

resolve the vasculature present within the wall. These studies demonstrate the translational potential of our purposed video rate hybrid endoscope to one-day image the human gastrointestinal tract

Chapter 7 OA endoscopy image reconstruction

The spherically focused detector employed in our endoscope only has high lateral/axial resolution at the focal length of the detector. When imaging the esophagus, the vasculature present within the lumen can only be resolved within the focal range of the transducer with features outside the focal zone appearing smeared. To improve resolution outside the focal zone, synthetic aperture image reconstruction algorithms can be applied to recover resolution beyond the focal zone. This approach referred to as the synthetic aperture focusing technique (SAFT) is based on performing several measurements in different positions and combing them to synthesize a large effective aperture as depicted Fig 7.1. Several overlapping measurements away from focus observed by the transducer are combined to yield a large synthetic aperture with a narrow beam and high lateral resolution. As the number of overlapping measurements increases, the reconstructed image more accurately approximates the object.

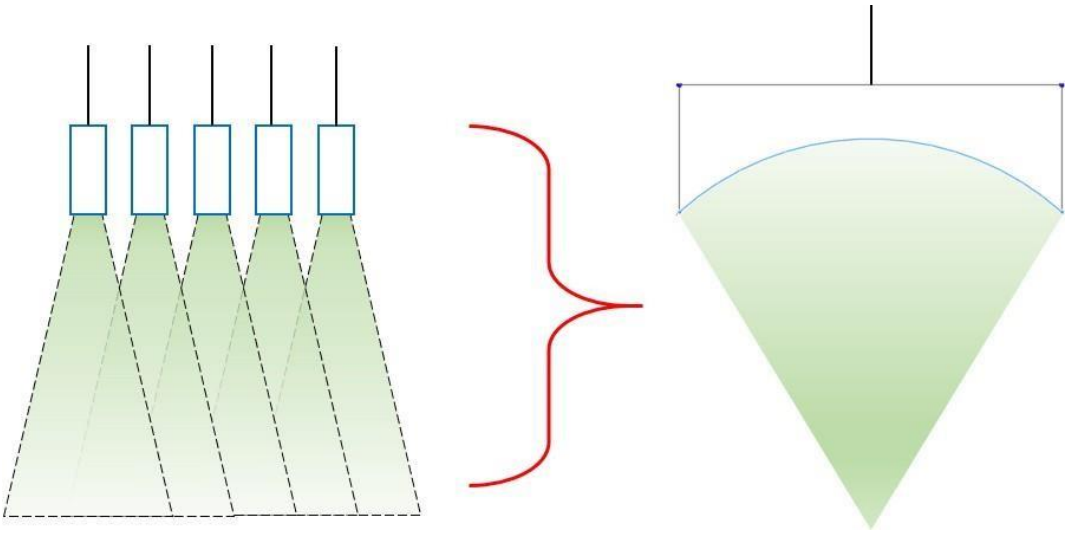

Figure. 7.1. illustration of the synthetic aperture focusing techniques where multiple overlapping measurements in space are combined to produce a large synthetic aperture, yielding high lateral resolution.

In this chapter we discuss a time domain (delay and sum) and frequency domain (phase shift migration) SAFT algorithm in cartesian coordinates and cylindrical coordinates. Each algorithm was initially implemented in MATLAB and applied to reconstruct 2D simulation and experimental datasets acquired in cartesian coordinates. These approaches were then extended tocylindrical coordinates for optoacoustic endoscopy image reconstruction and also applied to simulated and experimental datasets acquired in cylindrical geometry. Finally, the feasibility of employing these algorithms for real time optoacoustic endoscopy Bscan reconstruction was assessed.

7.1. Optoacoustic image reconstruction in cartesian coordinates

Scanning in cartesian coordinates, an optoacoustic probe acquires an A scan or optoacoustic signal at an equidistant spatial position dx with sampling interval dz defined by the DAQ system in depth along a linear line as shown in Figure 7.2. This configuration suitable for imaging skin tissue was previously demonstrated in RSOM [36]. To construct a B-scan image, the A-scan signals are arranged in a 2D array with each column representing an A-scan required at a unique spatial position dx along the scan direction. Extending to volumetric acquisition also referred to as a C-scan, the transducer probe is required to be mechanically raster scanned with equidistant spatial position intervals dx and dy. The depth interval dz in depth remains fixed by the sampling interval of the DAQ card. This scanning configuration was previously demonstrated in section 3.4. The acquired dataset being either B scan or C scan together with the corresponding scanning parameters are the main input variables required for SAFT to reconstruct the original source.

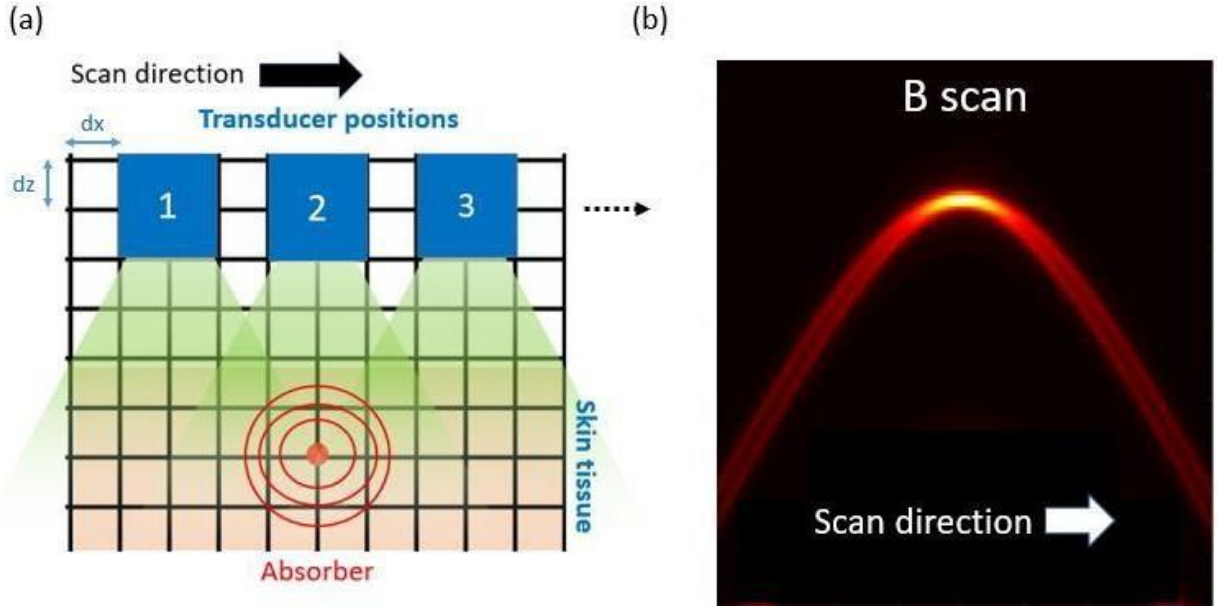

Figure. 7.2. Optoacoustic imaging configuration for reconstruction in cartesian coordinates. (a) An optoacoustic probe scans linearly along a point absorber where an A-scan is measured at each position with an equidistant spatial interval of dx and sampling interval of dz. (b) The raw optoacoustic B-scan image acquired of the point absorber is produced from the A scan signals measured at the different spatial position.

7.1.1 Delay and sum algorithm

SAFT can be synthesized in time domain by properly delaying and summing the A-scan signals recorded at each detector position. In our instance, because we employ a spherically focused transducer, the sensors focal point is considered as a virtual detector as illustrated in Figure 7.3.

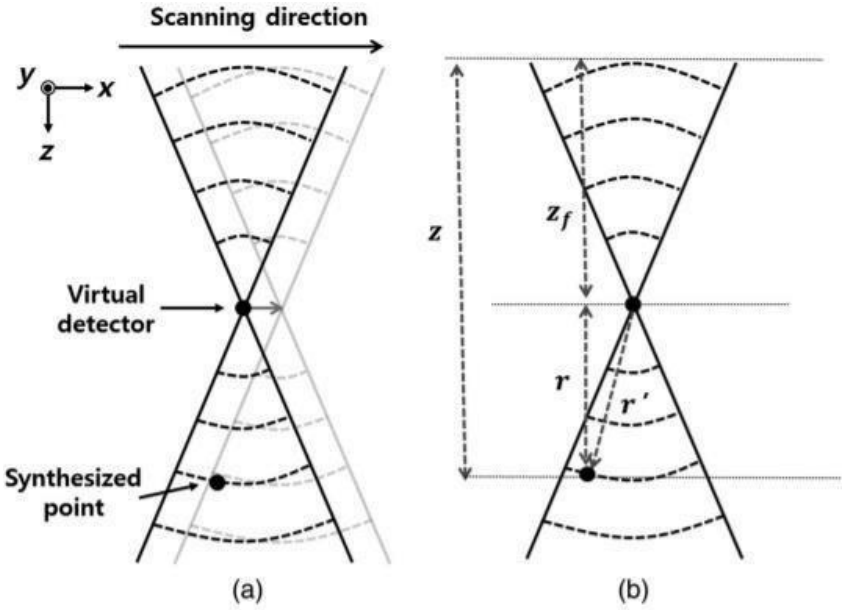

Figure. 7.3. Virtual detector concept for a spherically focused transducer (a) diagram of a virtual detector for SAFT. (b) Geometry to determine the time delay for SAFT, z is synthesized point, z_f is the position in depth of the virtual detector, r is axial distance and r' is the distance from the virtual point to the synthesized point z. Retrieved from [125]

During scanning, the sensitivity fields of the virtual detector's overlap at adjacent positions to form new optoacoustic A scans by combining delayed A scan signals that are adjusted to the virtual detector position at each scan following [125]:

$$S_{DAS}(x,z) = \sum_{i=i}^{N} s_{(i\cdot dx)}(t_{(x,z)} - \Delta t_{(i\cdot dx)}) \tag{7.1}$$

Where $S_{DAS}(x,z)$ is the synthesized SAFT plane generated by the delayed and summed procedure where, N is the number of A scans to be synthesized , $s_{i\cdot dx}(t_{(x,z)})$ is the received signal of the $i'th$ scan taken at an equidistant interval dx at time t, Δt_i is the time delay applied to the received signal of the $i'th$ scan at an equidistant interval dx to take into account the of the transducers focus by virtue of the virtual point detector . The time delay for a focused transducer is computed as:

$$\Delta t_{(i\cdot dx)} = sign(z - z_f)\,(\frac{r'}{c}) \tag{7.2}$$

Where z is the depth of the synthesized point, z_f is the depth of the virtual point , c is the speed of sound and r' is the distance from the virtual detector to the synthesized point.

The delay and sum algorithm on its own is prone to strong low frequency side lobes of recovered features resulting in poor lateral resolution. To improve quality, a coherence factor (CF) is

introduced as a weighting coefficient to suppress side lobes given by [125]:

$$CF = \frac{|\sum_{i=1}^{N} s_i(t)|^2}{N \sum_{i=1}^{N} |s_i(t)|^2} \tag{7.3}$$

Where $0 \leq CF \leq 1$. CF=1 means output of $S_{DAS}(t)$ should be maintained because signals are strongly coherent, CF=0 means output of $S_{DAS}(t)$ should be decreased because signals are strongly incoherent. Hence the CF weighted delay and sum algorithm is given by:

$$S_{DAS-CF}(x, z) = S_{DAS}(x, z) * CF \tag{7.4}$$

The B scan algorithm flow chart for the coherence weighted delay and sum algorithm in cartesian coordinates is presented in figure 7.4.

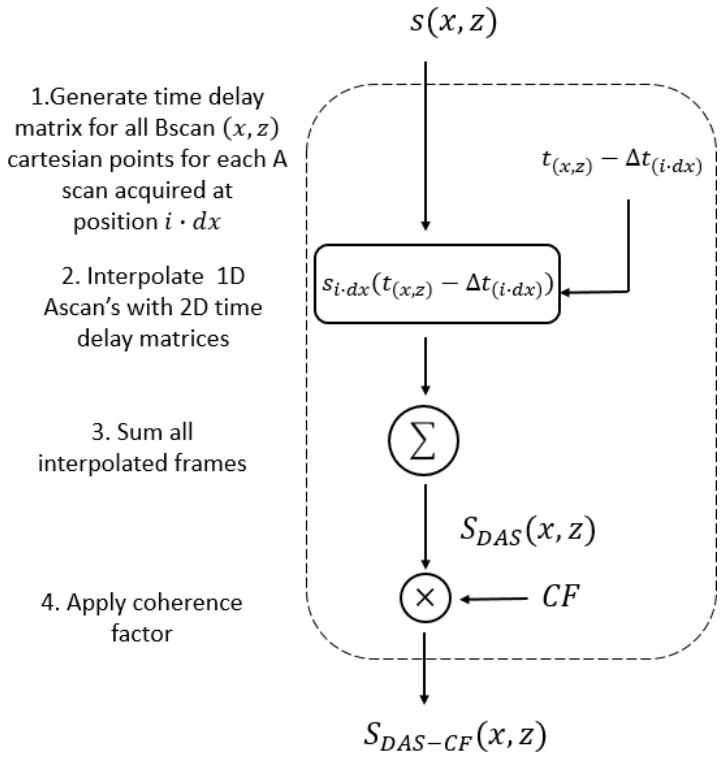

Figure. 7.4. Bscan coherence weighted delay and sum algorithm flow chart for cartesian coordinates. The input $s(x, z)$ is the raw Bscan acquired and the output $S_{DAS-CF}(x, z)$ is the SAFT reconstructed Bscan.

7.1.2 Phase shift migration

For an acoustically homogenous medium, if the measurement surface is planar, solutions to the wave equation in 2D geometry are in the form [127]:

$$s(t, x, z) \text{ a } e^{i(k_x + k_z z - \omega t)} \tag{7.5}$$

Where x, z, are the coordinates and k_x, k_z are the corresponding wavenumbers. The relationship between the wavenumbers and spatial frequency ω is given by:

$$\left(\frac{\omega}{c}\right)^2 = k_z^2 + k_x^2 \tag{7.6}$$

Solving the homogenous wave equation for t>=0 yields:

$$s(t,x,z) = \iint_{-\infty}^{\infty} A(\omega, k_x)\, e^{ik_z z} e^{ik_x x} e^{-i\omega t} dk_x d\omega \tag{7.7}$$

Where $A(\omega, k_x)$ is introduced as a complex amplitude . Note the term $A(\omega, k_x)e^{ik_z z}$ corresponds to the Fourier transform of $s(t,x,z)$. Hence, it can be shown that the forward Fourier transform $S(\omega, k_x, z)$ is given by [124]:

$$S(\omega, k_x, z) = \frac{1}{4\pi^2} \iint_{-\infty}^{\infty} s(t,x,z)\, e^{-ik_x x}\, e^{ik_x x}\, e^{i\omega t}\, dx dt \tag{7.8}$$

And equation 8.7 is the inverse Fourier transform:

$$s(t,x,z) = \iint_{-\infty}^{\infty} S(\omega, k_x, z)\; e^{ik_x x} e^{-i\omega t} dk_x d\omega \tag{7.9}$$

Assuming an arbitrary origin Z where the wave field the recorded is $S(\omega, k_x, Z)$, we can solve for $A(\omega, k_x)$ in Eqn 7.7 and obtain the expression:

$$S(\omega, k_x, z) = S(\omega, k_x, Z) e^{ik_z (z-Z)} \tag{7.10}$$

Hence in the Fourier domain the wave field can be extrapolated from Z to z via multiplication with the phase term $e^{ik_z(z-Z)}$. By inserting eqn 7.10 into eqn 7.7 an expression for the extrapolated wave field in obtained:

$$s(t,x,z) = \iint_{-\infty}^{\infty} S(\omega, k_x, Z)\, e^{ik_z (z-Z)} e^{ik_x x} e^{-i\omega t} dk_x d\omega \tag{7.11}$$

To obtain a focused image of the measured acoustic signal, t is set equal to 0 from the extrapolated wave field, therefore eqn 7.11 simply reduces to a simple integration over ω:

$$s(x,z) = \iint_{-\infty}^{\infty} S(\omega, k_x, Z)\, e^{ik_z (z-Z)} e^{ik_x x} e^{-i\omega t} dk_x d\omega \tag{7.12}$$

Eqn 7.12 produces a 1D focused line at a defined depth z. To reconstruct a SAFT Bscan eqn 7.12 needs to be iteratively applied for each depth z of the original raw B scan acquired and vertically concatenated.

$$s_{PSM}(x,z) = s_1(x,z) \frown s_2(x,z) \frown s_n(x,z) \tag{7.13}$$

Where n is the total number z depths.

This approach is called phase shift migration (PSM) and since this algorithm operates in the Fourier domain, it can process B scans significantly faster compared to the delay and sum algorithm which performs interpolation in the time domain. At the same time exponential computation for every depth z can be time consuming, to overcome this problem the exponential could be precomputed and applied recursively per loop for each depth inside a for loop to produce a focused B scan. The Bscan algorithm flow chart for the phase shift migration algorithm is presented in figure 7.5. Finally, for a focused transducer to apply the virtual detector concept from Fig 7.3 in frequency domain, the time delay to focus is compensated for by multiplication with the phase term $e^{\left(\frac{i\omega f}{c}\right)}$. Here c is the speed of sound and f is the transducers focal length.

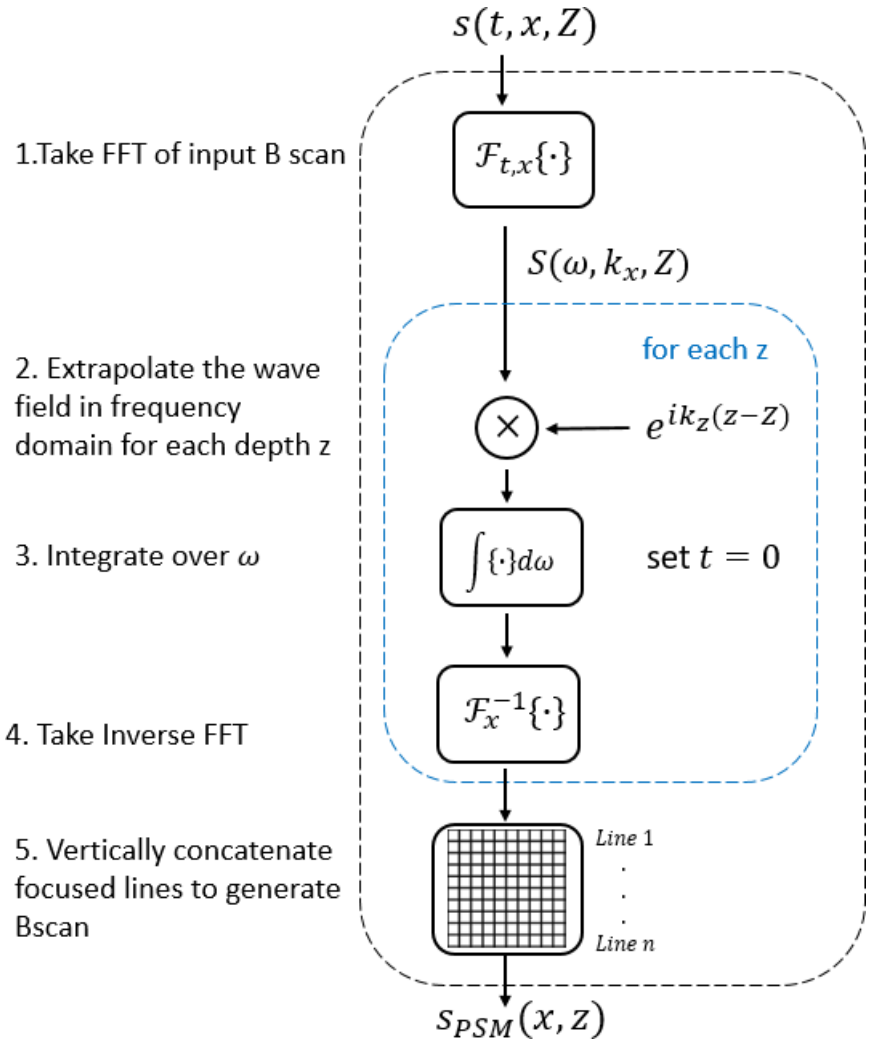

Figure. 7.5. Bscan phase shift migration algorithm flow chart. The input $s(t,x,Z)$ is the raw Bscan acquired and the output $s_{PSM}(x,z)$ is the reconstructed phase shift migration Bscan..

7.1.3 Cartesian Bscan image reconstruction with simulated data

The delay and sum and phase shift migration algorithms proposed in 7.1.1 and 7.1.2 were implemented in MATLAB. The Kwave acoustic toolbox was utilized to simulate a B scan consisting of a focused detector of similar dimensions as the HFM23 previously presented in Fig 3.8a imaging five-point sources with 5µm diameter and 500 µm spacing intervals beyond the focus in the axial direction. Simulation parameters included a sampling rate of 300MHz, speed of sound of 1500m/s and scan step interval of 5 µm in the x-direction. The simulated Kwave configuration and generated raw Bscan are illustrated in Figure 7.6.

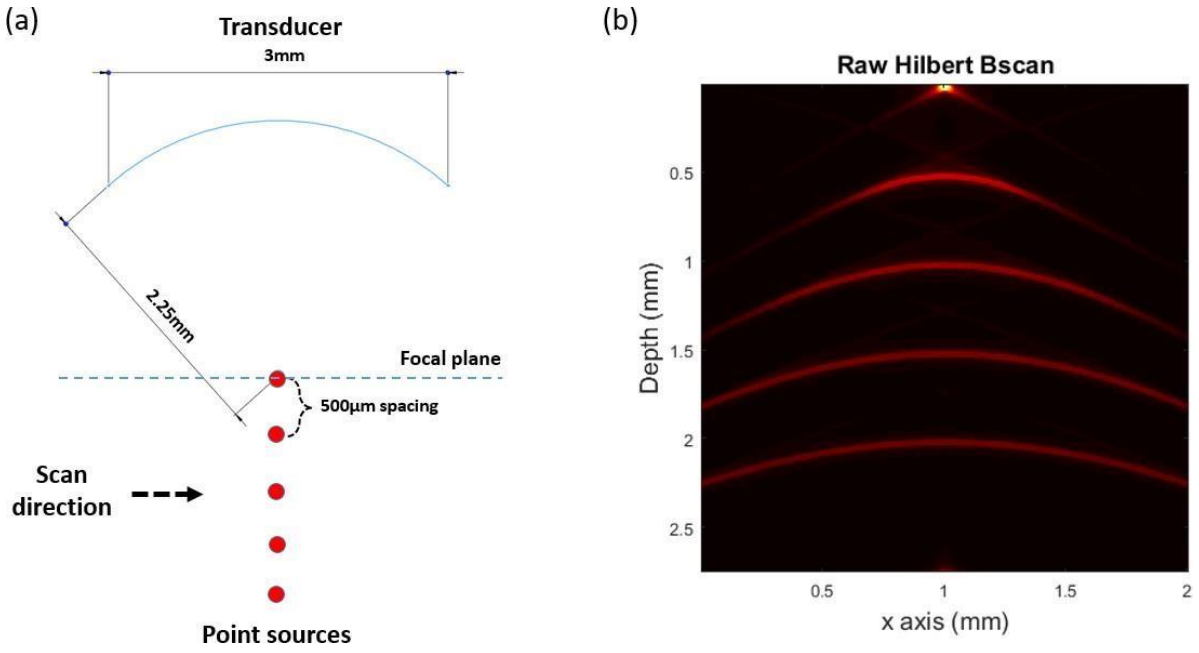

Figure. 7.6. Kwave simulation of HFM23 transducer linearly scanning over 5µm point sources placed at and beyond the transducer focus with 500 µm spacing intervals. (a) The simulated scanning configuration (b) The raw B scan acquired following the simulation scan where Depth=0 mm corresponds to the focal length of the transducer.

Applying the delay and sum with coherence weighting (DAS-CF) and phase shift migration (PSM) algorithms on the raw Bscan in Fig 7.6b we obtained the reconstructed SAFT Bscans depicted in Fig 7.7a and Fig 7.7b respectively. The computational time required to reconstruct the Bscan in Fig 7.6b was 7.2 seconds with the DAS-CF and 0.12 seconds with PSM algorithm. As PSM performs interpolation in the frequency domain rather than the time domain the algorithm is significantly faster than the DAS-CF algorithm. From the DAS-CF reconstructed Bscan SNR increases as the acoustic sources moves away from the virtual point or focus of the transducer. This is because there is more overlap of acoustic signals away from the focus and when delayed signals are combined the acoustic sources are more correctly estimated. As a result of the lack of

overlap at focus between adjacent A scans, the point source at focus is not visible in this case. From the reconstructed DAS-CF Bscan one could suggest to improve reconstruction quality it would be best to place the acoustic source away from the focus, although in reality the acoustic source should be placed place ~500µm away from focus. This is because transducer sensitivity significantly degrades away from focus and our simulation model does not take into account acoustic attenuation within the coupling medium which flattens and broadens the original high frequency optotoacoustic signal as it propagates though an absorbing media with high frequencies more readily absorbed than lower frequencies following the power law. Alternatively, with PSM reconstruction SNR decreases moving away from focus which corresponds to the signal strength of the raw signals measured. Fig 7.7c provide measurements of the FWHM of the point sources in the axial and lateral resolutions. The axial resolutions measured with both algorithms range between 40-45µm over 2mm depth. Lateral resolution is observed to degrade as the acoustic source moves away from the focus with both algorithms, though the DAS-CF algorithm seems to resolve the point source more accurately compared to the PSM algorithm.

(a)

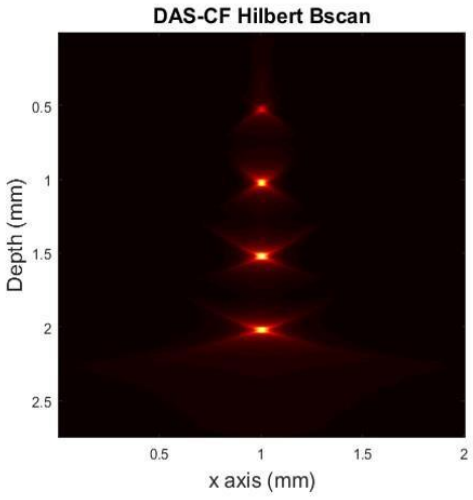

(b)

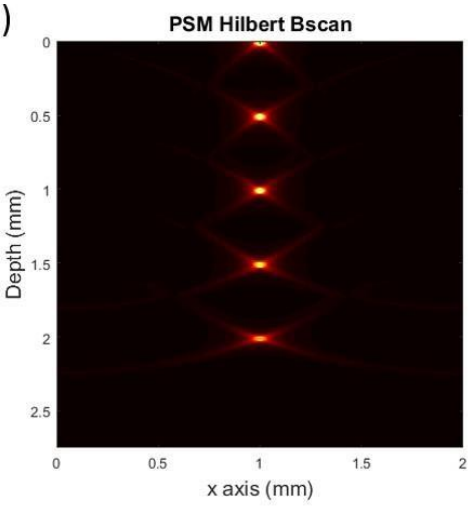

(c)

Point Source Number	DAS–CF Bscan		PSM Bscan	
	Axial(µm)	Lateral (µm)	Axial (µm)	Lateral (µm)
1	NA	NA	43.8	57
2	44.4	38.3	43	57.7
3	44.8	38	43.2	57.6
4	44	47	41.5	69
5	42.7	62	40	87.4

Figure. 7.7. Bscan Delay and sum (DAS) and Phase shift migration (PSM) image reconstructions (a) DAS Bscan reconstruction with coherence factor (CF) (b) PSM Bscan reconstruction (c) Lateral and axial FWHM values of the reconstructed point sources.

7.1.4 Cartesian Bscan image reconstruction with experimental data

Both algorithms were next assessed with experimental Bscan data acquired in cartesian coordinates. The experimental configuration is depicted in 7.8a, here a line scan is performed to image five 50µm sutures arranged in a diagonal using the HFM36 transducer with the custom made grin lens depicted in Figure 5.11a. Scanning was performed using the system in section 3.4 with a lateral sampling interval of 10µm. Figure 7.8b presents the raw Hilbert Bscan acquired, the grin lens interrogation beam limits the viewing window of acoustic signals measured by the transducer as it travels over the point absorber along the scanning direction. If the interrogation spot size were increased the measured Bscan would be similar to the simulated Bscan in Figure 7.6b where the wings of the hyperbolic function would appear. The Reconstructed PSM Bscan shown in Fig 7.8c illustrates SNR is reduced moving away from focus. In contrast the reconstructed DAS-CF B scan in Fig 7.8d shows SNR reaches a maximum at point source 3, moving towards focus reduces the overlap between adjacent A-scans thereby reducing SNR and moving towards point 5 from point 3 reduces SNR because the transducer itself becomes less sensitive moving away from focus.

The FWHM axial and lateral measurements of reconstructed acoustic sources in Fig 7.8e show that axial resolution remains approximately the same over the 1.5mm depth between point sources and lateral resolution reduces moving away from the focus of the transducer. The exception being the 91µm axial resolution measured at point 1 source with the DAS-CF, this is because this point source is very close to the focus where the DAS-CF algorithm performs poorly as previously discussed in 7.1.3.

To enhance recovered lateral resolution of the reconstructed Bscans, more A scans could be acquired by reducing the lateral sampling interval from dx=10µm. Additionally, the illumination spot size could also be increased to measure more off-axis A scans such that more of the hyperbolic shape appears in the measured raw Bscan and the focal length of the transducer also reduced to increase the numerical aperture. All three methods increase the number of A scans present in the measured B scan to improve the interpolation process of each algorithm and more accurately estimate the original source.

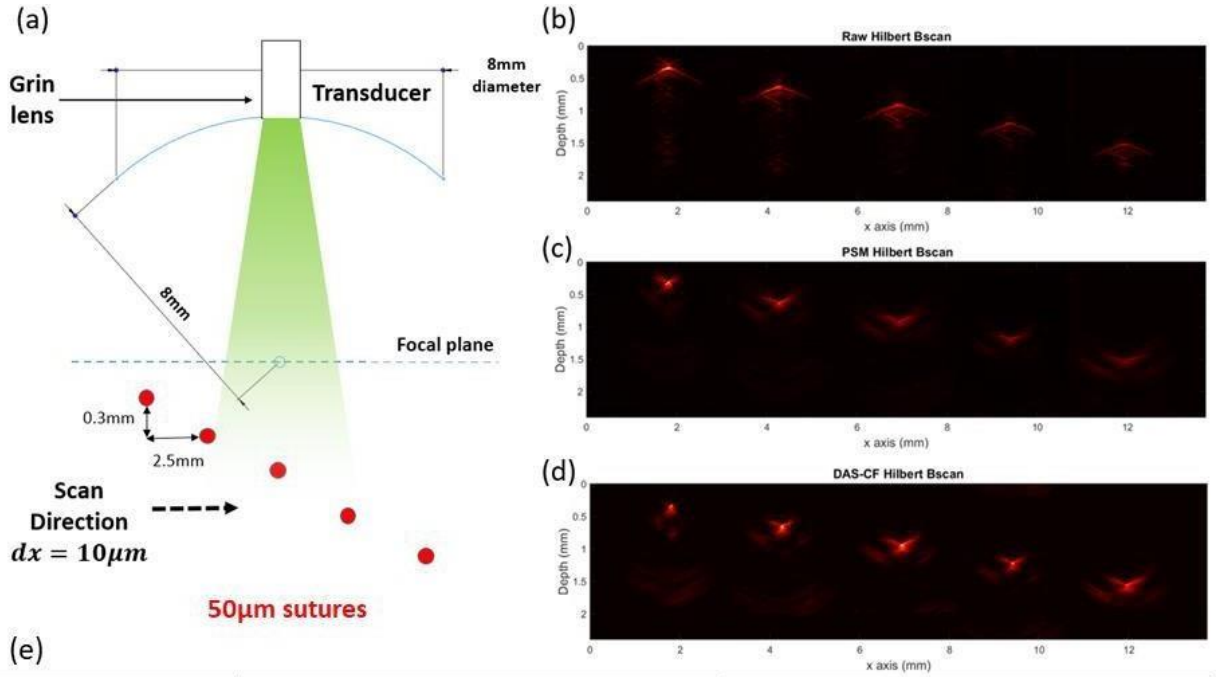

(e)

Point Source Number	DAS–CF Bscan		PSM Bscan	
	Axial(µm)	Lateral (µm)	Axial (µm)	Lateral (µm)
1	91	50	32	44
2	37	58	31	59
3	36	67	32	61
4	38	78	34	85
5	37	109	35	158

Figure. 7.8. Experimental Bscan measurement and reconstruction in cartesian coordinates (a) The experiment configuration of measuring five 50µm sutures arranged in a diagonal in the axial direction with the HFM36 transducer and scanning performed with the raster scanning setup in 3.4. The lateral sampling distance between adjacent A-scans is dx=10µm (b) The raw Hilbert B scan measured where depth=0 mm corresponds to the focal length of the transducer. (c & d) correspond to the PSM and DAS-CF reconstructed Bscans generated. (e) Lateral and Axial FWHM values of the reconstructed acoustic sources.

7.2. Optoacoustic image reconstruction in cylindrical coordinates

Imaging the cylindrical esophagus surface with our proposed design in chapter 6 requires the transducer rotate and measure the optoacoustic echo generated from the lumen wall travelling inwards as presented in Figure 7.9. A scans acquired in this configuration have a constant axial sampling interval dr in depth and a constant angular sampling resolution dθ. Although the lateral displacement in dr between adjacent A scans is reduced with increasing depth. A B-scan is produced following a 360º revolution where each column in the 2D array of A scans measured represents a unique equidistant angular sampling interval multiple of dθ over the rotational scan direction. The reconstruction algorithms presented for cartesian coordinates in section 7.1 are modified in this section for cylindrical coordinates and the feasibility of applying these algorithms at 50Hz video rate for our hybrid endoscope is assessed.

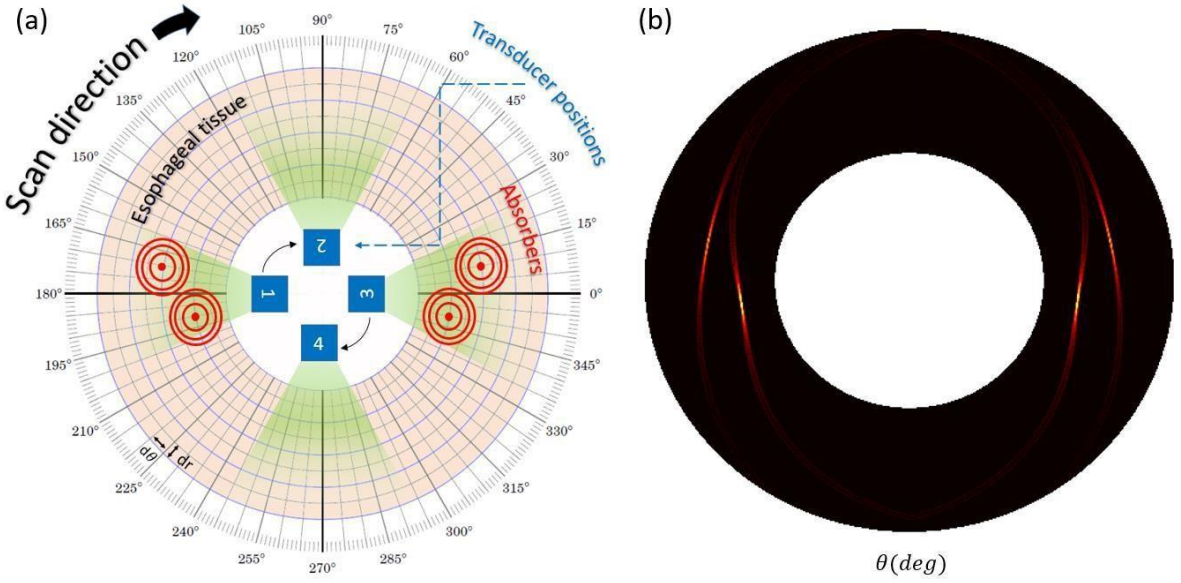

Figure. 7.9. Optoacoustic imaging configuration for reconstruction in cylindrical coordinates. (a) An optoacoustic probe scans rotationally around esophageal tissue with point absorbers embedded. The dr depth sampling interval between adjacent A-scan is constant whereas the lateral displacement between a fixed angular sampling interval dθ degrades with increasing depth. (b) The raw cylindrical optoacoustic B scan image acquired of the point absorbers is produced from the A scan signals measured at the different angular positions over 360 degrees.

7.2.1 Cylindrical delay and sum

Akin to synthesizing SAFT in the time domain with cartesian coordinates, A scan signals acquired in cylindrical coordinates are appropriately delayed and summed at each angular position.

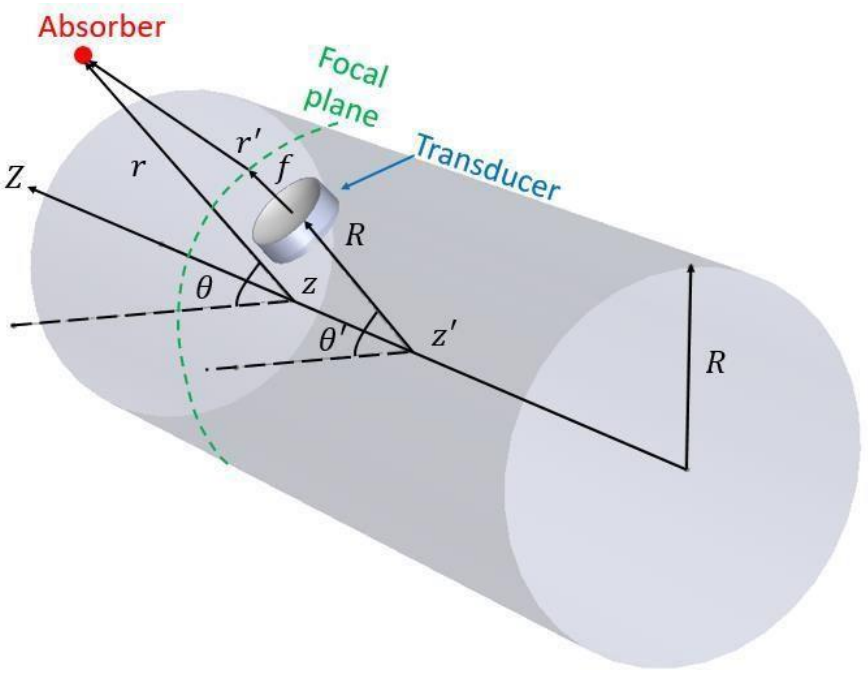

Figure 7.10 3D cylindrical scanning configuration. R is the distance from the rotational axis to the transducer's active element facing the cylindrical surface and f is the focal length of the transducer. The cylindrical coordinates (R, θ', z') represent coordinates of the transducer position and coordinates (r, θ, z) represents absorber position with respect to the rotational axis. r' is the distance between the absorber and transducer with respect to each other.

Hence, the cylindrical delay and sum algorithm is given by:

$$S_{CDAS}(r, \theta) = \sum_{i=i}^{N} s_{(i \cdot d\theta)}(t_{(r,\theta)} - \Delta t_{(i \cdot d\theta)}) \tag{7.14}$$

Where $S_{CDAS}(r, \theta)$ is the synthesized SAFT cylindrical plane generated by the delayed and summed procedure where, N is the number of A scans to be synthesized , $s_{i \cdot d\theta}(t_{(r,\theta)})$ is the received signal of the $i'th$ scan taken at an equidistant angular interval $d\theta$ at time t, $\Delta t_{(i \cdot d\theta)}$ is the time delay applied to the received signal of the $i'th$ scan at an equidistant interval $d\theta$ to take into account the of the transducers focus by virtue of the virtual point detector . In cylindrical coordinates following the illustration of Fig 7.10 the time delay for a focused transducer is given by:

$$\Delta t_{(i \cdot d\theta)} = sign(r - (R + f)) \left(\frac{r'}{c}\right) \tag{7.15}$$

Where R is the distance of the transducer from the rotational axis, f is the focal length of the transducer, c is the speed of sound , r' is the distance from the virtual detector or transducer focus to the synthesized point and r is the depth of the synthesized point.

The B-scan algorithm flow chart for the coherence weighted delay and sum algorithm in cylindrical coordinates is presented in Fig 7.11. When comparing this flow chart to the delay and sum algorithm in cartesian coordinates in Fig 7.4 the only difference is the first step of the algorithm where the time delay matrices generated are in polar coordinates to match the coordinates of the input B-scan $s(r, \theta)$ prior to synthesizing new A scans during interpolation. Following this step, the interpolated frames are summed, and the coherence factor applied to suppress side lobes and improve lateral resolution resulting in the reconstructed SAFT B-scan $S_{CDAS-CF}(r, \theta)$.

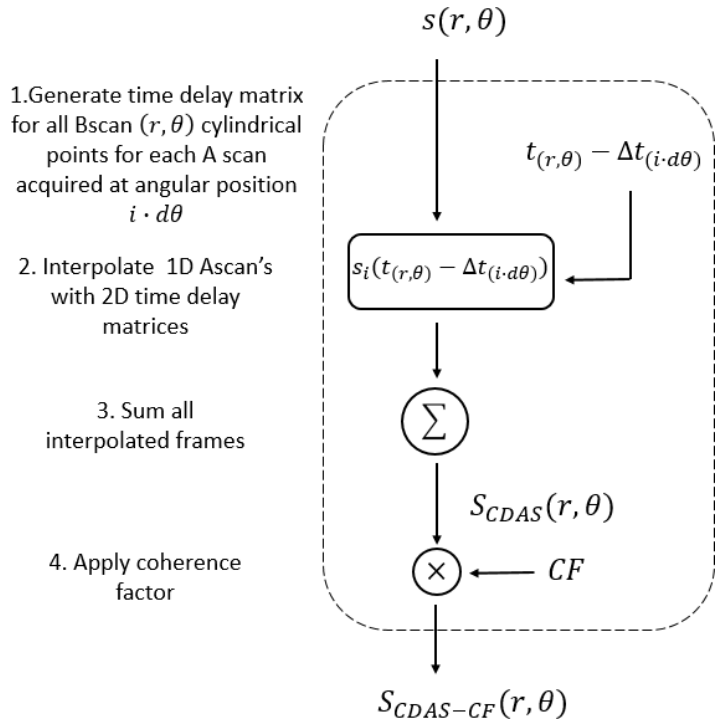

Figure. 7.11. B scan coherence weighted delay and sum algorithm flow chart for cylindrical coordinates. The input $s\ (r, \theta)$ is the raw B scan acquired in cylindrical coordinates and the output $S_{CDAS-CF}(r, \theta)$ is the reconstructed B scan.

7.2.2 Cylindrical phase shift migration

Solutions to the wave equation in cylindrical coordinates are of the form [128]:

$$s(t, \theta, z, r) \text{ a } \underset{n}{H}^{1,2}(k_r r) e^{\pm in\theta} e^{\pm k_z z} e^{\pm i\omega t} \tag{7.16}$$

Where $H_n^{1,2}(k_r r)$ represents a Hankel function of the first or second order n , k_r and k_z are the wave numbers for the r and z coordinates and ω is the angular frequency. The relationship between wavenumbers and angular frequency is given by the dispersion relation:

$$k_r = \sqrt{\left(\frac{\omega}{c}\right)^2 - k_z^2} \tag{7.17}$$

In our imaging configuration presented in Fig 7.10 the transducer is placed at a distance space $r = R$ from the center of rotation measuring optoacoustic waves generated in the space $r > R$. Hence only waves travelling inwards are measured which correspond to the second order Hankel function whereas the first order Hankel function represents outwards travelling waves. Under these conditions the general solution to the wave equation in cylindrical coordinates is given by [128]:

$$s(t, \theta, z, r) = \sum_{n=-\infty}^{\infty} e^{in\theta} \iint_{-\infty}^{\infty} A_n(\omega, k_z)\, H_n^2(k_r r) e^{ik_z z} e^{-i\omega t} dk_z d\omega \tag{7.18}$$

Where $A_n(\omega, k_z)$ is introduced as a complex amplitude.

The optoacoustic signals measured at the plane $r = R$ denoted by $s(t, \theta, z, R)$ in the Fourier domain is given by :

$$S_n(\omega, k_z, R) = \left(\frac{1}{2\pi}\right)^3 \int_0^{2\pi} d\theta \iint_{-\infty}^{\infty} s(t, \theta, z, R)\, e^{-in\theta} e^{-ik_z z} e^{i\omega t} dz dt \tag{7.19}$$

And the corresponding inverse Fourier transform is:

$$s(t, \theta, z, R) = \sum_{n=-\infty}^{\infty} e^{in\theta} \iint_{-\infty}^{\infty} S_n(\omega, k_z, R)\, e^{ik_z z} e^{-i\omega t} dk_z d\omega \tag{7.20}$$

From equations 7.18 and 7.20 we obtain an expression for $A_n(k_z, \omega)$:

$$S_n(\omega, k_z, R) = A_n(\omega, k_z) H_n^2(k_r R) \rightarrow A_n(\omega, k_z) = \frac{S_n(\omega, k_z, R)}{H_n^2(k_r R)} \tag{7.21}$$

Using this relation, we can eliminate A_n from equation 7.18 to obtain:

$$s(t, \theta, z, r) = \sum_{n=-\infty}^{n=\infty} e^{in\theta} \frac{1}{(2\pi)^2} \int_{-\infty}^{\infty} \int_{-\infty}^{\infty} S_n(\omega, k_z, R)\, \frac{H_n^2(k_r r)}{H_n^2(k_r R)}\, e^{ik_z z} e^{-i\omega t} dk_z d\omega \tag{7.22}$$

Eqn 7.22 states that we can perform wave field extrapolation from R to r in the Fourier domain by multiplication with the transfer function G:

$$G(\omega, n, k_z, r, R, c) = \frac{H_n^2(k_r r)}{H_n^2(k_r R)} = \frac{H_n^2\left(r\sqrt{\left(\frac{\omega}{c}\right)^2 - k_z^2}\right)}{H_n^2\left(R\sqrt{\left(\frac{\omega}{c}\right)^2 - k_z^2}\right)} \tag{7.23}$$

Calculating the Hankel functions in Eqn 7.23 are computationally expensive hindering wavefield extrapolation. Alternatively, Huan et al developed an approximate solution for the transducer function G by using the Rayleigh-Sommerfeld diffraction formula [129]:

$$G(\omega, n, k_z, r, R, c) \sim \frac{\sqrt{r}}{R} e^{(i(r-R)\sqrt{\frac{\omega^2}{c^2} - \frac{n^2}{Rr} - k_z^2})} \tag{7.24}$$

Following the scanning configuration depicted in 7.10 , where the transducer position is (R, θ', z') , absorber position is (r, θ, z) and the distance between the absorber and transducer r' is given by:

$$r' = \sqrt{R^2 + r^2 - 2Rr\cos(\theta - \theta') + (z - z')^2} \tag{7.25}$$

Eqn 7.24 is valid when the term cos $(\theta - \theta')$ which corresponds to the angular displacement between the transducer and absorber in Eqn 7.25 can be approximated as $1 - (\theta - \theta')^2/2$. This is valid when the transducer has a narrow beam width. An in-depth analysis of the accuracy of Eqn 7.24 is performed in Haun et al [129].

A focused image plane at position r can be acquired by extrapolating the wave field from R to r by multiplication with the transfer function G and evaluating it at t=0 reduces Eqn 7.22 to a simple integral over ω in the Fourier domain. Inverse Fourier transformation following integration to spatial coordinates results in the focused image plane $s_p(t = 0, \theta, z, r)$.

$$s_p(t = 0, \theta, z, r) = \sum_{n=-\infty}^{n=\infty} e^{in\varphi} \frac{1}{(2\pi)^2} \int_{-\infty}^{\infty} \int_{-\infty}^{\infty} S_n(R, k_z, \omega) G(\omega, n, k_z, r, R, c)\, e^{ik_z z} dk_z d\omega \tag{7.26}$$

Equation 7.26 can then be used to iteratively build a 3D focused over range of r values with each focused plane in r being vertically concatenated. This procedure referred to as cylindrical phase shift migration

$$s_{CPSM}(\theta, z, r) = s_{p_1}(\theta, z, r) \frown s_{p_2}(\theta, z, r) \frown s_{p_m}(\theta, z, r) \tag{7.27}$$

Where m is the total number of r steps in depth.

The 2D or Bscan algorithm flow chart for the cylindrical phase shift migration algorithm is presented in figure 7.12.

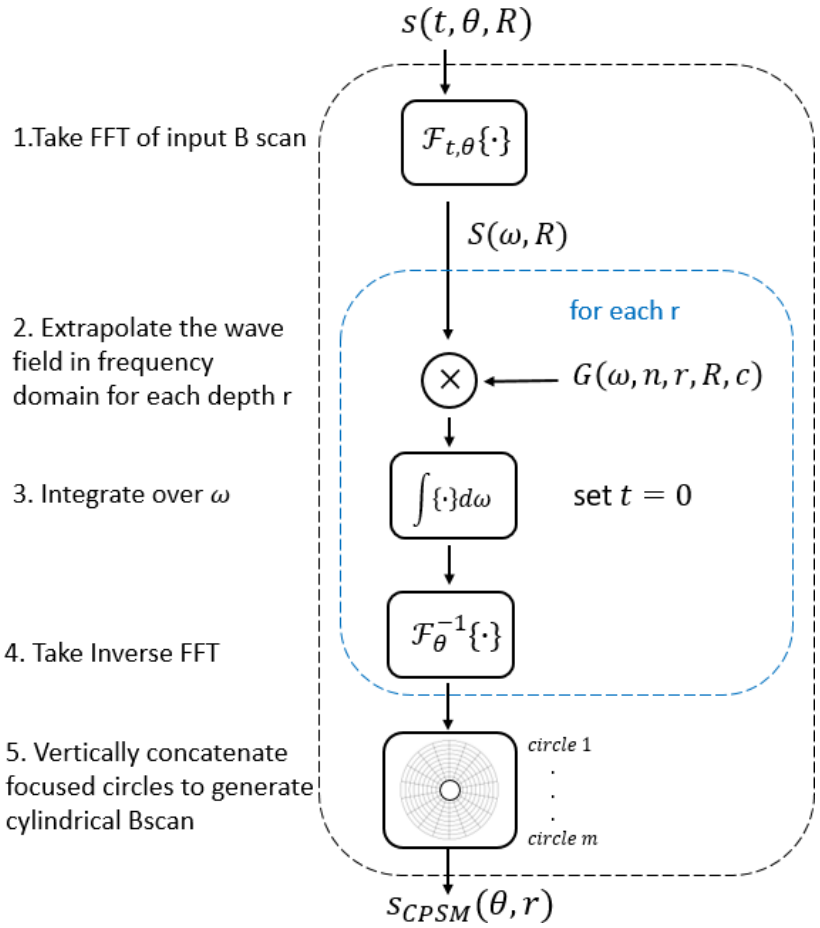

Figure. 7.12. Bscan cylindrical phase shift migration algorithm flow chart. The input $s(t,\theta,R)$ is the raw Bscan acquired at range R from the center of rotation and the output $s_{CPSM}(\theta,r)$ is the reconstructed cylindrical phase shift migration Bscan wavefield interpolated from R to r .

7.2.3 Cylindrical Bscan image reconstruction with simulated data

The cylindrical delay and sum and cylindrical phase shift migration algorithms proposed in 7.2.1 and 7.2.2 were implemented in MATLAB and the Kwave toolbox used to generate a simulated B-scan of a transducer rotating over a 180-degree angle around the central axis and measuring the echo of point sources travelling inwards. Because Kwave does not support cylindrical coordinates to accurately map rotation of a transducer following an arc trajectory, a high resolution 10mmx10mm cartesian grid simulated with 2µm spacing was generated. expanding the grid size or improving grid resolution further drastically increases computational scanning duration. Hence, considering size of the transducer to be simulated and the distance between the transducer and center of rotation R, we decided not to simulate HFM23 transducer previously generated in 7.1.3. In this instance a planar transducer with diameter 0.2mm was generated and the distance between transducer to center of rotation was set to R=2mm. The simulation sampling rate was

200MHz, speed of sound set to c=1500m/s and angular step scan interval between 0º to 180º was 1º. Four point absorbers of size 50 µm were placed at random angular positions between r=1mm to r=6mm as illustrated in Fig 7.13.

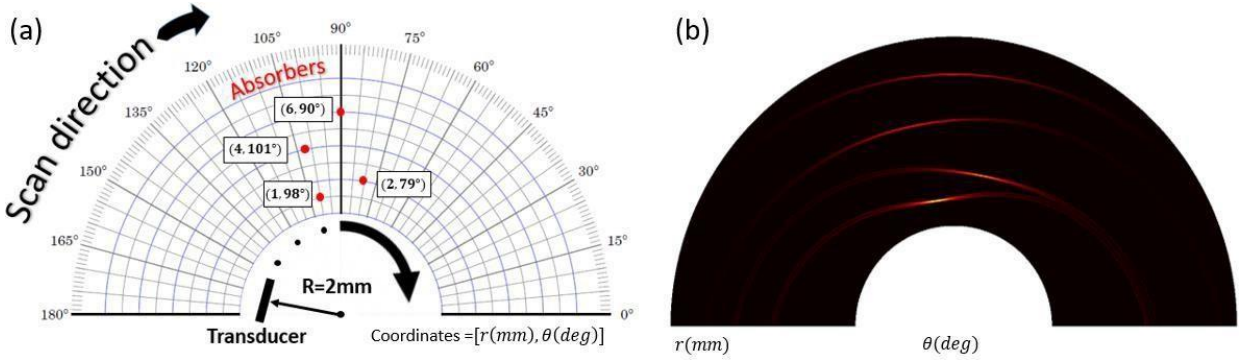

Figure. 7.13. 2D 180º Kwave simulation of an 0.2mm planar transducer cylindrically scanning over four 50µm point sources placed at random angular positions between r=1mm to r=6 mm. (a) The simulated configuration scanning over a 180º arc with an angular step of 1º (b) The raw Hilbert B scan acquired following the simulation scan trajectory in (a).

Applying the cylindrical delay and sum with coherence weighting (CDAS-CF) and cylindrical phase shift migration algorithms (CPSM) on the raw B scan in Fig 7.13b we obtained the reconstructed Bscans depicted in Fig 7.14a and Fig 7.14b respectively. The computational time required to reconstruct the B scan was 3.2 seconds with the CPSM algorithm and 2.7 seconds with the CDAS algorithm. Conversely in cartesian coordinates in 7.1.3 the phase shift migration algorithm was faster than the delay and sum. This is because the wavefield extrapolation transfer function in cartesian coordinates is a simpler arithmetic to perform per step in depth compared to the derived G transfer function in cylindrical coordinates given by Eqn 7.24. In both instances the SNR decreases moving away from the transducer. Interestingly in cartesian coordinates the DAS algorithm illustrated SNR improved moving away from the transducer because there was more overlap of acoustics signals between adjacent A scans synthesized. The inverse is observed in cylindrical coordinates, and this is because the acoustic sources arranged are at least 1mm away from the transducer where there is sufficient overlap between adjacent A scans to recover the original source with point sources beyond r=1mm experiencing additional acoustic attenuation and thereby resulting in a lower SNR.

Figure 7.14c presents the FWHM lateral and axial resolution measurements of the reconstructed point source. Moving away from the transducer the recovered lateral resolution reduces with both algorithms as the arc interval between adjacent A-scans increases and signal strength reduces, although the CDAS-CF algorithm recovers the sources with higher accuracy than the CPSM

algorithm. This could be attributed as a result of the additional coherence weighting factor applied to the CDAS algorithm to suppress side lobes. Excluding the exception where the axial resolution of 126μm is observed at r=1mm with the CDAS-CF algorithm, the axial resolutions remain much the same over the depth range r=1mm to r=6mm.

(a)

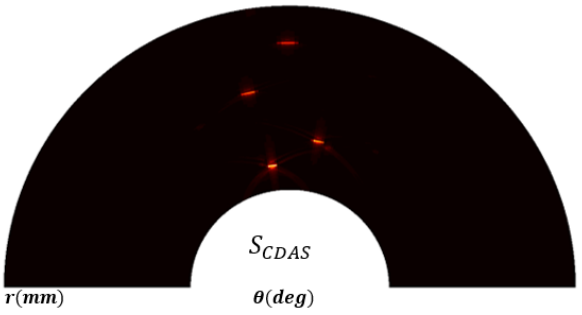

(b)

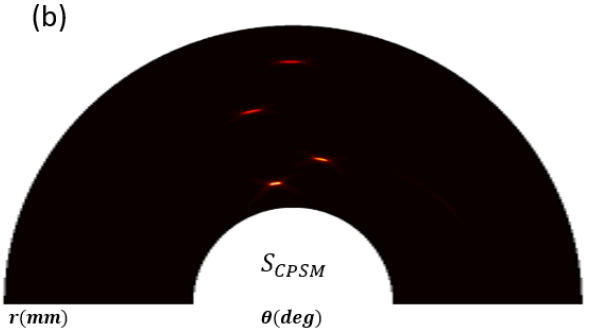

(c)

Point Source Number	CDAS–CF Bscan		CPSM Bscan	
	Axial(μm)	Lateral (μm)	Axial (μm)	Lateral (μm)
1	126	216	69.5	250
2	60	278	74	331
3	56	425	75	525
4	61	599	75	686

Figure. 7.14. Cylindrical Delay and sum with coherence weighting (CDAS-CF) and Cylindrical Phase shift migration (CPSM) Bscan image reconstructions (a) CDAS-CF B scan reconstruction with coherence factor (CF) (b) CPSM B scan reconstruction (c) Lateral and Axial FWHM values of the reconstructed point sources in cylindrical coordinates where point 1 is closest to the transducer and point 4 is furthest from the transducer

7.2.4 Cylindrical Bscan image reconstruction with experimental data

Subsequently, the cylindrical reconstruction algorithms were applied to experimental data acquired in cylindrical coordinates. Here the HFM36 transducer with the custom-made grin lens from figure 7.11a was carefully mounted to a 360° rotational Thorlabs step scanner model: K10CR1. The experimental configuration is illustrated in figure 7.15a where a rotational scan is performed over +30° to -30° with step size of 0.05° to image five 50μm sutures arranged in a diagonal in the axial direction. The raw Hilbert Bscan measured is presented in Fig 7.15b in cylindrical coordinates where $r = 0$ corresponds to the focal plane of the HFM36 transducer. The visible segment of the hyperbolic shape is limited by the interrogation spot size determine by the grin lens. If the interrogation spot size were increased more of the hyperbolic shape would be observable as demonstrated in Fig 7.13b and overall reconstruction improved. The reconstructed CDAS-CF Hilbert Bscan represented by Figure 7.15c displays SNR of the reconstructed image

increases as the acoustic source generated moves away from the focal plane of the transducer, reaching a maximum SNR at point source 3 located approximately 1mm away from focus and then decreases as the acoustic attenuation beyond this limit overwhelms the algorithm as a consequence of reduced transducer sensitivity. In contrast the CPSM reconstructed B scan in Figure 7.15d indicates the SNR decreases in a linear fashion away from the focal plane.

The FWHM axial and lateral measurements of reconstructed point sources in Fig 7.15e show that axial resolution reduces by approximately 10 μm and lateral resolution reduces from 42μm to approximately 100μm over the 1.5mm depth beyond the transducers focal plane. To reduce the low frequency signals surrounding the reconstructed point sources in Figs 7.15c and 7.15d the step angle could be reduced from 0.05º which corresponds to an arc length of 12μm at the focal plane and 13 μm along the plane of point source 5 to improve the algorithms A-scan interpolation operation. The illumination source spot size could also be increased and focal distance of the transducer reduced to measure a larger segment of the hyperbolic function in the raw B-scan and improve reconstruction. Finally, the 2D algorithms presented could be extended to 3D for helical pullback scanning and thereby more accurately estimate the acoustic sources as a result of additional A scans between adjacent Bscans utilized during each algorithms interpolation process.

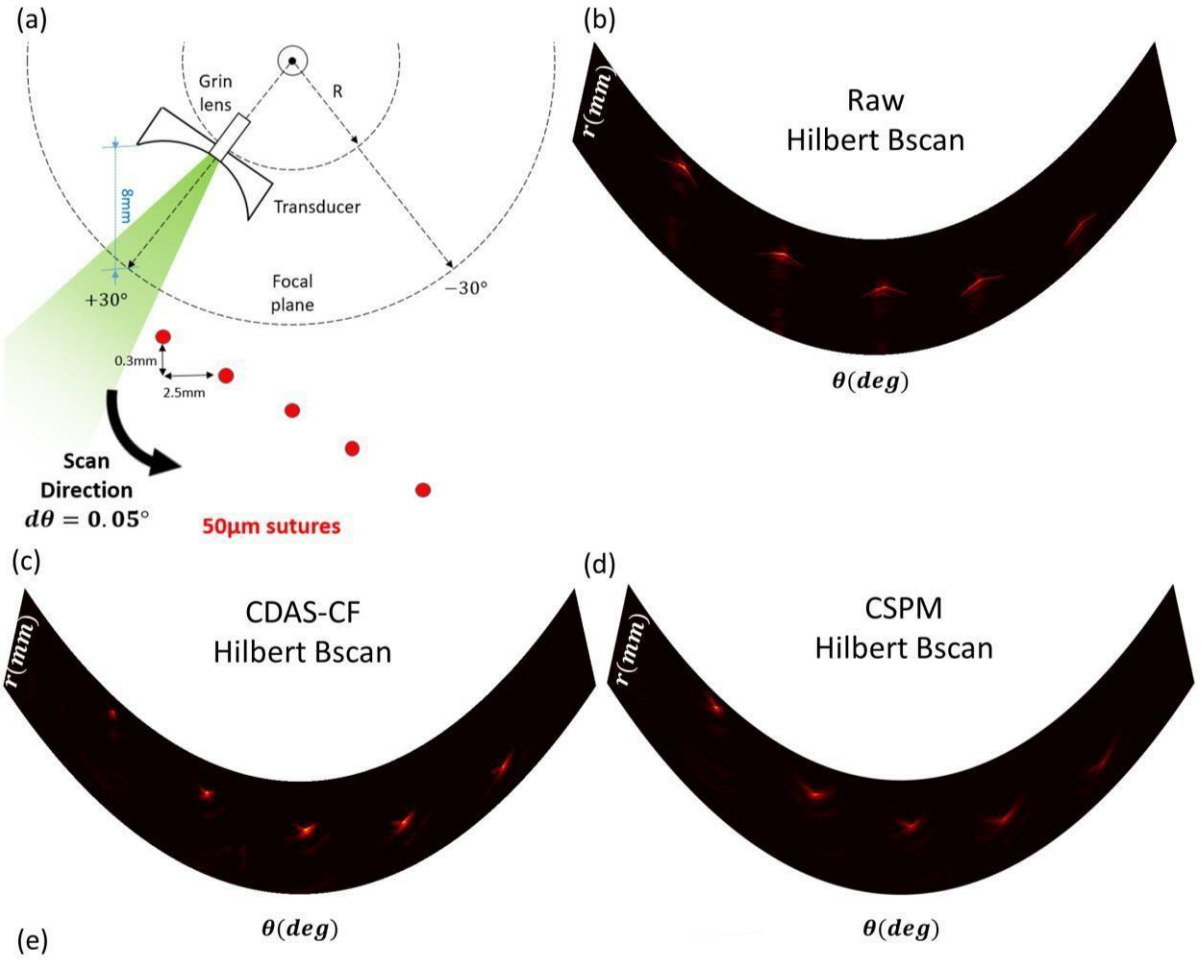

(e)

Point Source Number	CDAS–CF Bscan		CPSM Bscan	
	Axial(µm)	Lateral (µm)	Axial (µm)	Lateral (µm)
1	33	42	27	42
2	42	61	30	53
3	41.8	77	36	66
4	44	83	36	78
5	46	101	37	98

Figure. 7.15. Experimental B-scan measurement and reconstruction in cylindrical coordinates (a) The experiment configuration of measuring five 50µm sutures arranged in a diagonal in the axial direction with the HFM36 transducer. The value of R here is 5.5mm and the angular sampling distance between adjacent A-scans is $d\theta$=0.05º (b) The raw Hilbert B scan acquired over 60º where r=0 mm corresponds to the focal plane of the transducer. The imaging depth of the cylindrical Bscan presented is 2mm (c) The reconstructed CDAS-CF Hilbert Bscan measured over 60º(d) The reconstructed CPSM Hilbert Bscan measured over 60º (e) Lateral and Axial FWHM values of the reconstructed acoustic sources.

7.2.5 Feasibility of Cylindrical Bscan image reconstruction at 50Hz

Our endoscope presented in chapter 6 has the ability to operate upto 50Hz Bscan rate and therefore a corresponding image construction method is required to operate at this rate. When comparing the computational speeds of the present algorithms, CPSM algorithm in 8.2.3 was 1.2 times slower than the CDAS algorithm because the wavefield had to be recursively extrapolated per r

step with the transfer function G given by Eqn 7.24. However, this procedure could be significantly accelerated by precomputing a lookup table for the transfer function G for all r in advance. Then during reconstruction, wavefield extrapolation could be by a simple multiplication, removing the need to iterate. In addition to further accelerate reconstruction, the CPSM code was vectorized and programmed to perform the FFT and matrice operations using the PC's built in GPU. Finally, algorithm variables were declared in single precision rather than double precision to further increase computational speed. Double precision useful when storing values exceeding 3.4×10^{38} or lower than -3.4×10^{38}, in our case the maximum voltage limit of our DAQ card is 400mV and the noise level is 1mV . Hence reducing precision from double to single will not influence optoacoustic image quality. Modifying the CPSM algorithm with all these changes we obtain the accelerated CPSM algorithm.

To assess the feasibility of applying the accelerated CPSM algorithm with our endoscope at 50Hz, the simulated B-scan over 180º from Figure 7.13 was mirrored to complete a full revolution and cropped to 2mm in depth as illustrated in Fig 7.16. Applying our modified CPSM algorithm on the simulated dataset the B-scan was reconstructed in 11ms. Considering each revolution of our endoscope is 20ms, applying our modified CPSM algorithm to this data set allows for 9ms to update the frame on the display before the next revolution begins. Here the axial sampling interval is 7.5µm and considering our hybrid endoscope from chapter 6 the lateral sampling interval at the focal plane which is located at the capsule surface would be 18µm. Hence the accelerated CPSM algorithm is suitable for optoacoustic endoscopy image reconstruction at 50Hz under these conditions

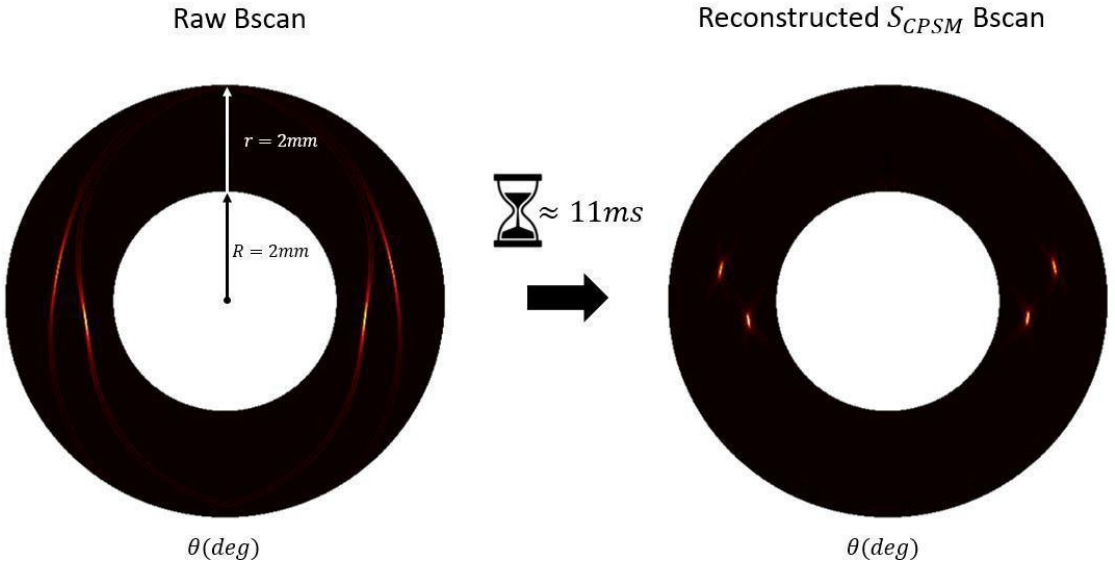

Figure. 7.16. 360° accelerated cylindrical phase shift migration Bscan reconstruction (a) Raw simulated 360° Bscan with four 50µm point absorbers (b) Reconstructed 360° cylindrical phase shift migration Bscan in approximately 11ms.

7.3. Summary and disucussion

Two algorithms including the delay sum and phase shift migration in cartesian coordinates were introduced. Both algorithms capability to recover lateral resolution over depth were assessed in kwave simulations and experimental measurements with the HFM36 spherical transducer. As phase shift migration performed interpolation in the frequency domain, it was able to compute reconstructed Bscans faster when compared to interpolating A-scans in time domain using delay and sum image reconstruction. Interestingly using the delay and sum the SNR of the reconstructed Bscans improves when moving away from the focus of the transducer or the virtual point due to additional overlap of acoustic signals, whereas SNR decreases when moving away from the focus when employing phase shift migration which corresponds to a lower signal strength of the raw signal.

The algorithms were then extended to cylindrical coordinates for optoacoustic endoscopy image reconstruction. Both modified algorithms were applied to simulated and experimental data acquired in cylindrical geometry. The SNR of the reconstructed Bscans over depth observed followed a similar pattern when comparing to the observations made to the reconstructed Bscans in cartesian coordinates. Finally, the feasibility of employing these algorithms for real time optoacoustic endoscopy Bscans reconstruction was assessed. Cylindrical phase shift migration was able to reconstruct Frame's at 11ms thereby suggesting that such an algorithm could be used one day in-vivo human esophagus at Bscans frame rates upto 50Hz

Chapter 8 Conclusion and outlook

8.1. Conclusion

As the incidence rates of esophageal cancer continue to rise, endoscopy units are burdened with the need to perform routine surveillance as a result of poor detection of dysplasia with WLE. In pursuit of superior methods to reveal 3D information of the gastrointestinal tract, OCT and OA have been explored. OCT has offered improved detection accuracy of human dysplasia as opposed to WLE. Albeit the modality on its own has yet to be widely accepted into clinical practice as deciphering early signs of dysplasia purely by means of differences in refractive indices remains challenging. In contrast, OA endoscopy is highlighted primarily in small animal experiments with a single study in large animals (i.e., pigs) where the esophagus anatomy better resembles the

human gastrointestinal tract. Although early results are promising by revealing the vasculature network within the esophageal wall, the potential of OA endoscopy in-vivo human esophagus has yet to be realized. Imaging the human esophagus with the combination of optoacoustic imaging to reveal pathophysiological information in addition to the already proven structural imaging with OCT could further enhance the detection of early signs of dysplasia and provide routes for improved diagnosis. Present hybrid OCT-OA endoscope implementations are designed for imaging small animal organs or intravascular applications, which are not suitable imaging the human esophagus.

To design a hybrid OCT-OA endoscope for imaging the human GI tract we began development by producing several side-looking optoacoustic detectors with a central aperture for collinear OCT-OA illumination for scanning the lumen wall. To retain high lateral resolution with extended depth of focus the axicon geometry was investigated as an alternative to the common spherical transducer harnessed in OA endoscopy. An optoacoustic transducer characterization rig was built with a broadband omnidirectional point source to determine the 4D total impulse response of each transducer built. The lithium niobate transducers with focusing achieved via a glass shaped lens offered clean spatial responses with highest sensitivity. Additionally, the axicon transducer offered a depth focus 4.2 larger than a spherical transducer similar in size. However during OA imaging the axicon transducer produced a blurred image when scanning a tilted 100µm suture whereas the spherical transducer correctly resolves the suture at focus.

To explain the discrepancy in axicon performance between the characterization and imaging measurements, we simulated the axicon and spherical transducer in 3D of the same dimension at ½ half scale using Kwave. 3D Kwave simulations were conducted with the generated transducers to scan around a point and line source mimicking the experimental characterization and imaging conditions. The spherical transducer produced spatial maps which were independent of the acoustic sources shapes whereas the axicon produced spatial maps where were dependent upon the acoustic source shapes. High lateral resolution was only obtained over an extended depth of focus when imaging a point source. Alternatively, in the case of imaging a line source, the axicon was prone to high amplitude low frequency off-axis signals degrading the lateral resolution. This behavior suggested the axicon would be better suited for OA microscopy applications where the transducer always responds to an optically excited point source and in particular an optical Bessel beam could be applied to exploit the axicon's elongated acoustic sensitivity profile. Hence an inverted OA microscope was established to evaluate imaging potential with a Gaussian/Bessel illumination and spherical/axicon detection. By matching Bessel illumination with axicon

detection we demonstrated a 17x increase in depth of focus over the common Gaussian-spherical OA microscope configuration. When imaging a tilted mouse ear, the Bessel-axicon combination afforded imaging depths exceeding 4.2mm. Accordingly the matched sensitivity line profiles enable a number of new applications within the field of OA microscopy. Overall, our studies demonstrate the axicon is not well suited for OA endoscopy but rather for OA microscopy. Therefore, the spherical transducer was selected to be adapted in size for endoscopy.

Aside from the transducer, design concepts such as forward viewing/side viewing, proximal/distal rotation and common mode/ split path illumination were discussed with the best concepts forwarded to the development phase of the front-end system. Several optical materials were analyzed for the capsule window to maximize optical and acoustic transmission efficiency. At the same time for the backend setup a custom made double clad fiber coupler was selected to combine OCT-OA illumination into a single double clad fiber with beam conditioning performedinside the endoscope via a custom-made lens designed on optic studio. The lens was designed to ensure OCT would focus inside esophageal tissue and OA beam would interrogate the esophaguswith a low divergence beam as a result of chromatic aberration experienced. Defining the OA interrogation spot size, central wavelength, and pulse width we were able to estimate the maximumpermissible exposures derived from the ANSI standards as a function of pulse repetition and rotational scanning speed. We found to perform high resolution imaging with increasing B scan rate, the MPE limit decreases. Therefore, the optoacoustic endoscopes sensitivity must in responseincrease to retain contrast and the penetration depth needed to image the esophagus wall which can range upto several mm's in thickness.

Two benchtop capsule prototypes were built to demonstrate hybrid OCT-OA endoscopy for esophageal imaging. The first design named semicapsule was 16mm in diameter and presented video rate endoscopy with only optoacoustics since OCT experienced a strong back reflection occurring within the custom-made grin lens which significantly degraded SNR. Hence the first-generation capsule demonstrated for the first-time optoacoustic capsule endsocopy at 50Hz Bscan rate and acquisition at 100kHz A-scan rate. High speed and resolution imaging practicability was assessed by imaging a stainless-steel mesh phantom arranged in Archimedean spiral with 3mm pitch to illustrate OA response as a function of depth. Our prototype was able to resolve the mesh over the entire field of view and capture 1790mm^3 voxels at a volume rate of 0.24Hz. Introducing intralipid solution to mimic light scattering conditions when interrogating the esophageal tissue, we estimated a penetration depth ~0.84mm in-vivo human esophagus. Subsequently a second-generation capsule prototype called the partial capsule was assembled with a smaller diameter of

12.5mm to match the diameter of white light capsules presently used in capsule endoscopy. A new custom-made grin lens was designed to ensure both modalities could operate in harmony. The partial capsule was able to demonstrate for the first time the ability to synchronously acquireand display OCT-OA hybrid Bscans at 30Hz frame rate and 85kHz OCT/42.5kHz OA A-scan rate. During transducer characterization, the partial capsule transducer provided improved optoacoustic resolution and sensitivity when compared to the semicapsule transducer. The potential of hybrid imaging was demonstrated by imaging a number of black and white sutures arranged in a Archimedean spiral, where all sutures present were revealed only in the hybrid Bscans. Helically scanning a mesh, ex-vivo pig esophagus and human mucosal tissue in hybrid mode revealed high resolution esophageal wall layers measured by OCT and vasculature measured by OA. This study showed the possibility of the additional structural and functional information gained when scanning the esophagus with OCT and OA together.

A side from technical innovation, the delay sum and phase shift migration reconstruction algorithms previously applied for optoacoustic tomography were investigated for optoacoustic endoscopy. The algorithms were implemented initially in Cartesian coordinates to reconstruct simulated Kwave Bscans of point sources and experimental B scans of sutures. Building on this foundation both algorithms were adapted for reconstruction in cylindrical coordinates and assessed with simulated and experimental Bscan data measured in cylindrical coordinates. The viability of employing these algorithms at 50Hz frame rate with partial capsule were evaluated. Cylindrical phase shift migration was able to reconstruct B frames faster than 50Hz with high resolution and displaying information over 2 mm’s depth making the algorithm suitable for real time optoacoustic endoscopy image reconstruction.

In conclusion, the work herein presents the development and characterization of a hybrid OCT-OA capsule endoscope suitable for imaging the human esophagus. Results from tissue mimicking phantoms and ex-vivo pig esophagus demonstrate great potential of combining OCT and OA to complement anatomical structures with metabolic features respectively. Overall, the hybrid capsule endoscope designed offers promising translational characteristics for label-free human GI surveillance delivering 3D structural and functional information not available to WLE.

8.2. Outlook

The ability to acquire hybrid OCT-OA endoscopy data in this work has only been demonstrated

in phantoms, ex-vivo samples and in-vivo human mucosal tissue of the inferior lip. For in-vivo imaging of the esophagus a miniature hollowshaft motor is required be to mounted at the proximal end of the partial capsule prototype as depicted in figure 8.1. Motor requirements include a small diameter to ensure capsule size retains the 12.5mm diameter of the partial capsule design and the ability to support the load of the transducer upto 50Hz frame rate. Figure 8.1 indicates how rotation would occur by highlighting the rotatory components in blue and the stationary components in grey.

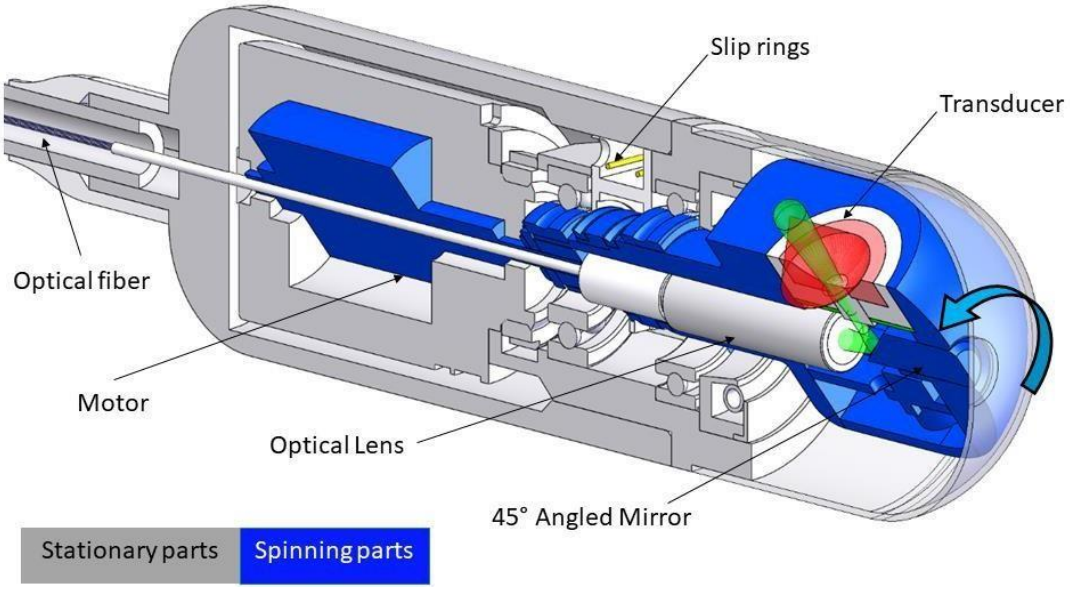

Figure. 8.1. Rotational scanning within the final hybrid capsule concept, Blue components represent moving parts whereas grey components are the stationary parts.

To scan the esophagus, the endoscopist could manually pullback the capsule as hybrid acquisition is performed following a helical scan as illustrated in Fig 8.2. Alternatively, to perform a more controlled scan to ensure the pullback pitch remains constant, a secondary linear translational motor placed near the mouth entry could pull the shaft of the capsule at constant velocity. Here a thin flexible shaft which houses the optical fiber and electronic cables for the transducer and motor is required to ensure smooth translation inside the esophagus. A white light micro-camera could also be added to monitor position and provide complimentary information. Should the capsule loose contact between the circumference of the wall and capsule surface during pullback then the probe should be adapted to the capsule with the inflatable balloon interface discussed in section 4.3.

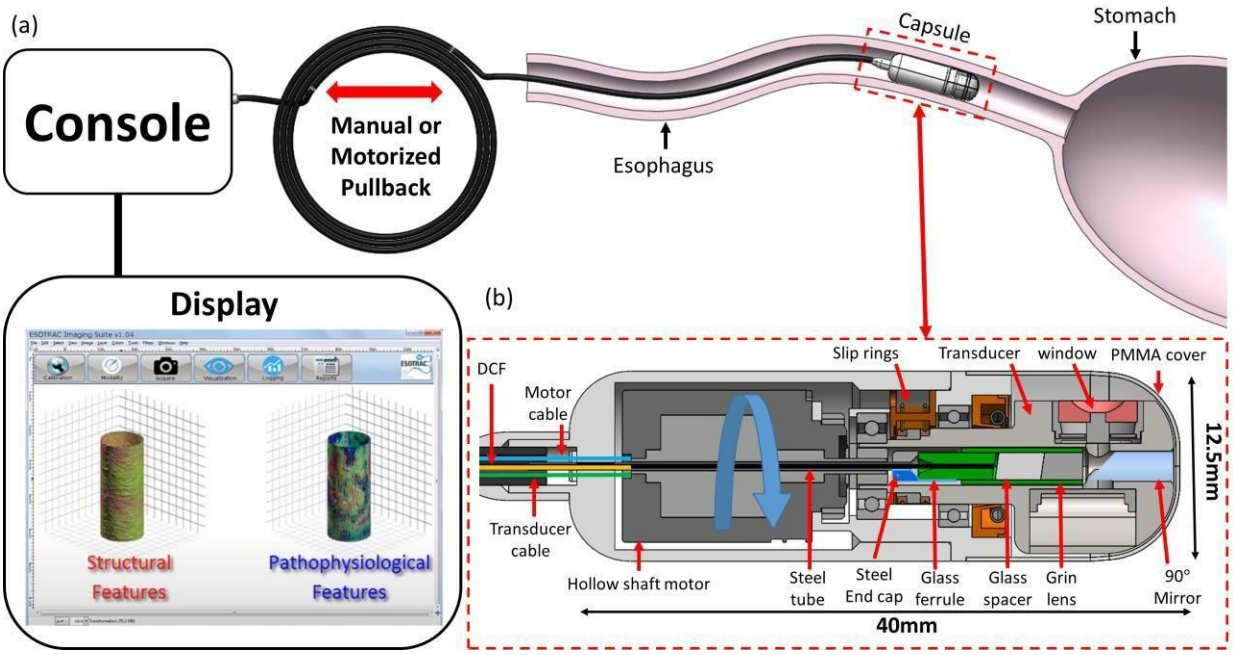

Figure. 8.2: In-vivo hybrid OCT-OA capsule endoscopy volumetric imaging. Pullback could be either manual or controlled via a translational stepper motor. The Display shows volumetric renders of structure features acquired by OCT and the pathophysiological features from OA. The 12.5mmx40mm capsule dimension is a hypothetical value.

Imaging performance could be further improved by tuning the endoscopic transducer inside the partial capsule. In particular, a preamplifier could be mounted inside the casing to improve SNR rather than performing pre amplification externally. Secondly the central aperture of the transducer could be reduced to improve sensitivity by further developing the grin lens to minimizethe OCT and OA spot sizes in this region. Thirdly, sensitivity can also be increased by extendingthe diameter of the active element. Finally, the focal length of the transducer could be reduced to minimize the propagation distance of optoacoustic waves generated within the esophageal wall and further enhance sensitivity. In return, OCT SNR would also improve by reducing the heavy water absorption in the confined optical path. Making these changes reduces the fluence required to obtain high contrast images and thereby permits higher rotational speeds.

Extending optoacoustic endoscopy to multispectral optoacoustic endoscopy by including multiple high repetition rate lasers of different wavelengths into the back-end console and detecting optoacoustic waves emitted by different photoabsorbing molecules within the esophagus could enable visualizing functional information including tissue oxygenation, hemoglobin concentration or hypoxia. To achieve this a fiber or free space combiner could be implemented to couple the light from each source to the OA input port of the DCF. Then during scanning the appropriate light source triggered by a trigger driver which is synchronized to the OCT laser. Because of the MPE constraint at high rotational speeds (>50Hz) the pulse energy requirement is limited to

<10μJ, hence low-cost laser diodes which have been shown to operate in several hundreds of kHz could potentially be exploited for this application [131].

In regard to optoacoustic endoscopy image reconstruction, we presented two algorithms which could be employed with the hybrid capsule. Although they were only demonstrated in simulations and phantoms. In the future as more experimental data is available from in-vivo experimentation, the algorithms will be further adapted to improve contrast and resolution in cylindrical coordinates. Furthermore, the point spread function of the transducer used should be determined experimentally following the characterization methodology presented in Chapter 4 and integrated into the image reconstruction process to improve resolution and SNR. Subsequently reconstructed optoacoustic images together with OCT images could then be fed into a neural network to distinguish esophageal wall characteristics with regions of interest highlighted which may contain the presence of dysplasia for the further inspection.

Experimental findings of hybrid OCT-OA capsule endoscopy at video presented in this work illustrate the ability to require 3D structural and functional information not available to WLE. The additional information gained could hasten the screening duration and provide routes for improved patient outcome. However, to validate the benefit of the added information, several in-vivo human clinical trials are required to fully investigate the translational potential of our proposed design. From these clinical studies several interesting questions could be answered such as the improvement in detection accuracy of early neoplasia with hybrid imaging as opposed to single modality systems, what the additional benefits of multispectral optoacoustic endoscopy for human esophageal imaging include, the feasibility to stage esophageal cancer and determine the extent of tumor invasion.

Acknowledgements

I would like to thank my supervisors, Prof. Vasilis Ntziachristos and Dr. Christian Zakian, for their support throughout the course of this project. Without their guidance, the work documented in this report would not be possible.

Many Thanks to Herr Gerlach for manufacturing all the test jigs used during my experiments without his help some of the experiments presented would not be possible.

I would like to thank Roman Shnaiderman, Dr. Korbinian Paul-Yuan, Qutaiba Mustafa and Dr Evangelos liapis for their support, fruitful ideas, direction, and discussions during the course of my PhD.

Thanks to Uwe Klemm, Sarah Glasl, Roland Boha and Pia Anzenhofer for assisting me with my experimental setups and Susanne Stern for helping me out with administrative tasks. I was also very grateful to have Manfred Turke on board the ESOTRAC project as project coordinator, ensuring project deliverables were completed on time.

I am very grateful for Milly's encouragement over the course of my PhD. Our weekly calls and adventures gave me the energy to continue pursuing my research. Also, thanks to her cat Dark for making me smile a lot.

I would also like to thank the Future of Biomedical Imaging students including Paratoo Asfarai and Antonia Longo for their support during the different courses we attended together over the first 3 years of my doctoral degree.

Finally, I would like to thank my parents and friends back in New Zealand for providing encouragement and support, while I have been performing research at the Technical University of Munich and Helmholtz Zentrum München

Publications

1. Ali, Z., Zakian, C. & Ntziachristos, V. Ultra-broadband axicon transducer for optoacoustic endoscopy. *Sci Rep* **11,** 1654 (2021).

   https://doi.org/10.1038/s41598-021-81117-7 (published)

2. Ali, Z., Zakian, C. & Ntziachristos, V. "Elongated focus optoacoustic microscopy with matched Bessel beam illumination and ultra-broadband axicon detection", Advanced Photonics Research (2022)
   https://onlinelibrary.wiley.com/doi/10.1002/adpr.202100249 (published)
3. Ali, Z., Zakian, C., Li, Q., Gloriod, J., Crozat, S., Bouvet, F., Pierre, G., Sarantos, V., Di Pietro, M., Flisikowski, K., Andersen, P., Drexler, W., & Ntziachristos, V. "360^0 Video rate optoacoustic endoscopy for esophageal imaging", Photoacoustics (2022)
   https://www.sciencedirect.com/science/article/pii/S2213597922000052?via%3Dihub (published)

International conference contributions and proceedings

1. **Zakiullah Ali**, Christian Zakian and Vasilis Ntziachristos, "Conical through-hole transducer for optoacoustic endoscopy with expanded depth of focus",
   SPIE, European conferences on biomedical optics, Optoacoustic methods and applications in bio photonics, Germany, Munich, 2019. Poster presentation.
2. **Zakiullah Ali**, Christian Zakian and Vasilis Ntziachristos, "Multimodal Endoscopic Imaging", SPIE, Biophotonics summer school 2017, Sweden, Island of ven. Poster presentation

References

[1] Bray, F., Ferlay, J., Soerjomataram, I., Siegel, R.L., Torre, L.A., & Jemal, A. (2018). Global cancer statistics 2018: GLOBOCAN estimates of incidence and mortality worldwide for 36 cancers in 185 countries. CA: A Cancer Journal for Clinicians, 68: 394-424.

[2] J. Natl Cancer Inst. (2011). Cancer Prevalence and Cost of Care Projections (sections 2.1.2). National Cancer Institute. Retrieved from: http://costprojections.cancer.gov

[3] Bird-Lieberman, E., Neves, A., Lao-Sirieix, P., O'Donovan, M., Novelli, M., Lovat, L., … Fitzgerald, R. (2012). Molecular imaging using fluorescent lectins permits rapid endoscopic identification of dysplasia in Barrett's esophagus. Nature medicine, 18(2), 315–21.

[4] Berman, M. R. (2013). What's wrong with Morrissey's esophagus? Retrieved May 17, 2016, from http://www.medpagetoday.com/CelebrityDiagnosis/37196

[5] Ntziachristos, V. (2010). Going deeper than microscopy: the optical imaging frontier in biology. *Nature Methods*, 7(8), 603-614.

[6] Lee, N. M., & Eisen, G., M. (2010). 10 Years of Capsule Endoscopy: An Update Expert review of gastroenterology & hepatology. Vol.4(4), pp.503-512

[7] Mick, J. (2014). Colon-probing pill camera finally wins FDA approval. Retrieved May 19,2016, from:http://www.dailytech.com/ColonProbing+Pill+Camera+Finally+Wins+FDA+Approval/article34270.htm

[8] University of Birmingham Health Services Management Centre, Midlands, Lancashire Commissioning Support Unit. (2015). SCOPING THE FUTURE: An evaluation of endoscopy capacity across the NHS in England. Cancer Research UK.

[9] Hoffman, A., Goetz, M., Vieth, M., Galle, P. R., Neurath, M. F., & Kiesslich, R. (2006). Confocal laser endomicroscopy: technical status and current indications. Endoscopy, 38(12), 1275–1283.

[10] Liu, J., Li, M., Li, Z., Zuo, X. L., Li, C. Q., Dong, Y. Y., Zhou, C. J., & Li, Y. Q. (2014). Learning curve and interobserver agreement of confocal laser endomicroscopy for detecting precancerous or early-stage esophageal squamous cancer. PLOS one, 9(6), e99089.

[11] Liu, H., Li, Y. Q., Yu, T., Zhao, Y. A., Zhang, J. P., Zuo, X. L., Li, C. Q., Zhang, J. N., Guo, Y. T., & Zhang, T. G. (2009). Confocal laser endomicroscopy for superficial esophageal squamous cell carcinoma. Endoscopy, 41(2), 99–106.

[12] Pech, O., Rabenstein, T., Manner, H., Petrone, M. C., Pohl, J., Vieth, M., Stolte, M., & Ell, C. (2008). Confocal laser endomicroscopy for in vivo diagnosis of early squamous cell carcinoma in the esophagus. Clinical gastroenterology and hepatology: the official clinical practice journal of the American Gastroenterological Association, 6(1), 89–94.

[13] Wallace, M. B., & Fockens, P. (2009). Probe-Based Confocal Laser Endomicroscopy. *Gastroenterology*, *136*(5), 1509-1513.

[14] Goetz, M., & Wang, T. D. (2010). Molecular imaging in gastrointestinal endoscopy. Gastroenterology, 138(3), 828–33.e1.

[15] Nagengast, W. B., et al. (2019). Near-infrared fluorescence molecular endoscopy detects dysplastic oesophageal lesions using topical and systemic tracer of vascular endothelial growth factor A." Gut **68**(1): 7-10.

[16] De Jongh, S. J., Voskuil, F. J., Schmidt, I., Karrenbeld, A., Kats-Ugurlu, G., Meersma, G. J., Westerhof, J., Witjes, M., van Dam, G. M., Robinson, D. J., & Nagengast, W. B. (2020). C-Met targeted fluorescence molecular endoscopy in Barrett's esophagus patients and identification of outcome parameters for Phase-I studies. Theranostics, 10(12), 5357–5367.

[17] Waterhouse, D. J., Joseph, J., Neves, A. A., di Pietro, M., Brindle, K. M., Fitzgerald, R. C., & Bohndiek, S. E. (2016). Design and validation of a near-infrared fluorescence endoscope for detection of early esophageal malignancy. *Journal of biomedical optics*, *21*(8), 84001.

[18] Sturm, M. B., Joshi, B. P., Lu, S., Piraka, C., Khondee, S., Elmunzer, B. J., Kwon, R. S., Beer, D. G., Appelman, H. D., Turgeon, D. K., & Wang, T. D. (2013). Targeted imaging of esophageal neoplasia with a fluorescently labeled peptide: first-in-human results. Science translational medicine, 5(184).

[19] Gora, M. J., Sauk, J. S., Carruth, R. W., Gallagher, K. A., Suter, M. J., Nishioka, N. S., Kava, L. E., Rosenberg, M., Bouma, B. E., & Tearney, G. J. (2013). Tethered capsule endomicroscopy enables less invasive imaging of gastrointestinal tract microstructure. Nature medicine, 19(2), 238–240.

[20] Leggett, C. L., Gorospe, E. C., Chan, D. K., Muppa, P., Owens, V., Smyrk, T. C., Anderson, M., Lutzke, L. S., Tearney, G., & Wang, K. K. (2016). Comparative diagnostic performance of volumetric laser endomicroscopy and confocal laser endomicroscopy in the detection of dysplasia associated with Barrett's esophagus. Gastrointestinal endoscopy, 83(5), 880–888.e2.

[21] Hoffman, A., Manner, H., Rey, J. W., & Kiesslich, R. (2017). A guide to multimodal endoscopy imaging for gastrointestinal malignancy - an early indicator. Nature reviews. Gastroenterology & hepatology, 14(7), 421–434.

[22] Drezek, R., Guillaud, M., Collier, T., Boiko, I., Malpica, A., Macaulay, C., Follen, M., & Richards-Kortum, R. (2003). Light scattering from cervical cells throughout neoplastic progression: influence of nuclear morphology, DNA content, and chromatin texture. Journal of biomedical optics, 8(1), 7–16.

[23] Vakoc, B. J., Fukumura, D., Jain, R. K., & Bouma, B. E. (2012). Cancer imaging by optical coherence tomography: preclinical progress and clinical potential. Nature reviews. Cancer, 12(5), 363–368.

[24] Tsai, T. H., Fujimoto, J. G., & Mashimo, H. (2014). Endoscopic Optical Coherence Tomography for Clinical Gastroenterology. Diagnostics (Basel, Switzerland), 4(2), 57–93.

[25] Vazquez-Sequeiros, E., & Wiersema, M. J. (2002). High-frequency US catheter-based staging of early esophageal tumors. Gastrointestinal endoscopy, 55(1), 95–99.

[26] Liu, J., Carpenter, S., Chuttani, R., Croffie, J., Disario, J., Mergener, K., Mishkin, D. S., Shah, R., Somogyi, L., Tierney, W., & Petersen, B. T. (2006). Endoscopic ultrasound probes. Gastrointestinal endoscopy, 63(6), 751–754.

[27] Yoshinaga, S., Oda, I., Nonaka, S., Kushima, R., & Saito, Y. (2012). Endoscopic ultrasound using ultrasound probes for the diagnosis of early esophageal and gastric cancers. World journal of gastrointestinal endoscopy, 4(6), 218–226.

[28] Attila, T., & Faigel, D. O. (2009). Role of endoscopic ultrasound in superficial esophageal cancer. Diseases of the esophagus: official journal of the International Society for Diseases of the Esophagus, 22(2), 104–112.

[29] Krill, T., Baliss, M., Roark, R., Sydor, M., Samuel, R., Zaibaq, J., Guturu, P., & Parupudi, S. (2019). Accuracy of endoscopic ultrasound in esophageal cancer staging. Journal of thoracic disease, 11(Suppl 12), S1602–S1609.

[30] Kaul, V., et al. (2010). Interventional EUS." Gastrointestinal Endoscopy **72**(1): 1-4.

[31] Steeg, P. S. (2006). Tumor metastasis: mechanistic insights and clinical challenges. Nature medicine, 12(8), 895–904.

[32] Young, P. E., Gentry, A. B., Acosta, R. D., Greenwald, B. D., & Riddle, M. (2010). Endoscopic ultrasound does not accurately stage early adenocarcinoma or high-grade dysplasia of the esophagus. Clinical gastroenterology and hepatology: the official clinical practice journal of the American Gastroenterological Association, 8(12), 1037–1041.

[33] Pouw, R. E., Heldoorn, N., Alvarez Herrero, L., Kate, F. J., Visser, M., Busch, O. R., van Berge Henegouwen, M. I., Krishnadath, K. K., Weusten, B. L., Fockens, P., & Bergman, J. J. (2011). Do we still need EUS in the workup of patients with early esophageal neoplasia? A retrospective analysis of 131 cases. Gastrointestinal endoscopy, 73(4), 662–668.

[34] Trindade, A. J., & Berzin, T. M. (2013). Clinical controversies in endoscopic ultrasound. Gastroenterology report, 1(1), 33–41.

[35] Schwarz, M., Soliman, D., Omar, M., Buehler, A., Ovsepian, S. V., Aguirre, J., & Ntziachristos, V. (2017). Optoacoustic Dermoscopy of the Human Skin: Tuning Excitation Energy for Optimal Detection Bandwidth with Fast and Deep Imaging in vivo. IEEE transactions on medical imaging, 36(6), 1287–1296.

[36] Aguirre, J., Schwarz, M., Garzorz, N., Omar, M., Buehler, A., Eyerich, K., & Ntziachristos, V. (2017). Precision assessment of label-free psoriasis biomarkers with ultra-broadband optoacoustic mesoscopy. Nature Biomedical Engineering 1:0068.

[37] Schwarz, M., Omar, M., Buehler, A., Aguirre, J., & Ntziachristos, V. (2015). Implications of Ultrasound Frequency in Optoacoustic Mesoscopy of the Skin. IEEE Transactions on Medical Imaging, 34(2), 672-677.

[38] Aguirre, J., Schwarz, M., Soliman, D., Buehler, A., Omar, M., & Ntziachristos, V. (2014), Broadband mesoscopic optoacoustic tomography reveals skin layers, Opt. Lett., vol. 39, p. 6297.

[39] Omar, M., Schwarz, M., Soliman, D., Symvoulidis, P., & Ntziachristos, V. (2015). Pushing the optical imaging limits of cancer with multi-frequency-band raster-scan optoacoustic mesoscopy (RSOM). Neoplasia (New York, N.Y.), 17(2), 208–214.

[40] Yang, J. M., Maslov, K., Yang, H. C., Zhou, Q., Shung, K. K., & Wang, L. V. (2009). Photoacoustic endoscopy. Optics letters, 34(10), 1591–1593.

[41] Yang, J. M., Chen, R., Favazza, C., Yao, J., Li, C., Hu, Z., Zhou, Q., Shung, K. K., & Wang, L.

V. (2012). A 2.5-mm diameter probe for photoacoustic and ultrasonic endoscopy. Optics express, 20(21), 23944–23953.

[42] He, H., Wissmeyer, G., Ovsepian, S. V., Buehler, A., & Ntziachristos, V. (2016). Hybrid optical and acoustic resolution optoacoustic endoscopy. Optics letters, 41(12), 2708–2710.

[43] Karpiouk, A. B., Wang, B., & Emelianov, S. Y. (2010). Development of a catheter for combined intravascular ultrasound and photoacoustic imaging. The Review of scientific instruments, 81(1), 014901

[44] Ansari, R., Zhang, E. Z., Desjardins, A. E., & Beard, P. C. (2018). All-optical forward-viewing photoacoustic probe for high-resolution 3D endoscopy. Light Sci Appl **7,** 75.

[45] Yang, J. M., Favazza, C., Chen, R., Yao, J., Cai, X., Maslov, K., Zhou, Q., Shung, K. K., & Wang, L. V. (2012). Simultaneous functional photoacoustic and ultrasonic endoscopy of internal organs in vivo. Nature medicine, 18(8), 1297–1302.

[46] Li, Y., Lin, R., Liu, C., Chen, J., Liu, H., Zheng, R., Gong, X., & Song, L. (2018). In vivo photoacoustic/ultrasonic dual-modality endoscopy with a miniaturized full field-of-view catheter. Journal of biophotonics, 11(10), e201800034.

[47] Li, Y., Zhu, Z., Jing, J. C., Chen, J. J., Heidari, E., He, Y., Zhu, J., Ma, T., Yu, M., Zhou, Q., & Chen, Z. (2019). High-Speed Integrated Endoscopic Photoacoustic and Ultrasound Imaging System. IEEE journal of selected topics in quantum electronics : a publication of the IEEE Lasers and Electro-optics Society, 25(1), 7102005.

[48] Lei, H., Johnson, L. A., Eaton, K. A., Liu, S., Ni, J., Wang, X., Higgins, P., & Xu, G. (2019). Characterizing intestinal strictures of Crohn's disease in vivo by endoscopic photoacoustic imaging. Biomedical optics express, 10(5), 2542–2555.

[49] He, H., Stylogiannis, A., Afshari, P., Wiedemann, T., Steiger, K., Buehler, A., Zakian, C., & Ntziachristos, V. (2019). Capsule optoacoustic endoscopy for esophageal imaging. Journal of biophotonics, 12(10), e201800439.

[50] Martí-Bonmatí, L., Sopena, R., Bartumeus, P., & Sopena, P. (2010). Multimodality imaging techniques. Contrast media & molecular imaging, 5(4), 180–189.

[51] Pichler, B. J., Judenhofer, M. S.,Pfannenberg, C. (2008). Multimodal Imaging Approaches: PET/CT and PET/MRI. Molecular Imaging I, 109–132.

[52] Bell, A.G. (1880). On the production and reproduction of sound by light. American Journal of Science. s3-s20(118);305

[53] Kruger, R. A., Liu, P., Fang, Y. R., & Appledorn, C. R. (1995). Photoacoustic ultrasound (PAUS)—reconstruction tomography. Medical physics, 22(10), 1605–1609.

[54] Esenaliev, R. O., Karabutov, A. A., Tittel, F. K., Fornage, B. D., Thomsen, S. L., Stelling, C. & Oraevsky, A. A. (1997). Laser optoacoustic imaging for breast cancer diagnostics: limit of detection and comparison with x-ray and ultrasound imaging. Proc. SPIE 2979, 71–82.

[55] Hoelen, C. G., de Mul, F. F., Pongers, R., & Dekker, A. (1998). Three-dimensional photoacoustic

Imaging of blood vessels in tissue. Optics letters, 23(8), 648–650.

[56] Oraevsky, A. A., Andreev, V. A., Karabutor, A. A., Declan Fleming, K. R., Gatalica, Z., Singh, H. & Esenalier, R. O. (1999). Laser optoacoustic imaging of the breast: detection of cancer angiogenesis. Proc. SPIE 3597, 352–363.

[57] Zhou, Y., Yao, J., & Wang, L. V. (2016). Tutorial on photoacoustic tomography. Journal of biomedical optics, 21(6), 61007.

[58] Beard, P.(2011).Biomedical photoacoustic imaging. Interface focus, 1(4),602–631.

[59] Huang, D., Swanson, E. A., Lin, C. P., Schuman, J. S., Stinson, W. G., Chang, W., Hee, M. R., Flotte, T., Gregory, K., & Puliafito, C. A. (1991). Optical coherence tomography. Science (New York, N.Y.), 254(5035), 1178–1181.

[60] Fercher, A. F., Hitzenberger, C. K., Drexler, W., Kamp, G., & Sattmann, H. (1993). In vivo optical coherence tomography. American journal of ophthalmology, 116(1), 113–114.

[61] Ţălu, Ş., et al. (2011). The history and use of optical coherence tomography in ophthalmology. Human and Veterinary Medicine **3**: 29-32.

[62] Li, Y., Jing, J., Heidari, E., Zhu, J., Qu, Y., & Chen, Z. (2017). Intravascular Optical Coherence Tomography for Characterization of Atherosclerosis with a 1.7 Micron Swept-Source Laser. Scientific reports, 7(1), 14525.

[63] Levine, A., Wang, K., & Markowitz, O. (2017). Optical Coherence Tomography in the Diagnosis of Skin Cancer. Dermatologic clinics, 35(4), 465–488.

[64] Choma, M., Sarunic, M., Yang, C., & Izatt, J. (2003). Sensitivity advantage of swept source and Fourier domain optical coherence tomography. *Optics express*, *11*(18), 2183–2189.

[65] Leitgeb, R., Hitzenberger, C., & Fercher, A. (2003). Performance of fourier domain vs. time domain optical coherence tomography. Optics express, 11(8), 889–894.

[66] de Boer, J. F., Cense, B., Park, B. H., Pierce, M. C., Tearney, G. J., & Bouma, B. E. (2003). Improved signal-to-noise ratio in spectral-domain compared with time-domain optical coherence tomography. *Optics letters*, *28*(21), 2067–2069.

[67] Bille, J. F. (2019). High resolution imaging in microscopy and Ophthalmology New Frontiers in biomedical optics. Springer International Publishing.

[68] Hatta, W., Uno, K., Koike, T., Iijima, K., Asano, N., Imatani, A., & Shimosegawa, T. (2012). A prospective comparative study of optical coherence tomography and EUS for tumor staging of superficial esophageal squamous cell carcinoma. Gastrointestinal endoscopy, 76(3), 548–555.

[69] Mathews, S. J., Little, C., Loder, C. D., Rakhit, R. D., Xia, W., Zhang, E. Z., Beard, P. C., Finlay, M. C., & Desjardins, A. E. (2018). All-optical dual photoacoustic and optical coherence tomography intravascular probe. Photoacoustics, 11,65–70.

[70] Dai, X., et al. (2017). Miniature Endoscope for Multimodal Imaging. ACS Photonics **4**(1): 174-180.

[71] Yang, Y., Li, X., Wang, T., Kumavor, P. D., Aguirre, A., Shung, K. K., Zhou, Q., Sanders, M., Brewer, M., & Zhu, Q. (2011). Integrated optical coherence tomography, ultrasound and photoacoustic imaging for ovarian tissue characterization. *Biomedical optics express*, *2*(9), 2551–2561.

[72] Strohm, E. M., Berndl, E. S., & Kolios, M. C. (2013). High frequency label-free photoacoustic microscopy of single cells. Photoacoustics, 1(3-4), 49–53.

[73] Preisser, S., Rohringer, W., Liu, M., Kollmann, C., Zotter, S., Fischer, B., & Drexler, W. (2016). All-optical highly sensitive akinetic sensor for ultrasound detection and photoacoustic imaging. Biomedical optics express, 7(10), 4171–4186.

[74] Rebling, J., Warshavski, O., Meynier, C., & Razansky, D. (2017). Optoacoustic characterization of broadband directivity patterns of capacitive micromachined ultrasonic transducers. Journal of biomedical optics, 22(4), 41005.

[75] Buma, T., et al. (2001). High-frequency ultrasound array element using thermoelastic expansion in an elastomeric film. Applied Physics Letters **79**(4): 548-550.

[76] Pham, K. T., & Nguyen, N. L. (2017). A study on acoustic characterization of medical ultrasound transducers using pulse-echo methods. 2017 International Conference on Advanced Technologies for Communications (ATC).

[77] Beard, P., et al. (1999). Characterization of a polymer film optical fiber hydrophone for the measurement of ultrasound fields for use in the range 1-30MHz: a comparison with PVDF needle and membrane hydrophones. IEEE Trans Ultrason Ferroelectr Freq Control **47**.

[78] Omar, M., Gateau, J., & Ntziachristos, V. (2013). Raster-scan optoacoustic mesoscopy in the 25-125 MHz range. Optics letters, 38(14), 2472–2474.

[79] Won Baac, H., Ling, T., Huang, S. W., Ashkenazi, S., & Guo, L. J. (2009). Characterization of optical microring ultrasound detector by using a high frequency focused photoacoustic transmitter. Applied physics letters, 95(14), 144105.

[80] Schwarz, M., Omar, M., Buehler, A., Aguirre, J., & Ntziachristos, V. (2015). Implications of ultrasound frequency in optoacoustic mesoscopy of the skin. IEEE transactions on medical imaging, 34(2), 672–677.

[81] Aguirre, J., Schwarz, M., Soliman, D., Buehler, A., Omar, M., & Ntziachristos, V. (2014). Broadband mesoscopic optoacoustic tomography reveals skin layers. Optics letters, 39(21), 6297–6300.

[82] Omar, M., Schwarz, M., Soliman, D., Symvoulidis, P., & Ntziachristos, V. (2015). Pushing the optical imaging limits of cancer with multi-frequency-band raster-scan optoacoustic mesoscopy (RSOM). Neoplasia (New York, N.Y.), 17(2), 208–214.

[83] Xia, F., Mao, J., Ding, J., & Yang, H. (2009). Observation of normal appearance and wall thickness of esophagus on CT images. European journal of radiology, 72(3), 406–411.

[84] Kierszenbaum, A. L., & Tres, L. (2011). Histology and Cell Biology: An Introduction to Pathology with Student Consult Online Access 3rd edn.

[85] He, H., Buehler, A., Bozhko, D., Jian, X., Cui, Y., & Ntziachristos, V. (2018). Importance of Ultrawide Bandwidth for Optoacoustic Esophagus Imaging. IEEE transactions on medical imaging, 37(5), 1162–1167.

[86] Xu, M., & Wang, L. V. (2005). Universal back-projection algorithm for photoacoustic computed tomography. Physical review. E, Statistical, nonlinear, and soft matter physics, 71(1 Pt 2), 016706.

[87] Araque Caballero, M. Á., Rosenthal, A., Gateau, J., Razansky, D., & Ntziachristos, V. (2012). Model-based optoacoustic imaging using focused detector scanning. Optics letters, 37(19), 4080–4082.

[88] Ding, Z., Ren, H., Zhao, Y., Nelson, J. S., & Chen, Z. (2002). High-resolution optical coherence tomography over a large depth range with an axicon lens. Optics letters, 27(4), 243–245.

[89] Passler, K., et al. (2009). Laser-generation of ultrasonic X-waves using axicon transducers. Applied Physics Letters **94**(6): 064108.

[90] Passler, K., Nuster, R., Gratt, S., Burgholzer, P., Berer, T., & Paltauf, G. (2010). Scanning acoustic-photoacoustic microscopy using axicon transducers. Biomedical optics express, 1(1), 318–323.

[91] Gratt, S., Passler, K., Nuster, R. & Paltauf, G. (2009). Photoacoustic imaging using a conical axicon detector. *SPIE Proc. (SPIE)* **1**, 73710W.

[92] Treeby, B. E., & Cox, B. T. (2010). k-Wave: MATLAB toolbox for the simulation and reconstruction of photoacoustic wave fields. Journal of biomedical optics, 15(2), 021314.

[93] Omar, M., Aguirre, J., & Ntziachristos, V. (2019). Optoacoustic mesoscopy for biomedicine. Nature biomedical engineering, 3(5), 354–370.

[94] Kellnberger, S., Soliman, D., Tserevelakis, G. J., Seeger, M., Yang, H., Karlas, A., Prade, L., Omar, M., & Ntziachristos, V. (2018). Optoacoustic microscopy at multiple discrete frequencies. Light, science & applications, 7, 109.

[95] Pleitez, M.A., Khan, A.A., Soldà, A. et al. (2020). Label-free metabolic imaging by mid-infrared optoacoustic microscopy in living cells. Nat Biotechnol **38,** 293–296.

[96] Soliman, D., Tserevelakis, G. J., Omar, M., & Ntziachristos, V. (2015). Combining microscopy with mesoscopy using optical and optoacoustic label-free modes. *Scientific reports*, *5*, 12902.

[97] Born, M., Wolf, E., Bhatia, A., Clemmow, P., Gabor, D., et al. (1999). Image-forming instruments. In Principles of Optics: Electromagnetic Theory of Propagation, Interference and Diffraction of Light (pp. 261-285). Cambridge: Cambridge University Press.

[98] Durnin, J., Miceli, J. J., Jr., & Eberly, J. H. (1988). Comparison of Bessel and Gaussian beams. Optics letters, 13(2), 79.

[99] Collier, B., Awasthi, S., Lieu, D. et al. (2015). Non-Linear Optical Flow Cytometry Using a Scanned, Bessel Beam Light-Sheet. Sci Rep **5,** 10751

[100] Vuillemin, N., et al. (2016). Efficient second-harmonic imaging of collagen in histological slides using Bessel beam excitation." Scientific Reports **6**(1): 29863.

[101] Lu, R., Sun, W., Liang, Y., Kerlin, A., Bierfeld, J., Seelig, J. D., Wilson, D. E., Scholl, B., Mohar, B., Tanimoto, M., Koyama, M., Fitzpatrick, D., Orger, M. B., & Ji, N. (2017). Video-rate

volumetric functional imaging of the brain at synaptic resolution. Nature neuroscience, 20(4), 620–628.

[102] Fahrbach, F., Simon, P., & Rohrbach, A. (2010). Microscopy with self-reconstructing beams. Nature Photon **4,** 780–785.

[103] Lee, K. S., & Rolland, J. P. (2008). Bessel beam spectral-domain high-resolution optical coherence tomography with micro-optic axicon providing extended focusing range. *Optics letters*, *33*(15), 1696–1698.

[104] Planchon, T. A., Gao, L., Milkie, D. E., Davidson, M. W., Galbraith, J. A., Galbraith, C. G., & Betzig, E. (2011). Rapid three-dimensional isotropic imaging of living cells using Bessel beam plane illumination. Nature methods, 8(5), 417–423

[105] Shi, J., Wang, L., Noordam, C., & Wang, L. V. (2015). Bessel-beam Grueneisen relaxation photoacoustic microscopy with extended depth of field. Journal of biomedical optics, 20(11), 116002.

[106] Jiang, B., Yang, X., & Luo, Q. (2016). Reflection-mode Bessel-beam photoacoustic microscopy for in vivo imaging of cerebral capillaries. Optics express, 24(18), 20167–20176.

[107] Park, B., Lee, H., Jeon, S., Ahn, J., Kim, H. H., & Kim, C. (2019). Reflection-mode switchable subwavelength Bessel-beam and Gaussian-beam photoacoustic microscopy in vivo. Journal of biophotonics, 12(2), e201800215.

[108] Hu, Y., Chen, Z., Xiang, L., & Xing, D. (2019). Extended depth-of-field all-optical photoacoustic microscopy with a dual non-diffracting Bessel beam. Optics letters, 44(7), 1634–1637.

[109] Moore, M. J., El-Rass, S., Xiao, Y., Wang, Y., Wen, X. Y., & Kolios, M. C. (2018). Simultaneous ultra-high frequency photoacoustic microscopy and photoacoustic radiometry of zebrafish larvae in vivo. Photoacoustics, 12, 14–21.

[110] Yang, J. M., Li, C., Chen, R., Rao, B., Yao, J., Yeh, C. H., Danielli, A., Maslov, K., Zhou, Q., Shung, K. K., & Wang, L. V. (2015). Optical-resolution photoacoustic endomicroscopy in vivo. Biomedical optics express, 6(3), 918–932.

[111] Xiong, K., et al. (2019). Shape-adapting panoramic photoacoustic endomicroscopy. Optics letters **44**(11): 2681-2684.

[112] Nedosekin, D. A., Fahmi, T., Nima, Z. A., Nolan, J., Cai, C., Sarimollaoglu, M., Dervishi, E., Basnakian, A., Biris, A. S., & Zharov, V. P. (2017). Photoacoustic in vitro flow cytometry for nanomaterial research. Photoacoustics, 6, 16–25.

[113] Cai, C., Nedosekin, D. A., Menyaev, Y. A., Sarimollaoglu, M., Proskurnin, M. A., & Zharov, V. P. (2016). Photoacoustic Flow Cytometry for Single Sickle Cell Detection In Vitro and In Vivo. Analytical cellular pathology (Amsterdam)

[114] Zhang, P., Li, L., Lin, L., Hu, P., Shi, J., He, Y., Zhu, L., Zhou, Y., & Wang, L. V. (2018). High-resolution deep functional imaging of the whole mouse brain by photoacoustic computed tomography in vivo. Journal of biophotonics, 11(1), 10.1002/jbio.201700024.

[115] Gottschalk, S., Degtyaruk, O., Mc Larney, B., Rebling, J., Hutter, M. A., Deán-Ben, X. L., Shoham, S., & Razansky, D. (2019). Rapid volumetric optoacoustic imaging of neural dynamics across the mouse brain. Nature biomedical engineering, 3(5), 392–401.

[116] Tsai, T. H., Leggett, C. L., Trindade, A. J., Sethi, A., Swager, A. F., Joshi, V., Bergman, J. J., Mashimo, H., Nishioka, N. S., & Namati, E. (2017). Optical coherence tomography in gastroenterology: a review and future outlook. Journal of biomedical optics, 22(12), 1–17.

[117] Ferhatoglu, M. F., & Kıvılcım, T. (2017). Anatomy of esophagus. Esophageal Abnormalities.

[118] Michels, R., et al. (2008). Optical properties of fat emulsions. Optics Express **16**(8): 5907-5925.

[119] Sweer, J. A., et al. (2019). Wide-field optical property mapping and structured light imaging of the esophagus with spatial frequency domain imaging. Journal of Biophotonics **12**(9): e201900005.

[120] Kuo, B. & Urma, D. (2006). Esophagus - anatomy and development. GI Motility online.

[121] Shamsudhin, N., et al. (2017). Magnetically guided capsule endoscopy. Medical Physics **44**(8): e91-e111.

[122] Koulaouzidis, A., Lakovidis, D. K., Karargyris, A., & Rondonotti, E. (2015). Wireless endoscopy in 2020: Will it still be a capsule?. World journal of gastroenterology, 21(17), 5119–5130.

[123] Ali, Z., Zakian, C., & Ntziachristos, V. (2021). Ultra-broadband axicon transducer for optoacoustic endoscopy. Scientific Reports, 11(1)

[124] Skjelvareid, M. (2012). Synthetic aperture ultrasound imaging with application to interior pipe inspection. Doctoral Thesis. University of Tromsø

[125] Jongin, P., et al. (2016). Delay-multiply-and-sum-based synthetic aperture focusing in photoacoustic microscopy. Journal of Biomedical Optics **21**(3): 1-10.

[126] Yao, J., & Wang, L. V. (2013). Photoacoustic Microscopy. Laser & photonics reviews, *7*(5), 10.1002/lpor.201200060.

[127] Olofsson, T. (2010). Phase shift migration for imaging layered objects and objects immersed in water. IEEE Transactions on Ultrasonics, Ferroelectrics, and Frequency Control **57**(11): 2522-2530.

[128] Skjelvareid, M. H., et al. (2012). Synthetic aperture focusing of outwardly directed cylindrical ultrasound scans. IEEE Transactions on Ultrasonics, Ferroelectrics, and Frequency Control **59**(11): 2460-2469.

[129] Haun, M. A., et al. (2002). Efficient three-dimensional imaging from a small cylindrical aperture. IEEE Transactions on Ultrasonics, Ferroelectrics, and Frequency Control **49**(7): 861-870.

[130] Stylogiannis, A., et al. (2018). Continuous wave laser diodes enable fast optoacoustic imaging. Photoacoustics **9**: 31-38.

[131] Zhang, W., et al. (2020). Simultaneous photoacoustic microscopy, spectral-domain optical coherence tomography, and fluorescein microscopy multi-modality retinal imaging. Photoacoustics **20**: 100194.

[132] Wartak, A., et al. (2021). Dual-modality optical coherence tomography and fluorescence tethered capsule endomicroscopy. Biomedical Optics Express 12(7): 4308-4323.

[133] Wartak, A., et al. (2021). In vivo optical endomicroscopy: two decades of translational research towards next generation diagnosis of eosinophilic esophagitis. Translational Medicine Communications 6(1): 2.

[134] Leitgeb, R. A. & Baumann, B. (2018). Multimodal Optical Medical Imaging Concepts Based on Optical Coherence Tomography. Frontiers in physics, 6.

[135] Kim, S. H. & Chun H. J. (2021). Capsule Endoscopy: Pitfalls and Approaches to Overcome. Diagnostics (Basel) 11(10),1765.